Dynamics Modeling, Simulation and Analysis of a Floating Offshore Wind Turbine

Mohammed Khair Hamdan Al-Solihat

Supervisor: Prof. Meyer Nahon
Department of Mechanical Engineering
McGill University, Montreal
Canada

April 2017

A thesis submitted to McGill University
in partial fulfillment of the requirements of the degree of
Doctor of Philosophy

Dedicated to:

my father and mother
my wife and kids
my brothers and sisters
the soul of my grandfather Mnizel

ABSTRACT

Floating Offshore Wind Turbines (FOWTs) are a promising technology to harness the abundant offshore wind energy resources in open ocean areas. A FOWT consists of a floating platform, the moorings, and the wind turbine structure (tower + Rotor-Nacelle Assembly (RNA)). The main focus of this thesis is to develop multibody dynamic models that integrate the structural dynamics, and hydrostatic, hydrodynamic, aerodynamic and mooring system loads. Special efforts are also devoted to characterize the mooring and hydrostatic loads as main sources of systems stiffness that shapes the dynamic behavior of the system.

Two approaches for modeling the platform/tower dynamics are developed, a rigid multibody model and a coupled rigid-flexible multibody model. Both models treat the platform, nacelle and rotor as six-degrees-of-freedom (6-DOF) rigid bodies. However, modeling the wind turbine tower dynamics differs between these approaches. The rigid model considers the tower as a 6-DOF rigid body while the flexible model represents the tower as a three-dimensional (3D) tapered damped Euler-Bernoulli beam undergoing coupled general rigid body and elastic motions. In both approaches, the wind turbine drivetrain dynamics is also considered to capture the rotor spin response. The equations of motions of both models are derived symbolically using Lagrange's equation.

The hydrostatic restoring loads are evaluated through development of a novel nonlinear hydrostatic approach. This approach allows evaluating the exact hydrostatic force and moment and position of the center of buoyancy as function of the platform displacement and *finite* rotation. New exact expressions for the water plane area restoring moments are developed. The hydrostatic stiffness matrix at an arbitrary position and orientation of the platform is subsequently derived.

A quasi-static approach is then developed to determine the cable tensions of the single-segment or multi-segment the mooring system configurations proposed to moor the platform to the seabed. The approach uses different governing equations, depending on whether the mooring lines partially rest on the seabed; are suspended; or fully taut. The exact mooring stiffness is subsequently derived and the influence of several mooring system parameters on the mooring system stiffness is investigated.

As an alternative to the quasi-static cable model, a lumped mass cable model incorporating the cable-seabed contact effect is developed to integrate the cable dynamics into the FOWT system dynamics. The equations of motion of the mooring line nodes are assembled for the two mooring system configurations under consideration. A new methodology is also presented to calculate the equilibrium profile of the mooring line lying on a seabed as desirable initial conditions for solving the discretized cable equations of motion.

Finally, the theoretical models are implemented through a large simulation tool to analyze the dynamic behavior of the spar FOWT system under study. A series of simulations under defined external loads (*load cases*) are performed to validate the dynamic models. The simulation results are compared with similar results obtained from well-known offshore wind simulation tools. The simulation results are found to be in very good agreement with the reported results. Numerical experiments are also performed to investigate the influence of the tower flexibility, mooring system configuration, rotor gyroscopic moment and cable dynamics on the system dynamic behavior. The results show that the system responses obtained from the rigid body model under-predict the platform yaw response and exhibit less damping than those obtained from the flexible model. It is also found that the mooring system configuration choice does not influence the platform roll and pitch responses or tower elastic deflections.

RÉSUMÉ

Les éoliennes offshores flottantes (EOFs) sont une technologie prometteuse pour exploiter les ressources abondantes d'énergie éolienne dans les zones des eaux océaniques ouvertes. Un EOF se compose d'une plateforme flottante, des amarres, et d'une structure de turbine éolienne (tour + Assemblage Rotor-Nacelle(ARN)). L'objectif principal de cette thèse est de développer des modèles dynamiques multicorps qui intègrent la dynamique structurelle, hydrostatique, hydrodynamique et aérodynamique ainsi que les charges de système d'amarrage. Des efforts particuliers ont été également consacrés pour caractériser l'amarrage et les charges hydrostatiques comme sources principales de la rigidité des systèmes qui façonne le comportement dynamique du système.

Deux approches de modélisation de la dynamique plateforme/tour ont développées, un modèle multicorps rigide et un modèle multicorps couplé rigide et flexible. Les deux modèles traitent la plateforme, la nacelle et le rotor en six degrés de liberté (6-DDL) de mouvement de corps rigides. Cependant, la modélisation dynamique de la turbine éolienne de la tour se distingue de ces approches. Le modèle rigide considère la tour comme un corps rigide 6-DDL tandis que le modèle flexible considère la tour comme une poutre tridimensionnelle (3D) de type Euler-Bernoulli conique amorti subissant un mouvement couplé de corps rigide général et élastique. Dans les deux approches, la dynamique du groupe motopropulseur de l'éolienne est également considérée pour déterminer la réponse de la rotation du rotor. Les équations de mouvement des deux modèles sont dérivées symboliquement en utilisant les équations de Lagrange.

Les charges hydrostatiques de rappel ont été évaluées à travers le développement d'une nouvelle approche hydrostatique non linéaire. Cette approche permet d'évaluer la force hydrostatique exacte, le moment et la position du centre de carène en fonction du déplacement et de la rotation finie de la plateforme. Des nouvelles expressions exactes de la zone de plan d'eau des moments restaurés sont développées. La matrice de raideur hydrostatique a été ensuite dérivée à une position et une orientation arbitraire de la plateforme.

Comme une alternative au modèle du câble quasi-statique, un modèle de masse ponctuelle d'un câble incorporant l'effet de contact (câble-fond marin) a été conçu pour intégrer la dynamique des câbles dans le système dynamique des EOF. Les équations de mouvement des nœuds de ligne d'amarrage ont été assemblées pour les deux configurations de système d'amarrage envisagées. Une nouvelle méthodologie a été également présentée pour calculer le profil de la ligne de mouillage se trouvant sur un fond marin (comme conditions initiales désirables) pour la résolution des équations discrètes du mouvement des câbles.

Enfin, les modèles théoriques ont été implémentés à travers un outil important de simulation pour analyser le comportement dynamique du longeron EOF à l'étude. Une série de simulations soumises à des charges externes définies (cas de charge) ont été effectuées pour valider les modèles dynamiques. Les résultats de la simulation ont été comparés aux résultats similaires obtenus à partir des codes de conception éolienne offshore bien connus. Les résultats de simulation ont été trouvés en très bon accord avec les résultats rapportés. Des expériences numériques ont été également réalisées pour étudier l'influence de la flexibilité de la tour, la configuration du système d'amarrage, la rotation du tour et la dynamique du câble sur le comportement dynamique du système. Les résultats montrent que les réponses du système obtenues à partir du modèle de corps rigide sous-prédisent la réponse de lacet de la plate-forme et présentent moins d'amortissement que celles obtenues à partir du modèle flexible. Il est également constaté que le choix de la configuration du système d'amarrage n'a aucune influence sur la réponse de la plate-forme de roulis et de tangage, ni la tour débattements élastique.

ACKNOWLEDGEMENTS

First and foremost, praise be to Allah almighty for His countless blessings and for giving me the health and strength to accomplish this work.

I would like to express my ultimate gratitude to my supervisor Prof. Meyer Nahon for his valuable guidance, support, mentoring and constructive criticism during the course of this work. I am also indebted to him for his continuous assistance not only in research but also in many different non-technical aspects. I would like to thank Dr. Marco Masciola for his sincere help and sharing his knowledge and experience with no limits. I am also grateful to him for his assistance and hospitality during my visit to NREL, CO, USA.

I would like to thank Prof. Inna Sharf for her constructive discussions in flexible dynamic modeling of the wind turbine tower. I am grateful to Dr. Jason Jonkman (NREL) for providing the simulation data and answering my inquiries by email. I would like to thank Dr. Finn Gunnar Nielsen (Statoil) for providing the bridle mooring system data. I would like also to thank my colleague Dr. Waqas Khan for discussing the aerodynamics of the turbine. Special thanks go to my friend Ahmad Hassan from École Polytechnique (Montreal) for translating the thesis abstract into French. I wish to express my sincere thanks to my friend Prof. Muhammad H. Alu'datt for his assistance and support.

The financial supports provided by the FQRNT, Faculty of Engineering–McGill University, NSERC and Prof. Nahon are gratefully appreciated.

Finally, I want to express my deepest appreciation to my parents. Words cannot describe my gratitude to their endless love, encouragement and support throughout my life. I am grateful to my wife for her patience, valuable assistance and sacrifice. I wish also to thank my kids for bringing happiness to our lives. I am also grateful to my parents-in-law for their great help and support in the hardest times during my PhD study. My appreciation is also extended to my brothers, sisters, brothers-in-law, sisters-in-law and all family members.

CLAIM OF ORIGINALITY

Following are the main original contributions of this thesis:

- An analytical formulation to determine the exact nonlinear hydrostatic restoring loads and stiffness of floating offshore platforms. Closed-form formulae are derived for calculating the exact buoyancy force and the corresponding moments for general 3D displacements of cylindrical platforms (of different cross sections such as circular, square, and rectangular).
- Development of an exact nonlinear analysis for the stiffness of a mooring system as a function of the displacement and orientation of the floating structure. The analysis allows a derivation of the mooring stiffness matrix while considering slack mooring line resting on the seabed, as well as slack and taut suspended lines.
- An exact three-dimensional nonlinear quasi-static model for computing the tensions of general mooring configurations, including delta lines and clump weights. These components are important in many proposed designs for offshore wind turbine platforms, notably the OC3-Hywind concept.
- Development of a closed-form rigid body dynamic model of a spar FOWT that considers the generator torque control.
- A comprehensive 3D flexible multibody dynamic model to analyze the dynamics of a spar FOWT. The model considers the coupled rigid and flexible motions arising from the platform, nacelle, and rotor rigid bodies and the flexible tower structure. As well, the generator torque control is integrated into the model to capture the rotor spin dynamics.
- Development of a lumped mass cable model incorporating the seabed contact for a single line and bridle mooring systems.
- Development a novel static solver for single line and bridle mooring systems. The solver determines the equilibrium profile of the cable whether suspended or resting on the seabed.

TABLE OF CONTENTS

LIST OF FIGURES

LIST OF TABLES

Chapter 1

INTRODUCTION

1.1 Motivation and Background

Wind energy currently supplies around 3% of the world's electricity. In particular, Northern European countries have made great strides in exploitation this source of clean energy, including Denmark where wind power met 28% of its electricity needs in 2012. This source of energy is growing at 25-30 % annually and is expected to fulfill 12% of the world's electricity demand by 2050 [8]. Most of this produced wind energy is obtained from land-based wind farms.

Recently, renewable energy investments are being directed to exploit the open ocean environment, which is rich in wind power, as an advantageous location for wind turbines fields. The exploitation of offshore wind power began two decades ago, existing offshore wind turbines are installed in shallow water and are fixed to the seabed by structures like monopoles and lattice towers. The harvesting of ocean wind power could constitute an abundant source of low cost energy. Installing wind turbines on floating platforms far offshore, in deeper water, where the wind is stronger and steadier, maximizes the obtained wind power. This can only be achieved using floating platforms to support the wind turbine due to the high cost of the fixed-bottom structures. Offshore placement also avoids the problems associated with noise and visual impacts. Several Floating Offshore Wind Turbine (FOWT) concepts have been proposed.

FOWT systems are in an early stage of research and development, a few prototypes are currently under construction and some are deployed in the ocean and equipped with instrumentation for testing and design evaluation. There are few guidelines for system design and the costs are high. At present, offshore wind energy research is focused on the design of a durable floating system which can be deployed in deep water and can withstand the harsh ocean waves and wind environment at a reasonable cost.

1.2 FOWT Concepts

A FOWT system consists of a buoyant platform supporting the wind turbine and anchored to the sea bottom by a series of cables (mooring system) to hold the system in position. The platform and tethers are subjected to hydrodynamic disturbances, while the wind turbine tower and rotor are subject to aerodynamic loads. FOWT preliminary designs and prototypes utilize the same floating platforms concepts conventionally used in the offshore oil and gas industry namely, spar-buoy, tension-leg platform (TLP), semi-submersible, and pontoon-type (barge-type) [1], as shown in Figure 1.1.

Spar-buoy platforms consists of a cylindrical floater made of steel and concrete filled with ballast of water and gravel. The draft of the spar is usually larger than the turbine hub height. A solid metal permanent ballast is used at the bottom of the floater to further lower the centre of gravity to be well below the center of buoyancy, thus stabilizing the floater and attenuating the wave/current-induced translational and rotational motions [9]. The floater is held in position by a catenary mooring system comprised of at least three lines. However, a recent proposed design by the SWAY company suggested mooring a spar FOWT by a single vertical taut tendon connected to the seabed anchor by a universal joint that allows the tower to yaw according to wind direction, so that the turbine rotor always faces the oncoming wind [10], a model of the SWAY concept was deployed in 2010, but it collapsed due to extreme environmental conditions in 2011.

The TLP design is comprised of a floater connected to the seabed by taut vertical mooring lines that stabilize the system. The high tension of the mooring lines is produced by the floater excess buoyancy, which in turn yields high heave, roll and pitch stiffnesses. Mooring stiffness in surge, sway and yaw directions are lower which allows the system to move a few feet horizontally. However this large amplitude of motion is not dangerous since the turbine tower stands vertical and there are no excessive nacelle and tower inertia forces [10, 11].

The Semi-submersible design consists of three pontoons connected together by steel tubu-

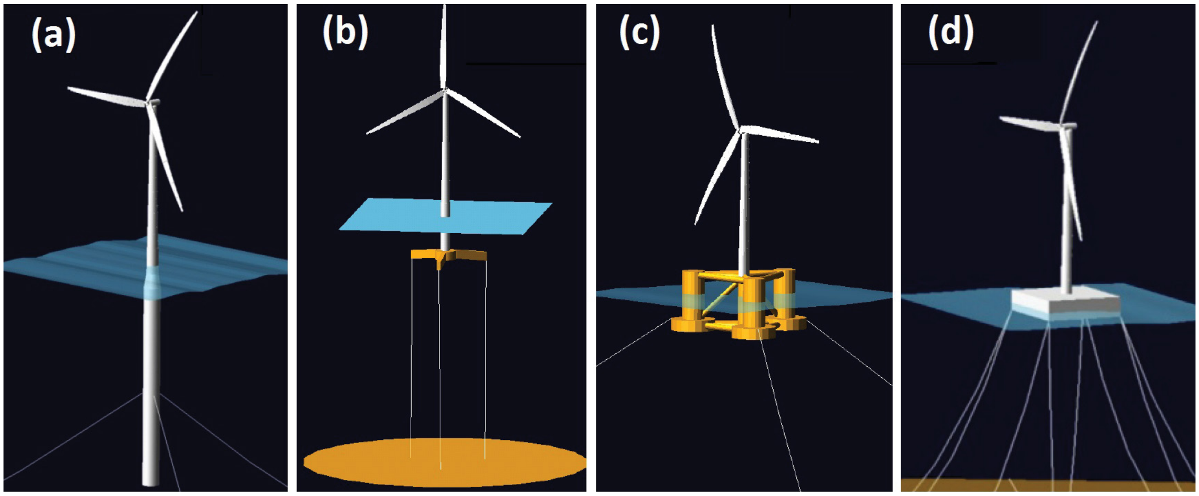

Figure 1.1: FOWT design concepts: (a) Spar-buoy; (b) TLP; (c) semi-submersible; and (d) barge [1]

lar beams to form an equilateral triangle structure moored to the seabed by catenary mooring lines. This design can support 1-3 turbines placed on the pontoons centers, or can be modified to install a single turbine on the platform center as in the proposed Dutch tri-floater concept [11]. The large waterplane area of platform yields high hydrostatic restoring moment that stabilizes the system.

The barge concept is simply a catenary-moored wide pontoon (compared to its height) that can support single or multiple FOWTs [11, 12]. In addition to the aforementioned platform concepts, there are several proposed hybrid designs that combine two or more concepts designs, for instance the tension-leg spar (TLS) concept that merges the spar-buoy and TLP design concepts [11]. A further review for all the concepts of FOWT and existing models can be found in literature survey papers [9, 10].

A few prototypes have been recently deployed in the ocean. The first full scale prototype of a spar-buoy type in operation was launched close to the south-west coast of Norway in 2009 by STATOIL, with a power capacity of 2.3 MWT. In October 2011, Principle Power Inc., launched the WINDFLOAT prototype, a 2-MWT submersible FOWT installed near the north coast of Portugal. Beyond these, several renewable energy companies intend to launch their full scale models in the coming years.

1.3 Mooring System

The mooring system is a system of cables connecting the floating platform to the anchors installed on the seabed to maintain the platform in position and restrain the platform displacement against the aerodynamic and hydrodynamic loads: this is referred to as station-keeping [13–15]. Mooring systems can be constructed using either cables, chains, synthetic ropes or a mix of them e.g. a metal chain at the bottom and light cable or rope close to the structure attachment points [13–15]. A review of the mooring lines materials and anchor types can be found in [15]. In some designs, buoys could be attached to the mooring lines to reduce the mooring system weight carried by the floating structure. Also, clump weights can be attached along the mooring lines to enhance the mooring system stiffness and reduce the anchor tension fluctuations [14].

Mooring systems are classified as catenary, taut-leg and tension leg. The material and design of these systems depend on the structure type and water depth [14, 15]. Catenary moorings are the most common where the mooring line is slack and hangs under its own weight. Part of the line may lie on the seabed. In both the taut and tension leg mooring, the mooring line is pretensioned by the floating structure excess buoyancy force, the line is highly taut and almost no sag exists. In the tension leg mooring system, most of the line restoring force acts in the vertical direction and this requires a special anchor designs that are expensive to construct and install [16].

1.4 Literature Review

Dynamic modeling of FOWT is a multidisciplinary problem combining different disciplines, including flexible and rigid body dynamics, hydrostatics, hydrodynamics, aerodynamics, and cable mechanics. Following is an overview of the relevant literature on the main topics related to the dynamics of FOWTs.

1.4.1 System stiffness

System stiffness characteristics have a large impact on the floating structure's static stability and dynamic response to environmental loads. The system stiffness is mainly attributed to the platform buoyancy (including gravity) and mooring system stiffnesses. Hydrostatic stiffness in conjunction with the mooring stiffness, determines the static offset of floating structure when steady loads act on the platform. The hydrostatic stiffness is the main contributor to the system stiffness for offshore platforms that use slack moorings such as spar, barge and semi-submersible platforms. In barge platforms, for instance, the main contributor to system stability is the large water plane area which produces a large hydrostatic restoring moment in response to the platform rotations. By contrast, the taut mooring is the main contributor to the system stiffness for TLPs. Hydrostatic (buoyancy) stiffness influences the heave, pitch and roll dynamics of offshore floating platforms and has a large impact on the natural frequency of the floating structure [17].

Mooring stiffness contributes to the load-excursion relationship and the natural frequency of the floating structures particularly in surge, sway and yaw modes where the hydrostatic stiffness is nonexistent [15, 17]. The mooring stiffness is mainly influenced by the line tension and length, footprint area (anchor radius), material properties, mooring configuration and number of lines [18, 19]. Static analysis of the mooring lines determines the equilibrium line shape and tension under the actions of self-weight and steady loads which offset the floating structure from its equilibrium position [14, 19].

The changes in static forces and moments exerted by mooring lines and buoyancy with respect to the floating structure displacements are represented using a stiffness matrix. The following sections review the main approaches used to determine the hydrostatic and mooring restoring loads and stiffness characteristics.

1.4.1.1 Hydrostatic loads and stiffness

Hydrostatic and gravity loading characteristic are the main determinant of a floating structure's static stability and have a large impact on the structure's dynamic response to environmental loads [17, 18, 20]. Typically, the hydrostatic restoring forces and moment are computed using a linear hydrostatic approach. This assumes the submerged structure is a rigid body and any structural deformations are ignored and the hydrostatic restoring force and moment are due to the infinitesimal changes of translational and rotational displacements [17]. The change in hydrostatic force and moments with respect to these displacements are represented using a stiffness matrix conventionally calculated at the initial static equilibrium position or even keel [17, 18, 20, 21]. However, different initial positions can be experienced due to steady loading (e.g. from water currents).

Hydrostatic restoring force and moments are nonlinear in translational and rotational displacements particularly heave, roll and pitch displacements if measured relative to a fixed space frame [21–26]. The nonlinear hydrostatics are a topic of importance in coupled dynamics of ships [26–29]. The hydrostatic nonlinearity can magnify the motion response amplitude and lead to ship capsizing [30]. The influence of nonlinearity is induced by large displacement and coupling among heave, roll and pitch displacements. Thus the linear approach cannot precisely estimate the hydrostatic loads required to determine equilibrium position and orientation of the floating structure and simulate the motion response [22, 31].

A few models characterizing the nonlinear hydrostatic restoring forces and moments for offshore platforms are available in literature. Most these models consider partial coupling among the displacements i.e. either heave-roll or heave-pitch coupling. Yim et al. [25] developed a coupled heave-roll regression-based hydrostatic model to capture the nonlinear response of a tethered barge for large roll angle motion. The hydrostatic restoring force and moments are represented by high degree polynomials as functions of position and roll rotation of the barge. Dalane et al. [24] developed an exact analytical representation for nonlinear heave-pitch restoring forces and moment for arctic canonical platforms and general expressions for its metacentric height. Soylemez [23] presented a method for approximate calculation of nonlinear restoring forces to simulate the motion response of a semi-submersible platform. Ku et al. [21] developed an iterative approach to determine the equilibrium position and hydrostatic stiffness considering large inclination angle for a barge supporting a floating crane. Zeng et al. [22] compared the 6-DOF dynamic response of a tethered circular cylinder using linear and nonlinear hydrostatic approaches. The difference between these approaches was significant for rotation responses at higher wave heights. A similar dynamic analysis considered the platform finite rotation and the associated nonlinearities in calculating the hydrostatic loads for a TLP [31]. Similar observations were noted when comparing the displacement responses of the TLP using the linear and nonlinear hydrostatic models.

1.4.1.2 Mooring stiffness

Similar to hydrostatic loads, the restoring force and moments exerted by the mooring system are nonlinear in translational and rotational displacements of the floating structure. The nonlinearities become more pronounced for large displacements and due to coupling among the displacements. The mooring system stiffness is mainly dependent on the elastic and geometric stiffnesses of a cable which are the most significant, while the bending stiffness is always ignored when the cable is sufficiently long [32]. When a cable is slack or has a low tension, its geometric stiffness (resulting from the shape change) is the key contributor to its stiffness behavior, because the cable deformation leads mostly to a change in its profile shape i.e. sag rather than structural deformation of the cable itself [19, 32].

A few models characterizing the nonlinear mooring stiffness of catenary moorings are available in literature. Most of these models ignore the line elasticity. The line elasticity can be neglected for heavy slack mooring line such as a chain and particularly when a portion of its length lies on seabed [18, 19]. However, when the line is lifted off the seabed, its elasticity should be considered especially for large horizontal excursions of the attachment point. Jain [33] derived the 2×2 stiffness matrix (surge and heave) of an inextensible slack mooring line neglecting seabed interactions. Lee and Cho [34] presented a similar stiffness matrix form for an inextensible slack mooring line resting on the seabed. Sannasiraj et al. [35] extended these works by deriving the mooring line stiffness matrix of a slack mooring line in sway, heave and roll modes to predict the motion response of a pontoon-type floating breakwater. Loukogeorgaki [36] presented a generic model to determine the mooring stiffness matrix (6×6) of a floating breakwater to study its dynamic response. The stiffness coefficients were represented in terms of the differential change of the line tension with respect to its chord elevation angle.

The nonlinear mooring restoring forces due to large changes in displacement and orientation of a platform is a topic of importance in the dynamics of tension leg platforms (TLPs) [37]. Jain [38] presented a stiffness matrix considering the surge, sway and yaw modes for a rectangular TLP. Chandrasekaran et al. [39] derived a nonlinear stiffness matrix as functions of the platform displacements for a triangular TLP to simulate the 6-DOF response to regular wave loads. The derived form considered coupling among the displacements based on some geometric approximations. Senjanovic et al. [37,40] derived a new 6×6 stiffness matrix formulation for a TLP considering large displacements in surge, sway and yaw displacements. Low [41] derived the stiffness matrix of a TLP using an energy approach to perform a dynamic analysis for a rectangular TLP in the frequency domain.

1.4.2 System dynamics

1.4.2.1 Structural analysis

A FOWT tower can be idealized as a beam with a tip mass attached to a rigid moving base (platform). Similarly, the rotor blades can be modeled as rotating cantilever beams. Many studies have investigated the dynamics of a beam attached to a moving base particularly the so-called *hub-beam system* problem, usually in aerospace and robotics applications such as helicopter rotor blades and robot arms [42–46]. Most of these models considered partial coupling among the beam elastic deformations namely the two bending, axial and twist deformations. Among these works, Cai et al. [4] analyzed the dynamics of a flexible hub system with a tip point mass considering the coupled stretch and bending elastic motions using a finite element method (FEM). Yang et al. [47] presented a FEM dynamic model for a flexible hub-beam system with a tip point mass. The damping forces due to the beam's internal structure, hub friction and air drag were considered. Hamilton's principle was used to derive the equations of motion. Bhadbhade et al. [48] developed a coupled bending and torsion dynamic model of a rotating cantilever with a rigid body at the tip. The extended Hamilton's principle was used to derive the equations of motion. Another study by Sakawa and Luo [49] presented a coupled bending and torsion vibration analaysis of a rotating beam carrying a tip rigid body.

Formulations for the flexible dynamics of beams undergoing general coupled bending-bending-axial-twist elastic motion are rarely found in literature. This is attributed to the modeling and computational complexities in treating the interaction between the elastic motions. Most recent, a work by Cooley and Parker [50] presented a linear flexible dynamic model of a spinning cantilever beam undergoing coupled bending-bending-torsional-axial motions with an attached tip rigid body. The equations of motion were discretized using Galerkin's method to determine the natural frequencies, mode shapes and system stability. All the previous reviewed works dealt with a prescribed base motion of the beam. Thus, the equations of motion were derived in terms of the elastic coordinates since the rigid body motion was prescribed. However, this is not the case in the FOWT system where the platform motion (base) is not prescribed, yielding coupled rigid body and elastic motions which is far more complex.

The kinematic formulation of beam motion is a crucial aspect in modeling flexible body dynamics. This includes defining the beam elastic displacements and the elastic rotation matrix of the beam cross section along the deformed elastic axis [51]. Characterizing the beam deformations using the conventional linear deformation field yields linear dynamic equations free of the geometric stiffening [47,52–54]. The major disadvantage of this approach is its failure in capturing the dynamic behavior of coupled rigid-flexible systems experiencing large elastic deformations particularly due to high rotational speeds [50, 54]. Therefore, more sophisticated nonlinear deformation formulations that include the geometric stiffening effect were introduced. Kane [42] presented a dynamic analysis of a beam attached to a moving base undergoing general translational and rotational motion. The longitudinal and bending-bending, torsion motions of the beam were formulated. Yoo et al. [55] presented a flexible dynamic model for an Euler-Bernoulli beam undergoing overall motion and small strain elastic deformations. The model considered the bending in two planes together with longitudinal stretching. A similar model was developed by Boutaghou et al. [56] for flexible beams and thin plates using Hamilton's principle assuming arbitrary deformation kinematics. Liu and Hong [52] presented a geometric nonlinear formulation of a three-dimensional beam undergoing large overall motion. The coupled bending-bending and stretch elastic motion were considered and a criterion for validity of the linear kinematic approach was proposed. The comprehensive work of Shi et al. [51] presented a nonlinear deformation field for Euler-Bernoulli beams. Their main effort was devoted to develop a new second order elastic rotation matrix based on the two-Euler angle approach [57].

1.4.2.2 Dynamic modeling of flexible land-based wind turbine

Owing to the increasing interest in wind energy, several flexible dynamic models for wind turbines have been proposed in the literature. Larsen and Nielsen [58] developed a nonlinear dynamic model for a land-based wind turbine structure considering the tower and blade flexibility. The model included geometric nonlinearities caused by the structure deflections. Kessentini et al. [59] conducted a modal analysis using a linear dynamic model considering the flapping deflections of the tower and blades. The effects of pitch angle and blade orientation on the wind turbine natural frequencies and mode shapes were also investigated.

Lee et al. [60] presented a multibody dynamics model for the wind turbine considering the coupled dynamics among the rigid body (nacelle and hub) and flexible (tower and blades) subsystems assuming a prescribed rotor speed to determine system natural frequencies and mode shapes. Another modal analysis for a tapered wind tower was performed by Makarios [61]. In this model the rotor nacelle assembly mass and inertia were ignored. More recently, Kang [62] conducted a stability analysis for the coupled flexible tower-blade system. The theoretical results were validated experimentally using a small scale prototype. However, all these models are restricted to land-based wind turbines and a flexible dynamic model of a FOWT has not been addressed yet in the literature.

1.4.2.3 Dynamic modeling of FOWTs

Unlike land based wind turbines, FOWTs are subject to combined wind and hydrodynamic, hydrostatic, and mooring loads that have significant impact on the system behavior. This requires rigorous multi-physics dynamic analysis for an efficient design to avoid the risk of structural failure. The complexity of this system makes the dynamic analysis quite challenging.

Few theoretical rigid body dynamic models of FOWTs have been presented in literature. Matsukuma and Utsunomiya [63] developed a multibody dynamic model of a 2 MW spar FOWT assuming steady wind and still water. The influence of gyroscopic moment due to the rotor spin was found to be considerable on the system dynamics. Wang and Sweetmn [64, 65] developed a rigid multibody dynamic model for a tension leg FOWT. The equations of motion were formulated using a Newton Euler approach. Sandner [66, 67] presented a spar FOWT model based on the OC3 design concept. Simple aerodynamic, hydrodynamic models were integrated to simulate the system response in combined wind and wave loads. Ramachandran et al. [68] presented a coupled 3D rigid body dynamic model of a TLP FOWT. The aerodynamic loads were evaluted using unsteady blade-element-momentum (BEM) theory. The dynamic response results were also validated against the *Flex5* code. None of these works considered the elastic motion of flexible components and the coupling between the flexible and rigid body motions although it can be considerable. However, these works [66–68] approximated the tower fore-aft motion using a spring-mass system placed on the tower tip.

1.4.2.4 Simulation tools

Several FOWT simulation codes incorporating aerodynamic, structural dynamic, hydrodynamic, control and cable models have been developed to capture the coupled dynamic response of FOWTs to the environmental loads [5, 69]. These codes vary in their capabilities. Following is a list of the most widely used flexible multibody dynamics codes, ordered accoding to their popularity:

- FAST: this code for dynamic analysis of land based and offshore wind turbines was developed by the National Renewable Energy Laboratory (NREL) and is publically available.

- HAWC2: a widely used code for simulating FOWTs developed by Riso National Laboratory.

- GH Bladed: developed by GL Garrad Hassan to perform dynamic analyses for bottom-fixed wind turbines (land based and offshore). The code has recently promoted its capabilities to analyze FOWTs [69].

- 3DFloat: developed by the Norwegian University of Life Sciences (UMB) to simulate FOWTs [69]. Unlike the above-listed codes, this code ignores the rotor blade flexibilities while considering the tower elasticity.

- ADAMS: developed by MSC Software Corporation as commercial software for general multibody modeling i.e. it is not dedicated only for FOWT dynamic analyses as the previous codes. The software has been used by many researchers to build dynamic models of FOWTs [69].

Additionally, other simulation tools adopting the rigid multibody modeling approach such as SIMO and SEASAME/DEEPC were developed to analyze the FOWT system dynamics with neglecting the flexible motions of the tower and rotor blades. A thorough review of all these codes, their capabilities, and the techniques they adopted to model the system structural dynamics and the fluid-structure-interactions can be found in [69]. However, the detailed theoretical dynamic models on which these codes are based are not available in literature. Moreover, most these codes use simplified linear structural models which could introduce inaccurate response if the structure experiences large deflections [58]. Owing to the rise in interest in FOWTs systems, new codes are being developed and other current codes are being improved and extended.

These codes, particularly FAST, are used in many research studies to investigate the dynamic aspects of different types of FOWTs. Jonkman [12] performed a fully coupled aero-hydro-servo-elastic dynamic analysis of a 5 MW barge type FOWT with slack catenary mooring using a quasi-static cable model. Many simulations were done to determine the potential loads and associated instabilities. Wayman [70] developed a coupled dynamic analysis including the gyroscopic effects of the turbine rotor utilizing linear wave theory for the MIT/NREL TLP FOWT concept in the frequency domain. The influence of water depth and wind speed were investigated. Another work by Matha et al. [71] conducted a dynamic analysis for a 5 MW TLP FOWT to identify the system instabilities and compare the loads of the TLP FOWT with its land-based counterpart. Robertson et al. [1] carried out dynamic response analyses for 6 designs of a 5 MW FOWT. The fatigue loads and stability analyses were performed using the FAST code [72]. The results showed that the barge type platform exhibits the worst performance and results in high loads namely bending moments of the blade root, the low speed shaft, yaw bearing and the tower base. Sclavounos et al. [73] compared the rms nacelle acceleration and rms mooring lines tensions for a TLP and taut leg buoy (TLB) platforms. They investigated systems to support 3 MW and 5 MW wind turbines in 30-50 and 50-150 m water depth, respectively, subjected to wave heights of 6-14

m. Their results showed that the TLP exhibits both lower nacelle acceleration and anchor tension in deeper water, while higher nacelle acceleration and anchor tension were observed as the water depth increases for the TLB.

FOWT dynamic studies were also performed using HAWC2, especially in the Nordic countries. Nielsen et al. [74] developed an integrated dynamic analysis of the STATOIL spar FOWT, and compared simulation results with model experiments. Their experiment results showed that the blade pitch control at high wind speeds leads to a negative damping instability for the tower motion. Karimard et al. [7, 75] performed several dynamic analyses particularly for a spar FOWT with tension leg and catenary mooring system. These analyses aimed to (i) discuss the hydrodynamic and aerodynamic effect on FOWT dynamics, and (ii) present a simplified method to determine aerodynamic forces with reasonable accuracy. Another stochastic dynamic response analysis of a spar FOWT [76] was conducted to evaluate the fatigue limit under combined wave and wind loading and structural response in harsh wave and wind conditions.

1.4.3 Cable models

Early cable models approximate the cables as massless springs with constant stiffness, which might be valid for taut moorings. It can also be used for slack moorings in the case of a small cable displacement i.e., the cable nonlinear stiffness is linearized around an equilibrium condition [15]. However, this approach is inaccurate particularly if the structure experiences large displacement. Alternatively, the mooring line tension can be determined using the quasi-static and dynamic cable models. The first approach uses the equation of an elastic catenary that can be solved numerically, this approach is illustrated in many references e.g. [18, 32, 33, 77]. Oscillatory forces such as wave and fluid-cable interactions as well as inertia forces and internal cable damping can not be considered in this analysis, and the tension determined using this approach is referred to as the *quasi-static* tension. Most dynamic analyses of FOWTs [16] utilize this quasi-static approach which is considered appropriate for shallow water and low frequency restoring force. However, the maximum dynamic tension can be considerably higher than the quasi static counterpart, particularly for high frequency motion and in deep water [14, 78].

It has been observed that the hydrodynamic damping at higher frequency mooring line motion forces the cable to stretch instead of changing its sag yielding a higher dynamic cable tension than that predicted by quasi-static approach [14, 79]. This observation is also justified by Kreuzer et al. [79] when investigating the dynamics of a single mooring line while including the effect of fluid-structure interaction. The analysis was conducted using a multibody system approach (MBS) for an 800-m steel wire anchored at 500 m water depth. The free cable end is considered to translate harmonically at 10 m amplitude with frequency varying from 0.025 to 0.25 rad/s. The results showed that the computed dynamic tension at low frequency is similar to that of quasi-static approach, while at high frequency excitation the maximum dynamic tension is more than twice the quasi-static tension. Moreover, a phase shift between the dynamic and quasi-static tension responses was noted.

Cable dynamics can be evaluated numerically through discretization techniques such as lumped mass and finite element methods [80, 81]. The lumped mass approach models the cable as system of discrete masses connected to each other by massless springs and dampers, neglecting the cable bending and torsional stiffnesses. The influence of hydrodynamic forces and fluid drag and cable-seabed interaction can be considered. The equations of motion of the lumped masses can be solved in the time domain. Van Den Boom [78] used this method by lumping all the inertial and external forces while ignoring the cable damping to analyze the mooring system dynamics. The results agreed reasonably with experiments. Jeffery et al. [82] presented a linear and nonlinear FEM dynamic models for a taut a mooring system to study the spatial variation of tether tension. Another FEM cable model that includes the bending torsion effect to study the cable dynamics of slack cables in three dimensions was developed by Buckham et al. [83]. A thorough review of the main numerical techniques used in cable dynamics can be found in [80, 81].

1.4.4 Wind and wave loads

Realistic environmental loads modeling is an important aspect in the simulation of offshore structures. Wave loads are considered the most severe compared to current and wind loads [14]. The wave hydrodynamics is generally characterized by linear Airy wave theory when the wave height is small compared to water depth and wave length. Assuming the fluid is incompressible and inviscid and the flow is irrotational allows the use of the potential flow theory [13, 18]. Nonlinear wave theories are used to predict the steady and slowly varying drift force components and also in the case of breaking waves and severe sea states [14]. The hydrodynamic analysis in generally performed using Morison's equation which is only valid for slender structures accounting for the inertial and drag forces acting on the submerged part of the structure and ignoring wave diffraction effect [18, 84, 85]. The effect of combined wave and current is included in Morison's equation through vectorial addition of the fluid velocity. The total wave force on the structure can also be determined by integrating the pressure distribution over the submerged part of the structure [18, 84].

Wind loads can be determined using similar approaches used for land-based wind turbines. The aerodynamic lift and drag forces acting on the wind turbine blades due to steady and turbulent wind can be determined using blade element momentum theory (BEM) [72]. Wind speed increases logarithmically with height due to wind shear in the planetary boundary layer. Therefore, a higher tower increases the obtained wind energy [86]. The variation of wind speed with height depends on the surface roughness. In smooth terrain such as open sea, the wind speed reaches its free stream value at a lower height with lower levels of turbulence intensity compared to land. Therefore, wind speed at the same height above water level is higher than that above ground level for the same nominal storm conditions [85]. Sometimes, fluctuating wind gusts can excite a resonant motion of the structure [18].

1.5 Thesis Objectives and Organization

The FOWT is an emerging technology. Design of this system requires deep understanding of the system dynamics which implies developing reliable dynamic models capable of predicting the system dynamic response. Thus, the primary objective of this thesis is to build a high-fidelity structural dynamic model of a FOWT coupled with quasi-static and lumped mass cable models for different mooring system configurations, including single and delta (bridle) arrangements. Effort is focused on developing a validated coupled rigid and flexible multibody dynamic models of a spar FOWT as well as building a reliable hydrostatic and cable models to simulate the system dynamics.

This thesis consists of seven chapters. Chapter 1 presents background and motivation behind the research, a review for the works related to the research problem, and thesis objectives and organization. The developments of rigid and flexible multibody dynamic models of the FOWT are detailed in Chapter 2. The chapter begins by defining the platform kinematics then deriving the equation of motion of the FOWT in terms of the platform quasi-coordinates and rotor spin speed for the rigid model. The development of the flexible dynamic model then follows. The kinematics of the flexible and rigid body motions and discretization of the elastic motion in space and time are established. Then, the coupled rigid-flexible equations of motion are derived using Lagrange's equation. Modeling the hydrodynamic and aerodynamic loads is also presented at the end of this chapter.

Chapter 3 presents the development of the nonlinear hydrostatic model to compute the exact buoyancy force and hydrostatic moments of cylindrical floaters undergoing general displacements (translation and rotation). In addition, the hydrostatic stiffness matrix is derived as a function of instantaneous position and orientation of the platform.

In Chapter 4, the mooring loads are formulated using the quasi-static approach. The analysis begins with developing a quasi-static model for the single configuration. Further extension is then undertaken to develop an exact 3D quasi-static cable model of the bridle mooring line with a clump weight. As well, a theoretical approach is developed to derive the exact mooring stiffness matrix. The influence of the mooring system configuration and geometry on the stiffness of the mooring system is also investigated.

In Chapter 5, the lumped mass cable model is formulated for a single cable. A new added mass matrix is developed together with seabed contact model. The model is also extended for the bridle mooring configuration with a suspended clump weight. Static solvers are developed to determine the equilibrium profile of the mooring line for the both mooring configurations to provide appropriate initial conditions for the cable nodes displacements in the coupled dynamic simulation.

In Chapter 6, the analytical models of the system dynamics and applied loads are implemented to simulate the FOWT dynamics under combined wind and wave loads. Several simulations are performed to validate the dynamic models against the reported simulation data from different simulation tools. Furthermore, series of simulations are performed using different dynamic models, cable models and mooring configurations to investigate the influence of the tower flexibility, mooring configuration, rotor gyroscopic effect and cable dynamics on the system dynamics. Finally, Chapter 7 summarizes the conclusions of the research undertaken in this thesis and suggests directions for future works.

Chapter 2

SYSTEM DYNAMICS

The spar FOWT system under consideration is based on the OC3-Hywind concept [6], as shown in Figure 2.1. The FOWT consists of a cylindrical floating platform supporting a horizontal axis wind turbine structure. The turbine structure is comprised of a tower, nacelle and three-bladed rotor. The platform is anchored to the seabed through a mooring system composed of a series of cable or chains and in some designs the cable include clump weights to increase the mooring system stiffness.

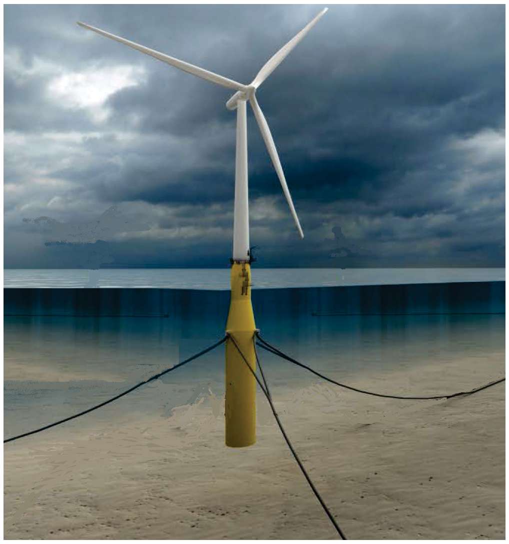

Figure 2.1: OC3-Hywind FOWT concept [2]

This chapter presents two approaches with different levels of complexity for modeling the nonlinear dynamics of the FOWT: a simplified rigid multibody model and a coupled rigid-flexible multibody model. In both models, the floating platform is modeled as a six-degrees-of-freedom (6-DOF) rigid body subject to buoyancy, hydrodynamic and moorings loads. The nacelle is modeled as a rigid body attached to the tower tip. The rotor is modeled as a rigid disc spinning around its axis and subject to aerodynamic load. The main difference between the two modeling approaches is in the modeling of the tower dynamics.

The rigid model treats the tower as a rigid body while in the flexible model it is modeled as a three-dimensional (3D) damped tapered Euler-Bernoulli beam undergoing coupled general rigid body and elastic motions. The beam bending-bending and twist motions are considered whereas extensibility is ignored.

The dynamic analysis of the rigid multibody system begins with formulations of the kinematics of the platform. Then, equations of motion of the rigid multibody model are derived using Lagrange's equation in terms of the platform quasi-coordinates. The turbine drivetrain equation of motion which governs the rotor spin dynamics is also derived. Likewise, the development of the flexible model begins with kinematic description of the tower flexible motion. The flexible displacements are then discretized in space using the assumed mode method (AMM) utilizing new orthogonal polynomial comparison functions developed herein. The applicability of these mode functions is tested by simulating the flexible dynamics of a rotating cantilever with a tip mass, illustrated in Appendix B.2. Accordingly, the equations of motion of the system are derived using Lagrange's equation.

Lastly, the ocean environment is characterized by a wave spectrum to describe the wave field kinematics required to formulate the hydrodynamic loads using Morison's equation in Section 2.3.2. As well, the aerodynamics loads are characterized based on the power and thrust coefficient performance curves of the rotor.

2.1 Rigid Multibody Dynamic Model

A schematic diagram of the spar FOWT system to be analyzed is shown in Figure 2.2. For simplicity, it is assumed the turbine rotor tilt angle is zero for this model and the flexible model[1]. The FOWT is comprised of 4 rigid bodies, ordered as depicted in Figure 2.2:

- **Body 1**: the floating platform, with mass m_p, and inertia matrix $\mathbf{I}_p = diag(I_{px},\, I_{py},\, I_{pz})$. This platform has been proposed to support the NREL 5 MW baseline wind turbine [87].
- **Body 2**: the nacelle, a rigid body, with mass m_{nc}, and inertia matrix $\mathbf{I}_{nc} = diag(I_{ncx},\, I_{ncy},\, I_{ncz})$.

---

[1] The tilt angle based on [87] is 5^o.

- **Body 3**: the rotor, a rigid disc spinning around its axis with angular velocity $\Omega(t)$. The mass is m_r, and inertia matrix $\mathbf{I}_r = diag(I_{rx},\, I_{ry},\, I_{rz})$, where $I_{ry} = I_{rz}$.

- **Body 4**: the tower, with mass m_t, and inertia matrix $\mathbf{I}_t = diag(I_{tx},\, I_{ty},\, I_{tz})$. The tower supports the Rotor-Nacelle-Assembly (RNA).

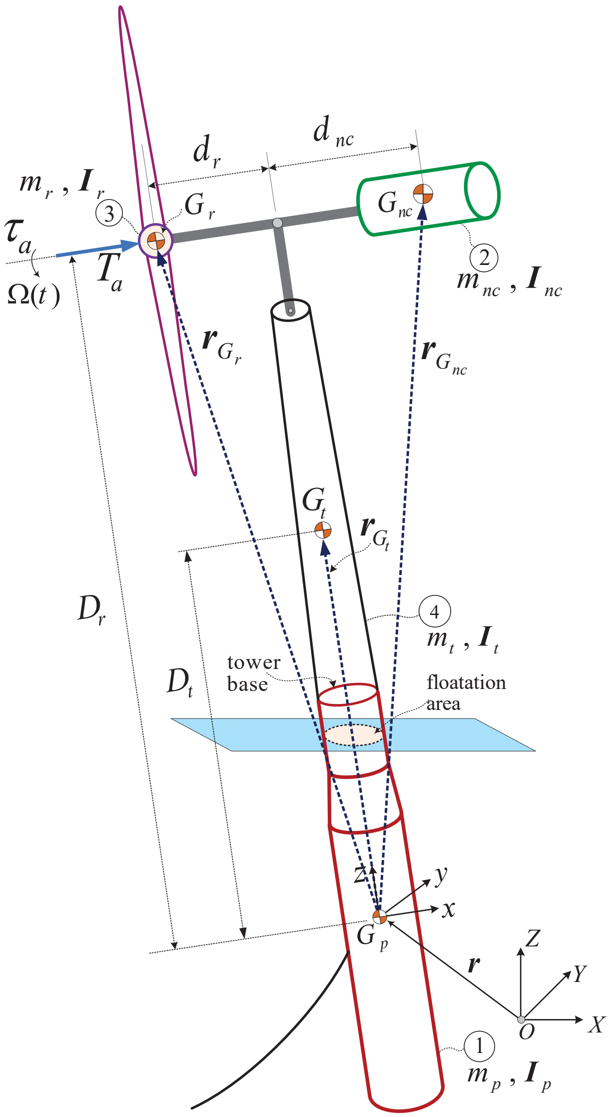

Figure 2.2: FOWT rigid multibody dynamic model

The platform floats in sea water of density ρ and supported to the seabed by a catenary mooring system comprised of three lines (detailed in Chapters 4). The platform, tower, nacelle and rotor related dimensions and mass and inertial properties are available in [6,87], and also listed in Appendix A.

2.1.1 System kinematics

Two reference frames are defined to characterize the displacement and rotation of the system components. The inertial frame, $\boldsymbol{\mathcal{F}}_I$ is an earth-fixed frame, with the earth's motion assumed to have negligible impact on the platform's dynamics. The body-fixed frame $\boldsymbol{\mathcal{F}}_p$ is attached to the platform center of gravity (G_p). The properties of these frames are listed in Table 2.1. A unified vector notation is used in this thesis to simplify the description of the system kinematics. The left superscript denoted by the frame abbreviation (in Table 2.1) is used exclusively to express a vector in the respective frame. If no superscript is used, this indicates an arbitrary frame. The principal axes associated with the inertia matrices of the rigid bodies are parallel to $\boldsymbol{\mathcal{F}}_p$. The third frame ($\boldsymbol{\mathcal{F}}_B$) listed in Table 2.1 is not relevant to the rigid body model and will be used later for the flexible model (Section 2.2).

Table 2.1: Reference frames definitions

Frame	Abbreviation	Frame axes	Unit vectors	Frame origin
$\boldsymbol{\mathcal{F}}_I$	I	X, Y, Z	$\hat{\mathbf{I}},\ \hat{\mathbf{J}},\ \hat{\mathbf{K}}$	Fixed on earth, point O
$\boldsymbol{\mathcal{F}}_p$	p	x, y, z	$\hat{\mathbf{i}},\ \hat{\mathbf{j}},\ \hat{\mathbf{k}}$	Platform c.g., point G_p
$\boldsymbol{\mathcal{F}}_B$	b	x_1, y_1, z_1	$\hat{\mathbf{b}}_1,\ \hat{\mathbf{b}}_2,\ \hat{\mathbf{b}}_3$	Tower tip, point B_t

Vector ${}^{I}\mathbf{r} = [r_X\ r_Y\ r_Z]^T$ defines the translational displacements of the platform body-fixed frame ($\boldsymbol{\mathcal{F}}_p$) origin relative to the inertial frame and represented in $\boldsymbol{\mathcal{F}}_I$. The Z-axis of $\boldsymbol{\mathcal{F}}_I$ is opposite to the direction of gravity. The displacements r_X, r_Y and r_Z indicate the platform, surge, sway and heave, respectively. The origin of $\boldsymbol{\mathcal{F}}_p$ coincides with that of $\boldsymbol{\mathcal{F}}_I$ at zero translation and rotation. The rotation of the platform is represented by an Euler angle triad $\boldsymbol{\theta} = [\phi\ \theta\ \psi]^T$ corresponding to roll, pitch and yaw angles, respectively. The 3-2-1 Euler angle sequence, commonly used for marine and flight/space vehicles [88], is selected to describe the platform rotation kinematics. The corresponding rotation matrix $\mathbf{R}$ is [20]

$$\mathbf{R} = \begin{bmatrix} R_{11} & R_{12} & R_{13} \\ R_{21} & R_{22} & R_{23} \\ R_{31} & R_{32} & R_{33} \end{bmatrix} = \begin{bmatrix} c_\psi\, c_\theta & c_\psi\, s_\theta\, s_\phi - s_\psi\, c_\phi & c_\psi\, s_\theta\, c_\phi + s_\psi\, s_\phi \\ s_\psi\, c_\theta & s_\psi\, s_\theta\, s_\phi + c_\psi\, c_\phi & s_\psi\, s_\theta\, c_\phi - c_\psi\, s_\phi \\ -s_\theta & c_\theta\, s_\phi & c_\theta\, c_\phi \end{bmatrix} \tag{2.1}$$

where $s_{(.)} = \sin(.)$ and $c_{(.)} = \cos(.)$. The rotation matrix $\mathbf{R}$ transforms vectors in $\boldsymbol{\mathcal{F}}_p$ to $\boldsymbol{\mathcal{F}}_I$. The velocity of the platform center of gravity can be expressed in $\boldsymbol{\mathcal{F}}_p$ as

$$ {}^p\boldsymbol{\nu} = \begin{Bmatrix} \nu_x \\ \nu_y \\ \nu_z \end{Bmatrix} = \mathbf{R}^T \, {}^I\dot{\mathbf{r}} \tag{2.2} $$

The platform angular velocity in terms of the Euler angle rates can be expressed in $\boldsymbol{\mathcal{F}}_p$ as [88]

$$ {}^p\boldsymbol{\omega} = \begin{Bmatrix} \omega_x \\ \omega_y \\ \omega_z \end{Bmatrix} = \mathbf{J}\dot{\boldsymbol{\theta}} = \underbrace{\begin{bmatrix} 1 & 0 & -s_\theta \\ 0 & c_\phi & s_\phi \, c_\theta \\ 0 & -s_\phi & c_\phi \, c_\theta \end{bmatrix}}_{\mathbf{J}} \underbrace{\begin{Bmatrix} \dot{\phi} \\ \dot{\theta} \\ \dot{\psi} \end{Bmatrix}}_{\dot{\boldsymbol{\theta}}} \tag{2.3} $$

It is worth mentioning that the matrices ($\mathbf{R}$ and $\mathbf{J}$) become singular when the pitch angle, $\theta = \pi/2$. However, such extreme excursions would lead to complete platform and mooring failure, which are not relevant scenarios in the present work. The velocities of the center of gravity of the tower (G_t), nacelle (G_{nc}), and the rotor (G_r) can be then formulated as

$$ \mathbf{v}_t = \boldsymbol{\nu} + \boldsymbol{\omega} \times \mathbf{r}_{G_t} \quad , \quad \mathbf{v}_{nc} = \boldsymbol{\nu} + \boldsymbol{\omega} \times \mathbf{r}_{G_{nc}} \quad , \quad \mathbf{v}_r = \boldsymbol{\nu} + \boldsymbol{\omega} \times \mathbf{r}_{G_r} \tag{2.4} $$

where the centers of gravity coordinates are ${}^p\mathbf{r}_{G_t} = [0 \;\; 0 \;\; D_t]^T$, ${}^p\mathbf{r}_{G_{nc}} = [d_{nc} \;\; 0 \;\; D_r]^T$, and ${}^p\mathbf{r}_{G_r} = [-d_r \;\; 0 \;\; D_r]^T$, as illustrated in Figure 2.2.

2.1.2 Equations of motion

The total kinetic energy (KE) of the four bodies comprising the rigid multibody system is

$$ \begin{aligned} \mathcal{T} =& \tfrac{1}{2} m_p \;\; \boldsymbol{\nu} \bullet \boldsymbol{\nu} + \tfrac{1}{2} \, {}^p\boldsymbol{\omega} \bullet (\mathbf{I}_p \, {}^p\boldsymbol{\omega}) + \tfrac{1}{2} m_t \; \mathbf{v}_t \bullet \mathbf{v}_t + \tfrac{1}{2} \, {}^p\boldsymbol{\omega} \bullet (\mathbf{I}_t \, {}^p\boldsymbol{\omega}) \\ & + \tfrac{1}{2} m_{nc} \; \mathbf{v}_{nc} \bullet \mathbf{v}_{nc} + \tfrac{1}{2} \, {}^p\boldsymbol{\omega} \bullet (\mathbf{I}_{nc} \, {}^p\boldsymbol{\omega}) + \tfrac{1}{2} m_r \; \mathbf{v}_r \bullet \mathbf{v}_r + \tfrac{1}{2} \, {}^p\boldsymbol{\omega}_r \bullet (\mathbf{I}_r \, {}^p\boldsymbol{\omega}_r) \end{aligned} \tag{2.5} $$

The platform, tower and the nacelle are rotating with an angular velocity, $\boldsymbol{\omega}$. The angular velocity of the rotor is $\boldsymbol{\omega}_r = \boldsymbol{\omega} + \boldsymbol{\Omega}$ and the rotor spin rate is ${}^p\boldsymbol{\Omega} = \Omega \; \hat{\mathbf{i}}$

The potential energy of the rigid multibody system is attributable to the gravity, can be expressed as

$$\mathcal{V} = m_p\, g\, r_Z + m_t\, g\, \left(\mathbf{r}_{tO} \bullet \hat{\mathbf{K}}\right) + m_{nc}\, g\, \left(\mathbf{r}_{ncO} \bullet \hat{\mathbf{K}}\right) + m_r\, g\, \left(\mathbf{r}_{rO} \bullet \hat{\mathbf{K}}\right) \tag{2.6}$$

where ($\bullet$) denotes the dot product, g is the acceleration of gravity, and the vectors $\mathbf{r}_{tO}$, $\mathbf{r}_{ncO}$ and $\mathbf{r}_{rO}$ measure the positions of the center of gravity of the tower, nacelle and rotor relative to the origin of $\boldsymbol{\mathcal{F}}_I$, respectively, formulated as

$$^{I}\mathbf{r}_{tO} = {}^{I}\mathbf{r} + \mathbf{R}\, {}^{p}\mathbf{r}_{G_t} \quad , \quad {}^{I}\mathbf{r}_{ncO} = {}^{I}\mathbf{r} + \mathbf{R}\, {}^{p}\mathbf{r}_{G_{nc}} \quad , \quad {}^{I}\mathbf{r}_{rO} = {}^{I}\mathbf{r} + \mathbf{R}\, {}^{p}\mathbf{r}_{G_r} \tag{2.7}$$

The system dynamics is characterized by the platform translation and rotation degrees of freedom and the rotor spin yielding a 7-DOF dynamic model. The equations of motion are derived utilizing Lagrange's equation in terms of the quasi-coordinates of the platform ($\boldsymbol{\nu}$ and $\boldsymbol{\omega}$) as [89–91]

$$\frac{d}{dt}\left(\frac{\partial \mathcal{L}}{\partial ({}^{p}\boldsymbol{\nu})}\right) + {}^{p}\tilde{\boldsymbol{\omega}} \frac{\partial \mathcal{L}}{\partial ({}^{p}\boldsymbol{\nu})} - \mathbf{R}^T \frac{\partial \mathcal{L}}{\partial ({}^{I}\mathbf{r})} = {}^{p}\mathbf{F} \tag{2.8}$$

$$\frac{d}{dt}\left(\frac{\partial \mathcal{L}}{\partial ({}^{p}\boldsymbol{\omega})}\right) + {}^{p}\tilde{\boldsymbol{\nu}} \frac{\partial \mathcal{L}}{\partial ({}^{p}\boldsymbol{\nu})} + {}^{p}\tilde{\boldsymbol{\omega}} \frac{\partial \mathcal{L}}{\partial ({}^{p}\boldsymbol{\omega})} - \mathbf{J}^{-T} \frac{\partial \mathcal{L}}{\partial \boldsymbol{\theta}} = {}^{p}\mathbf{M} \tag{2.9}$$

where $\mathcal{L} = \mathcal{T} - \mathcal{V}$ is the Lagrangian, ${}^{p}\tilde{\boldsymbol{\omega}}$ and ${}^{p}\tilde{\boldsymbol{\nu}}$ are the skew symmetric matrices of ${}^{p}\boldsymbol{\omega}$ and ${}^{p}\boldsymbol{\nu}$, respectively. For an arbitrary vector $\boldsymbol{\mathcal{B}} = [\mathcal{B}_1 \quad \mathcal{B}_2 \quad \mathcal{B}_3]^T$, $\tilde{\boldsymbol{\mathcal{B}}}$ is written as

$$\tilde{\boldsymbol{\mathcal{B}}} = \begin{bmatrix} 0 & -\mathcal{B}_3 & \mathcal{B}_2 \\ \mathcal{B}_3 & 0 & -\mathcal{B}_1 \\ -\mathcal{B}_2 & \mathcal{B}_1 & 0 \end{bmatrix} \tag{2.10}$$

The total external forces acting on the system and corresponding moments around the platform frame origin are denoted by $\mathbf{F}$ and $\mathbf{M}$, respectively. The equation of motion of the wind turbine drivetrain can be obtained as

$$\frac{d}{dt}\left(\frac{\partial \mathcal{L}}{\partial \Omega}\right) = \tau_a - \tau_g \tag{2.11}$$

where τ_a and τ_g are the aerodynamic and generator torques, respectively. When the wind speed is less than the rated value, the generator torque can be determined from the generator torque control law as will be discussed in Section 2.3.3. The resulting form of the equations of motion can be then expressed as

$$[\mathbf{M}_{sys}]\begin{bmatrix}\dot{\boldsymbol{\nu}}\\ \dot{\boldsymbol{\omega}}\\ \dot{\Omega}\end{bmatrix}+\underbrace{\begin{bmatrix}\tilde{\boldsymbol{\omega}} & \mathbf{0}_{3\times3} & \mathbf{0}_{3\times1}\\ \tilde{\boldsymbol{\nu}} & \tilde{\boldsymbol{\omega}} & \mathbf{0}_{3\times1}\\ \mathbf{0}_{1\times3} & \mathbf{0}_{1\times3} & 0\end{bmatrix}}_{\tilde{S}}[\mathbf{M}_{sys}]\begin{bmatrix}\boldsymbol{\nu}\\ \boldsymbol{\omega}\\ \Omega\end{bmatrix}=\begin{bmatrix}\mathbf{R}^T\frac{\partial\mathcal{L}}{\partial\mathbf{r}}\\ \mathbf{J}^{-T}\frac{\partial\mathcal{L}}{\partial\boldsymbol{\theta}}\\ 0\end{bmatrix}+\begin{bmatrix}{}^{p}\mathbf{F}\\ {}^{p}\mathbf{M}\\ \tau_a-\tau_g\end{bmatrix}\tag{2.12}$$

The mass matrix ($\mathbf{M}_{sys}$) form is obtained as

$$\begin{bmatrix}m_T & 0 & 0 & 0 & M_{15} & 0 & 0\\ & m_T & 0 & -M_{15} & 0 & M_{26} & 0\\ & & m_T & 0 & -M_{26} & 0 & 0\\ & & & M_{44} & 0 & M_{46} & I_{rx}\\ & & sym. & & M_{55} & 0 & 0\\ & & & & & M_{66} & 0\\ & & & & & & I_{rx}\end{bmatrix}\tag{2.13}$$

the mass matrix entries are

$$\begin{aligned}m_T =& m_p+m_t+m_{nc}+m_r \quad , \quad M_{15}=D_r\left(m_r+m_{nc}\right)+m_tD_t\\ M_{26} =& d_{nc}m_{nc}-d_rm_r \quad , \quad M_{44}=I_{Tx}+{D_r}^2\left(m_r+m_{nc}\right)+{D_t}^2m_t\\ M_{46} =& D_rd_rm_r-D_rd_{nc}m_{nc} \quad , \quad M_{66}=I_{Tz}+m_r{d_r}^2+m_{nc}{d_{nc}}^2\\ M_{55} =& I_{Ty}+m_r\left({D_r}^2+{d_r}^2\right)+m_{nc}\left({D_r}^2+{d_{nc}}^2\right)+{D_t}^2m_t\end{aligned}\tag{2.14}$$

where $I_{Tx}=I_{px}+I_{tx}+I_{ncx}+I_{rx}$, $I_{Ty}=I_{py}+I_{ty}+I_{ncy}+I_{ry}$, and $I_{Tz}=I_{pz}+I_{tz}+I_{ncz}+I_{rz}$. The terms $\mathbf{R}^T\frac{\partial\mathcal{L}}{\partial\mathbf{r}}$ and $\mathbf{J}^{-T}\frac{\partial\mathcal{L}}{\partial\boldsymbol{\theta}}$ in Equation (2.12) yield the gravity force and moment around the origin of platform frame, respectively, obtained in the platform frame ($\boldsymbol{\mathcal{F}}_p$), as

$$\begin{aligned} \mathbf{R}^T \frac{\partial \mathcal{L}}{\partial \mathbf{r}} =& g \begin{bmatrix} m_T\, s_\theta \\ -m_T\, c_\theta s_\phi \\ -m_T\, c_\phi c_\theta \end{bmatrix} \\ \mathbf{J}^{-T} \frac{\partial \mathcal{L}}{\partial \boldsymbol{\theta}} =& g \begin{bmatrix} c_\theta s_\phi \left(D_r \left(m_{nc} + m_r\right) + D_t m_t\right) \\ s_\theta \left(D_r \left(m_{nc} + m_r\right) + D_t m_t\right) + c_\phi c_\theta \left(d_{nc} m_{nc} + d_r m_r\right) \\ -s_\phi c_\theta \left(d_{nc} m_{nc} + d_r m_r\right) \end{bmatrix} \end{aligned} \tag{2.15}$$

The external forces and corresponding moments acting on the FOWT arise from hydrostatic, hydrodynamic, aerodynamics and mooring loads, denoted by the subscripts hs, hd, aer, and mor, respectively, as

$$\begin{aligned} \mathbf{F} &= \mathbf{F}_{hs} + \mathbf{F}_{hd} + \mathbf{F}_{aer} + \mathbf{F}_{mor} \\ \mathbf{M} &= \mathbf{M}_{hs} + \mathbf{M}_{hd} + \mathbf{M}_{aer} + \mathbf{M}_{mor} \end{aligned} \tag{2.16}$$

the hydrodynamic force ($\mathbf{F}_{hd}$) and moment ($\mathbf{M}_{hd}$) around the platform body-fixed frame origin are expressed as

$$\mathbf{F}_{hd} = \mathbf{F}_{iner} + \mathbf{F}_{hd*} \quad , \quad \mathbf{M}_{hd} = \mathbf{M}_{iner} + \mathbf{F}_{hd*} \tag{2.17}$$

where the subscript ($iner$) denotes the inertial terms which are functions of the platform kinematics, as will be discussed in Section 2.3.2. The inertial terms in Equation (2.17) can be reformulated in a matrix form as [20]

$$\begin{bmatrix} \mathbf{F}_{iner} \\ \mathbf{M}_{iner} \end{bmatrix} = [\mathbf{A}] \begin{bmatrix} \dot{\boldsymbol{\nu}} \\ \dot{\boldsymbol{\omega}} \end{bmatrix} + [\mathbf{C}_A] \begin{bmatrix} \boldsymbol{\nu} \\ \boldsymbol{\omega} \end{bmatrix} \tag{2.18}$$

where $\mathbf{A}$ is the added mass matrix and $\mathbf{C}_A$ is the hydrodynamic Coriolis and centripetal matrix [20], both of size (6×6). The hydrodynamic loads will be investigated in detail in Section 2.3.2

Substituting Equations (2.16) to (2.18) into Equation (2.12), the final form of the equations of motion of the rigid multibody model can be expressed in the following form

$$\left[\mathbf{M}_{sys} + \bar{\mathbf{A}}\ \right] \begin{bmatrix} \dot{\boldsymbol{\nu}} \\ \dot{\boldsymbol{\omega}} \\ \dot{\Omega} \end{bmatrix} + \left[\tilde{\mathcal{S}}\mathbf{M}_{sys} + \bar{\mathbf{C}}_A\right] \begin{bmatrix} \boldsymbol{\nu} \\ \boldsymbol{\omega} \\ \Omega \end{bmatrix} = \begin{bmatrix} \mathbf{R}^T \frac{\partial \mathcal{L}}{\partial \mathbf{r}} \\ \mathbf{J}^{-T} \frac{\partial \mathcal{L}}{\partial \boldsymbol{\theta}} \\ 0 \end{bmatrix} + \begin{bmatrix} {}^p\mathbf{F}_{hs} + {}^p\mathbf{F}_{aer} + {}^p\mathbf{F}_{mor} + {}^p\mathbf{F}_{hd*} \\ {}^p\mathbf{M}_{hs} + {}^p\mathbf{M}_{aer} + {}^p\mathbf{M}_{mor} + {}^p\mathbf{M}_{hd*} \\ \tau_a - \tau_g \end{bmatrix} \tag{2.19}$$

where

$$\bar{\mathbf{A}} = \begin{bmatrix} \mathbf{A} & \mathbf{0}_{6\times1} \\ \mathbf{0}_{1\times6} & 0 \end{bmatrix} \quad , \quad \bar{\mathbf{C}}_A = \begin{bmatrix} \mathbf{C}_A & \mathbf{0}_{6\times1} \\ \mathbf{0}_{1\times6} & 0 \end{bmatrix}$$

The equations of motion of the large multibody system have thus been reduced to the simple form of Equation (2.19) which can be easily implemented.

2.2 Flexible Multibody Dynamic Model

The rigid dynamic model previously developed considers the tower as a rigid body. However, to predict the elastic structural deflections responses of the tower, a more sophisticated flexible dynamic model is introduced. This will allow us to later evaluate the importance of tower flexibility on the system performance. The schematic diagram of the flexible multibody model to be analyzed is shown in Figure 2.3. The coupled rigid-flexible multibody dynamic model is comprised of 3 rigid and 1 flexible bodies, ordered as depicted in Figure 2.3. The properties of the rigid bodies 1, 2 and 3 are similar to their counterparts of the rigid model (Section 2.1).

Body 4 representing the tower, is now considered as a flexible tapered 3D beam of annular circular section. The beam is of length l, density ρ_t, and variable cross sectional area per length $A_t(z)$. The moments of inertia of the cross section as functions of the tower height around the x_1 and y_1 axes are $I_{t,xx}(z)$ and $I_{t,yy}(z)$, respectively. The corresponding polar moment of inertial is $J_t(z)$. The material properties of the beam are characterized by Young's modulus E and modulus of rigidity G. The tower properties are detailed in Appendix A.3. In this model, the rotor blade flexibility is ignored.

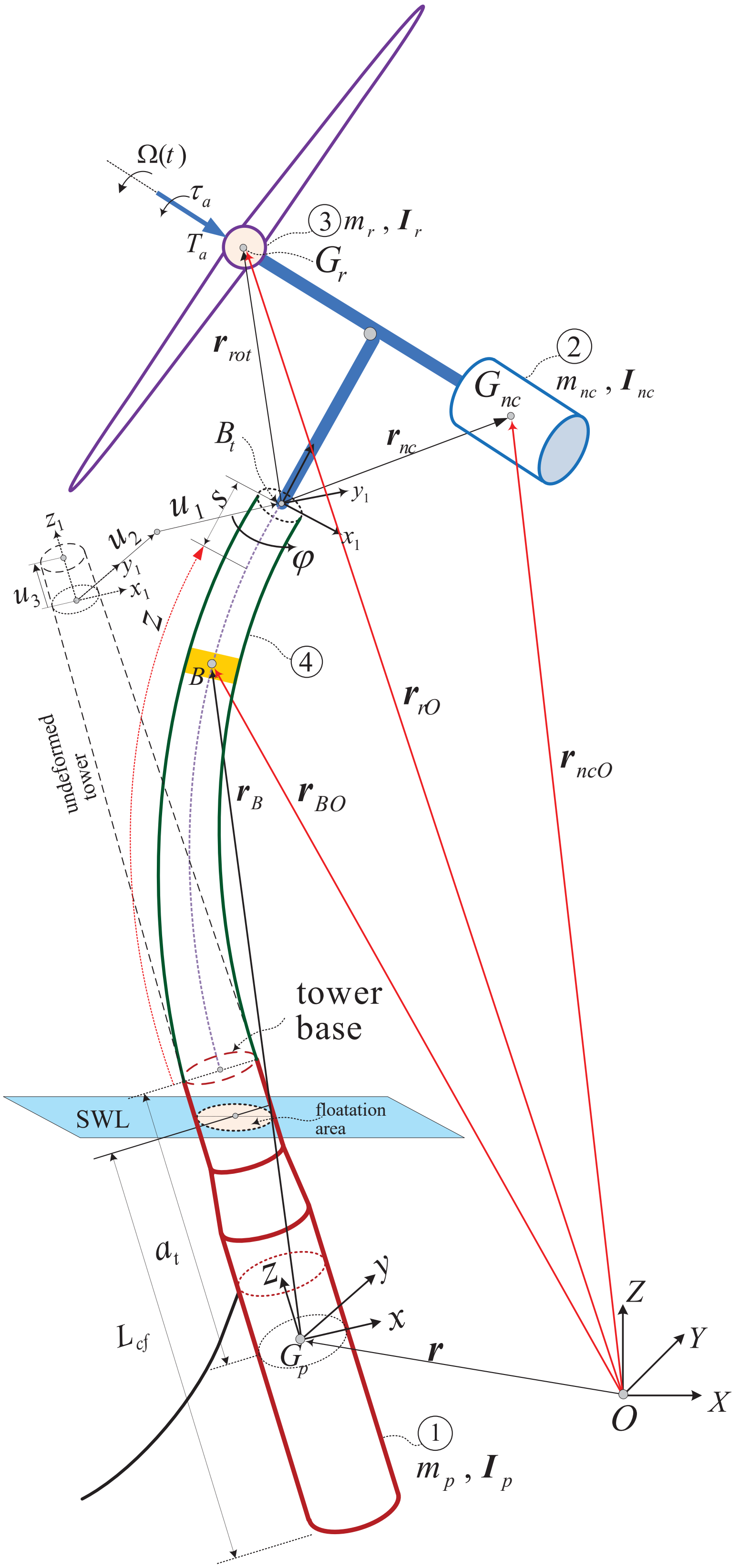

Figure 2.3: Spar FOWT flexible dynamic model

2.2.1 System kinematics

The displacement and rotation of the FOWT components are characterized using the three reference frames illustrated previously in Table 2.1. The frames, $\boldsymbol{\mathcal{F}}_I$ and $\boldsymbol{\mathcal{F}}_p$ are already defind for the rigid model (Section 2.1.1). A third frame, $\boldsymbol{\mathcal{F}}_B$ is introduced, which is a body-fixed frame attached to the tower tip center, as shown in Figure 2.3. The principal axes associated with the inertia matrix of the platform are parallel to $\boldsymbol{\mathcal{F}}_p$, and for the nacelle and the rotor are parallel to $\boldsymbol{\mathcal{F}}_B$. The platform kinematics description is similar to that of the rigid body model already defined in Equations (2.1) to (2.3).

The tower is modeled as a cantilever beam undergoing general motion because of the beam base attachment to a free-floating platform. The Euler-Bernoulli beam theory is adopted to characterize the bending motion of the tower because the tower is a *thin beam* and the ratio of the tower length to its average diameter ≈ 15 which is considerably larger than 10 as recommended [92, 93]. Thus, the shear and rotary inertia effects can be ignored since the beam is slender. The elastic deformations of a material point (B) located on a differential element of the beam are characterized in the platform frame ($\boldsymbol{\mathcal{F}}_p$) by $u_1(t, z)$ and $u_2(t, z)$ representing the bending deformations, $s(t, z)$ the beam stretch, and $\varphi(t, z)$ the beam twist angle. These distributed deformations are illustrated at the beam tip for clarity in Figure 2.3. The elastic displacement $u_3(t, z)$ is dependent on u_1, u_2 and s, can be expressed as [55]

$$u_3 \cong s - \frac{1}{2} \int_0^z \left[(u_1')^2 + (u_2')^2 \right] d\sigma \ , \quad (.)' = \frac{\partial (.)}{\partial z} \tag{2.20}$$

where σ is a dummy variable. The beam stretch can be assumed negligible, therefore the inextensibility constraint can be enforced as $s = s' = 0$. As a result, u_3 then represents the beam shortening (i.e. $u_3 \leq 0$) due to beam bending deformations, can be then formulated as

$$u_3 \cong -\frac{1}{2} \int_0^z \left[(u_1')^2 + (u_2')^2 \right] d\sigma \tag{2.21}$$

The displacement of material point B, located on the elastic axes of the beam, as measured relative to the $\boldsymbol{\mathcal{F}}_p$ origin, is

$${}^{p}\mathbf{r}_B = [u_1 \quad u_2 \quad (a_t + z + u_3)]^T \tag{2.22}$$

where a_t denotes the distance between the tower base and origin of the platform frame, as shown in Figure 2.3. The velocity of B can be obtained as

$$\mathbf{v}_B = \boldsymbol{\nu} + \boldsymbol{\omega} \times \mathbf{r}_B + \dot{\mathbf{u}} \quad , \quad \dot{(.)} = \frac{\partial (.)}{\partial t} \tag{2.23}$$

where ${}^p\dot{\mathbf{u}} = [\dot{u}_1 \ \dot{u}_2 \ \dot{u}_3]^T$ and × denotes the cross product. Differentiating Equation (2.21) with respect to time, $\dot{u}_3$ can be obtained

$$\dot{u}_3 \cong - \int_0^z [u_1' \ \dot{u}_1' + u_2' \ \dot{u}_2'] \, d\sigma \quad , \quad \dot{(.)}' = \frac{\partial^2 (.)}{\partial t \partial z} \tag{2.24}$$

The frame $\boldsymbol{\mathcal{F}}_B$ is attached to tower tip center and is parallel to $\boldsymbol{\mathcal{F}}_p$ if the beam is undeformed. The elastic rotation transformation of the Euler-Bernoulli beam cross section is characterised by an *elastic rotation matrix* which can be defined at the beam tip ($z = l$) as [51]

$$\mathbf{R}_{el} = \begin{bmatrix} 1 - \frac{1}{2}(u_1')^2 - \frac{1}{2}\varphi^2 & -\varphi - \frac{1}{2}u_1' \ u_2' & u_1' \\ \varphi - \frac{1}{2}u_1' \ u_2' & 1 - \frac{1}{2}(u_2')^2 - \frac{1}{2} \ \varphi^2 & u_2' \\ -u_1' - u_2' \ \varphi & -u_2' + u_1' \ \varphi & 1 - \frac{1}{2}\left[(u_1')^2 + (u_2')^2\right] \end{bmatrix}_{z=l} \tag{2.25}$$

This form is of second order in the elastic deflections which is sufficient to capture the kinematics of the system since the strain deformation is small. The rotation matrix $\mathbf{R}_{el}$ transforms the vectors in $\boldsymbol{\mathcal{F}}_B$ to $\boldsymbol{\mathcal{F}}_p$. Accordingly, the angular velocity of the frame $\boldsymbol{\mathcal{F}}_B$ relative to $\boldsymbol{\mathcal{F}}_p$ (${}^p\boldsymbol{\omega}_{Bl}$) and resolved in the latter frame can be determined from [51, 88]

$${}^p\tilde{\boldsymbol{\omega}}_{Bl} = \dot{\mathbf{R}}_{el} \, \mathbf{R}_{el}^T \tag{2.26}$$

the angular velocity of the nacelle can be expressed as

$$\boldsymbol{\omega}_{nc} = \boldsymbol{\omega} + \boldsymbol{\omega}_{Bl} \tag{2.27}$$

and for the rotor

$$\boldsymbol{\omega}_r = \boldsymbol{\omega} + \boldsymbol{\omega}_{Bl} + \boldsymbol{\Omega} \tag{2.28}$$

where the rotor spin rate expressed in the tower tip frame is ${}^b\boldsymbol{\Omega} = \Omega \ \hat{\mathbf{b}}_1$. The velocity of the nacelle center of gravity (G_{nc}) can be formulated as

$$\mathbf{v}_{nc} = \mathbf{v}_{Bl} + \boldsymbol{\omega}_{nc} \times \mathbf{r}_{nc} \tag{2.29}$$

where $\mathbf{v}_{Bl}$ is the velocity of the tower tip section center i.e. $\mathbf{v}_{Bl} = \mathbf{v}_B|_{z=l}$. The velocity of the rotor center of gravity (G_r)

$$\mathbf{v}_r = \mathbf{v}_{Bl} + \boldsymbol{\omega}_{nc} \times \mathbf{r}_{rot} \tag{2.30}$$

The position of the nacelle and rotor center of gravity relative to the tower tip center are $\mathbf{r}_{nc}$ and $\mathbf{r}_{rot}$, respectively. These vectors are constants in $\boldsymbol{\mathcal{F}}_B$.

2.2.2 Spatial discretization

The Assumed Mode Method (AMM) is used to discretize the continuous variables $u_1(z,t)$, $u_2(z,t)$, and $\varphi(z,t)$ using the following form [94]

$$\begin{aligned} u_1(z,t) &= \sum_{i=1}^{n_b} \Phi_i(z)\, \xi_i(t) &&= \boldsymbol{\Phi}^T \boldsymbol{\xi} \\ u_2(z,t) &= \sum_{i=1}^{n_b} \Phi_i(z)\, \Theta_i(t) &&= \boldsymbol{\Phi}^T \boldsymbol{\Theta} \\ \varphi(z,t) &= \sum_{i=1}^{n_t} \eta_i(z)\, \delta_i(t) &&= \boldsymbol{\eta}^T \boldsymbol{\delta} \end{aligned} \tag{2.31}$$

where $\Phi_i(z)$ and $\eta_i(z)$ are the assumed mode shape spatial functions: $\Phi_i(z)$ are shape functions in bending in the two lateral directions, while $\eta_i(z)$ are shape functions in twist. $\boldsymbol{\Phi}, \boldsymbol{\eta}$ are the corresponding modal vectors. The numbers of mode shapes used for bending and twist discretization are n_b and n_t, respectively. $\xi_i(t)$, $\Theta_i(t)$ and $\delta_i(t)$ are generalized coordinates to be determined. $\boldsymbol{\xi}$, $\boldsymbol{\Theta}$ and $\boldsymbol{\delta}$ are the corresponding generalized coordinates vectors.

2.2.2.1 Mode shapes

The direct choice of the $\Phi_i(z)$ and $\eta_i(z)$ shape function are the system natural (eigen) modes for a *stationary*[2] cantilever bending and the twist vibrations of a clamped free shaft

---

[2] i.e. the mode shapes of free end beams undergoing pure elastic motions without any rigid body motion (either translation or rotation)

[37], respectively. The eigen mode function selected for $\eta_i(z)$, is written as [92]

$$\eta_i(z) = \sin\left(\frac{(2i-1)\,\pi\,z}{2l}\right) \ , \ \ i = 1, 2, ..., n_t \tag{2.32}$$

However, the bending eigen mode shapes are not the choice due to the high computation cost of integrating mixed hyperbolic and trigonometric functions forming these modes. Alternatively, a new family of polynomial comparison functions is developed. These functions satisfy the geometrical and natural boundary conditions (BCs) of a cantilever beam, $\Phi_i(0) = \Phi_i'(0) = 0\,,\ \Phi_i''(l) = \Phi_i'''(l) = 0$, and the orthogonality condition

$$\int_0^l \Phi_i \Phi_j \, dz = \begin{cases} 0 & \text{for} \quad i \neq j \\ \text{nonzero} & \text{for} \quad i = j \end{cases} \tag{2.33}$$

The first polynomial can be directly produced by imposing the 4 BCs, can be expressed as

$$\Phi_1(\hat{z}) = \frac{1}{3}\hat{z}^4 - \frac{4}{3}\hat{z}^3 + 2\,\hat{z}^2 \quad , \quad \hat{z} = z/l \tag{2.34}$$

The remaining list of polynomials is obtained sequentially such that the i-th polynomial is generated based on the preceding set. The following polynomial is always a degree higher than the preceding one. Starting from i=2 onwards, the polynomial coefficients can be determined by enforcing the BCs, orthogonality condition (Equation (2.33)), and $\Phi_i(1) = 1$ to normalize these modes, $\Phi_2(\hat{z})$ can be then expressed as

$$\Phi_2(\hat{z}) = b_5\hat{z}^5 + b_4\hat{z}^4 + b_3\hat{z}^3 + b_2\ \hat{z}^2 + b_1\ \hat{z} + b_0$$

The 6 coefficients ($b_0 - b_5$) are determined by solving 6 linear algebraic equations corresponding to the 4 BCs, $\Phi_2(1) = 1$, and $\int_0^1 \Phi_2 \Phi_1 d\hat{z} = 0$, where Φ_1 is already known from a previous step. Following the same procedure, the required number (n_b) of shape functions can be generated. Appendix B.1 lists the first 10 shape functions being developed. These polynomials are reasonably similar in shape to their corresponding eigen modes, as shown in Figure 2.4. However, some deviations between these two families of mode shapes are still observed particularly in higher modes and at $z/l < 0.7$, as illustrated in Figure 2.4. Moreover, polynomial shape functions are computationally efficient particularly in symbolic integration. We found that computing the tower kinetic energy (as will be formulated in Section 2.2.3.1) when the bending motion is discretized using polynomial shape functions is in the order of seconds using the Matlab Symbolic Math Toolbox while the same operation requires hours when using the eigen functions. The convergence of the AMM using these polynomial shape functions has been verified using a benchmark problem illustrated in Appendix B.2.

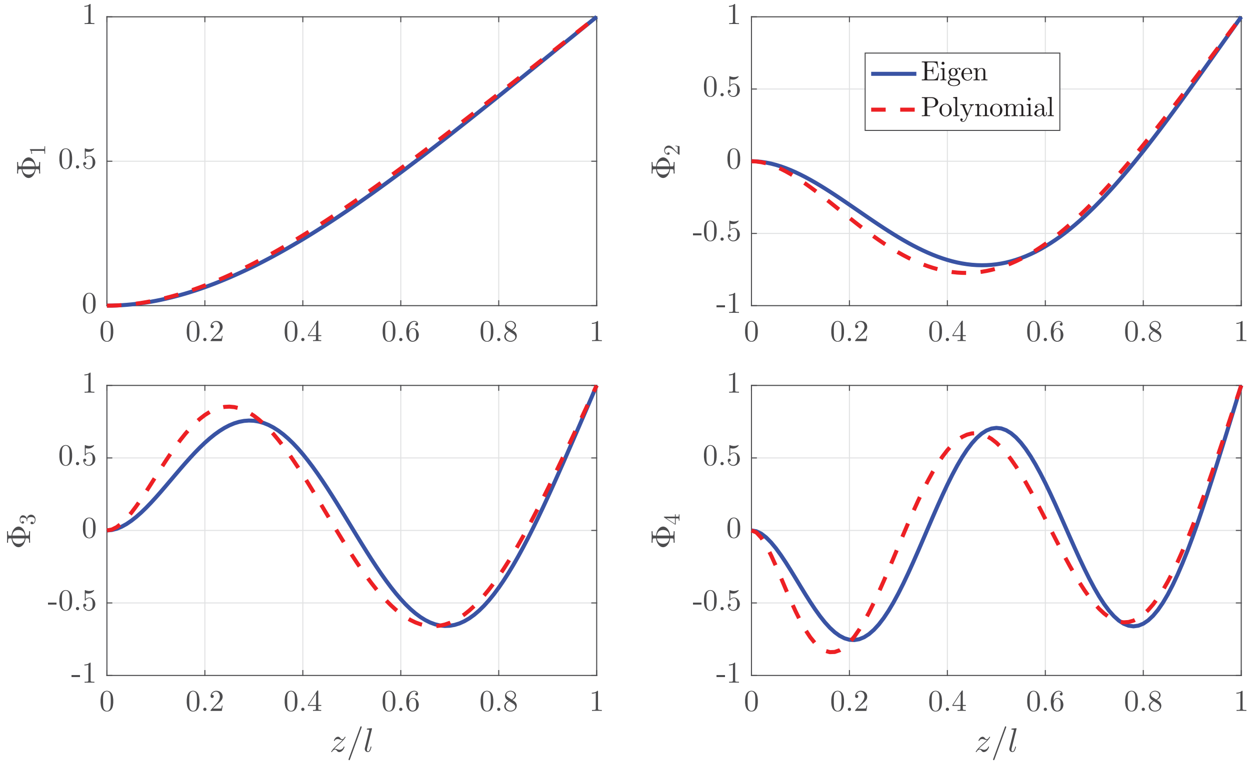

Figure 2.4: Comparisons of the cantilever bending eigen and orthogonal polynomial mode shapes

2.2.3 Equations of motion

The coupled rigid body and elastic equations of motion are derived using Lagrange's equation. This requires formulation of the kinetic and potential energies of the system, as shown below.

2.2.3.1 Kinetic energy

The total kinetic energy of the FOWT system includes the kinetic energies of the four bodies comprising the multibody system. The KE of the platform is

$$\mathcal{T}_p = \tfrac{1}{2} m_p \; \boldsymbol{\nu} \bullet \boldsymbol{\nu} + \tfrac{1}{2} \; {}^{p}\boldsymbol{\omega} \bullet (\mathbf{I}_p \; {}^{p}\boldsymbol{\omega}) \tag{2.35}$$

The KE of the tower can be written as

$$\mathcal{T}_t = \frac{1}{2}\int_0^l \bar{m}_t\,(\mathbf{v}_B \bullet \mathbf{v}_B)\,dz + \frac{1}{2}\int_0^l \rho_t\,J_t\,\dot{\varphi}^2 dz \tag{2.36}$$

where $\bar{m}_t = \rho_t\,A_t$ is the mass per unit length of the tower, the tower properties are detailed in Appendix A.3. The KE of the nacelle is

$$\mathcal{T}_{nc} = \tfrac{1}{2} m_{nc}\,\mathbf{v}_{nc} \bullet\ \mathbf{v}_{nc} + \tfrac{1}{2}\,({}^{b}\boldsymbol{\omega}_{nc})\bullet \left(\mathbf{I}_{nc}\ {}^{b}\boldsymbol{\omega}_{nc}\right) \tag{2.37}$$

where ${}^{b}\boldsymbol{\omega}_{nc} = \mathbf{R}_{el}^T\,({}^{p}\boldsymbol{\omega} + {}^{p}\boldsymbol{\omega}_{Bl})$. The KE of the rotor is

$$\mathcal{T}_r = \tfrac{1}{2} m_r\,\mathbf{v}_r \bullet\ \mathbf{v}_r + \tfrac{1}{2}({}^{b}\boldsymbol{\omega}_r)\bullet \left(\mathbf{I}_r\ {}^{b}\boldsymbol{\omega}_r\right) \tag{2.38}$$

The total kinetic energy of the system is

$$\mathcal{T} = \mathcal{T}_p + \mathcal{T}_t + \mathcal{T}_{nc} + \mathcal{T}_r \tag{2.39}$$

2.2.3.2 Potential energy

The potential energy of the elastic tower is attributed to the strain energy due the elastic deformations of the tower and gravitational energy. The tower strain energy due to bending-bending and twist deformations can be written as

$$\mathcal{V}_t^e = \frac{1}{2}\int_0^l EI_{t,yy}\,(u_1'')^2 dz + \frac{1}{2}\int_0^l EI_{t,xx}\,(u_2'')^2 dz + \frac{1}{2}\int_0^l G\,J_t\,(\varphi')^2 dz \tag{2.40}$$

where $I_{t,xx} = I_{t,yy}$ since the tower cross section is circular. The tower gravitational potential energy

$$\mathcal{V}_t^g = \int_0^l \bar{m}_t\,g\,\left(\mathbf{r}_{BO} \bullet \hat{\mathbf{K}}\right)\,dz \tag{2.41}$$

where $\mathbf{r}_{BO}$ is the displacement of material point B relative to the origin of frame $\boldsymbol{\mathcal{F}}_I$, as shown in Figure 2.3, and can be expressed as

$$ {}^{I}\mathbf{r}_{BO} = {}^{I}\mathbf{r} + \mathbf{R}\ {}^{p}\mathbf{r}_B \tag{2.42}$$

The gravitational potential energy of the rigid bodies (the platform, nacelle and rotor) is expressed as

$$\mathcal{V}_{RB} = m_p\, g\, r_Z + m_{nc}\, g\, \left(\mathbf{r}_{ncO} \bullet \hat{\mathbf{K}}\right) + m_r\, g\, \left(\mathbf{r}_{rO} \bullet \hat{\mathbf{K}}\right) \tag{2.43}$$

where the vectors $\mathbf{r}_{ncO}$ and $\mathbf{r}_{rO}$ measure the positions of the center of gravity of the nacelle and the rotor relative to the origin of $\boldsymbol{\mathcal{F}}_I$, respectively, formulated as

$$\begin{aligned} {}^I\mathbf{r}_{ncO} &= {}^I\mathbf{r} + \mathbf{R}\ {}^p\mathbf{r}_{Bl} + \mathbf{R}\,\mathbf{R}_{el}\ {}^b\mathbf{r}_{nc} \\ {}^I\mathbf{r}_{rO} &= {}^I\mathbf{r} + \mathbf{R}\ {}^p\mathbf{r}_{Bl} + \mathbf{R}\,\mathbf{R}_{el}\ {}^b\mathbf{r}_{rot} \end{aligned} \tag{2.44}$$

The system total potential energy can be then expressed as

$$\mathcal{V} = \mathcal{V}_t^e + \mathcal{V}_t^g + \mathcal{V}_{RB} \tag{2.45}$$

2.2.3.3 Rayleigh dissipation

Rayleigh's dissipation function is often used to account for linear damping forces in Lagrangian mechanics. The beam internal structural damping can be accordingly formulated as [89]

$$\Upsilon = \frac{1}{2}\int_0^l c_{u1}\, E\, I_{t,yy}(\dot{u}_1''\,)^2 dz + \frac{1}{2}\int_0^l c_{u2}\, E\, I_{t,xx}(\dot{u}_2''\,)^2 dz + \frac{1}{2}\int_0^l c_\varphi\, G\, J_t\, (\dot{\varphi}'\,)^2 dz \tag{2.46}$$

where c_{u1} , c_{u2} and c_φ are the damping coefficients associated with the two bending deformations and twist, respectively, and can be calculated as [89]

$$c_{u1} = 2\varsigma/\lambda_{u1}\ , \quad c_{u2} = 2\varsigma/\lambda_{u2}\ , \qquad c_\varphi = 2\varsigma/\lambda_\varphi \tag{2.47}$$

where ς is the structural damping ratio equals 0.01 based on [6] . λ_{u1}, λ_{u2}, and λ_φ are the fundamental natural frequencies (in rad/s) for the corresponding elastic deformations. The system natural frequencies will be obtained in Chapter 6.

2.2.3.4 Lagrange's equation

The nonlinear coupled rigid-flexible equations of motion are derived utilizing Lagrange's equation in terms of quasi-coordinates of the platform using Equations (2.8) and (2.9). The equation of motion of the wind turbine drivetrain is similar to Equation (2.11). As well, the conventional form of Language's equations is used to derive the coupled equations of motion correspond to the generalized flexible coordinates, such that [89]

$$\frac{d}{dt}\left(\frac{\partial \mathcal{L}}{\partial \dot{\mathbf{q}}}\right) - \frac{\partial \mathcal{L}}{\partial \mathbf{q}} + \frac{\partial \Upsilon}{\partial \dot{\mathbf{q}}} = \mathbf{Q} \tag{2.48}$$

where $\mathbf{q} = [\boldsymbol{\xi} \quad \boldsymbol{\Theta} \quad \boldsymbol{\delta}]^T$ is the vector of the flexible generalized coordinates. The principle of virtual work is utilized to compute the generalized forces ($\mathbf{Q}$) associated with ($\mathbf{q}$) as [88]

$$\mathbf{Q} = \frac{\partial \mathbf{v}_r}{\partial \dot{\mathbf{q}}} \bullet \mathbf{F}_{aer} + \frac{\partial \boldsymbol{\omega}_r}{\partial \dot{\mathbf{q}}} \bullet \left(\tau_a \, \hat{\mathbf{b}}_1\right) \tag{2.49}$$

The complex system kinematics particularly due to nonlinear terms of the beam shortening, elastic rotation of the tower tip and coupling among the rigid body and flexible coordinate leads to a very lengthy form of the system kinetic energy. Therefore, a MATLAB$^{\circledR}$ symbolic code is developed to produce the equations of motion. The general form of the equation of motions, can be then written

$$\left[\mathbf{M}_{sys} + \bar{\mathbf{A}}\right] \begin{bmatrix} \dot{\boldsymbol{\nu}} \\ \dot{\boldsymbol{\omega}} \\ \dot{\Omega} \\ \ddot{\mathbf{q}} \end{bmatrix} = \begin{bmatrix} \mathbf{F}_{hs} + \mathbf{F}_{aer} + \mathbf{F}_{mor} + \mathbf{F}_{hd*} \\ \mathbf{M}_{hs} + \mathbf{M}_{aer} + \mathbf{M}_{mor} + \mathbf{M}_{hd*} \\ \tau_a - \tau_g \\ \mathbf{Q} \end{bmatrix} + \left[\mathbf{f}(\mathbf{r}, \boldsymbol{\theta}, \boldsymbol{\nu}, \boldsymbol{\omega}, \Omega, \mathbf{q}, \dot{\mathbf{q}})\right] \tag{2.50}$$

the size of $\mathbf{M}_{sys}$ is $(7 + n_e)$ where $n_e = 2\,n_b + n_t$, $\bar{\mathbf{A}}$ is written as

$$\bar{\mathbf{A}} = \begin{bmatrix} \mathbf{A} & \mathbf{0}_{6\times(1+n_e)} \\ \mathbf{0}_{(1+n_e)\times 6} & \mathbf{0}_{(1+n_e)\times(1+n_e)} \end{bmatrix} \tag{2.51}$$

and $\mathbf{f}$ is a vector with nonlinear elements in $\mathbf{r}, \boldsymbol{\theta}, \boldsymbol{\nu}, \boldsymbol{\omega}, \Omega, \mathbf{q}, \dot{\mathbf{q}}$. Unfortunately, due to the complex system kinematics a closed form for the mass matrix, $\mathbf{M}_{sys}$ and $\mathbf{f}$ could not be achieved as was previously done for the rigid model.

2.3 External Forces

The external loads includes hydrostatic, hydrodynamic, aerodynamics and mooring loads as previously described in Equation (2.16). The computation of hydrostatic loads will be investigated in Chapter 3 where a new exact nonlinear hydrostatic analytical formulation is developed and subsequently used to calculate these loads. The mooring loads are computed using a simplified quasi-static cable or lumped mass cable models. The latter approach will be thoroughly investigated in Chapter 5 while the former will be discussed in Chapter 4. The approaches used to evaluate hydrodynamic and aerodynamic loads will be presented in the following subsections. The characterization of the wave field kinematics is presented first to allow for formulation of the hydrodynamic loads exerted on the submerged part of the platform. The aerodynamic loads are then discussed.

2.3.1 Wave kinematics

Based on the Airy linear wave theory, the water surface elevation of a regular water wave is described by a traveling harmonic sinusoidal signal propagating along the horizontal axis X, expressed as

$$\mathcal{H}(X,t) = \mathcal{H}_a \cos(\omega t - cX) \tag{2.52}$$

Where $\mathcal{H}$ is the wave surface elevation from the Mean Water Level (MWL), $\mathcal{H}_a$ is the wave amplitude, ω is the wave frequency, and c is the wave number. The wave number and wave frequency are related by a dispersion relation as [18, 95]

$$\omega^2 = g\, c \tanh(d_w c) \tag{2.53}$$

where d_w is the water depth. Real random sea environment is described by an irregular wave which is characterized as a sum of N_ω regular wave components of different amplitudes, frequencies, and phases as [18]

$$\mathcal{H}(X,t) = \sum_{i=1}^{N_\omega} \mathcal{H}_{a_i} X \cos(\omega_i t - c_i X + \epsilon_i) \tag{2.54}$$

where ω_i, c_i, and $\mathcal{H}_{a_i}$ are the i-th wave frequency, wave number, and amplitude , respectively, and ϵ_i is a uniformly distributed random phase angle in the range $[0 \quad 2\pi]$.

The relationship between the wave amplitude ($\mathcal{H}_{a_i}$) and frequency (ω_i) in Equation (2.54) can be constructed utilizing a wave spectrum that represents the wave energy content distribution over the wave frequency band. The wave spectrum is characterized based on measurements recording the wave elevation time series in a certain location. Although there are several wave spectra describing the ocean environments in different places, the Jonswap spectrum is chosen here since it is widely used for evaluating and validating the FOWT stochastic dynamics, expressed as [96]

$$S_J(\omega) = \left(1 - 0.287 \ln(\gamma)\right) \frac{5}{16} H_s^2 \, \omega_p^4 \, \omega^{-5} \exp\left(-\frac{5}{4}\left(\frac{\omega}{\omega_p}\right)^{-4}\right) \quad \gamma^{\exp\left(-\frac{1}{2}\left[\frac{\omega-\omega_p}{\sigma_w \omega_p}\right]\right)} \tag{2.55}$$

where H_s is the significant wave height which represents the mean of 1/3 of the highest waves, $\omega_p = 2\pi/T_p$ is the peak frequency and T_p is the corresponding period, and σ_w is a spectral width parameter defined as [96]

$$\sigma_w = \begin{cases} 0.07 & \text{for} \quad \omega \leq (2\pi/T_p) \\ 0.09 & \text{for} \quad \omega > (2\pi/T_p) \end{cases} \tag{2.56}$$

and the peak shape parameter (γ) is defined as [97]

$$\gamma = \begin{cases} 5 & \text{for} \quad \frac{T_p}{\sqrt{H_s}} \leq 3.6 \\ \exp\left(5.75 - 1.15\frac{T_p}{\sqrt{H_s}}\right) & \text{for} \quad 3.6 < \frac{T_p}{\sqrt{H_s}} \leq 5 \\ 1 & \text{for} \quad \frac{T_p}{\sqrt{H_s}} > 5 \end{cases} \tag{2.57}$$

The i-th wave amplitude $\mathcal{H}_{a_i}$ corresponds to the i-th wave component (of frequency ω_i) can be obtained as [98]

$$\mathcal{H}_{a_i} = \sqrt{2 \int\limits_{\omega_i - 0.5\Delta\omega_i}^{\omega_i + 0.5\Delta\omega_i} S_J(\omega)\, d\omega} \quad , \quad \Delta\omega_i = \omega_i - \omega_{i-1} \tag{2.58}$$

Generating the wave elevation time histories using Equation (2.58) should be done with care to avoid self-repetition [98]. The time series of the wave elevation repeats every $(2\pi/\Delta\omega)$

seconds for a uniform discretization of the wave spectrum i.e if $\Delta\omega$ is constant. A simple way to avoid this problem is to reduce $\Delta\omega$ to generate wave elevation time history for a sufficient time period to perform the dynamic simulation before the wave time history repeats. However, this implies using a small $\Delta\omega$ resulting in a large number of wave component (N_ω) which is computationally expensive. The most efficient approach to solve this problem is to use a variable frequency step by increasing the frequency step with a fixed increment, for example $\Delta\omega_i = 1.1\,\Delta\omega_{i-1}$ as recommended in [98]. Figure 2.5 shows the wave spectrum for $H_s = 5$ m and $T_p = 10$ s and Figure 2.6 illustrates the corresponding generated wave elevation time history using the latter approach.

Having the wave spectrum discretization realized, the wave kinematic relations can be then established. The horizontal fluid velocity at depth Z (measured negative from MWL downwards) can be expressed as [18, 95]

$$\breve{u}(X,Z,t) = \sum_{i=1}^{N_\omega} \omega_i \mathcal{H}_{a_i} \left[\frac{\cosh(c_i(Z+d_w))}{\sinh(c_i\,d_w)}\right] \cos(\omega_i t - c_i X + \epsilon_i) \tag{2.59}$$

The vertical fluid velocity is [18, 95]

$$\breve{w}(X,Z,t) = \sum_{i=1}^{N_\omega} -\omega_i \mathcal{H}_{a_i} \left[\frac{\sinh(c_i(Z+d_w))}{\sinh(c_i\,d_w)}\right] \sin(\omega_i t - c_i X + \epsilon_i) \tag{2.60}$$

If the wave propagates with a heading angle β_w relative to the X-axis, as shown in Figure 2.7, the fluid velocity $\mathbf{v}_f$ can be expressed as

$$^{I}\mathbf{v}_f(X,Y,Z,t) = \begin{bmatrix} \breve{u}\cos\beta_w & \breve{u}\sin\beta_w & \breve{w} \end{bmatrix}^T \tag{2.61}$$

and X in Equations (2.54), (2.59) and (2.60) should be replaced with ($\breve{X} = X\cos(\beta_w) + Y\sin(\beta_w)$). The fluid acceleration is simply determined by differentiating Equations (2.59) and (2.60) with respect to time.

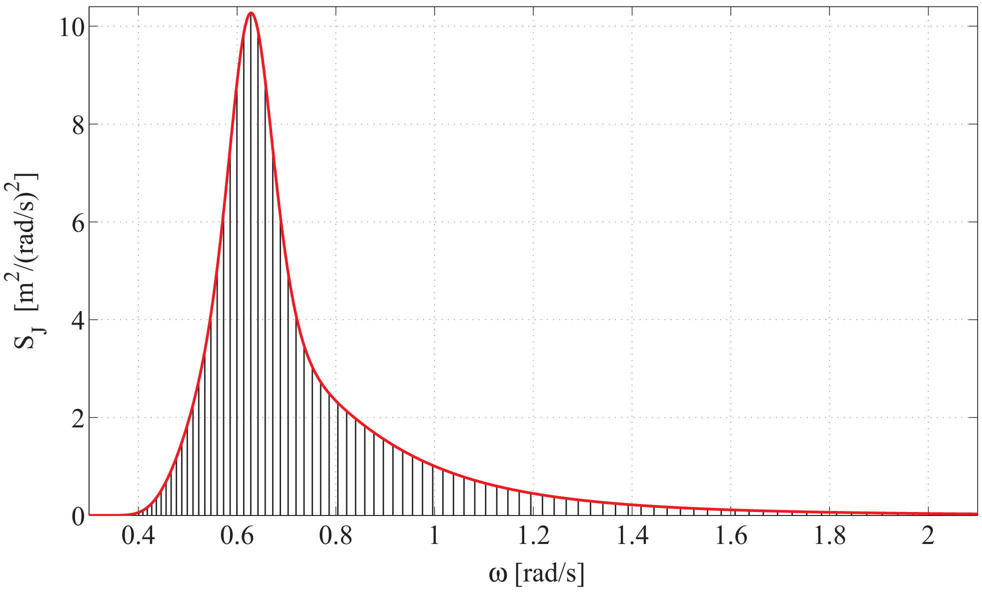

Figure 2.5: Jonswap wave spectrum with variable frequency step discretization, $H_s = 6$ m, $T_p = 10$ s and $N_\omega = 100$

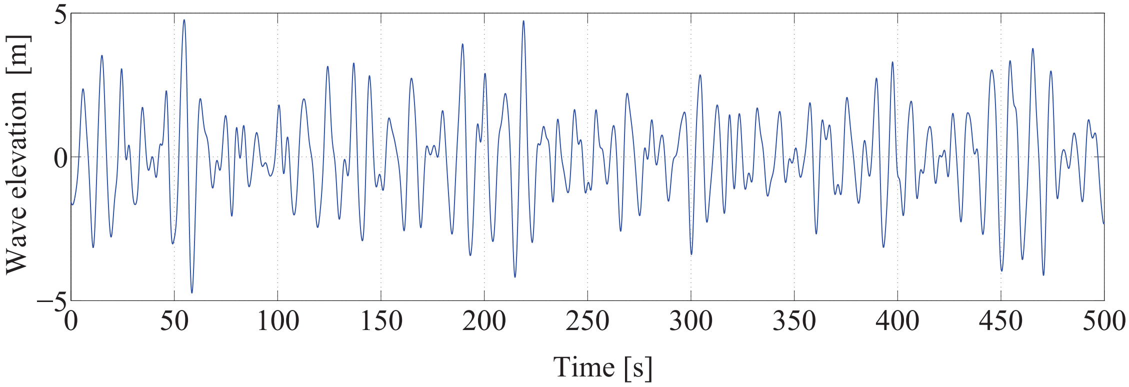

Figure 2.6: Wave elevation time history generated from the wave spectrum in Figure 2.5

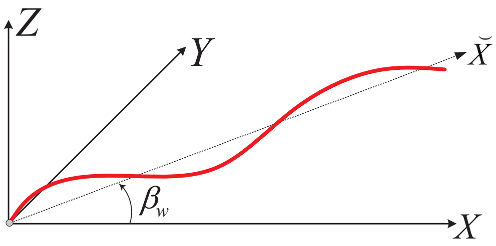

Figure 2.7: Wave heading angle

2.3.2 Hydrodynamic loads

Because of the platform structure slenderness, Morison's equation can be applied to compute the hydrodynamic loads acting on the floating platform [99]. Accordingly, the hydrodynamic force ($\mathbf{F}_{hd}$) and moment ($\mathbf{M}_{hd}$) around the platform body-fixed frame origin exerted on the submerged part of the platform acts normal to the platform centerline (z). $\mathbf{F}_{hd}$ is already expressed as a sum of the inertial ($\mathbf{F}_{iner}$) and combined drag and Froude-Krylov terms hydrodynamic loads ($\mathbf{F}_{hd*}$) in Equation (2.17) and likewise $\mathbf{M}_{hd}$.

The inertial terms which are functions of the platform kinematics are often shifted to the left hand side of the equations of motion as in Equation (2.19). While $\mathbf{F}_{hd*}$ term remains on the right hand side of the equations of motion together with the hydrostatic, aerodynamic, and mooring loads terms. $\mathbf{F}_{hd*}$ and $\mathbf{M}_{hd*}$ can be obtained as

$$\begin{aligned} \mathbf{F}_{hd*} &= \int_{-a_{pf}}^{L_{cf}-a_{pf}} \left(\rho\left(1+C_a\right)A_{cs}(\dot{\mathbf{v}}_f)_\perp + \frac{1}{2}\rho C_D D_{cs}(\mathbf{v}_{rel})_\perp \left\|(\mathbf{v}_{rel})_\perp\right\| \right) dz \\ \mathbf{M}_{hd*} &= \int_{-a_{pf}}^{L_{cf}-a_{pf}} \mathbf{r}_z \times \left(\rho\left(1+C_a\right)A_{cs}(\dot{\mathbf{v}}_f)_\perp + \frac{1}{2}\rho C_D D_{cs}(\mathbf{v}_{rel})_\perp \left\|(\mathbf{v}_{rel})_\perp\right\|\right) dz \end{aligned} \tag{2.62}$$

where C_a and C_D are the added mass and drag coefficients, respectively. The distance between the origin of $\boldsymbol{\mathcal{F}}_p$ and platform base center is denoted by a_{pf}, and L_{cf} is the submerged length, as shown in Figure 2.8. The procedure of computing L_{cf} will be investigated in Chapter 3. The position of a generic point on the platform centerline is $\mathbf{r}_z = [0 \quad 0 \quad z]^T$ and z changes according to the integration limits in Equation (2.62). The velocity and acceleration of this point is $\mathbf{v}_p$ and $\dot{\mathbf{v}}_p$, respectively, as shown in Figure 2.8. The corresponding fluid velocity and acceleration are $\mathbf{v}_f$ and $\dot{\mathbf{v}}_f$, respectively, which can be determined from the wave field kinematics (Section 2.3.1). If there are no waves, then $\mathbf{v}_f$ and $\dot{\mathbf{v}}_f$ vanish. The relative fluid velocity required to determine the drag force in Equation (2.62) is given as

$$\mathbf{v}_{rel} = \mathbf{v}_f - \mathbf{v}_p \tag{2.63}$$

The component of (.) perpendicular to the platform centerline is denoted by $(.)_\perp$. The local cross section diameter and area are D_{cs} and A_{cs}, respectively, which they vary along the plat-

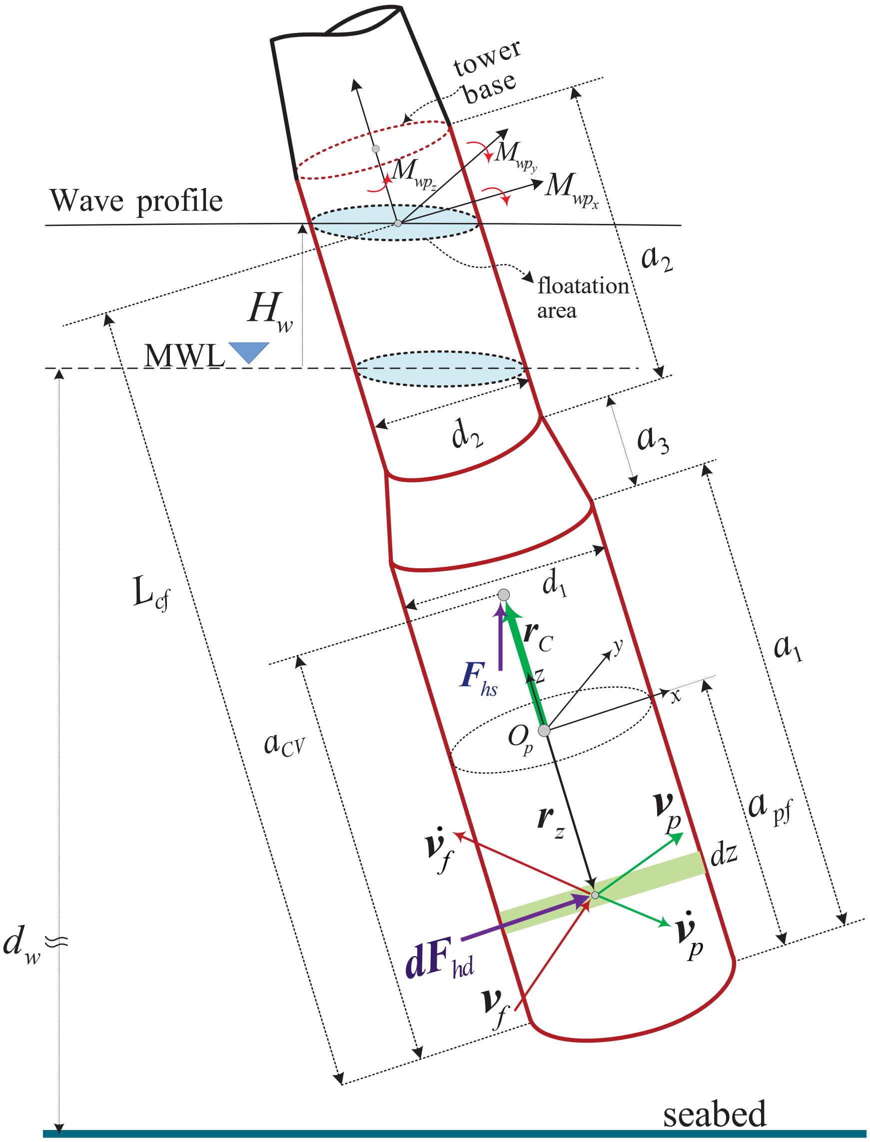

Figure 2.8: Hydrostatic and hydrodynamic loads

form span as the platform is composed of multiple sections. The integrals in Equation (2.62) are calculated numerically by discretizing the platform submerged length into a number of disks and summing the resulting force and moment contributed by all sections along the submerged length. The hydrodynamic inertial force and moment around the origin of $\boldsymbol{\mathcal{F}}_p$ based on Morison's equation are obtained as

$$\mathbf{F}_{iner} = \int_{-a_{pf}}^{L_{cf}-a_{pf}} -\rho\, C_a\, A_{cs}\, (\dot{\mathbf{v}}_p)_\perp \, dz \quad , \quad \mathbf{M}_{iner} = \int_{-a_{pf}}^{L_{cf}-a_{pf}} -\mathbf{r}_z \times \left(\rho\, C_a\, A_{cs}\, (\dot{\mathbf{v}}_p)_\perp\right) dz \tag{2.64}$$

Equation (2.64) can be reformulated in a matrix form as previously done in Equation (2.18) that introduced $\mathbf{C}_A$ and $\mathbf{A}$. The added mass matrix is mainly dependent on the submerged body shape, can be expressed for a cylindrical platform as [100]

$$\mathbf{A} = \begin{bmatrix} A_{11} & 0 & 0 & 0 & A_{15} & 0 \\ & A_{22} & 0 & A_{24} & 0 & 0 \\ & & A_{33} & 0 & 0 & 0 \\ & sym. & & A_{44} & 0 & 0 \\ & & & & A_{55} & 0 \\ & & & & & 0 \end{bmatrix} \tag{2.65}$$

The off-diagonal elements exist because the origin of $\boldsymbol{\mathcal{F}}_p$ does not coincide with the platform center of volume which is varying during dynamic simulation. The elements of the added mass matrix are

$$\begin{aligned} A_{11} =& A_{22} = C_a \; \rho \, V_d \quad , \qquad\qquad A_{33} = C_a \left(\frac{1}{12} \rho \pi {d_1}^3 \right) \\ A_{15} =& - A_{24} = A_{11} \; (a_{CV} - a_{pf}) \quad , \quad A_{44} = A_{55} = C_a \; I_{add} \end{aligned} \tag{2.66}$$

where a_{CV} is the distance between the platform base and the center of the submerged volume of length L_{cf} assuming the platform is on an even keel (vertical). The added mass coefficient, C_a is approximately 1.0 for a slender circular cylinder [20, 96]. The added mass of a slender circular cylinder in a direction parallel to its centerline (A_{33}) is approximately equivalent to the fluid mass of a hemisphere of a similar diameter [101]. I_{add} denotes the inertia of the displaced volume in roll and pitch modes around origin of $\boldsymbol{\mathcal{F}}_p$. The methods used to calculate V_d, a_{CV} and I_{add} are illustrated in Appendix C.2. To formulate $\mathbf{C}_A$, $\mathbf{A}$ can be defined as a 4-block matrix, with 3×3 blocks, as

$$\mathbf{A} = \begin{bmatrix} \mathbf{A}_{11} & \mathbf{A}_{12} \\ \mathbf{A}_{21} & \mathbf{A}_{22} \end{bmatrix} \tag{2.67}$$

$\mathbf{C}_A$ is skew-symmetric, can be then expressed as [20]

$$\mathbf{C}_A = \begin{bmatrix} \mathbf{0}_{3\times 3} & -\widetilde{(\mathbf{A}_{11}\boldsymbol{\nu} + \mathbf{A}_{12}\boldsymbol{\omega})} \\ -\widetilde{(\mathbf{A}_{11}\boldsymbol{\nu} + \mathbf{A}_{12}\boldsymbol{\omega})} & -\widetilde{(\mathbf{A}_{21}\boldsymbol{\nu} + \mathbf{A}_{22}\boldsymbol{\omega})} \end{bmatrix} \tag{2.68}$$

When the platform is subject to steady current, the vortex shedding past the platform yields vortex-induced vibration (VIV). The VIV is found to be prominent particularly in surge/sway directions when the vortex shedding frequency matches the platform surge/sway natural frequency [102,103], which referred to as *lock-in* [103]. The magnitude of amplitude of the VIV could reach the order of the platform diameter [102]. The prediction of hydrodynamic loads associated with the vortex shedding and the resulting VIV is complex and not clearly addressed by analytical models [16]. Thus, the VIV behavior of the structure is usually characterized by experiment as in [104–106]. Therefore, this hydrodynamic effect is neglected in this thesis although it can be considerable (in case current exists) not only for the platform but also for the mooring lines.

2.3.3 Aerodynamic loads

The main wind loads are aerodynamic torque about the turbine shaft (τ_a) and the thrust force (T_a) acting along the shaft axis (normal to the rotor swept area and parallel to $\hat{\mathbf{b}_1}$). These loads, can be characterized as [107,108]

$$\begin{aligned} T_a &= \frac{1}{2}\rho_{air}\,\pi {R_{rot}}^2 \;\; C_T(\lambda, \beta) \;\; \left\| \, (\mathbf{U}_{rel})_{\parallel} \right\|^2 \\ \tau_a &= \frac{1}{2}\rho_{air}\,\pi {R_{rot}}^3 \;\; \frac{1}{\lambda} C_P(\lambda, \beta) \;\; \left\| \, (\mathbf{U}_{rel})_{\parallel} \right\|^2 \end{aligned} \tag{2.69}$$

where R_{rot} is the rotor radius and ρ_{air} is the air density. The relative wind velocity parallel to the wind turbine axis ($\hat{\mathbf{b}_1}$) can be calculated as

$$(\mathbf{U}_{rel})_{\parallel} = \Big((\mathbf{U} - \mathbf{v}_r) \bullet \hat{\mathbf{b}_1} \Big)\, \hat{\mathbf{b}_1} \tag{2.70}$$

The thrust and power coefficients C_T and C_P respectively, are both functions of the tip speed ratio and blade pitch angle (β). The tip speed ratio, λ is defined [3]

$$\lambda = \Omega \, R_{rot} / \left\| (\mathbf{U}_{rel})_{||} \right\| \tag{2.71}$$

The characteristics of C_T and C_P are often plotted versus λ at specific values of β, as shown in Figure 2.9 for the NREL 5 MW baseline wind turbine. These characteristics are obtained from an aerodynamic analysis using bade element momentum theory (BEM).

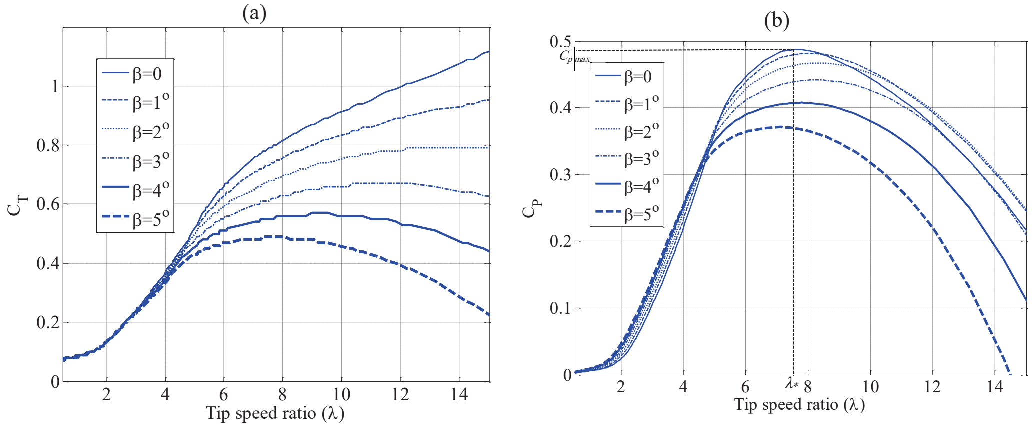

Figure 2.9: NREL 5 MW baseline wind turbine: (a) thrust coefficient; and (b) power coefficient [3]

The tip speed ratio and blade pitch angle should be specified to determine C_P and C_T required to calculate the wind loads using Figure 2.9. The rotor speed increases as wind speed increases at low to moderate wind speeds which results in different λ during operation, as well the blade pitch control changes the pitch angle at higher wind speed. Therefore, the wind turbine operates in different schemes (regions of operation) according to the wind speed. Thus, it is necessary to identify the wind turbine region of operation to determine C_P and C_T properly. The wind turbine regions of operation are illustrated in Figure 2.10. In region I, the wind speed is very low such that $U < U_{cut-in}$, there is insufficient wind power to run the turbine. In region II, the wind speed is less than the rated speed i.e. $U < U_{rated}$, as a result a fraction of the rated power can be captured. The blade pitch is maintained fixed ($\beta \approx 0$). The rotor speed increases as wind speed increases, to maintain λ at the optimal designed value (λ_*) which is coincident with the maximum power coefficient

($C_{P_{max}}$), as illustrated in Figure 2.9 (b). This can be achieved through generator torque control by controlling generator load to modify the rotor speed to approach the desired value λ_*, such that [108, 109]

$$\tau_g = \frac{1}{2}\rho_{air}\,\pi\,R_{rot}^5\,(C_{P_{max}}/\lambda_*^3)\,\Omega^2 \tag{2.72}$$

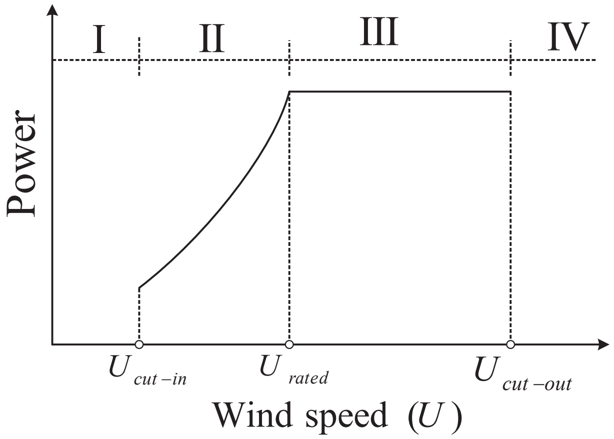

Figure 2.10: Wind turbine regions of operation

In region III, the wind speed is above the rated, $U_{rated} < U < U_{cut-out}$, i.e. the available wind power is larger than the rated wind power. Therefore, the blade pitch control increase the blade pitch angle as the wind speed increases to reduce C_P (Figure 2.9) to dissipate the excess wind power and regulate the extracted wind power to be within the turbine rated power and maintain the rotor speed at its rated value (Ω_{rated}) to protect the wind turbine from damage. When $U > U_{cut-out}$ (region IV), the turbine is shut down for protection. It is worth mentioning that Figure 2.10 represents generic operation modes of a variable-speed variable-pitch wind turbine. However, these regions of operation could involve transition regions or subregions based on the control system strategies used to optimize the wind turbine operation [107]. The reader can refer to [107–109] for further details about the wind turbine operation and control.

The design variables of the NREL wind turbine, U_{cut-in}, U_{rated}, $U_{cut-out}$, Ω_{rated}, and λ_* are 3 m/s, 11.4 m/s, 25 m/s, 12.1 rpm, and 7.55 respectively [87].

The aerodynamic force and corresponding moment (Equation (2.16)) around the origin of the platform frame can be obtained for the equations of motion of the flexible model

(Equation (2.50)) as

$$\begin{aligned} {}^{p}\mathbf{F}_{aer} =& \mathbf{R}_{el}\left(T_a \hat{\mathbf{b}_1}\right) \\ {}^{p}\mathbf{M}_{aero} =& \mathbf{R}_{el}\left(\tau_a\, \hat{\mathbf{b}_1}\right) + (\mathbf{r}_{Bl} + \mathbf{R}_{el}\,\mathbf{r}_{rot}) \times {}^{p}\mathbf{F}_{aer} \end{aligned} \tag{2.73}$$

The aerodynamic loads required for the equations of motion of the rigid model (Equation (2.19)) can be computed by replacing $\hat{\mathbf{b}_1}$ in Equation (2.70) by $\hat{\mathbf{i}}$, and Equation (2.73) should be accordingly modified to apply for the rigid model as

$${}^{p}\mathbf{F}_{aer} = [T_a \quad 0 \quad 0]^T \quad , \quad {}^{p}\mathbf{M}_{aer} = \tau_a\,\hat{\mathbf{i}} + \mathbf{r}_{G_r} \times {}^{p}\mathbf{F}_{aer} = [\tau_a \quad T_a\, D_r \quad 0]^T \tag{2.74}$$

Chapter 3

HYDROSTATICS

FOWT platforms can exhibit large deflections when acted upon by a combination of large steady wind and hydrodynamic loads. Large deflections particularly in heave, roll and pitch can also yield large hydrostatic loads and lead to nonlinear behavior. Most FOWT dynamic analyses model the hydrostatic loads using a linear approach. This chapter presents a new exact nonlinear coupled hydrostatic approach to calculate the magnitude of the buoyancy forces and the coupled hydrostatic restoring moments as functions of the instantaneous displaced position and orientation of offshore platforms.

The analysis begins by deriving the hydrostatic loads for a single-degree-of-freedom (SDOF) finite rotation of a floating cylinder which is later used to verify the results of the general model. The analysis is then extended to derive the instantaneous center of buoyancy for a floating cylinder undergoing a general displacement. Evaluating the position of the center of buoyancy is essential to the derivation of the buoyancy forces and moments which are subsequently used to obtain the hydrostatic stiffness matrix at an arbitrary position and orientation of the floating cylinder. As well, the developed approach is efficiently applied to determine the exact equilibrium positions and orientation of free floating cylindrical bodies. Finally, the hydrostatic loads are accordingly computed as a part of the external forces in the system dynamic equations of motion.

3.1 Single Degree-of-Freedom (SDOF) Rotation of Floating Cylinders

The hydrostatic restoring moment of water plane area of a floating circular/rectangular cylinder undergoing pure roll/pitch rotation arises from the lateral shift of the buoyancy center due to change of the submerged volume shape, as shown in Figure 3.1. Mathematically,

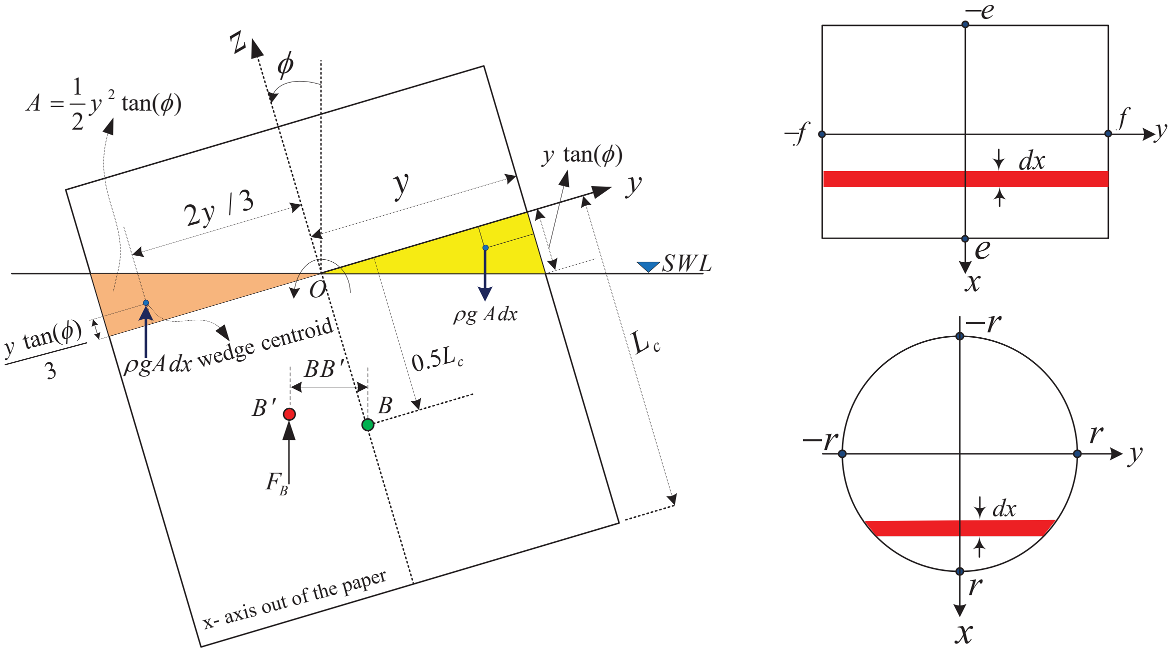

(a) (b)

Figure 3.1: (a) Rotated floating cylinder in roll motion; (b) cylinder cross sections. B and B' are the centers of buoyancy before and after the rotation, respectively, SWL: Still Water Level.

this moment is a couple generated by the buoyancy forces of the submerged wedge (with positive buoyancy) and emerged wedge (with negative buoyancy), as shown in Figure 3.1. This moment is equivalent to the moment of buoyancy force of the rotated cylinder (acting at B') around the center of buoyancy of the unrotated cylinder (acting at B) assuming that the buoyancy force does not change during rotation i.e. the submerged volume does not change during rotation [17, 20, 22]. This moment can be formulated as

$$M_{wp}^{x} = -\rho g \int \left[2\left(\tfrac{1}{2}y^2\tan(\phi)\right)\cos(\phi)\ \tfrac{2}{3}y + 2\left(\tfrac{1}{2}y^2\tan(\phi)\right)\sin(\phi)\ \tfrac{1}{3}y\tan(\phi)\right] dx \tag{3.1}$$

The integration limits in Equation (3.1) vary from $x = -r$ to r for a circular cylinder and from $x = -e$ to e for a rectangular cylinder, as shown in Figure 3.1. Equation (3.1) can be reduced to

$$M_{wp}^{x} = -\rho g \left(\sin(\phi) + \frac{1}{2}\sin(\phi)\tan^2(\phi)\right) \int \frac{2}{3}y^3 dx \tag{3.2}$$

where, again, the integration limits vary from $x = -r$ to r for a circular cylinder and from $x = -e$ to e for a rectangular cylinder. The integral in Equation (3.2), $\int (2/3)\, y^3 dx =$

$\int dI_{xx} = I_{xx}$, where I_{xx} is second moment of area of the floating cylinder section area, thus the water plane restoring moment can be expressed as:

$$M_{wp}^{x} = -\rho g \, I_{xx} \left(\sin(\phi) + \frac{1}{2} \sin(\phi) \tan^2(\phi) \right) \tag{3.3}$$

The relation in Equation (3.3) represents the exact restoring moment and it can be used to determine the restoring moments at any rotation angle as long as the cylinder top face is not in contact with the water surface. However, if the rotation is small, most texts authors simplify the analysis by dropping the higher order term (second term in the square brackets) and assume $\cos(\phi) \approx 1$ in Equation (3.1) as [110]:

$$M_{wp}^{x} = -\rho g \int 2 \left(\frac{1}{2} y^2 \tan(\phi) \right) \frac{2}{3} y \, dx \tag{3.4}$$

and in final form [110]:

$$M_{wp}^{x} = -\rho g \, I_{xx} \tan(\phi) \tag{3.5}$$

Equation (3.5) can be further simplified for small rotations as

$$M_{wp}^{x} \approx -\rho g \, I_{xx} \, \phi \tag{3.6}$$

Figure 3.2 (a) shows the normalized water plane moment (M_{wp} divided by $\rho g I_{xx}$) as computed using the exact form of Equation (3.3) and the analogous relations in Equations (3.5) and (3.6). The results of the three forms match up to 10° and the forms of Equations (3.3) and (3.5) yield a larger moment for further rotation. The latter forms match up to 30° and the exact form yields a larger moment for further rotation. The roll stiffness of water plane is formulated as $K_{wp}^{x} = -dM_{wp}^{x}/d\phi$. It is approximately equal to $\rho g I_{xx}$ (normalized value=1) if the roll angle is very small while it is larger than 1 for larger angles, as shown in Figure 3.2 (b). K_{wp}^{x} computed using the exact form and using Equation (3.5) match up to 15° and the exact form yields a larger stiffness for further rotation, as seen in Figure 3.2 (b). The horizontal shift in the buoyancy center can be simply determined as

$$\overline{BB'} = M_{wp}^{x}/F_B \quad , \quad F_B = \rho g V_d \tag{3.7}$$

where V_d is the submerged volume.

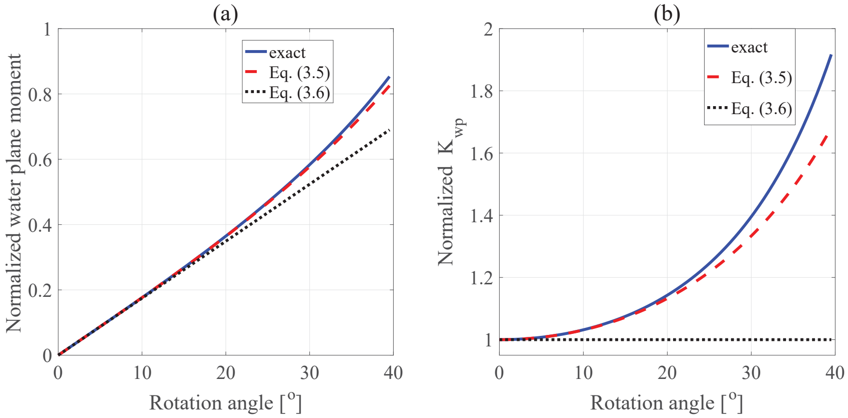

Figure 3.2: Normalized water plane area: (a) moment; (b) stiffness

3.2 Three-Dimensional Rotation Hydrostatics

The preceding analysis can be used to determine the restoring moments of a floating cylinder for a single-degree-of freedom rotation, i.e. pure roll or pitch displacements. It is also valid for small coupled roll, pitch and yaw displacements, in which case the nonlinear coupling between these rotational displacements can be neglected [17]. Large magnitude platform rotations due to harsh environmental loads give rise to a considerable nonlinear coupling effect. Therefore, it is important to consider nonlinear coupling in evaluating the restoring moments. In this section, a general analysis is developed for this purpose.

During the cylinder motion, the submerged volume changes, and the magnitude of the buoyancy force is expressed as

$$F_B = \rho\, g\, V_d = \rho\, g\, A_c\, L_{cf} \tag{3.8}$$

where A_c is the cylinder cross sectional area. L_{cf} is the submerged length that represents the distance along the cylinder centerline measured from the cylinder base center to the center of the flotation area. The flotation area (grey colored), as shown in Figure 3.3, is prescribed by the intersection of the cylinder and water line. L_{cf} must be obtained at any position and orientation of the floating cylinder to determine the exact magnitude of the buoyancy force. The Z component of the displacement of the base center relative to its analogous position at

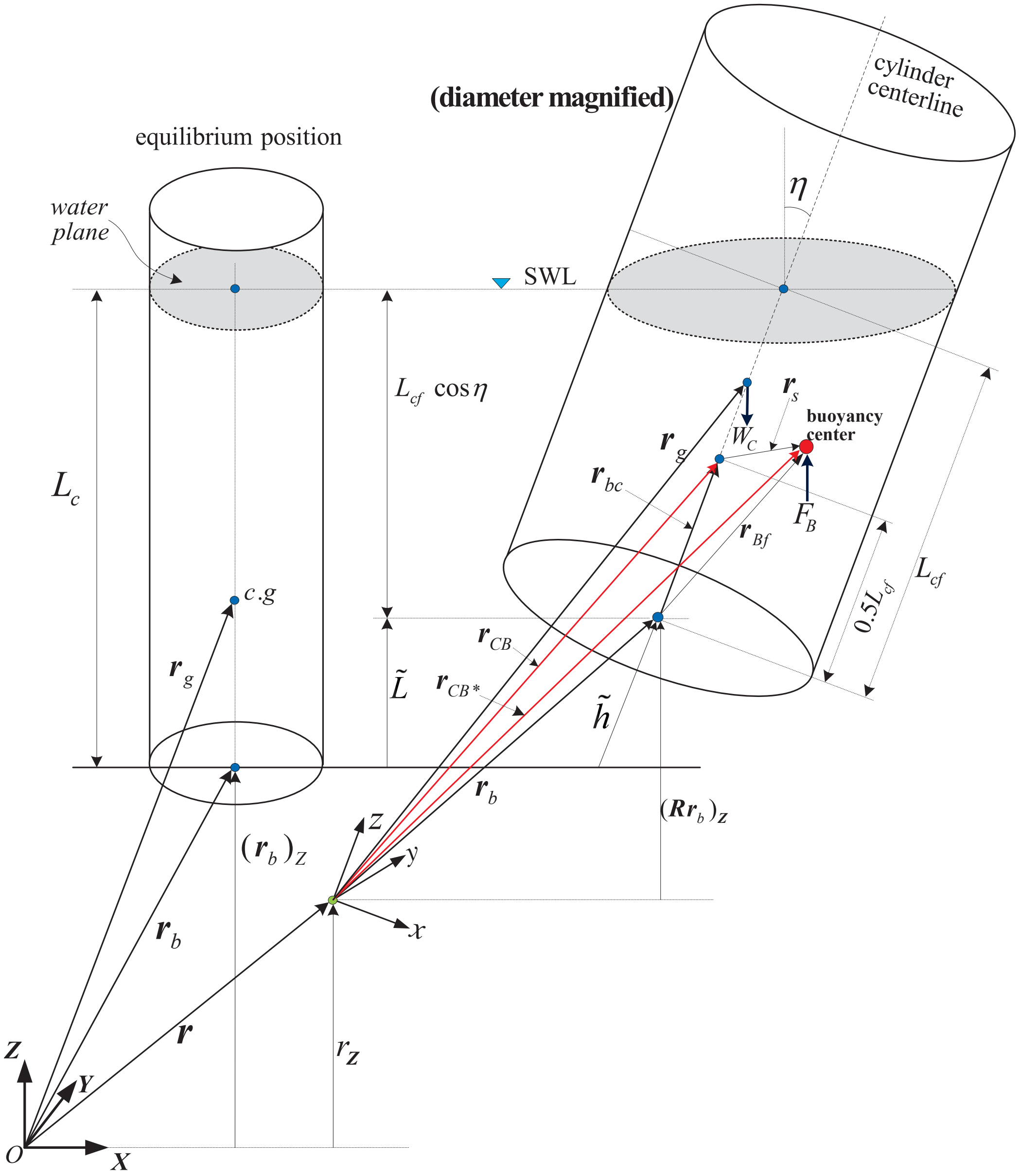

Figure 3.3: General coupled analysis for computing the hydrostatic loads

equilibrium determines the change of the cylinder depth, $\tilde{L}$, as illustrated in Figure 3.3.

$$\tilde{L} = -\left(\left(\mathbf{R}\,{}^{p}\mathbf{r}_b - {}^{p}\mathbf{r}_b\right)_Z + r_Z\right) \tag{3.9}$$

where the subscript Z denote the respective component, and $\mathbf{r}_b$ measures the position of the cylinder bottom base center relative to the origin of the body frame (xyz) which is fixed in the body frame. The change in the submerged length can be expressed as:

$$\tilde{h} = \tilde{L}/\cos(\eta) \tag{3.10}$$

η is the angle between the cylinder centerline and the Z axis i.e. the angle between $\hat{\mathbf{K}}$ and $\hat{\mathbf{k}}$, η can be expressed as

$$\cos(\eta) = \hat{\mathbf{K}} \bullet \hat{\mathbf{k}} = c_\theta \; c_\phi = R_{33} \tag{3.11}$$

Where R_{33} is last element of the rotation matrix $\mathbf{R}$ (Equation (2.1)). The general expression of the submerged length is:

$$L_{cf} = \frac{L_c}{R_{33}} + \tilde{h} = \frac{L_c + \tilde{L}}{R_{33}} \tag{3.12}$$

The buoyancy force can then be determined using (Equation (3.8).

3.2.1 Coupled restoring moments

The hydrostatic restoring moments are generated due to the cylinder's heave and rotations that alter the displaced volume, and hence the position of the center of buoyancy. Computing the position of the buoyancy center during general coupled displacement is the key to determining the coupled restoring moments. The center of buoyancy is the centroid of the submerged volume as shown in Figure 3.4. Without loss of generality, we can change the origin of the body fixed frame xyz to the center of the base of the submerged cylinder to simplify the calculations which are performed in the body frame.

The submerged volume of the cylinder and its center of volume (center of buoyancy) can be determined using a triple integral to compute the volume under the water plane over the base region. The equation of instantaneous water plane in xyz can be determined using the normal vector of the water plane which is simply $\hat{\mathbf{K}}$ in the inertial frame, and in the xyz frame can be represented as

$${}^{p}\mathbf{n} = \mathbf{R}^T[0 \quad 0 \quad 1]^T = R_{31}\,\hat{\mathbf{i}} + R_{32}\,\hat{\mathbf{j}} + R_{33}\,\hat{\mathbf{k}} \tag{3.13}$$

The point $(0, 0, L_{cf})$ is the center of the floatation area (grey-colored in Figure 3.4). Thus, the equation of the water plane area can be formulated in the body frame

$$z = L_{cf} - \frac{R_{31}}{R_{33}}x - \frac{R_{32}}{R_{33}}y = L_{cf} + a\,x + b\,y \tag{3.14}$$

where $a = -R_{31}/R_{33} = t_\theta/\,c_\phi\,$, $b = -R_{32}/R_{33} = -t_\phi$, and $t_{(.)} = \tan(.)$. The submerged

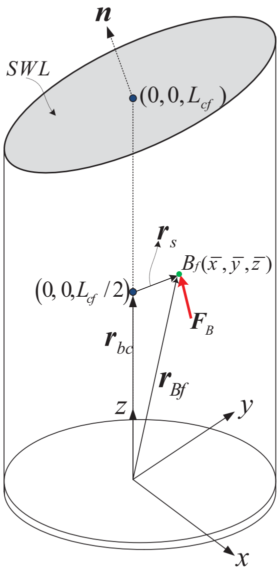

Figure 3.4: Submerged volume in the body fixed frame

volume of the cylinder can be determined to verify Equation (3.8) as

$$\begin{aligned} circular\ cylinder: V_d &= \iiint\limits_A dV_d = \int\limits_{-r}^{r}\ \int\limits_{-\sqrt{r^2-x^2}}^{\sqrt{r^2-x^2}}\ \int\limits_{0}^{L_{cf}+a\,x+by} dz\,dy\,dx \quad = \pi r^2 L_{cf} \\ rectangular\ cylinder: V_d &= \iiint\limits_A dV_d = \int\limits_{-e}^{e}\ \int\limits_{-f}^{f}\ \int\limits_{0}^{L_{cf}+a\,x+by} dz\,dy\,dx \quad = 4\,e\,f\,L_{cf} \end{aligned} \tag{3.15}$$

where A is the cylinder base region, as shown in Figure 3.5 . The x-coordinate of the center

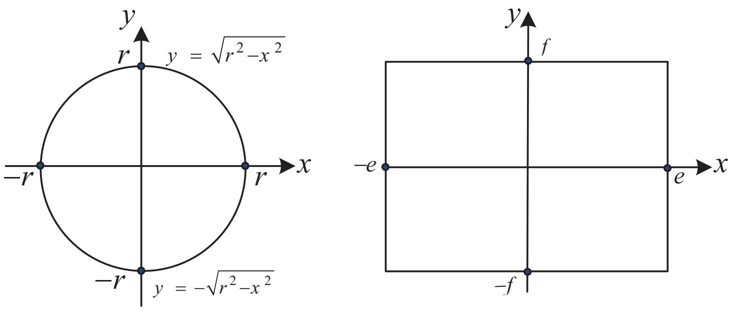

Figure 3.5: Integration region A for circular and rectangular cylinders

of submerged volume is:

$$\begin{aligned}
&\textit{circular cylinder}: \bar{x} = \frac{1}{V_d}\iiint_A x dV_d = \frac{1}{V_d}\int_{-r}^{r}\int_{-\sqrt{r^2-x^2}}^{\sqrt{r^2-x^2}}\int_{0}^{L_{cf}+a\,x+by} x\,dz\,dy\,dx = a\,r^2/4L_{cf}\\
&\textit{rectangular cylinder}: \bar{x} = \frac{1}{V_d}\iiint_A x dV_d = \frac{1}{V_d}\int_{-e}^{e}\int_{-f}^{f}\int_{0}^{L_{cf}+a\,x+by} x\,dz\,dy\,dx = a\,e^2/3L_{cf}
\end{aligned}\tag{3.16}$$

the y-coordinate is:

$$\begin{aligned}
&\textit{circular cylinder}: \bar{y} = \frac{1}{V_d}\iiint_A y dV_d = \frac{1}{V_d}\int_{-r}^{r}\int_{-\sqrt{r^2-x^2}}^{\sqrt{r^2-x^2}}\int_{0}^{L_{cf}+a\,x+by} y\,dz\,dy\,dx = b\,r^2/4L_{cf}\\
&\textit{rectangular cylinder}: \bar{y} = \frac{1}{V_d}\iiint_A y dV_d = \frac{1}{V_d}\int_{-e}^{e}\int_{-f}^{f}\int_{0}^{L_{cf}+a\,x+by} y\,dz\,dy\,dx = b\,f^2/3L_{cf}
\end{aligned}\tag{3.17}$$

the z-coordinate is:

$$\begin{aligned}
&\textit{circular cylinder}: \bar{z} = \frac{1}{V_d}\int_{-r}^{r}\int_{-\sqrt{r^2-x^2}}^{\sqrt{r^2-x^2}}\int_{0}^{L_{cf}+a\,x+by} z\,dz\,dy\,dx = \frac{L_{cf}}{2} + \frac{(a^2\ + b^2\,)r^2}{8L_{cf}}\\
&\textit{rectangular cylinder}: \bar{z} = \frac{1}{V_d}\int_{-e}^{e}\int_{-f}^{f}\int_{0}^{L_{cf}+a\,x+by} z\,dz\,dy\,dx = \frac{L_{cf}}{2} + \frac{(a^2\,e^2\ + b^2 f^2\,)}{6L_{cf}}
\end{aligned}\tag{3.18}$$

The expressions of the submerged volume and coordinates of its center in Equations (3.15) to (3.18) can also be represented in a generalized form in terms of the cross sections area and its second moments of area as:

$$V_d = \rho A_c L_{cf} \quad , \quad \bar{x} = \frac{a\, I_{yy}}{A_c L_{cf}} \quad , \quad \bar{y} = \frac{b\, I_{xx}}{A_c L_{cf}} \quad , \quad \bar{z} = \frac{L_{cf}}{2} + \frac{(a^2\, I_{yy} + b^2 I_{xx})}{2\, A_c L_{cf}} \tag{3.19}$$

where A_c, I_{xx} and I_{yy} expressions for the circular and rectangular cylinders are listed in Table 3.1. It is worth noting that the results in Equation (3.19) are also valid for an elliptic cross section.

Table 3.1: Expressions for A_c, I_{xx} and I_{yy} of the circular and rectangular cylinders

Expression	**Circular cylinder**	**Rectangular cylinder (Barge)**
A_c	πr^2	$4\, e\, f$
I_{xx}	$\pi r^4/4$	$4\, e\, f^3/3$
I_{yy}	$\pi r^4/4$	$4\, f\, e^3/3$

The restoring moments of the water plane area can be formulated in the body frame, as shown in Figure 3.4

$${}^p\mathbf{M}_{wp} = {}^p\mathbf{r}_s \times (\mathbf{R}^T\, \mathbf{F}_B) \quad , \quad \mathbf{r}_s = \mathbf{r}_{Bf} - \mathbf{r}_{bc} \quad , \quad {}^p\mathbf{r}_{bc} = \frac{L_{cf}}{2}\hat{\mathbf{k}} \quad , \quad {}^p\mathbf{r}_{Bf} = \bar{x}\,\hat{\mathbf{i}}, + \bar{y}\,\hat{\mathbf{j}} + \bar{z}\,\hat{\mathbf{k}} \tag{3.20}$$

where $\mathbf{r}_{Bf}$ is the vector from the center of the base to the center of buoyancy, $\mathbf{r}_{bc}$ is the vector from the center of the base to the half of the submerged length. $\mathbf{r}_s$ is the vector from the middle of the submerged length to the center of buoyancy and $\mathbf{F}_B$ is the buoyancy force vector resolved in the inertial frame as:

$${}^I\mathbf{F}_B = [0 \;\; 0 \;\; F_B]^T \tag{3.21}$$

The restoring moments of the water plane area in Equation (3.20) can be expressed as:

$${}^p\mathbf{M}_{wp} = \begin{Bmatrix} M^x_{wp} \\ M^y_{wp} \\ M^z_{wp} \end{Bmatrix} = \rho g \begin{Bmatrix} -\, I_{xx}\left[R_{32} + \frac{{R_{32}}^3}{2{R_{33}}^2}\right] - I_{yy}\left[\frac{R_{32}{R_{31}}^2}{2{R_{33}}^2}\right] \\ I_{yy}\left[R_{31} + \frac{{R_{31}}^3}{2{R_{33}}^2}\right] + I_{xx}\left[\frac{R_{31}{R_{32}}^2}{2{R_{33}}^2}\right] \\ (I_{xx} - I_{yy})\left[\frac{R_{31}R_{32}}{R_{33}}\right] \end{Bmatrix} \tag{3.22}$$

It is evident from the result in Equation (3.22) that the restoring moment components are affected by the rotation sequence since the elements of the rotation matrix have different forms for different sequences [88]. However, the magnitude $\|\mathbf{M}_{wp}\|$ is invariant for a given orientation in space. For the 3-2-1 rotation sequence [88] considered in this study, the water plane area restoring moment components are

$$ {}^{p}\mathbf{M}_{wp} = \rho g \left\{ \begin{array}{c} -I_{xx} c_\theta \left[s_\phi + \frac{1}{2} s_\phi \, t_\phi^2 \right] - \frac{1}{2} I_{yy} c_\theta \left[s_\phi \, \frac{t_\theta^2}{c_\phi^2} \right] \\ -I_{yy} \left[s_\theta + \frac{1}{2} s_\theta \, \frac{t_\theta^2}{c_\phi^2} \right] - \frac{1}{2} I_{xx} \left[s_\theta \, t_\phi^2 \right] \\ - s_\theta \, t_\phi \, \left[I_{xx} - I_{yy} \right] \end{array} \right\} \tag{3.23} $$

If $I_{xx} = I_{yy} = I$ such as in circular and square cylinders, the restoring moments of water plane area reduce to

$$ {}^{p}\mathbf{M}_{wp} = \left\{ \begin{array}{c} M_{wp}^{x} \\ M_{wp}^{y} \\ M_{wp}^{z} \end{array} \right\} = -\rho g \, I \left\{ \begin{array}{c} c_\theta \left[s_\phi + \frac{1}{2} s_\phi \left(\frac{t_\theta^2}{c_\phi^2} + t_\phi^2 \right) \right] \\ \left[s_\theta + \frac{1}{2} s_\theta \left(\frac{t_\theta^2}{c_\phi^2} + t_\phi^2 \right) \right] \\ 0 \end{array} \right\} \tag{3.24} $$

It is interesting to verify Equation (3.23) by substituting $\theta = 0$ (pure roll) to confirm that $M_{wp}^{y} = M_{wp}^{z} = 0$, while M_{wp}^{x} reduces to the same expression as Equation (3.3). In the same manner, substituting $\phi = 0$ (pure pitch) in Equation (3.23) yields $M_{wp}^{x} = M_{wp}^{z} = 0$, while M_{wp}^{y} reduces to the same result as Equation (3.3). The results in Equations (3.22) to (3.24) show that the yaw displacement (around the cylinder axis) has no effect on the water plane area restoring moment components since these components are functions of the 3rd row elements of $\mathbf{R}$ which are free of the angle ψ. However, with other rotation conventions, $\mathbf{M}_{wp}$ may be a function of ϕ, θ and ψ. The water plane area restoring moment resolved in the inertial frame can be expressed as ${}^{I}\mathbf{M}_{wp} = \mathbf{R}\,\mathbf{M}_{wp} = \; [M_{wp}^{X} \quad M_{wp}^{Y} \quad 0 \;]^{T}$. For the considered rotation sequence, the magnitude of the water plane area moment is a function of ϕ and θ only but the yaw displacement still affects the M_{wp}^{X} and M_{wp}^{Y} components while the magnitude $\|\mathbf{M}_{wp}\|$ is fixed for given ϕ and θ, irrespective of the value of ψ. For circular and square cylinders, the water plane restoring moment resolved in the inertial frame can be expressed as:

$$
{}^{I}\mathbf{M}_{wp} = -\rho g\, I \left\{ \begin{array}{c} \frac{(c_\phi^2\; c_\theta^2+1)\;(c_\psi\, s_\phi - s_\psi\; c_\phi\; s_\theta\;)}{2\; c_\phi^2\;\; c_\theta^2} \\ \frac{(c_\phi^2\; c_\theta^2+1)\;(s_\psi\, s_\phi + c_\psi\; c_\phi\; s_\theta\;)}{2\; c_\phi^2\;\; c_\theta^2} \\ 0 \end{array} \right\} \tag{3.25}
$$

There is no yaw restoring moment of the water plane around the Z-axis which is a basic principle in hydrostatics. The body frame yaw water plane restoring moment (around the z-axis) still exists and only vanishes for symmetric cross sections areas that possess identical I_{xx} and I_{yy} around their centroidal coordinates such as square, circular, pentagonal, hexagonal, octagonal shapes etc. Figure 3.6 (a) shows the normalized water plane area restoring moment components in the body frame (Equation (3.23)), $M^x_{wp}/\rho g I$ and $M^y_{wp}/\rho g I$, over a range of roll and pitch angles for those cross section shapes. Figure 3.6 (b) depicts the normalized magnitudes of water plane area moment $\left\|\mathbf{M}_{wp}\right\|/\rho g I$. The results show that the restoring moments increase as the rotation angles increases and the large coupling yields higher water plane moment magnitudes. The differential changes in ${}^{p}\mathbf{M}_{wp}$ can be expressed as

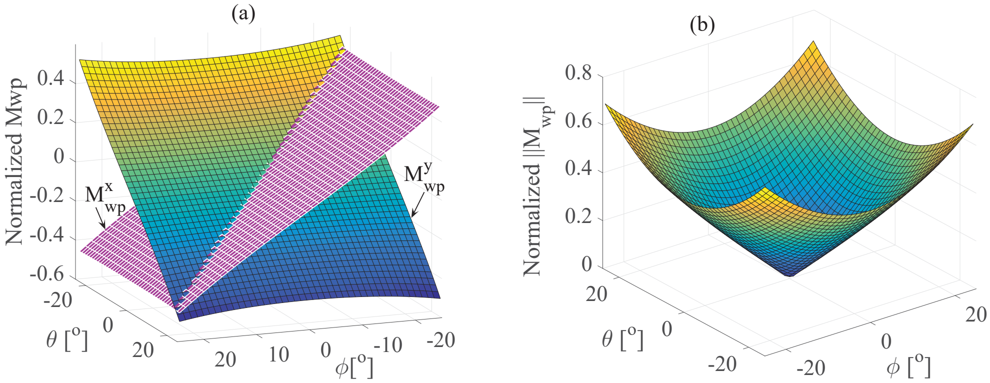

Figure 3.6: Normalized water plane: (a) moments M^x_{wp} and M^y_{wp}; and (b): moment magnitude for cylinders of identical I_{xx} and I_{yy}

$$
[dM^x_{wp} \quad dM^y_{wp} \quad dM^z_{wp}]^T = -\mathbf{K}_{wp}\,[d\phi \quad d\theta \quad d\psi]^T
$$

where $\mathbf{K}_{wp}$ is the water plane area stiffness matrix, formulated in the body frame as

$$
\mathbf{K}_{wp} = \begin{bmatrix} K^{44}_{wp} & K^{45}_{wp} & 0 \\ K^{54}_{wp} & K^{55}_{wp} & 0 \\ K^{64}_{wp} & K^{65}_{wp} & 0 \end{bmatrix} = - \begin{bmatrix} \frac{\partial M^x_{wp}}{\partial \phi} & \frac{\partial M^x_{wp}}{\partial \theta} & \frac{\partial M^x_{wp}}{\partial \psi} \\ \frac{\partial M^y_{wp}}{\partial \phi} & \frac{\partial M^y_{wp}}{\partial \theta} & \frac{\partial M^y_{wp}}{\partial \psi} \\ \frac{\partial M^z_{wp}}{\partial \phi} & \frac{\partial M^z_{wp}}{\partial \theta} & \frac{\partial M^z_{wp}}{\partial \psi} \end{bmatrix} \tag{3.26}
$$

The third column of $\mathbf{K}_{wp}$ is simply zero since $\mathbf{M}_{wp} = \mathbf{M}_{wp}(\phi, \theta)$. While this is not the case for some other rotation conventions in which $\mathbf{M}_{wp} = \mathbf{M}_{wp}(\phi, \theta, \psi)$. As demonstrated earlier, the linear model (Equation (3.5)) is only valid for small coupled rotational displacements. It is essential to capture the influence of nonlinear coupling between the roll and pitch displacements on the water plane area restoring stiffness. To clarify this effect, it is more convenient to consider a cylinder with identical I_{xx} and I_{yy}, such as a circular or square cylinders ($M^z_{wp} = K^{64}_{wp} = K^{65}_{wp} = 0, I_{xx} = I_{yy}$), making interpretation of the results easier. Accordingly, the third row and column of $\mathbf{K}_{wp}$ are zero, and can be ignored, leaving $[dM^x_{wp} \quad dM^y_{wp}]^T = -\mathbf{K}_{wp}[d\phi \quad d\theta]^T$, and $\mathbf{K}_{wp}$ reduces to

$$\mathbf{K}_{wp} = \begin{bmatrix} K^{44}_{wp} & K^{45}_{wp} \\ K^{54}_{wp} & K^{55}_{wp} \end{bmatrix} = - \begin{bmatrix} \frac{\partial M^x_{wp}}{\partial \phi} & \frac{\partial M^x_{wp}}{\partial \theta} \\ \frac{\partial M^y_{wp}}{\partial \phi} & \frac{\partial M^y_{wp}}{\partial \theta} \end{bmatrix} \tag{3.27}$$

It is well known that the diagonal elements of $\mathbf{K}_{wp}/\rho g I$ in Equation (3.27) ≈ 1 while the off-diagonal counterparts ≈ 0 at small roll and pitch angles where the coupling is negligible, as illustrated in Figures 3.7 and 3.8. However, the coupling increases the magnitude of the off-diagonal elements K^{45}_{wp} and K^{54}_{wp}, as seen in Figures 3.7 (b) and 3.8 (b), respectively. It is interesting to note that K^{54}_{wp} is more influenced by coupling and is almost 10 times larger than K^{45}_{wp}. K^{44}_{wp} and K^{55}_{wp} increase as the magnitude of roll angle and pitch angles, respectively increase, as shown in 3.7 (a) and 3.8 (a). This is attributed to the nonlinear behavior of the water plane stiffness, as previously presented in Figure 3.2 (b) noting that the normalized SDOF roll/pitch water plane stiffness ($K_{wp}/\rho g I$) $\approx \sec^2(\phi \text{ or } \theta)$. Surprisingly, K^{44}_{wp} is almost

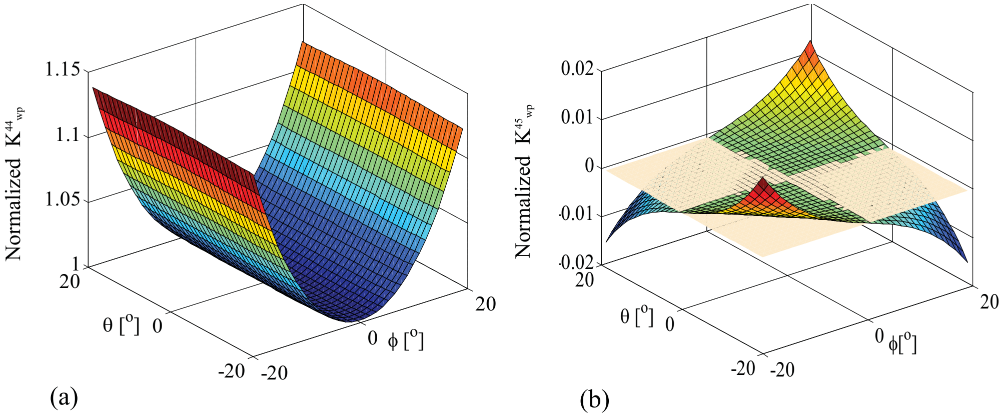

Figure 3.7: Normalized K^{44}_{wp} and K^{45}_{wp} for circular/square cylinder

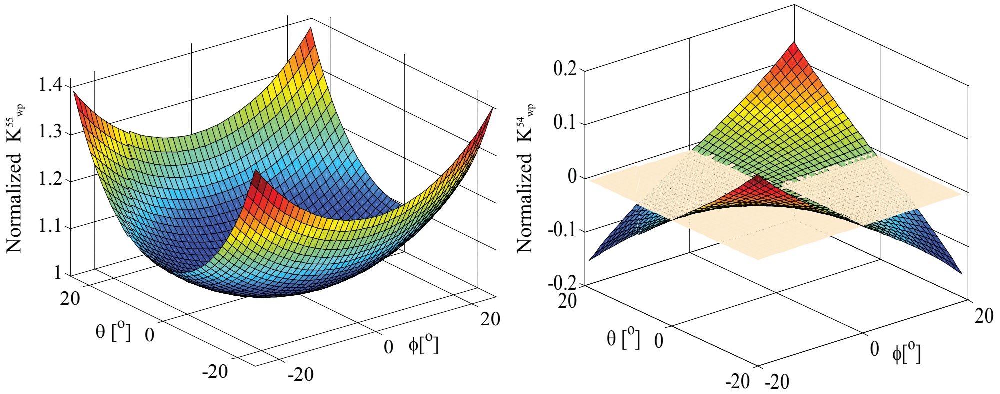

(a) (b)

Figure 3.8: Normalized K_{wp}^{55} and K_{wp}^{54} for circular/square cylinder

unaffected by coupling i.e. $K_{wp}^{44} \approx f(\phi)$ in the considered range of displacements, as seen in Figure 3.7 (a). By contrast, K_{wp}^{55} is considerably influenced by displacement coupling such that larger coupling yields higher pitch stiffness. In general, the water plane pitch stiffness coefficients (K_{wp}^{55} and K_{wp}^{54}) are more influenced by coupled pitch and roll displacements which is attributable to the rotation sequence used to describe the platform kinematics. It would be expected to obtain an opposite trend if the roll rotation precedes the pitch rotation in the rotation sequences used such as 3-1-2, 1-2-3, and 1-3-2 rotation sequences.

3.2.2 Displacement of center of buoyancy and buoyancy moment

In accordance with the analysis developed Section 3.2, the displacement of the center of buoyancy for general displacements can be easily determined, as illustrated in Figure 3.3. The instantaneous center of buoyancy position relative to the origin of the body frame can be represented as

$$\mathbf{r}_{CB*} = \mathbf{r}_b + \mathbf{r}_{Bf} \tag{3.28}$$

The hydrostatic moment exerted by the buoyancy force around the origin of the body frame and resolved in the body frame can be expressed as

$${}^{p}\mathbf{M}_B = {}^{p}\mathbf{r}_{CB*} \times (\mathbf{R}^T \ {}^{I}\mathbf{F}_B) = {}^{p}\mathbf{r}_{CB} \times (\mathbf{R}^T \ {}^{I}\mathbf{F}_B) + {}^{p}\mathbf{M}_{wp} = {}^{p}\mathbf{M}_{ZB} + {}^{p}\mathbf{M}_{wp} \tag{3.29}$$

This form will ease the derivation of the hydrostatic stiffness matrix as will be discussed in the next section. Referring to Figure 3.3, $\mathbf{r}_{CB}$ can be represented as:

$$\mathbf{r}_{CB} = \mathbf{r}_{CB*} - \mathbf{r}_s = \mathbf{r}_b + \mathbf{r}_{bc} \tag{3.30}$$

where $\mathbf{r}_{bc}$ is the position of the midpoint of the submerged length relative to the base center of the cylinder.

3.3 Hydrostatic Restoring Stiffness

The hydrostatic stiffness is attributed to both buoyancy and gravity restoring loads ($\mathbf{K}_h = \mathbf{K}_B + \mathbf{K}_G$). Since the submerged structure is a rigid body, the hydrostatic restoring forces and moments are only functions of the platform submerged shape, position and orientation. The derivations of $\mathbf{K}_B$ and $\mathbf{K}_G$ matrices that form the hydrostatic stiffness matrix ($\mathbf{K}_h$) are detailed in the following subsections.

3.3.1 Buoyancy stiffness ($\mathbf{K}_B$)

The position of the cylinder base center shown in Figure 3.3 can be expressed as ${}^p\mathbf{r}_b = x_f\hat{\mathbf{i}} + y_f\hat{\mathbf{j}} + z_f\hat{\mathbf{k}}$. The buoyancy moment previously derived in Section 3.2.2 can be resolved in the inertial frame as ${}^I\mathbf{M}_B = {}^I\mathbf{M}_{ZB} + {}^I\mathbf{M}_{wp}$, ${}^I\mathbf{M}_{ZB}$ can be evaluated as:

$${}^I\mathbf{M}_{ZB} = \mathbf{R}\,{}^p\mathbf{M}_{ZB} = (\mathbf{R}\,{}^p\mathbf{r}_{CB}) \times {}^I\mathbf{F}_B = \begin{Bmatrix} Y_F F_B \\ -X_F F_B \\ 0 \end{Bmatrix} \tag{3.31}$$

where

$$\mathbf{R}\,{}^p\mathbf{r}_{CB} = \begin{Bmatrix} X_F \\ Y_F \\ Z_F \end{Bmatrix} \quad , \quad {}^p\mathbf{r}_{CB} = \begin{Bmatrix} x_f \\ y_f \\ z_f + 0.5L_{cf} \end{Bmatrix}$$

and ${}^I\mathbf{M}_B$ can be then expressed as

$${}^I\mathbf{M}_B = \begin{bmatrix} M_B^X & M_B^Y & M_B^Z \end{bmatrix}^T = \begin{bmatrix} M_{wp}^X + Y_F F_B & M_{wp}^Y - X_F F_B & 0 \end{bmatrix}^T \tag{3.32}$$

If one defines the translational and finite rotational displacements of the cylinder by a matrix $\mathbf{X}$ and the corresponding buoyancy force and moment components by a matrix $\boldsymbol{\chi}_B$ as

$$\begin{aligned}\mathbf{X} &= \left[\begin{array}{cccccc} r_X & r_Y & r_Z & \phi & \theta & \psi \end{array}\right] \\ \boldsymbol{\chi}_B &= \left[\begin{array}{cccccc} 0 & 0 & F_B & M_B^X & M_B^Y & 0 \end{array}\right]\end{aligned} \tag{3.33}$$

the buoyancy stiffness matrix coefficients in the inertial frame can be derived as

$$\mathbf{K}_B = -\frac{\partial \boldsymbol{\chi}_B}{\partial \mathbf{X}} = \begin{bmatrix} 0 & 0 & 0 & 0 & 0 & 0 \\ 0 & 0 & 0 & 0 & 0 & 0 \\ 0 & 0 & K_B^{33} & K_B^{34} & K_B^{35} & K_B^{36} \\ 0 & 0 & K_B^{43} & K_B^{44} & K_B^{45} & K_B^{46} \\ 0 & 0 & K_B^{53} & K_B^{54} & K_B^{55} & K_B^{56} \\ 0 & 0 & 0 & 0 & 0 & 0 \end{bmatrix} \tag{3.34}$$

It is worth noting that the there are no hydrostatic forces in surge and sway and no yaw moment therefore the first 2 rows and columns are zero together with the last row. For the considered rotation sequence adopted in this study, the detailed derivation and symbolic expressions for these coefficients can be found in Appendix C.

3.3.2 Weight restoring stiffness ($\mathbf{K}_G$)

The moment of the cylinder weight, W_c around the origin of the body frame and resolved in the inertial frame is ${}^I\mathbf{M}_G = [M_G^X \quad M_G^Y \quad 0]^T = (\mathbf{R}\,{}^p\mathbf{r}_g) \times {}^I\mathbf{W}$, where ${}^I\mathbf{W} = [0 \quad 0 \quad -W_c]^T$, $W_c = mg$, m is the cylinder mass and $\mathbf{r}_g = [x_g \quad y_g \quad z_g]^T$, as illustrated in Figure 3.3. The weight and ${}^I\mathbf{M}_G$ components can be defined using matrix $\boldsymbol{\chi}_G$ as

$$\boldsymbol{\chi}_G = \left[\begin{array}{cccccc} 0 & 0 & -W_c & M_G^X & M_G^Y & 0 \end{array}\right] \tag{3.35}$$

The weight restoring stiffness coefficients can be can be derived in the same manner as Equation (3.34)

$$\mathbf{K}_G = -\frac{\partial \boldsymbol{\chi}_G}{\partial \mathbf{X}} = \begin{bmatrix} 0 & 0 & 0 & 0 & 0 & 0 \\ 0 & 0 & 0 & 0 & 0 & 0 \\ 0 & 0 & 0 & 0 & 0 & 0 \\ 0 & 0 & 0 & K_G^{44} & K_G^{45} & K_G^{46} \\ 0 & 0 & 0 & K_G^{54} & K_G^{55} & K_G^{56} \\ 0 & 0 & 0 & 0 & 0 & 0 \end{bmatrix} \tag{3.36}$$

since the platform weight is constant, the third row of $\mathbf{K}_G$ is zero. The weight restoring stiffness coefficients in Equation (3.36) can be found in Appendix C.

3.3.3 Zero displacement hydrostatic matrix

A special case can be considered if the rotational displacements are very small ($\phi \approx \theta \approx \psi \approx 0$) and weight and buoyancy are located along the platform centerline such that $x_f = x_g$ and $y_f = y_g$, and the body frame axes are located on the SWL plane, as shown in Figure 3.9. The heave restoring stiffness can be modeled as a translational spring while the water plane restoring moments in roll and pitch are represented as torsional springs, as shown in Figure 3.9. The hydrostatic stiffness matrix can then be expressed as

$$\mathbf{K}_h = \begin{bmatrix} 0 & 0 & 0 & 0 & 0 & 0 \\ 0 & 0 & 0 & 0 & 0 & 0 \\ 0 & 0 & K_{wp}^h & K_{wp}^h\, y_f & -K_{wp}^h\, x_f & 0 \\ 0 & 0 & K_{wp}^h\, y_f & K_h^{44} & -K_{wp}^h\, x_f\, y_f & (W_c - F_B)\, x_f \\ 0 & 0 & -K_{wp}^h\, x_f & -K_{wp}^h\, x_f y_f & K_h^{55} & (W_c - F_B)\, y_f \\ 0 & 0 & 0 & 0 & 0 & 0 \end{bmatrix} \tag{3.37}$$

where the hydrostatic stiffness matrix entries are

$$K_h^{44} = - W_c\, z_g + F_B\, z_B + K_{wp}^r + K_{wp}^h\, {y_f}^2$$

$$K_h^{55} = - W_c\, z_g + F_B\, z_B + K_{wp}^p + K_{wp}^h\, {x_f}^2$$

$$K_{wp}^h = \rho g\, A_c \quad , \qquad K_{wp}^r = \rho g\, I_{xx} \quad , \qquad K_{wp}^p = \rho g\, I_{yy}$$

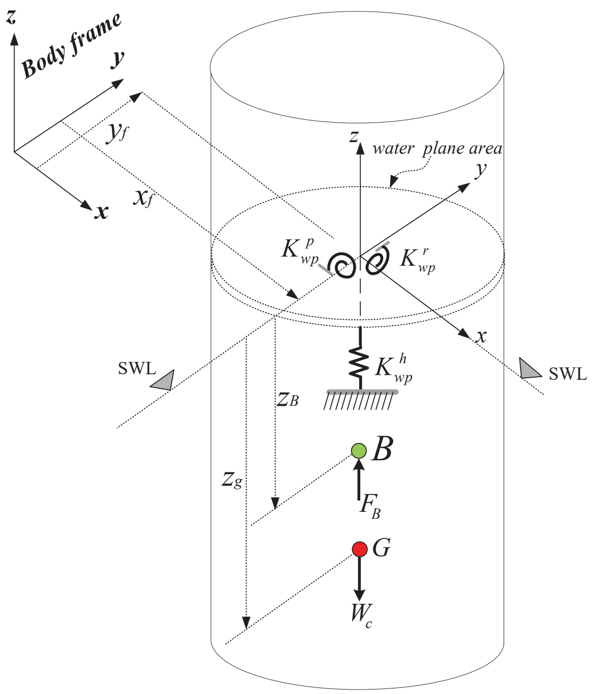

Figure 3.9: Buoyancy restoring forces and moments at zero rotation angles

This stiffness matrix is only symmetric if $K_h^{46} = K_h^{64}$, which happens only when $x_f = y_f = 0$ i.e. the body frame z-axis coincides with the cylinder centerline or if the $W_c = F_B$. z_B and z_g are measured negative downwards. The hydrostatic stiffness matrix in Equation (3.37) is often used in dynamics analyses of offshore platform [17, 20].

3.4 Three-Dimensional Equilibrium of a Free Floating Cylinder

The hydrostatic equilibrium of floating structures is generally analyzed numerically utilizing iterative approaches and searching techniques [17, 21] since the buoyancy force and moments are functions of the equilibrium position. Fortunately, the theoretical analyses developed here can be directly applied to find the exact 3D equilibrium position and orientation of cylinders that float freely or subject to external loadings. Moreover, it can be efficiently used to find the equilibrium position and orientation for an arbitrary position of the cylinder's center of gravity. The analysis is implemented for a rectangular cylinder in the following example.

Example : A rectangular cylinder of weight W_c floats freely in water ($\rho = 1000$ kg/m^3). The cylinders dimensions are $2 \times 1 \times 6$ m, as shown in Figure 3.10. The cylinder initially was at even keel ($\mu = 0$), the draft $L_c = 3$ m. The center of gravity is located 0.5 m above the bottom base center along the cylinder vertical centerline (z). An external vertical force $F_e = W_c/4$ is applied at the cylinder corner, the new equilibrium position and orientation (Euler angles) and the coordinates of the cylinders corners intercepts with the SWL are required.

Solution : Initially before applying the load F_e, all the cylinder corner intercepts with SWL are located at $z = -3$ m i.e. half of the cylinder volume was submerged and $W_c = F_B = 6\rho g$. After applying the external force F_e, the new buoyancy force is

$$F_B = W_c + F_e = 1.25\, W_c = 1.25(2 \cdot 1 \cdot 3)\ \rho g = 7.5\ \rho g \tag{3.38}$$

The submerged length L_{cf} can be determined using Equation (3.8)

$$L_{cf} = F_B/\rho g\, A_c = 3.75\,\mathrm{m} \tag{3.39}$$

The body frame location is arbitrarily chosen at the center of the upper face. The static equilibrium pose can be determined by invoking the moment balance around the body frame origin, as shown in Figure 3.10.

$$\sum \mathbf{M}_o = {}^{p}\mathbf{r}_{CB} \times (\mathbf{R}^T\ {}^{I}\mathbf{F}_B) + {}^{p}\mathbf{r}_g \times (\mathbf{R}^T\ {}^{I}\mathbf{W}) + {}^{p}\mathbf{r}_F \times (\mathbf{R}^T\ {}^{I}\mathbf{F}_e) + {}^{p}\mathbf{M}_{wp} = \mathbf{0} \tag{3.40}$$

where ${}^{p}\mathbf{r}_g = [0,\ 0,\ -5.5]^T$, ${}^{p}\mathbf{r}_F = [1,\ 0.5,\ 0]^T$, ${}^{p}\mathbf{r}_{CB} = [0,\ 0,\ -4.125]^T$, ${}^{I}\mathbf{F}_B = [0,\ 0,\ 7.5\rho g]^T$, ${}^{I}\mathbf{W} = [0,\ 0,\ -6\rho g]^T$, and ${}^{I}\mathbf{F}_e = [0,\ 0,\ -1.5\rho g]^T$. Equation (3.40) yields a system of 3 nonlinear equations in 2 unknowns, ϕ and θ. One can solve any two equations simultaneously, for instance the equilibrium equations in pitch and yaw are

$$\begin{aligned} &14715\ c_\phi\ c_\theta - (214185/8)\, s_\theta - 817.5\ t_\phi^2\ s_\theta - 1635\ s_\theta\ t_\theta^2/c_\phi^2 = 0 \\ &4905\ t_\phi\ s_\theta - 14715\ \ c_\theta\, s_\phi - 7357.5\ s_\theta = 0 \end{aligned} \tag{3.41}$$

Equation (3.41) can be solved to find $\phi = -17.83^o$ and $\theta = 26.76^o$ and the corresponding cylinder's corners intercepts with the SWL are shown in Figure 3.10. The coordinates of the intercepts can be evaluated in the body frame using the water plane equation that was

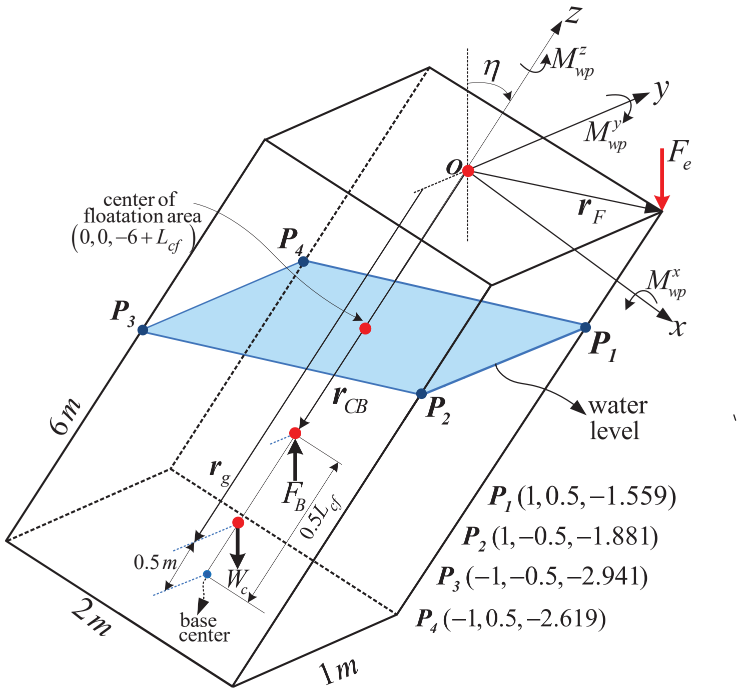

Figure 3.10: 3D equilibrium of a floating rectangular cylinder subject to a vertical load

previously discussed in Section 3.2. As expected, the corner where the load is applied is the closest to the water level at equilibrium, as seen in Figure 3.10. The angle between the cylinder centerline (z) and vertical direction (Z), $\eta = \cos^{-1}(\cos\theta\cos\phi)$ =31.79^o.

3.5 Hydrostatic Loads ($\mathbf{F}_{hs}$ and $\mathbf{M}_{hs}$) for the Equations of Motion

The hydrostatic force $\mathbf{F}_{hs}$ and moment $\mathbf{M}_{hs}$ terms in the equations of motion (Equations (2.19) and (2.50)) of both the dynamic models developed in Chapter 2 can be determined using the nonlinear hydrostatic approach already developed. Although this approach is derived for cylindrical floaters of uniform cross sections, it can be easily adapted for cylinders of multiple cross sections as the platform of the FOWT under consideration.

The floating platform structure is composed of a large lower cylinder of diameter d_1 and length a_1 and a smaller upper one with corresponding diameter and length d_2 and a_2, respectively. The two cylinders are connected through a conical frustum of length a_3. The small cylinder top face is the foundation of the tower base, as shown in Figure 2.8. The hydrostatic force and moment are mainly dependent on submerged shape of the structure and its cross section area piercing the water. The diameter of the platform cross section piercing the water (d_{wp}) is dependent on the submerged length (L_{cf}), as shown in Figure 2.8. The submerged length (L_{cf}) can be calculated using Equation (3.12) as

$$L_{cf} = (L_c - r_Z - a_{pf} + H_w + a_{pf}\, c_\phi\, c_\theta)\,/(c_\phi\, c_\theta) \tag{3.42}$$

where the platform draft $L_c = L_{cf}$ at $r_Z = 0$ and $\boldsymbol{\theta} = \mathbf{0}$. The draft is $L_c = 120$ m, as specified in the OC3-Hywind design data [6]. The distance between the $\boldsymbol{\mathcal{F}}_p$ origin and platform base center is denoted by a_{pf}. The wave height crossing the platform is H_w can be calculated using the analysis in Section 2.3.1. Since the platform is of slender shape and the the wave length is very large compared to the platform diameter, H_w can be assumed constant across the platform. The buoyancy (hydrostatic) force is the fluid weight of the submerged volume, written as

$${}^{I}\mathbf{F}_{hs} = (\rho\, V_d\, g)\,\hat{\mathbf{K}} \tag{3.43}$$

where the displaced volume (V_d) can be calculated based on the submerged shape geometry in Appendix C. The hydrostatic moment can be expressed as

$$\mathbf{M}_{hs} = \mathbf{r}_C \times \mathbf{F}_{hs} + \mathbf{M}_{wp} \tag{3.44}$$

where $\mathbf{r}_C = (a_{CV} - a_{pf})\,\hat{\mathbf{k}}$, a_{CV} is the distance between the platform base and the center the submerged volume of length L_{cf} assuming the platform is on an even keel (vertical), and $\mathbf{r}_C$ is the corresponding position vector of that center relative to the $\boldsymbol{\mathcal{F}}_p$ origin. The water plane area restoring moment ($\mathbf{M}_{wp}$) can be caculated from Equation (3.24) as

$${}^{p}\mathbf{M}_{wp} = -\rho g\, I_{wp}\Big[\; c_\theta s_\phi + \tfrac{1}{2} s_\phi c_\theta \left(\frac{t_\theta^2}{c_\phi^2} + t_\phi^2\right) \qquad s_\theta + \tfrac{1}{2} s_\theta \left(\frac{t_\theta^2}{c_\phi^2} + t_\phi^2\right) \qquad 0 \;\Big]^T \tag{3.45}$$

where the moment of inertia of the platform cross section piercing the water level is $I_{wp} = \pi d_{wp}^4/64$.

Chapter 4

QUASI-STATIC MOORING LOADS AND STIFFNESS

The main purpose of this chapter is to determine the mooring loads ($\mathbf{F}_{mor}$ and $\mathbf{M}_{mor}$) in the equations of motion developed earlier in Chapter 2. The mooring loads exerted on the platform will depend on the mooring system geometry, configuration, and cable properties. In this work, two mooring system configurations are studied. The mooring loads for each configuration are formulated utilizing quasi-static cable models.

The analysis is then extended to derive the exact stiffness matrix (6×6) of the mooring system for a structure undergoing a general displacement. Closed forms of the stiffness matrix are evaluated for symmetric slack catenary, taut-leg and tension leg mooring systems at equilibrium. Finally, the influence of the key mooring system design parameters such as anchor radius, number of tethers and mooring system configuration, on the mooring system stiffness is investigated for a taut-leg mooring system. It is worth noting that our analysis assumes that cables are only subject to gravity loads (weight) and no external steady loads (such as current) are considered.

4.1 Mooring System Loads

The mooring force ($\mathbf{F}_{mor}$) and moment around the origin of the platform frame ($\mathbf{M}_{mor}$) are evaluated for two different mooring system configurations (designs) for the OC3-Hywind FOWT under consideration. The original mooring system design was developed by Statoil and used to build a FOWT prototype deployed close to the south-west coast of Norway in 2011. The design involves multiple cable segments and suspended clump weights, as will be illustrated in Section 4.1.2. However, the original data of this design has not been published. A simplified design, in which each mooring line is composed of a single cable augmented by additional yaw stiffness coefficient (K_{add}) has been released to the public by the NREL [6].

Later on, the original multi-segments (bridle) design data was published [7]. Based on the geometry and cable properties data of the both deigns, it is noticed that the mooring system total mass (of the cables and clump weights (if any)), cable extensional stiffness (EA), and the anchor radius are identical for both designs. However, the cable mass per unit length of the simplified design is larger.

Most the published dynamic studies of this FOWT system considered the simplified mooring design. Therefore, the mooring load of both designs (configurations) will be formulated to perform the dynamic simulations. The dynamic simulations that use the simplified mooring system design will be used to validate the dynamic models developed herein. On the other hand, the dynamic simulation of the FOWT system using the more complex original mooring system design will be performed to investigate the dynamic behavior of the real system.

4.1.1 Single-segment configuration

In the simplified configuration, the catenary mooring system is comprised of 3 lines resting on the seabed when the system at equilibrium. The anchors are uniformly distributed in a circle with radius R_c and $2\pi/3$ radians apart. The upper attachment point (fairlead) radius is R_f and the attachment points circumferential distribution is similar to their corresponding anchors, as shown in Figure 4.1 (a). The tethers are identical in length and material properties.

The mooring loads are determined using the equation of an elastic catenary. The tension determined using this approach is referred to as the quasi-static tension [14]. In this approach, the cable-seabed interaction forces such as friction and damping are ignored. The absolute position of the upper attachment point (fairlead) of the i-th mooring line during a general displacement of the platform can be expressed in the inertial frame as

$$ {}^{I}\mathbf{r}_m = [X_p \; Y_p \; Z_p]^T = {}^{I}\mathbf{r} + \mathbf{R}\,{}^{p}\mathbf{r}_{POp} \tag{4.1} $$

where ${}^{p}\mathbf{r}_{POp} = [x_{po} \;\; y_{po} \;\; z_{po}]^T$ is the position of the i-th fairlead relative to the origin of $\boldsymbol{\mathcal{F}}_p$ which is a fixed dimension in the platform frame, as shown in Figure 4.1 (b). The inertial coordinate system $\bar{X}\,\bar{Y}\,\bar{Z}$ is defined for a mooring line and parallel to the inertial frame XYZ,

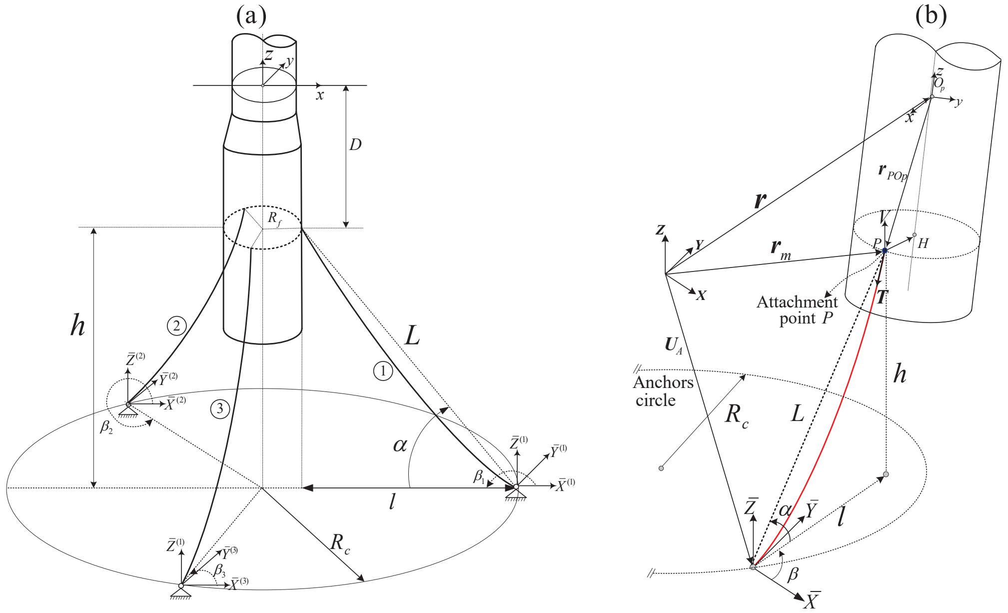

Figure 4.1: Single-segment Mooring system configuration and geometry

with origin at the corresponding anchor point. The position of the i-th anchor point in the inertial frame is ${}^{I}\mathbf{U}_A = [X_A \;\; Y_A \;\; Z_A]^T$. The i-th cable horizontal and vertical projections (l and h, respectively) are scalar quantities, can be expressed as

$$l = \sqrt{\left(X_p - X_A\right)^2 + \left(Y_p - Y_A\right)^2} \quad , \quad h = \left(Z_p - Z_A\right) \tag{4.2}$$

The angle β is the angle between the X-axis and l, calculated as

$$\beta = \text{atan2}\left(Y_p - Y_A \, , \, X_p - X_A\right) \tag{4.3}$$

where atan2 is the four-quadrant inverse tangent function. The tension exerted by a mooring line on the platform, as illustrated in Figure 4.1 (b), is

$$ {}^{I}\mathbf{T} = [T_X \quad T_Y \quad T_Z]^T = -[H\cos\beta \quad H\sin\beta \quad V]^T \tag{4.4}$$

The total mooring force is the sum of the mooring forces exerted by all mooring lines, can be written as

$$ {}^{p}\mathbf{F}_{mor} = \sum_{i=1}^{3} {}^{p}\mathbf{T}^{(i)} \tag{4.5}$$

The total moment exerted by the tensions of the mooring lines on the platform about the origin of the body frame,

$$
{}^{p}\mathbf{M}_{mor} = \sum_{i=1}^{3} {}^{p}\mathbf{r}_{POp}^{(i)} \times {}^{p}\mathbf{T}^{(i)} \tag{4.6}
$$

where the superscript (i) in Equations (4.5) and (4.6) denotes the respective quantities of the i-th mooring line.

Calculating the cable tension components (H and V) depends on the cable profile shape whether suspended or partially resting on the seabed. When part of the mooring line rests on the seabed, the corresponding anchor point experiences only horizontal tension, as shown in Figure 4.2 (a). The cable horizontal and vertical tension components (H and V) acting at the top attachment point, in the plane of the cable profile, can be determined using a catenary equation. This equation can be solved numerically for given unstretched cable length (L_o), cable equivalent weight (in fluid) per unit length (w), extensional stiffness (EA) and cable horizontal and vertical projections (l and h), as [17]

$$
\begin{aligned}
l &= L_o - \frac{V}{w} + \frac{L_o H}{EA} + \frac{H}{w}\sinh^{-1}\left(\frac{V}{H}\right) \\
h &= \frac{1}{w}\left(\sqrt{H^2+V^2} - H + \frac{V^2}{2EA}\right)
\end{aligned} \tag{4.7}
$$

When the line is suspended, as shown in Figure 4.2 (b), V computed from Equation (4.7) exceeds the line weight ($V > wL_o$), the line profile is then no longer tangent to the seabed and thus the result is no longer valid. Therefore, the line tension should instead be computed using the conventional form of the suspended catenary equation [32]

$$
\begin{aligned}
l &= (HL_0/EA) + (HL_0/W)\left[\sinh^{-1}(V/H) - \sinh^{-1}((V-W)/H)\right] \\
h &= (WL_0/EA)\left[(V/W) - 0.5\right] + (HL_0/W)\left[\sqrt{1+(V/H)^2} - \sqrt{1+((V-W)/H)^2}\right]
\end{aligned} \tag{4.8}
$$

where $W = wL_o$ is the line weight. During the dynamic simulation, the nonlinear algebraic equation of the catenary (Equation (4.7) or (4.8)), according to the line profile shape is solved to compute H and V using a Newton–Raphson technique at each time step.

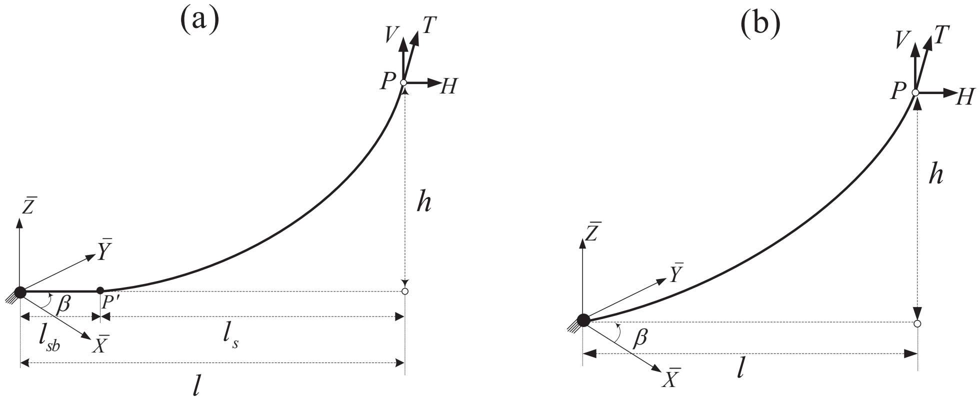

Figure 4.2: (a) Slack mooring line resting on the seabed; and (b) suspended line

4.1.2 Multi-segment (bridle) configuration

This catenary mooring system is comprised of 3 identical mooring lines that each includes a bridle component, as shown in Figure 4.3. Segments 1 and 2 form the bridle and are attached to the platform circumference (radius R_f), at nodes 1 and 2. The upper end of Segment 3 is connected to the bridle at node 3, and the other end is anchored to the seabed. The clump weight (W_{CL}) is a heavy cylindrical mass suspended on segment 3 at unstretched length s_1 measured from the bridle connection (node 3). The anchors are uniformly distributed in a circle with radius R_c and $2\pi/3$ rad apart. The segments are identical in material properties and diameter. The unstretched length of each bridle line and segment 3 are $L_{0\Delta}$ and L_{03}, respectively. The mooring system properties of the two configurations are listed in Appendix A.4. The fixed position of the anchor point (A) relative to the origin of the inertial frame is $\mathbf{U}_A$. The corresponding positions of nodes 1 and 2 can be expressed as

$$^{I}\mathbf{r}_1 = {}^{I}\mathbf{r} + \mathbf{R}\ {}^{p}\mathbf{U}_1\ \ ,\quad {}^{I}\mathbf{r}_2 = {}^{I}\mathbf{r} + \mathbf{R}\ {}^{p}\mathbf{U}_2 \tag{4.9}$$

where ${}^{p}\mathbf{U}_1$ and ${}^{p}\mathbf{U}_2$ are the fixed position of nodes 1 and 2 relative to origin of the platform frame, respectively.

The tensions of the cables comprising the mooring system can be determined using a catenary equation of a suspended cable with point vertical load (P_c) acting at unstretched

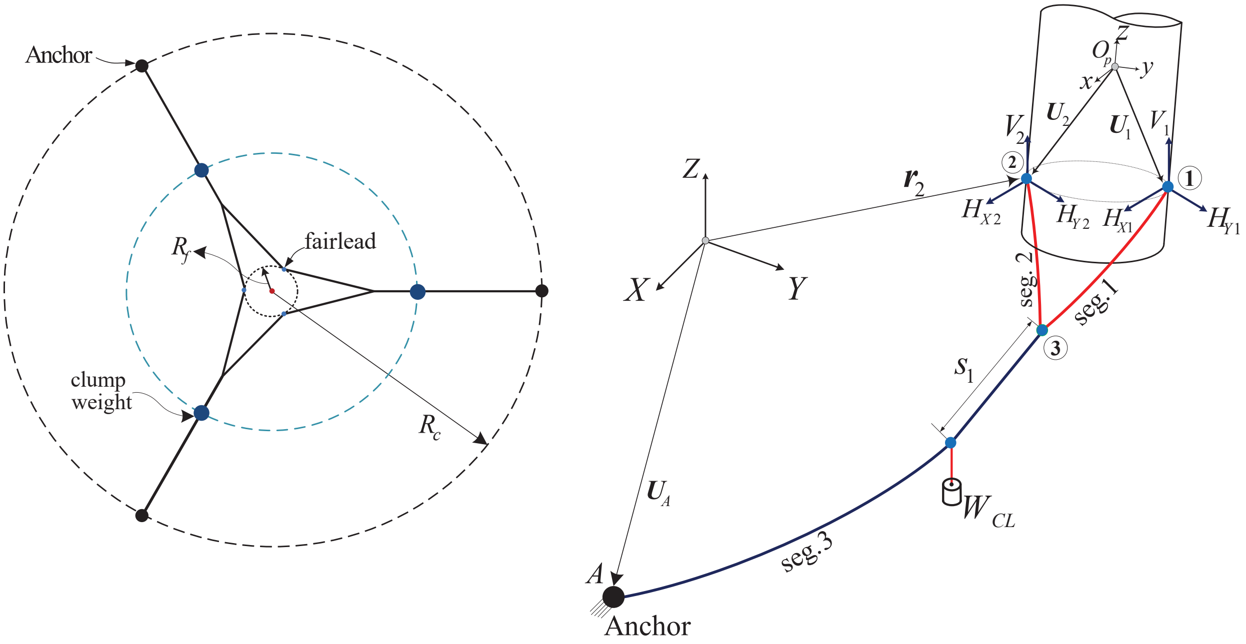

Figure 4.3: Mooring system configuration and geometry

length s_1 measured from the upper end (Figure 4.4), presented by Irvine [32]

$$
\begin{aligned}
l_c =& \frac{H L_0}{EA} + \frac{H}{w}\left[\begin{array}{c} \sinh^{-1}\left(\frac{V}{H}\right) - \sinh^{-1}\left(\frac{V-P_c-wL_0}{H}\right) \\ +\sinh^{-1}\left(\frac{V-P_c-ws_1}{H}\right) - \sinh^{-1}\left(\frac{V-ws_1}{H}\right) \end{array}\right] \\
h_c =& \frac{1}{EA}\left(V L_0 - \frac{w {L_0}^2}{2}\right) + \frac{H}{w}\left[\begin{array}{c} \sqrt{1+\left(\frac{V}{H}\right)^2} - \sqrt{1+\left(\frac{V-P_c-wL_0}{H}\right)^2} + \sqrt{1+\left(\frac{V-P_c-ws_1}{H}\right)^2} \\ -\sqrt{1+\left(\frac{V-w\,s_1}{H}\right)^2} + \frac{P_c\,w}{H\,EA}\left(s_1 - L_0\right) \end{array}\right]
\end{aligned}
\tag{4.10}
$$

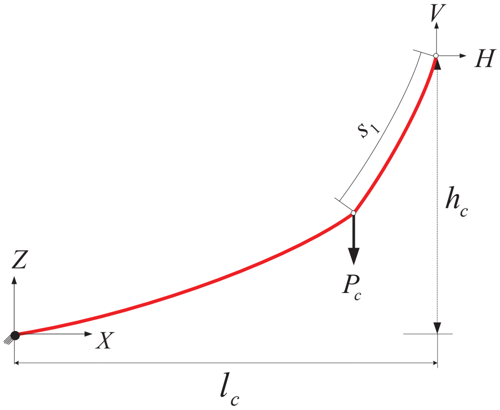

Figure 4.4: Suspended catenary cable with a point load

As discussed earlier, one or more lines could partially rest on the seabed due to platform displacement. Once the cable rests on the seabed i.e. if $V \leq P_c + wL_0$, the form of Equation (4.10) is no longer valid for computing the cable tension. Therefore, this form should be altered to account for the decrease in the weight of the suspended portion of the cable.

Consider the cable shown in Figure 4.5, the unstretched length of its suspended portion ($P'P$) is L_{s0} and that of the portion resting on the seabed is L_{sb0}. The unstretched length of the whole cable profile is $L_0 = L_{sb0} + L_{s0}$. The cable profile horizontal projection can be expressed as

$$l_c = l_e + l_s \tag{4.11}$$

where l_e is the stretched length of the resting portion, can be simply expressed as

$$l_e = L_{sb0}\left(1 + \frac{H}{EA}\right) \tag{4.12}$$

Since the point P' is tangent to the seabed, the cable static equilibrium yields

$$L_{sb0} = L_0 - \frac{V - P_c}{w} \tag{4.13}$$

One can now apply the catenary equation (Equation (4.10)) for the suspended portion ($P'P$) by substituting $L_0 = L_{s0}$, and $l_c = l_s$ and substitute the resulting from together with Equations (4.12) and (4.13) back into Equation (4.11), which can be finally expressed as

$$\begin{aligned} l_c =& L_0 + \frac{HL_0}{EA} - \frac{(V - P_c)}{w} + \frac{H}{w}\left[\begin{array}{l} \sinh^{-1}\left(\frac{V}{H}\right) + \sinh^{-1}\left(\frac{V - P_c - ws_1}{H}\right) \\ -\sinh^{-1}\left(\frac{V - ws_1}{H}\right) \end{array}\right] \\ h_c =& \frac{V^2 - {P_c}^2}{2EAw} + \frac{H}{w}\left[\begin{array}{l} -1 \;+\; \sqrt{1 + \left(\frac{V}{H}\right)^2} + \sqrt{1 + \left(\frac{V - P_c - ws_1}{H}\right)^2} \\ -\sqrt{1 + \left(\frac{V - w\,s_1}{H}\right)^2} + \frac{P_c}{H\,EA}\left(ws_1 - V + P_c\right) \end{array}\right] \end{aligned} \tag{4.14}$$

This new form represents the catenary equation for a cable partially resting on the seabed with a point vertical load (Figure 4.5).

The two-dimensional form of a suspended catenary (Equation (4.10)) can be slightly modified to the three-dimensional domain (Figure 4.6) to analyze the 3D static equilibrium

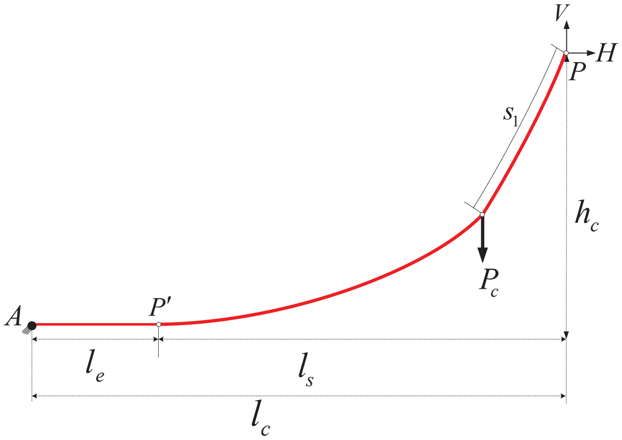

Figure 4.5: Cable partially resting on seabed with a point load

of the mooring, as

$$\begin{aligned}
l_X =& \frac{H_X L_0}{EA} + \frac{H_X}{w}\left[\begin{array}{l}\sinh^{-1}\left(\frac{V}{H}\right) - \sinh^{-1}\left(\frac{V-P_c-wL_0}{H}\right)\\ +\sinh^{-1}\left(\frac{V-P_c-ws_1}{H}\right) - \sinh^{-1}\left(\frac{V-ws_1}{H}\right)\end{array}\right]\\
l_Y =& \frac{H_Y L_0}{EA} + \frac{H_Y}{w}\left[\begin{array}{l}\sinh^{-1}\left(\frac{V}{H}\right) - \sinh^{-1}\left(\frac{V-P_c-wL_0}{H}\right)\\ +\sinh^{-1}\left(\frac{V-P_c-ws_1}{H}\right) - \sinh^{-1}\left(\frac{V-ws_1}{H}\right)\end{array}\right]\\
l_Z =& \frac{1}{EA}\left(VL_0 - \frac{w{L_0}^2}{2}\right) + \frac{H}{w}\left[\begin{array}{l}\sqrt{1+\left(\frac{V}{H}\right)^2} - \sqrt{1+\left(\frac{V-P_c-wL_0}{H}\right)^2} + \sqrt{1+\left(\frac{V-P_c-ws_1}{H}\right)^2}\\ -\sqrt{1+\left(\frac{V-w\,s_1}{H}\right)^2} + \frac{P_c\,w}{H\,EA}\left(s_1 - L_0\right)\end{array}\right]
\end{aligned} \tag{4.15}$$

Similarly, the catenary equation of a cable partially resting on the seabed (Equation (4.14)) can be extended to 3D as

$$\begin{aligned}
l_X =& L_0\frac{H_X}{H} + \frac{H_X L_0}{EA} - \frac{(V-P_c)\,H_X}{wH}\\
&+ \frac{H_X}{w}\left[\sinh^{-1}\left(\frac{V}{H}\right) + \sinh^{-1}\left(\frac{V-P_c-ws_1}{H}\right) - \sinh^{-1}\left(\frac{V-ws_1}{H}\right)\right]\\
l_Y =& L_0\frac{H_Y}{H} + \frac{HL_0}{EA} - \frac{(V-P_c)\,H_Y}{wH}\\
&+ \frac{H_Y}{w}\left[\sinh^{-1}\left(\frac{V}{H}\right) + \sinh^{-1}\left(\frac{V-P_c-ws_1}{H}\right) - \sinh^{-1}\left(\frac{V-ws_1}{H}\right)\right]\\
l_Z =& \frac{V^2 - {P_c}^2}{2EAw} + \frac{H}{w}\left[\begin{array}{l}-1 \;+\; \sqrt{1+\left(\frac{V}{H}\right)^2} + \sqrt{1+\left(\frac{V-P_c-ws_1}{H}\right)^2}\\ -\sqrt{1+\left(\frac{V-w\,s_1}{H}\right)^2} + \frac{P_c}{H\,EA}\left(ws_1 - V + P_c\right)\end{array}\right]
\end{aligned} \tag{4.16}$$

where $H = \sqrt{{H_X}^2 + {H_Y}^2}$, and (l_X, l_Y, l_Z) are the coordinates (in the inertial frame) of the cable upper end (P) relative to the lower end (anchor point).

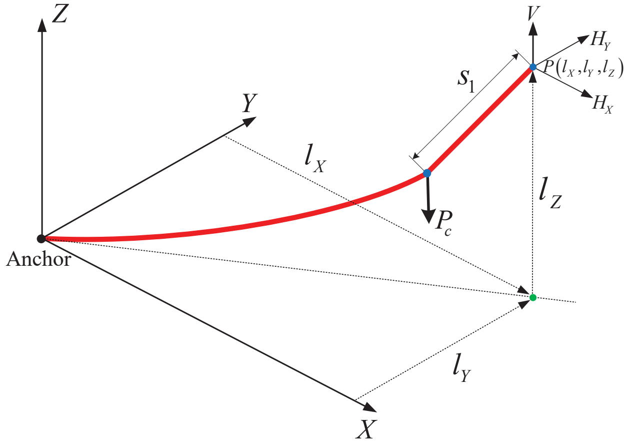

Figure 4.6: Catenary cable in 3D.

The obtained Equations (4.15) and (4.16) now can be used to analyze the general 3D static problem of the bridle mooring arrangement (Figure 4.3) in which segment 3 can be either suspended or partially resting on the seabed. The tension components at nodes 1, 2 and 3 can be determined by solving the 3D static equilibrium of the bridle which implies that the sum of the tension forces at node 3 is zero. It is assumed that the absolute coordinates of the nodes 1 and 2 (${}^I\mathbf{r}_1$ and ${}^I\mathbf{r}_2$) are known from the system kinematics. The procedure for computing the mooring loads of the bridle mooring line is illustrated as follows:

1. Since the coordinates of A and nodes 1 and 2 are known, the following kinematics constraints will hold

$$\begin{aligned} \begin{bmatrix} l_{X_1}+l_{X_3} & l_{Y_1}+l_{Y_3} & l_{Z_1}+l_{Z_3} \end{bmatrix}^T &= {}^I\mathbf{r}_1 - {}^I\mathbf{U}_A \\ \begin{bmatrix} l_{X_2}+l_{X_3} & l_{Y_2}+l_{Y_3} & l_{Z_2}+l_{Z_3} \end{bmatrix}^T &= {}^I\mathbf{r}_2 - {}^I\mathbf{U}_A \end{aligned} \tag{4.17}$$

   which represents a system of 6 algebraic equations in 12 unknowns (l_{X_j}, l_{Y_j}, and l_{Z_j}) for j=1, 2 and 3, where l_{X_j}, l_{Y_j}, l_{Z_j}, are the projections of the j-th segment on the X, Y, and Z axes , respectively.

2. Write the catenary equation of a suspended line (Equation (4.15)) for segments 1 and 2, substituting $P_c = 0$, $L_0 = L_{0\Delta}$, $l_X = l_{X_j}$, $l_Y = l_{Y_j}$, $l_Z = l_{Z_j}$, $H_X = H_{X_j}$, $H_Y = H_{Y_j}$, and $V = V_j$ for $j = 1$ and 2, and substitute the resulting equations into Equation (4.17).

3. Write the catenary equation of a suspended line (Equation (4.15)) for segment 3, substituting $P_c = W_{CL}$, $L_0 = L_{03}$, $l_X = l_{X_3}$, $l_Y = l_{Y_3}$, $l_Z = l_{Z_3}$, $H_X = H_{X_3}$, $H_Y = H_{Y_3}$, and $V = V_3$ and substitute the resulting equations into Equation (4.17). Now Equation (4.17) represents a system of 6 equations in 9 unknowns (H_{X_j}, H_{Y_j}, and V_j, for j=1, 2, and 3).

4. Solving for the equilibrium of node 3 yields

$$H_{X_3} = H_{X_1} + H_{X_2} \quad , \quad H_{Y_3} = H_{Y_1} + H_{Y_2} \quad , \quad V_3 = V_1 + V_2 - 2\,w\,L_{0\Delta} \tag{4.18}$$

   substituting these relations into the updated form of Equation (4.17) (step 3) makes the number of unknowns equal to its number of equations (6) which can be then solved numerically using a Newton-Raphson method to determine the tension components of nodes 1 and 2 (H_{X_j}, H_{Y_j}, and V_j, for j=1 and 2) .

5. Substitute the solution into Equation (4.18) to determine V_3 and check if $V_3 > W_{CL} + wL_{03}$. This condition ensures that segment 3 is suspended as presumed in Step 3. However, if this condition is violated i.e. if $V_3 < W_{CL} + wL_{03}$, this implies that segment 3 is resting on the seabed and thus the obtained solution is not valid. Therefore, Equation (4.15) should be replaced by Equation (4.16) in Step 3. The system of equations should be re-solved to determine the nodes tensions.

The previous steps are repeated for each mooring line to calculate their tensions. The tension exerted by the i-th mooring line on the platform can be expressed in the platform frame, as

$${}^{p}\mathbf{F}^{(i)}_{mor} = -\mathbf{R}^T \left([\; H^{(i)}_{X_1} \quad H^{(i)}_{Y_1} \quad V^{(i)}_1 \;]^T + [\; H^{(i)}_{X_2} \quad H^{(i)}_{Y_2} \quad V^{(i)}_2 \;]^T \right) \tag{4.19}$$

The moment exerted by i-th mooring line on the platform about the origin of the body frame, can be expressed in the platform frame as

$${}^{p}\mathbf{M}^{(i)}_{mor} = {}^{p}\mathbf{U}^{(i)}_1 \times \left(-\mathbf{R}^T [\; H^{(i)}_{X_1} \quad H^{(i)}_{Y_1} \quad V^{(i)}_1 \;]^T \right) + {}^{p}\mathbf{U}^{(i)}_2 \times \left(-\mathbf{R}^T [\; H^{(i)}_{X_2} \quad H^{(i)}_{Y_2} \quad V^{(i)}_2 \;]^T \right) \tag{4.20}$$

The total mooring force can computed as

$${}^{p}\mathbf{F}_{mor} = \sum_{i=1}^{i=3} {}^{p}\mathbf{F}^{(i)}_{mor} \tag{4.21}$$

In the same manner, the total moment is

$$ {}^{p}\mathbf{M}_{mor} = \sum_{i=1}^{3} {}^{p}\mathbf{M}_{mor}^{(i)} \tag{4.22} $$

4.2 Stiffness Analysis

Despite the analytical efforts to derive the mooring stiffness matrix for several types of floating structures undertaken in these studies [33–40], each is restricted to either slack or taut cables and may yield a considerable error for large displacements of the platform. Therefore, the mooring stiffness matrix is usually determined numerically using finite difference techniques. There is no exact analytical approach to derive the stiffness matrix at an arbitrary position and orientation of the floating structure. Here, we present a new comprehensive analysis to obtain the exact 6 × 6 stiffness matrix for slack and taut mooring system will be presented next.

4.2.1 Two-dimensional stiffness matrix of a single mooring line

We start our analysis by considering the stiffness characteristics of a single mooring line, which will later be used as a component in the stiffness of a mooring system. Consider a single mooring line suspended at P, already shown in Figure 4.2 (b). The stiffness matrix of the cable in the plane of the cable profile is expressed as [111, 112]

$$ \mathbf{K}^{p} = \begin{bmatrix} K_{11}^{p} & K_{12}^{p} \\ K_{21}^{p} & K_{22}^{p} \end{bmatrix} = \begin{bmatrix} \frac{\partial H}{\partial l} & \frac{\partial H}{\partial h} \\ \frac{\partial V}{\partial l} & \frac{\partial V}{\partial h} \end{bmatrix} \tag{4.23} $$

The procedure for calculating H, V and $\mathbf{K}^{p}$ varies according to the mooring line tension and profile shape. Three distinct cases can be considered: (a) suspended line, as shown in Figure 4.2 (b); (b) a slack line partially resting on the seabed, as shown in Figure 4.2 (a); and (c) taut line, as shown in Figure 4.7. It is worth noting that case (c) is a special case of case (a). The analysis assumes the line material and cross section are uniform and the line structural elongation is governed by Hooke's law. We now consider methods to determine $\mathbf{K}^{p}$ for each of these three cases in succession.

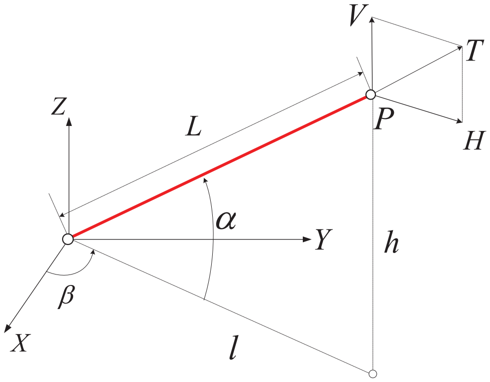

Figure 4.7: Taut line (case (c))

4.2.1.1 Suspended line (case a)

The line attains a non-zero angle with the seabed when the tension is sufficient to lift it up i.e. $V > W$. The catenary equation governs this case was previously presented in Equation (4.8). It is clear from Equation (4.8) that l and h are both functions of the horizontal and vertical tension components H and V, i.e. $l = l(H, V)$, and $h = h(H, V)$. Their differential changes can be expressed in matrix form as [112]

$$\begin{Bmatrix} dl \\ dh \end{Bmatrix} = \begin{bmatrix} \frac{\partial l}{\partial H} & \frac{\partial l}{\partial V} \\ \frac{\partial h}{\partial H} & \frac{\partial h}{\partial V} \end{bmatrix} \begin{Bmatrix} dH \\ dV \end{Bmatrix} = [\mathbf{F}_{lex}] \begin{Bmatrix} dH \\ dV \end{Bmatrix} \tag{4.24}$$

where $\mathbf{F}_{lex}$ is the flexibility matrix that represents the partial derivatives of the cable profile projections l and h with respect to horizontal and vertical tensions, H and V, respectively. It was demonstrated by [111] that $\mathbf{F}_{lex}$ is symmetric such that $\frac{\partial l}{\partial V} = \frac{\partial h}{\partial H}$. The elements of $\mathbf{F}_{lex}$ can be expressed as [19, 111]

$$\begin{aligned} \frac{\partial l}{\partial H} =& \frac{L_0}{EA} + \frac{L_0}{W}\left[\sinh^{-1}\left(\frac{V}{H}\right) - \sinh^{-1}\left(\frac{V-W}{H}\right)\right] \\ &+ \frac{L_0}{W}\left[-\frac{V}{\sqrt{H^2+V^2}} + \frac{V-W}{\sqrt{H^2+(V-W)^2}}\right] \\ \frac{\partial l}{\partial V} =& \frac{\partial h}{\partial H} = \frac{L_0}{W}\left[\frac{H}{\sqrt{H^2+V^2}} - \frac{H}{\sqrt{H^2+(V-W)^2}}\right] \\ \frac{\partial h}{\partial V} =& \frac{L_0}{EA} + \frac{L_0}{W}\left[\frac{V}{\sqrt{H^2+V^2}} - \frac{V-W}{\sqrt{H^2+(V-W)^2}}\right] \end{aligned} \tag{4.25}$$

Differential changes in H and V can be expressed as $[dH \quad dV]^T = [\mathbf{K}^p]\ [dl \quad dh]^T$. Thus, $\mathbf{K}^p$ can be expressed as [112]

$$\mathbf{K}^p = \mathbf{F}_{lex}^{-1} \tag{4.26}$$

$\mathbf{K}^p$ is also symmetric because $\mathbf{F}_{lex}$ is symmetric.

4.2.1.2 Line resting on seabed (case b)

A zero angle with seabed (assuming flat seabed) occurs in slack mooring systems i.e. when $V < W$. The catenary equation governs the cable statics is already expressed in Equation (4.7). Accordingly, the elements of the flexibility matrix ($\mathbf{F}_{lex}$) can be determined by differentiating Equation (4.7) as

$$\begin{aligned} \frac{\partial l}{\partial H} &= \frac{L_0}{EA} + \frac{1}{w}\left[\frac{-V}{\sqrt{H^2+V^2}} + \sinh^{-1}\left(\frac{V}{H}\right)\right] \\ \frac{\partial l}{\partial V} &= \frac{\partial h}{\partial H} = \frac{1}{w}\left[\frac{H}{\sqrt{H^2+V^2}} - 1\right] \quad , \quad \frac{\partial h}{\partial V} = \frac{V}{w}\left[\frac{1}{\sqrt{H^2+V^2}} + \frac{1}{EA}\right] \end{aligned} \tag{4.27}$$

Similarly, $\mathbf{K}^p$ can be determined using Equation (4.26). It is worth noting that in the case of an inextensible cable, such as slack heavy chains, one can substitute $EA = \infty$ in Equations (4.7) and (4.27) and accordingly all the corresponding terms can be dropped.

4.2.1.3 Taut line (case c)

Although the catenary equation yields an exact solution for the cable statics problems, it must be solved numerically which requires some computational effort. When the line is taut and no sag exists i.e. $H/V \approx l/h$, it can be modeled accurately as a massless linear spring to simplify the computations. The stiffness of the tether along its chord (L) can be assumed equal to $K_I = EA/L_o$, as shown in Figure 4.7. The results of the exact analysis in Section 4.2.1.1 were verified to approach those of the massless linear spring assumption as the platform excess buoyancy force is increased; or as the mooring line weight is reduced. The massless spring assumption dramatically simplifies the analysis and obviates the need to use the catenary equation. This simplified analytical approach can provide an accurate approximation of the stiffness for taut mooring system such as on TLPs.

Consider the cable shown in Figure 4.7 of unstretched length L_o, stretched length (chord length), $L = \sqrt{l^2 + h^2}$. Its configuration is defined by angles β and α. When the cable is stretched by ΔL, the associated variation of tension is $\Delta T = K_I \Delta L$. The cable tension is $T = K_I (L - L_o)$. The expressions for H, V, l, and h can be then written as

$$H = T\cos\alpha \quad , \quad V = T\sin\alpha \quad , \quad l = L\,\cos\alpha \quad , \quad h = L\,\sin\alpha \tag{4.28}$$

In contrast to the previous two cases, the elements of $\mathbf{K}^p$ can be directly derived as

$$\begin{aligned}
\frac{\partial H}{\partial l} &= \frac{\partial (T\cos\alpha)}{\partial l} = \cos\alpha\,\frac{\partial T}{\partial L}\frac{\partial L}{\partial l} + T\left(-\sin\alpha\frac{\partial \alpha}{\partial l}\right)\\
\frac{\partial H}{\partial h} &= \frac{\partial (T\cos\alpha)}{\partial h} = \cos\alpha\,\frac{\partial T}{\partial L}\frac{\partial L}{\partial h} + T\left(-\sin\alpha\frac{\partial \alpha}{\partial h}\right)\\
\frac{\partial V}{\partial l} &= \frac{\partial (T\sin\alpha)}{\partial l} = \sin\alpha\,\frac{\partial T}{\partial L}\frac{\partial L}{\partial l} + T\cos\alpha\frac{\partial \alpha}{\partial l}\\
\frac{\partial V}{\partial h} &= \frac{\partial (T\sin\alpha)}{\partial h} = \sin\alpha\,\frac{\partial T}{\partial L}\frac{\partial L}{\partial h} + T\cos\alpha\frac{\partial \alpha}{\partial h}
\end{aligned} \tag{4.29}$$

It is obvious that, when the cable is taut, $T = f(L)$ such that $\partial T/\partial L = dT/dL = K_I$. From kinematics we can evaluate the partial derivatives of L, with respect to l, and h as

$$\frac{\partial L}{\partial l} = \cos\alpha \quad , \quad \frac{\partial L}{\partial h} = \sin\alpha \quad , \quad \frac{\partial \alpha}{\partial l} = \frac{-\sin\alpha}{L} \quad , \quad \frac{\partial \alpha}{\partial h} = \frac{\cos\alpha}{L} \tag{4.30}$$

Substituting Equation (4.30) into Equation (4.29), we obtain the final form of the elements of the cable plane stiffness matrix $\mathbf{K}^p$

$$\frac{\partial H}{\partial l} = \cos^2\alpha\,K_I + \frac{T}{L}\sin^2\alpha\ ,\ \frac{\partial V}{\partial h} = \sin^2\alpha\,K_I + \frac{T}{L}\cos^2\alpha\ ,\ \frac{\partial H}{\partial h} = \frac{\partial V}{\partial l} = \cos\alpha\sin\alpha\left(K_I - \frac{T}{L}\right) \tag{4.31}$$

4.2.2 Derivation of the 6×6 stiffness matrix of the mooring line

The previous analysis (Section 4.2.1) can only be used to determine the 2D mooring line stiffness matrix in the cable profile plane. However, when a mooring line is attached to a floating platform undergoing general displacement, the platform kinematics should be considered to derive the 6 × 6 stiffness matrix of the mooring line.

The derivation of the mooring stiffness matrix which will be detailed in the next section requires evaluation of the differential changes of l, h (in Equation (4.2)), and β due to changes in the translational and rotational displacements of the platform. These can be represented for l as

$$\begin{aligned} \frac{\partial l}{\partial r_X} = \cos\beta, \quad \frac{\partial l}{\partial r_Y} = \sin\beta, \qquad \frac{\partial l}{\partial r_Z} = 0, \\ \frac{\partial l}{\partial \zeta} = \cos\beta \frac{\partial X_p}{\partial \zeta} + \sin\beta \frac{\partial Y_p}{\partial \zeta} \quad , \quad \zeta = \phi, \theta, \psi \end{aligned} \tag{4.32}$$

and for β as

$$\begin{aligned} \frac{\partial \beta}{\partial r_X} = \frac{-\sin\beta}{l}, \qquad \frac{\partial \beta}{\partial r_Y} = \frac{\cos\beta}{l}, \qquad \frac{\partial \beta}{\partial r_Z} = 0, \\ \frac{\partial \beta}{\partial \zeta} = \frac{1}{l}\left[\cos\beta \frac{\partial Y_p}{\partial \zeta} - \sin\beta \frac{\partial X_p}{\partial \zeta}\right] \end{aligned} \tag{4.33}$$

In the above equations we must evaluate the change of position of the upper attachment point, with respect to changes of orientation of the platform, formulated as

$$\frac{\partial \mathbf{r}_m}{\partial \zeta} = \frac{\partial \mathbf{R}}{\partial \zeta} \mathbf{r}_{po} \tag{4.34}$$

The closed form expressions of Equation (4.34) can be found in Appendix D (Equation (D.7)). Since ${}^{I}\mathbf{U}_A$ is constant, the differential change in the attachment point vertical displacement Z_p is equal to that of h such that $\partial Z_p = \partial h$

$$\frac{\partial h}{\partial r_X} = \frac{\partial Z_p}{\partial r_X} = 0, \quad \frac{\partial h}{\partial r_Y} = \frac{\partial Z_p}{\partial r_Y} = 0, \quad \frac{\partial h}{\partial r_Z} = \frac{\partial Z_p}{\partial r_Z} = 1 \quad , \quad \frac{\partial h}{\partial \zeta} = \frac{\partial Z_p}{\partial \zeta} \tag{4.35}$$

4.2.3 Mooring stiffness formulation of a single line

As mentioned earlier, the stiffness matrix of a mooring line represents the change of the mooring line forces and moment exerted on the platform with respect to the platform displacements. The moment exerted by the line tension force on the platform about the origin of the body frame, as illustrated in Figure 4.1 (b), expressed in the inertial frame as

$$
{}^{I}\mathbf{M}_{mor} = \left\{ \begin{array}{c} M_X \\ M_Y \\ M_Z \end{array} \right\} = \left\{ \begin{array}{c} X_p - r_X \\ Y_p - r_Y \\ Z_p - r_Z \end{array} \right\} \times \left\{ \begin{array}{c} T_X \\ T_Y \\ T_Z \end{array} \right\} = \left\{ \begin{array}{c} (Y_p - r_Y)\, T_Z - (Z_p - r_Z)\, T_Y \\ (Z_p - r_Z)\, T_X - (X_p - r_X)\, T_Z \\ (X_p - r_X)\, T_Y - (Y_p - r_Y)\, T_X \end{array} \right\} \tag{4.36}
$$

We can define the generalized displacement (translation and orientation) of the platform by $\mathbf{X}$ (as in Equation (3.33)), and the corresponding generalized force (tension/moment) for a mooring line by $\mathbf{F}_m$ as

$$
\mathbf{F}_m = \left[\begin{array}{cccccc} T_X & T_Y & T_Z & M_X & M_Y & M_Z \end{array} \right]^T \tag{4.37}
$$

The mooring stiffness matrix for a mooring line can be derived as

$$
\mathbf{K}_m = -\partial \mathbf{F}_m / \partial \mathbf{X} = [K_{ij}] = -[\partial (F_m)_i / \partial X_j] \tag{4.38}
$$

Where i and j are indices of the components of $\mathbf{F}_m$ and $\mathbf{X}$, respectively. The general exact 6×6 stiffness matrix for a single mooring line at an arbitrary position and orientation of the platform derived using Equation (4.38) is detailed in Appendix D. The mooring stiffness coefficients can be evaluated by choosing the elements of $\mathbf{K}^p$ according to the cable profile case considered (Section 4.2.1). As well, the partial derivatives of $l, h, , X_p, Y_p$, and Z_p with respect to the platform displacements can be determined using Equations (4.32) to (4.35). It is well known that the mooring stiffness matrix is not symmetric i.e. $K_{ij} \neq K_{ji}$. However, partial symmetry exists in the surge, sway, heave and yaw modes i.e. $K_{ij} = K_{ji}$ for $i, j = 1, 2, 3, 6$, resulting in 6 symmetric pairs of stiffness matrix coefficients.

The above generic analysis can be now applied to determine the exact (6×6) mooring stiffness matrix of a single taut mooring line at an arbitrary position and orientation of the platform, while assuming the lines remain taut as in the TLP, shown in Figure 4.8. The mooring stiffness coefficients can be determined directly by substituting the $\mathbf{K}^p$ elements (given by Equation (4.31)) together with expressions in Equation (4.28) into the general mooring stiffness matrix coefficients listed in Appendix D. It is worth noting that when

$\alpha = 90^o$, β is undefined. However, if we retain β in its symbolic form, all terms containing β will cancel out and hence all the corresponding terms will be free of β. Therefore, β can be arbitrarily chosen as zero in the calculations at $\alpha = 90^o$ for a taut line.

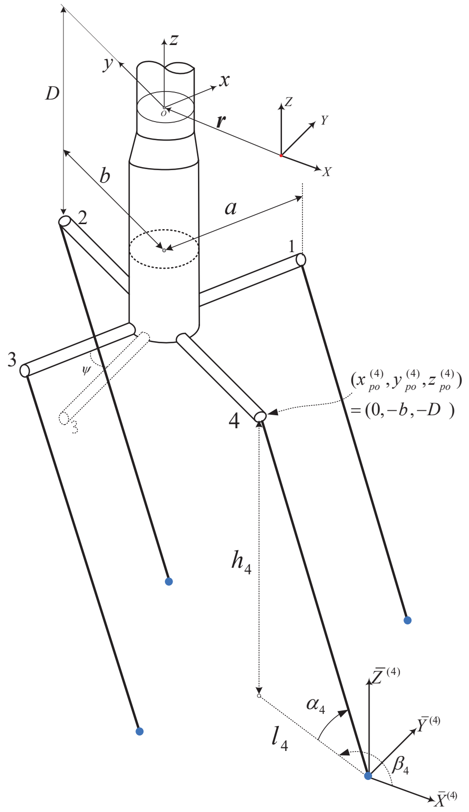

Figure 4.8: Rectangular TLP undergoes large displacement

The mooring system stiffness at equilibrium for the rectangular TLP (Figure 4.8) can be obtained by substituting $\mathbf{X} = \mathbf{0}$ and the attachment point coordinates in the body frame, $\mathbf{r}_{po}$ = [a 0 -D], [0 b -D], [-a 0 -D], and [0 -b -D] for the lines 1, 2, 3, 4, respectively into the Equations of Appendix D. The angles $\alpha = 90^o$, and $\beta = 0$ for all the lines. The resulting mooring system stiffness matrix form of this TLP will be presented in Section 4.2.4.3.

4.2.4 Mooring system stiffness

The stiffness matrix of a mooring system composed of multiple lines is evaluated by summing the stiffness matrices of the individual lines. If $\mathbf{K}_m^{(i)}$ denotes the stiffness matrix of the i-th mooring line, the stiffness matrix of a mooring system comprised of n lines can be evaluated as

$$\mathbf{K}_m = \sum_{i=1}^{n} \mathbf{K}_m^{(i)} \tag{4.39}$$

The general analysis developed here can be used to determine a closed form of the mooring system stiffness matrix for the following types of mooring systems at equilibrium.

- *Slack catenary mooring system*: the line is hanging freely and the whole cable profile is suspended (Figure 4.2 (b)) or part of its length rests on the seabed (Figure 4.2 (a)).

- *Taut-leg mooring system*: where the line does not contact the seabed and are taut due to the pretension caused by the platform excess buoyancy. The lines are inclined (with angle α) and the anchor experience horizontal and vertical loads. Most the restoring loads are generated by line elasticity. The mooring radius (R_c) of the taut-leg mooring system is smaller than that of the catenary mooring system if designed to support the same platform size and weight.

- *Tension leg mooring system*: the lines are vertical ($\alpha = 90^o$) and the anchor experiences mainly a vertical load. This type can be considered as a special case of the taut-leg mooring.

The mooring stiffness matrix at equilibrium is mainly required in the preliminary design and dynamic analyses of the floating structures. The detailed formulation of the mooring system matrix for these mooring system types are presented in the following subsections.

4.2.4.1 Catenary mooring system stiffness matrix

A catenary mooring system is comprised of n lines ($n \geq 3$) in its equilibrium configuration similar to that shown in Figure 4.1 (a). It is assumed that the anchors are uniformly distributed in a circle with radius R_c and $2\pi/n$ radians apart. The tethers are identical in length and material properties. The projected horizontal and vertical lengths, l and h, respectively are also identical for all tethers.

The stiffness matrix of the individual lines based on the line order in Figure 4.1 (a), can be determined by substituting $\mathbf{X} = \mathbf{0}$, and $\beta_i = \pi + 2\pi(i-1)/n$ for line $i = 1, 2, 3, ..., n$ into the stiffness coefficient expressions in Appendix D. In the same manner, substitute the i-th fairlead body frame coordinates, $x_{po}^{(i)} = R_f \cos(\beta_i - \pi), y_{po}^{(i)} = R_f \sin(\beta_i - \pi)$, and $z_{po}^{(i)} = -D$ for all tethers. The mooring stiffness matrix of the entire mooring system at equilibrium is symmetric, can be then expressed as

$$\mathbf{K}_m = \begin{bmatrix} K_{11} & 0 & 0 & 0 & K_{15} & 0 \\ 0 & K_{22} & 0 & K_{24} & 0 & 0 \\ 0 & 0 & K_{33} & 0 & 0 & 0 \\ 0 & K_{42} & 0 & K_{44} & 0 & 0 \\ K_{51} & 0 & 0 & 0 & K_{55} & 0 \\ 0 & 0 & 0 & 0 & 0 & K_{66} \end{bmatrix} \tag{4.40}$$

where

$$\begin{aligned} & K_{11} = \frac{1}{2} n \left(K_{11}^p + \frac{H}{l} \right) \quad , \quad K_{15} = -n \left(-\frac{R_f}{2} K_{12}^p + \frac{D}{2} K_{11}^p + \frac{DH}{l} \right) \\ & K_{22} = K_{11} \quad , \quad K_{24} = -K_{15} \quad , \quad K_{33} = n\, K_{22}^p \quad , \quad K_{42} = K_{24} \\ & K_{44} = n \left(-D\, R_f\, K_{12}^p + \frac{D^2}{2} K_{11}^p + \frac{R_f^2}{2} K_{22}^p + DV + \frac{H\, R_f}{2} + \frac{D^2 H}{2l} \right) \quad , \quad K_{51} = K_{15} \\ & K_{55} = K_{44} \quad , \quad K_{66} = n \left(\frac{H\, R_f^2}{l} + H\, R_f \right) \end{aligned} \tag{4.41}$$

Here, H, V, l, h, and the elements of $\mathbf{K}^p$ are identical for all the lines due to symmetry.

4.2.4.2 Taut-leg mooring system stiffness matrix

If the lines are taut, the stiffness matrix of a symmetric taut-leg mooring system (Figure 4.1 (a) but with taut lines) can be obtained by substituting the elements of $\mathbf{K}^p$ from Equation (4.31) into Equation (4.41). As well, the expressions of H, V, l, and h can be taken from Equation (4.28) and substituted into Equation (4.41) to get

$$\begin{aligned}
K_{11} =& 0.5n\left(\frac{T}{L}\left(1+\sin^2\!\alpha\right)+K_I\cos^2\!\alpha\right)\\
K_{15} =& -n\left[\frac{T}{2L}\left(D+D\sin^2\!\alpha+R_f\sin\alpha\,\cos\alpha\right)+\frac{K_I}{2}\left(D\cos^2\!\alpha-R_f\sin\alpha\,\cos\alpha\right)\right]\\
K_{22} =& K_{11} \quad , \quad K_{24}=-K_{15} \quad , \quad K_{33}=n\left(\frac{T}{L}\cos^2\!\alpha+K_I\sin^2\!\alpha\right) \quad , \quad K_{42}=K_{24}\\
K_{44} =& n\left[T\left(D\sin\alpha+\frac{1}{2}R_f\cos\alpha\right)+0.5\frac{T}{L}\left((R_f\cos\alpha+D\sin\alpha)^2+D^2\right)\right]\\
&\qquad +0.5n\,K_I(D\cos\alpha-R_f\sin\alpha)^2\\
K_{51} =& K_{15} \quad , \quad K_{55}=K_{44} \quad , \quad K_{66}=n\frac{TR_f}{L}\left(R_f+L\cos\alpha\right)
\end{aligned} \tag{4.42}$$

4.2.4.3 Tension leg system stiffness matrix

If the lines are taut and vertical, the mooring configuration becomes a tension leg structure. Substituting $\alpha = 90^{\mathrm{o}}$ into Equation (4.42), the stiffness matrix for triangular (Equilateral), square, pentagonal, hexagonal, ..., etc, TLPs can be expressed as

$$\mathbf{K}_m = \begin{bmatrix}
n\frac{T}{L} & 0 & 0 & 0 & -n\frac{T\,D}{L} & 0\\
0 & n\frac{T}{L} & 0 & n\frac{T\,D}{L} & 0 & 0\\
0 & 0 & nK_I & 0 & 0 & 0\\
0 & n\frac{T\,D}{L} & 0 & K_m^{44} & 0 & 0\\
-n\frac{T\,D}{L} & 0 & 0 & 0 & K_m^{55} & 0\\
0 & 0 & 0 & 0 & 0 & K_m^{66}
\end{bmatrix} \tag{4.43}$$

where $K_m^{44} = K_m^{55} = n\left(\frac{T\,D^2}{L}+0.5K_I\,R_f^2+T\,D\right)$, $K_m^{66} = n\frac{T\,R_f^2}{L}$ and n represents the number of legs. For a rectangular TLP with dimension $2a \times 2b$, as shown in Figure 4.8, the mooring stiffness matrix form is similar to that of Equation (4.43) (with $n = 4$), but with different expression for

$$\begin{aligned}K_m^{44} =&4\left(\frac{T\,D^2}{L} + 0.5K_I\,b^2 + T\,D\right)\\ K_m^{55} =&4\left(\frac{T\,D^2}{L} + 0.5K_I\,a^2 + \,T\,D\right)\\ K_m^{66} =&\frac{2T}{L}\left(a^2 + b^2\right)\end{aligned} \tag{4.44}$$

The results in Equation (4.44) can also be found in [37,40]. However, to our best knowledge, the term $4TD^2/L$ in K_{44} and K_{55} is missing in other works. If the platform undergoes general displacement where $\mathbf{X} \neq \mathbf{0}$, the stiffness matrix of each line should be determined based on its geometry and the platform displacements.

4.2.5 Influence of the mooring system design parameters

The mooring system configuration and geometry affect the mooring stiffness in a complex manner. For example, the TLP mooring system stiffness matrix given by Equation (4.43) shows that the roll, pitch and yaw stiffnesses increase as the anchor (or fairlead) radius (R_f) increases (R_f does not affect L or K_I), while the surge, sway and heave stiffnesses do not change. However, for a taut-leg mooring system where the taut lines are inclined, the change in the anchor radius implies a change in the line length which alters K_I. The effect of this concurrent change on the mooring stiffness of the system is now investigated.

The influence of mooring system design parameter is investigated for the taut leg floating wind turbine platform concept proposed by Sclavounos et al. [73] and Lee [113]. The mooring system forms 2 concentric quadrapods sharing the same anchors while the attachment points (fairleads) of each are located at different depths, as shown in Figure 4.9. The anchors are uniformly distributed in a circle with a radius R_c and 90^o apart. The cable diameter $d = 15$ mm, linear stiffness $EA = 1.50 \times 10^9$ N, and equivalent weight in water per unit length $w = 722.31$ N/m. The fairlead depths d_U and d_L are 0 and 20 m, respectively, and their radius, $R_f = 6$ m as proposed in [113]. The mooring system stiffness is computed using the exact analysis discussed in Section 4.2.4.1 where the cable weight is considered.

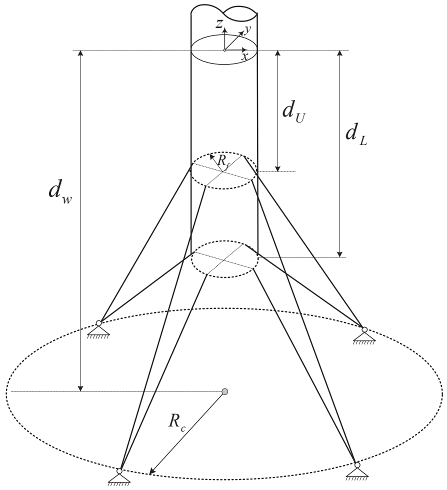

Figure 4.9: Taut leg floating wind turbine concept (4-anchor)

4.2.5.1 Influence of the anchor radius

The diagonal stiffness coefficients of the mooring system in all DOFs are computed for a range of R_c while water depth ($d_w = 100$ m as used in [113] is kept constant). The analysis is conducted at two different excess buoyancy forces $F_{e1} = 3.2 \times 10^6$ N (as calculated from [113]) and $F_{e2} = 4.0 \times 10^6$ N, where the excess buoyancy is the difference between the total weight of the platform and mooring system and buoyancy force.

Since this is a statically indeterminate system, the unstretched lengths of the upper and lower lines can be adjusted to support the same fairlead vertical tension such that each line supports one eighth of the excess buoyancy load ($V = F_e/8$).

Figure 4.10 (a)-(d) illustrate the effect of anchor radius, R_c on the diagonal coefficients of the mooring system stiffness matrix. The results show that the horizontal stiffnesses (K_{11} and K_{22}) initially increase with increasing anchor radius, reaching a peak, and then decrease. This occurs because when the anchors are moved outward, the tethers also lengthen and hence soften and this then eventually ends up overriding the benefits of orientation. It is interesting to note that the location of the maximum stiffness change significantly with the cable sag. When the line is more saggy i.e. at lower F_e, the peak occurs at lower anchor radius. The heave stiffness K_{33} decreases monotonically as R_c increases because the line becomes longer and hence softer (K_I decreases), and also becomes more inclined. Figure 4.10 (e) and (f) shows the tensions acting at the fairleads of the upper and lower lines. These plots simply

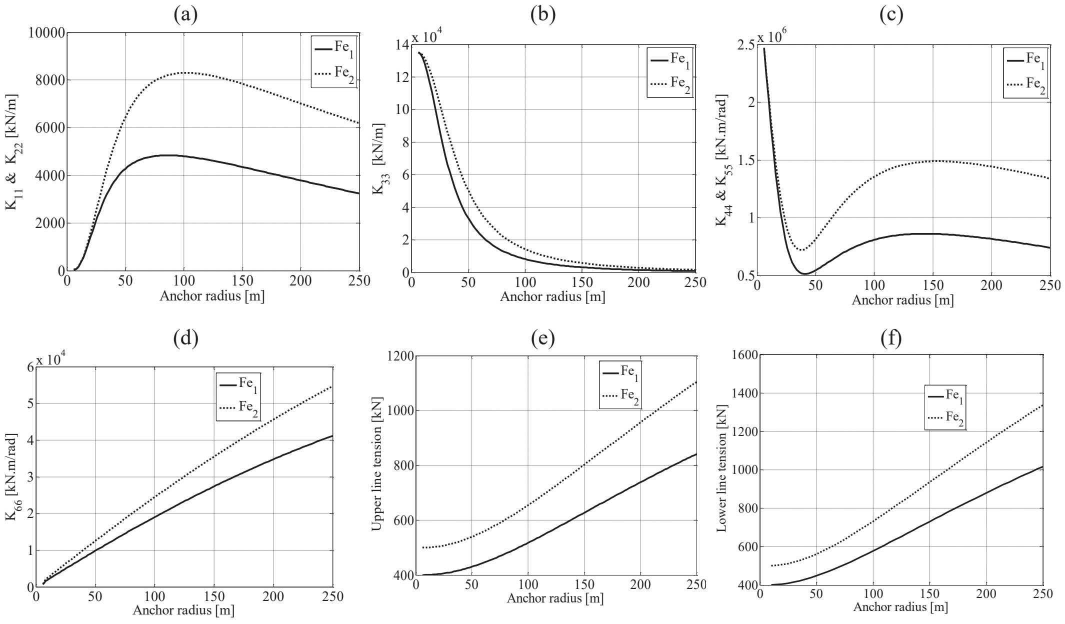

Figure 4.10: Influence of anchor radius on the system stiffness and tension

show that tension gets larger as the anchor radius increases. This leads to higher yaw stiffness (K_{66}) since it is proportional to the line tension. The roll/pitch mooring stiffnesses (K_{44} and K_{55}) decrease as R_c increase up to $R_c = 40$ m then increases. This is because K_{44} and K_{55} are proportional to TD^2 and K_I, as R_c increases K_I decreases and T increases. At larger R_c, T becomes more dominant yielding an increase in K_{44} and K_{55}. If all the fairleads and the local coordinate system are located at the same depth i.e. $D = 0$, the trends of K_{44} and K_{55} will be similar to K_{33} since they are then only proportional to K_I which decreases as R_c increases.

4.2.5.2 Influence of number of lines

The proposed taut-leg mooring system under consideration has 4 anchors that support 4 pairs of lines (Figure 4.9). However, a system with fewer anchors consisting of 3 pairs of lines attached to 3 anchors also can be used. Ideally, as the number of tethers increases, the mooring system stiffness increases assuming all tethers are fully taut (sag free). However, the mooring lines are inclined and maintaining zero sag would require very large tensions. If the excess buoyancy is not increased, the addition of lines could increase sag, and possibly reduce the mooring stiffness.

The mooring system stiffness of the original 4-anchor mooring system (Figure 4.9) is compared with a similar 3-anchor system where the 3 anchors holding 6 mooring lines are distributed evenly on a circle 120^o apart, as seen in Figure 4.9 (but with 3 anchors). The cable properties, system geometry and platform characteristics are not changed. The comparisons of these 2 designs, assuming the same excess buoyancy force $F_e = 3.2 \times 10^6$ N, are detailed in Figure 4.11 (a)-(d). The results show that the increase in the number of tethers reduces the system stiffnesses in all directions at large R_c (> 30 m). This occurs because the lines of the system with fewer anchors are less saggy due to a higher tension per line and hence they are stiffer, as illustrated in Figure 4.11 (e)-(f). At $R_c < 30$ m, the horizontal stiffnesses (K_{11} and K_{22}) do not change with the change of the number of lines since the mooring configuration is close to a TLP and these stiffnesses are more influenced by the total line tension ($\approx F_e$) which does not change since the excess buoyancy is the same for both systems. At $R_c <$ 30 m, K_{33}, K_{44} and K_{55} are higher for the 4-anchor system since the sag is small and the cable stiffness becomes proportional to K_I.

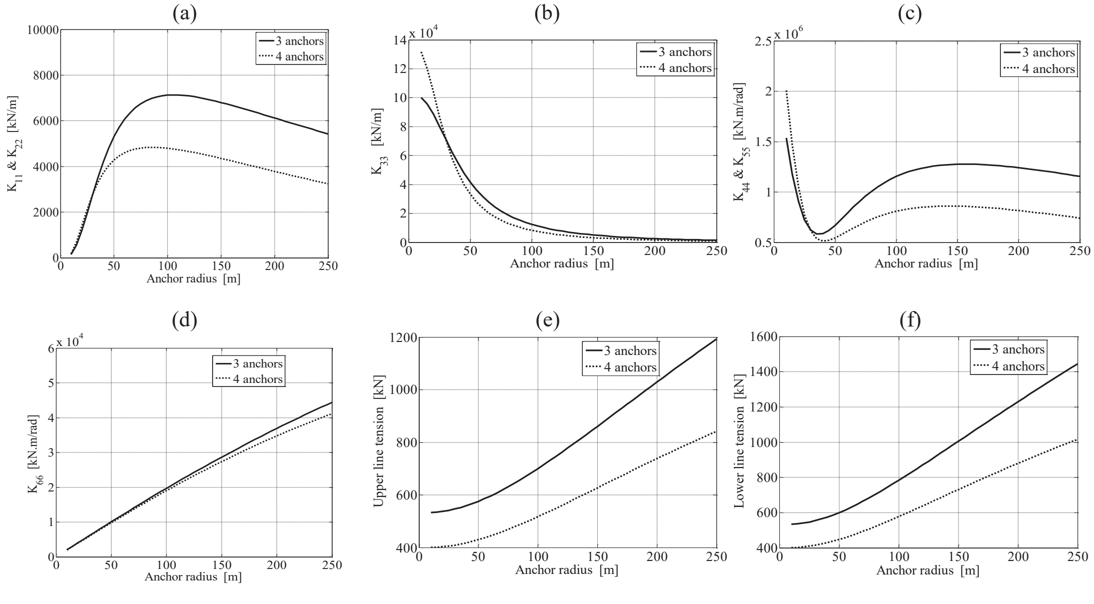

Figure 4.11: Influence of number of lines on the system stiffness and tension

It is clear that adding tethers will soften the system when the excess buoyancy force is not sufficient. It is thus recommended to replace the proposed design with a 3-anchor system to reduce the mooring system construction cost by avoiding the high cost of an extra anchor. If it is still required to have the stiffness properties of the 4-anchor system, this can still be achieved with a 3-anchor system utilizing softer cables which would lead to a further reduction in the mooring system cost. A possible advantage of the 4-anchor system is its better survivability in the case of rupture of one or more lines.

4.2.5.3 Influence of the mooring system configuration

The bridle mooring system described in Section 4.1.2 is altered such that Segment 3 is eliminated and the bridle segments are directly attached to the anchor point, as shown in Figure 4.12. The lines are circumferentially distributed around the cylindrical floating platform. The adjacent fairleads that hold lines sharing the same anchor create an angle 2γ with the radial line passing through the floaters cross section center, as shown in Figure 4.12. The fairleads are located at the same depth i.e. $d_u = d_L = d_f = 10$ m. When $\gamma = 0$, the number of fairleads reduces to 3 and each fairlead holds 2 lines as in the conventional single-segment configuration (Figure 4.1 (a)).

The influence of the angle γ on the mooring system stiffness is investigated at a range of R_c, as shown in Figure 4.13. The results show that the K_{11}, K_{22} and K_{33} stiffnesses are insensitive to the change in γ, as shown in Figure 4.13 (a) and (b). The roll and pitch stiffnesses (K_{44} and K_{55}) increase slightly as γ increases, as illustrated in Figure 4.13 (c). However, the yaw stiffness (K_{66}) is strongly influenced by γ, and it increases sharply as γ increases. For example, at R_c=100, $\gamma = 10^o$ and 20^o yield almost 2 and 4 + the yaw stiffness of that at $\gamma = 0^o$, respectively, as illustrated in Figure 4.13 (d). The benefit from this configuration is stiffening the yaw mode without affecting the stiffness of other directions. As a result, such configuration could reduce the yaw response of the platform.

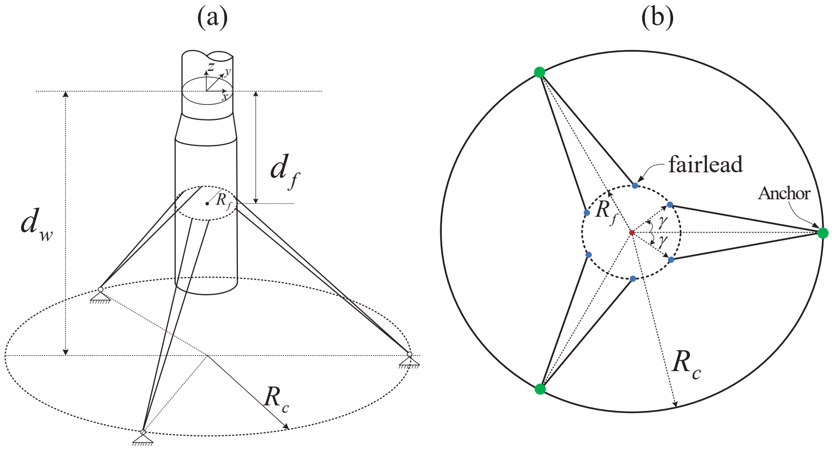

Figure 4.12: (a) Taut-leg mooring system configurations; and (b) top view

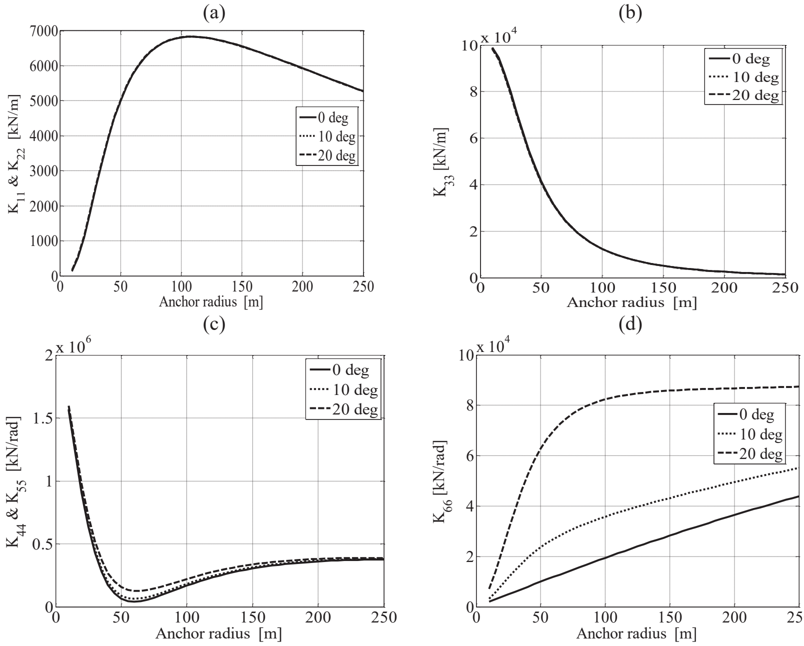

Figure 4.13: Influence of mooring system geometry on the stiffness

Chapter 5

LUMPED MASS CABLE MODEL

In the previous chapter, quasi-static cable models were developed to determine the mooring lines tensions using different forms of the catenary equations. These models ignore the cable inertia forces, external fluid loads such as drag and added mass forces, and cable–seabed interaction forces. Quasi–static cable models are often used in dynamic simulations of offshore structures due to the ease of implementation. When the floating structure is deployed in deep water, long mooring lines would lead to large cable mass such that the cable dynamics could influence the system dynamics. As well, the mooring line tensions computed using the quasi-static approach are usually less than those calculated considering cable dynamics. This necessitates having a realistic mooring system dynamic model to ensure an accurate system simulation, particularly for mooring system design.

This chapter presents the development of a lumped mass cable model to be incorporated into the FOWT dynamic model developed earlier in Chapter 2. In general, the model follows the formulations in [80, 114]. However, theses works dealt with suspended cable i.e. there is no contact between the cable and seabed. This is not the case in the present work where the lines can be partially in contact with the seabed. Therefore, the model is augmented by a cable seabed interaction model, developed to determine the contact forces for the cable portion in contact with seabed. As well, a new added mass matrix form is developed and replaces the one of [80, 114].

The lumped mass cable modeling methodology begins by describing the discretized cable kinematics followed by formulating the internal tension and damping forces along the cable elements. The external hydrodynamic forces are evaluated using Morison's equation. The added mass force term is reformulated in a matrix form. A cable-seabed interaction model is introduced to compute the reaction, friction and damping forces at cable-seabed interface.

The lumped mass discretized model is first assembled for a single cable mooring line configurations, then the assembly process is extended to the multi-segment bridle configuration to derive the equations of motion of the mooring lines.

New static solvers are developed to determine the equilibrium profile of the mooring system configurations under consideration. Finally, the mooring loads exerted on the platform are formulated to evaluate the mooring force and moment terms in the FOWT equations of motion developed earlier in Chapter 2.

5.1 Kinematics

The lumped mass approach models the cable as a series of N viscoelastic straight elements which form $N+1$ nodes, the displacement of the i-th node is ${}^{I}\mathbf{r}_i = [r_{X,i} \quad r_{Y,i} \quad r_{Z,i}]^T$, as shown in Figure 5.1. The cable unstretched length is L_0 and the corresponding length of each element is $l_u = L_0/N$. The i-th cable element is bounded by the nodes i and $i+1$. The first and last nodes (cable ends) are attached to the platform and the anchor point, respectively. Their corresponding displacements (in the inertial frame) are $\mathbf{r}_1$ and $\mathbf{r}_{N+1}$, respectively. These displacements are prescribed[1] where the anchor point ($\mathbf{r}_{N+1}$) is fixed in space and $\mathbf{r}_1$ can be determined from the platform kinematics as

$$ {}^{I}\mathbf{r}_1 = {}^{I}\mathbf{r} + \mathbf{R}\, {}^{p}\mathbf{r}_{po} \tag{5.1} $$

To specify the kinematics of the cable elements, an element-fixed frame attached to each element such that the i-th element frame is defined by the $e_{1,i}$, $e_{2,i}$ and $e_{3,i}$ axes where the latter axis direction is aligned along the element and directed towards the platform, the other axes are normal to the element, as shown in Figure 5.1. The orientation of the element frame is defined using two Euler angles describing the 2-1 rotation sequence since the cable torsion is neglected [80], i.e. no 3rd rotation angle is required. Therefore, the rotation matrix that

---

[1] The anchor point is fixed while the attachment point displacement is function of the platform displacement

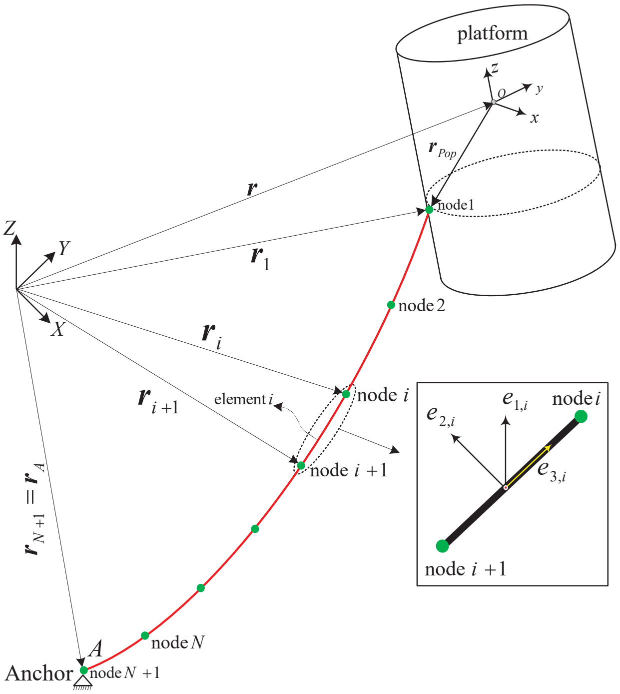

Figure 5.1: Lumped mass cable model

transforms the i-th cable element frame into the inertial frame can be expressed as [80]

$$\mathbf{R}_{e,i} = \begin{bmatrix} c_{\theta_i} & s_{\theta_i}\, s_{\phi_i} & s_{\theta_i}\, c_{\phi_i} \\ 0 & c_{\phi_i} & -\, s_{\phi_i} \\ -s_{\theta} & c_{\theta_i}\, s_{\phi_i} & c_{\theta_i}\, c_{\phi_i} \end{bmatrix} \tag{5.2}$$

where ϕ_i and θ_i are the Euler angles characterizing the i-th element rotations, θ_i, can be computed as

$$\theta_i = \operatorname{atan2}\left((r_{X,i} - r_{X,i+1}),\, (r_{Z,i} - r_{Z,i+1})\right) \tag{5.3}$$

and ϕ_i as

$$\phi_i = \begin{cases} \operatorname{atan2}\left(-(r_{Y,i} - r_{Y,i+1}),\, (r_{X,i} - r_{X,i+1})/s_{\theta_i}\right) & \text{for} \quad c_{\theta_i} < s_{\theta_i} \\ \operatorname{atan2}\left(-(r_{Y,i} - r_{Y,i+1}),\, (r_{Z,i} - r_{Z,i+1})/c_{\theta_i}\right) & \text{for} \quad c_{\theta_i} \geq s_{\theta_i} \end{cases} \tag{5.4}$$

where the subscripts X, Y, and Z denote the respective component. Either inequality in Equation (5.4) is sufficient to compute the angle. However, this form enhances the numerical stability to insure that the denominator of the second argument of the atan2 function is as large as possible to reduce numerical error.

5.2 Internal Forces

The tension arises from the element stretch due to the cable elasticity and internal damping force, such that

$$T_i = T_{s,i} + T_{d,i} \tag{5.5}$$

The element tension due to stretch can be computed as a function of the cable extensional stiffness EA using Hooke's law as

$$T_{s,i} = EA\left(L_i - l_{u,i}\right)/l_{u,i} \tag{5.6}$$

The stretched length of the i-th element is L_i, can be determined from the displacements of their nodes as

$$L_i = \|\mathbf{r}_i - \mathbf{r}_{i+1}\| \tag{5.7}$$

The damping force can be represented as [114]

$$T_{d,i} = C_i(\dot{\mathbf{r}}_i - \dot{\mathbf{r}}_{i+1})_{e3,i} \tag{5.8}$$

where C_i is the internal damping coefficient and $(\dot{\mathbf{r}}_i - \dot{\mathbf{r}}_{i+1})_{e3,i}$ indicates the relative velocity component between the element ends (nodes) along the element direction $(e3, i)$. Since the cable cannot hold a compressive load, the following constraint is imposed

$$T_i = \tfrac{1}{2}\left(T_i + \|T_i\|\right) \tag{5.9}$$

This relation modifies the tension computed from Equation (5.5) to keep the positive values unchanged and switch the negative values to zero. The tension force acting along the i-th element, can be expressed in a vector form as

$${}^{I}\mathbf{T}_i = \mathbf{R}_{e,i}[0 \quad 0 \quad T_i]^T \tag{5.10}$$

5.3 External Forces

The hydrodynamic loads exerted on the cable elements are determined using Morison's Equation in a manner similar to the platform (Section 2.3.2). The hydrodynamic force exerted on the i-th element can be then calculated assuming the velocity and acceleration of the element and fluid along the element span are uniform and equivalent to that at the element midpoint.

$$\mathbf{H}_{e,i} = \underbrace{\tfrac{1}{2}\rho\, C_{Dc}\, l_{u,i}\, d_c \left\|(\mathbf{v}_{rel,i})_{\perp}\right\| (\mathbf{v}_{rel,i})_{\perp} + \rho\, l_{u,i}\, A_e(1+C_a)(\dot{\mathbf{v}}_{f,i})_{\perp}}_{\mathbf{H}_{e*,i}} - \underbrace{\rho\, l_{u,i}\, A_e\, C_a(\mathbf{a}_{e,i})_{\perp}}_{\mathbf{A}_{e,i}} \tag{5.11}$$

where $\mathbf{A}_{e,i}$ is the added mass force of the i-th element and $\mathbf{H}_{e*,i}$ represent the sum of drag (1st term) and Froude-Krylov forces terms (2nd term) i.e. the hydrodynamic force excluding the added mass. The cable diameter is d_c, cable cross section area is $A_e = \pi d_c^2/4$ and C_{Dc} is drag coefficient of the cable, and $(.)_{\perp}$ denotes the component of $(.)$ normal to the element (i.e. normal to $e_{3,i}$ axis). The velocity and acceleration of the element midpoint can be calculated assuming the element as a rigid body and neglecting the element elongation rate because it is very small [115]. Accordingly, the element midpoint velocity and acceleration can be then expressed as

$$\mathbf{v}_{e,i} = \tfrac{1}{2}(\dot{\mathbf{r}}_i + \dot{\mathbf{r}}_{i+1}) \quad , \quad \mathbf{a}_{e,i} = \tfrac{1}{2}(\ddot{\mathbf{r}}_i + \ddot{\mathbf{r}}_{i+1}) \tag{5.12}$$

The relative fluid velocity at the midpoint of the i-th element can be expressed as

$$\mathbf{v}_{rel,i} = (\mathbf{v}_{f,i} - \mathbf{v}_{e,i}) \tag{5.13}$$

where $\mathbf{v}_{f,i}$ and $\dot{\mathbf{v}}_{f,i}$ are the fluid velocity and acceleration at the i-th element midpoint, respectively. Only the normal drag force is considered in Equation (5.11) while the skin friction drag is neglected.

Since the equation of motions of the cable point masses will be represented in the inertial frame ($\boldsymbol{\mathcal{F}}_I$) as will be discussed later, the external forces exerted on the cable elements should be represented in the inertial frame, ${}^{I}(\mathbf{a}_{e,i})_{\perp}$, can be computed as

$$ {}^{I}(\mathbf{a}_{e,i})_{\perp} = \underbrace{\mathbf{R}_{e,i}\;\mathbf{R}_{110}\;\mathbf{R}_{e,i}^{T}}_{\bar{\mathbf{B}}_i}\;{}^{I}\mathbf{a}_{e,i} \tag{5.14} $$

where

$$ \mathbf{R}_{110} = \begin{bmatrix} 1 & 0 & 0 \\ 0 & 1 & 0 \\ 0 & 0 & 0 \end{bmatrix} \tag{5.15} $$

$\mathbf{R}_{110}$ pre-multiplies $(\mathbf{a}_{e,i})$ expressed in the element frame to insure that its 3rd component (in the element frame) reduces to zero. The vectors $(\mathbf{v}_{rel,i})_{\perp}$ and $(\dot{\mathbf{v}}_{f,i})_{\perp}$ can be evaluated in the same manner.

5.4 Cable-Seabed Interaction Forces

A three-dimensional contact model is now developed to evaluate the forces generated at the cable-seabed interface, as shown in Figure 5.2. This model characterizes the cable-seabed interactions with the following forces

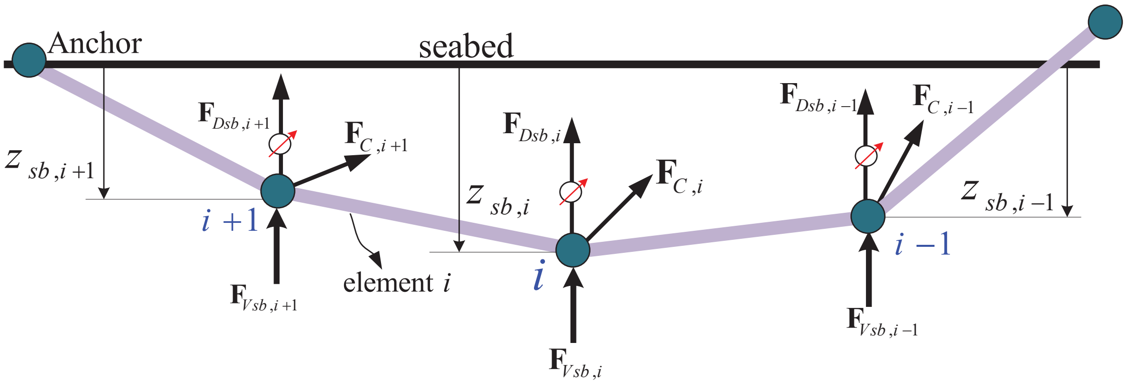

Figure 5.2: Cable-seabed interaction model

(1) Vertical seabed stiffness force

The cable portion rest on the seabed experiences a normal force from the seabed proportional to the node penetration $(z_{sb,i})$ into the soil, which can be expressed as [116]

$$ F_{Vsb,i} = \hat{a}\, l_u\, (0.1/d_c)^{\hat{b}}\, \sqrt{10 z_{sb,i}/d_c}\;\; d_c\, (S_{uo} + \rho_{sb} z_{sb,i}) \tag{5.16} $$

where S_{uo} shear strength of soil at seabed, ρ_{sb} is the shear strength gradient. These properties are dependent on the soil type (clay, sand,...etc.). If we choose clay, S_{uo}=5000 Pa and ρ_{sb}= 1500 Pa/m. The constants $\hat{a}$ and $\hat{b}$ vary according to line surface (rough or smooth), for a smooth line/pipe $\hat{a}$=6, and $\hat{b}$=0.25 [116, 117].

(2) Vertical seabed damping force

The vertical damping due to seabed contact exists when the cable node penetrates the seabed and vanishes when the node moves upwards, this force can be formulated as [118]

$$F_{Dsb,i} = -\begin{cases} C_{sbz}(\dot{\mathbf{r}}_i)_Z & \text{for} \quad (\dot{\mathbf{r}}_i)_Z < 0 \\ 0 & \text{for} \quad (\dot{\mathbf{r}}_i)_Z \geq 0 \end{cases} \tag{5.17}$$

where the seabed damping coefficient $C_{sbz} = 2\zeta_{sb}\sqrt{m_{nod,i}k_{sb}}$, ζ_{sb} is the seabed damping ratio, $m_{nod,i} = \bar{m}_c\, l_{u,i}$ is the nodal mass in vacuum, $\bar{m}_c$ is the mass per unit length of the cable in vacuum and k_{sb} is the seabed vertical stiffness coefficient, which can be determined from force-penetration relationship (Equation (5.16)) by calculating the slope at zero penetration.

(3) Friction forces

The friction force developed between the moving cable portion lying on the seabed and the seabed can be modeled using a Coulomb friction model. This model considers the friction force along the element (tangential) direction and in the lateral direction. These effects can be formulated as [118, 119]

$${}^{I}\mathbf{F}_{c,i} = -\mathbf{R}_{e,i}\begin{bmatrix} \mu_l\, F_{Vsb,i}\ \text{sign}[(\dot{\mathbf{r}}_i)_{e1,i}] \\ \mu_l\, F_{Vsb,i}\ \text{sign}((\dot{\mathbf{r}}_i)_{e2,i}) \\ \mu_t\, F_{Vsb,i}\ \text{sign}((\dot{\mathbf{r}}_i)_{e3,i}) \end{bmatrix} \tag{5.18}$$

where μ_t and μ_l are the tangential and lateral friction coefficients, respectively. Their values depend on the seabed type (sand, clay,..., etc.) and mooring line type (chain or wire rope) [119]. The latter study recommended using μ_l =1.5–2 times μ_t, and μ_t=0.18 for a wire cable sliding on a clay surface. The total force exerted on the i-th node due to contact with the seabed can be then written as

$$\mathbf{F}_{sb,i} = \mathbf{F}_{Vsb,i} + \mathbf{F}_{Dsb,i} + \mathbf{F}_{c,i} \tag{5.19}$$

5.5 Model Assembly

The equations of motion represinting the translation of the lumped masses attached to the cable nodes, can be formulated in the inertial frame as

$$\mathbf{M}_{e,i}\ {}^{I}\ddot{\mathbf{r}}_i = {}^{I}\mathbf{F}_{e,i} \quad , \quad i = 2, 3, \ldots, N \tag{5.20}$$

where $\mathbf{F}_{e,i}$ is the sum of the applied force at i-th node (lumped mass) and $\mathbf{M}_{e,i}$ is the corresponding mass matrix (3×3), written as

$$\mathbf{M}_{e,i} = m_{nod,i}\ \mathbf{I}_{3\times 3} \tag{5.21}$$

where $\mathbf{I}_{3\times 3}$ is the identity matrix. The equations of motion (Equation (5.20)) are formulated for the interior nodes since the displacements of the boundary nodes (1 and $N + 1$) are prescribed.

The lumped mass cable model assumes that external force and the element weight in fluid acting at each element midpoint are lumped at the element nodes such that each node bears half of the element load. Thus, each node supports half the external forces of the adjacent elements. The applied internal and external forces at the i-th node is expressed as

$$\mathbf{F}_{e,i} = \underbrace{\mathbf{T}_{i-1} - \mathbf{T}_i + \tfrac{1}{2}(\mathbf{W}_{e,i} + \mathbf{W}_{e,i-1}) + \tfrac{1}{2}(\mathbf{H}_{e*,i} + \mathbf{H}_{e*,i-1}) + \mathbf{F}_{sb,i}}_{\mathbf{F}_{e*,i}} + \underbrace{\tfrac{1}{2}(\mathbf{A}_i + \mathbf{A}_{i-1})}_{\mathbf{F}_{add,i}} \tag{5.22}$$

where ${}^{I}\mathbf{W}_{e,i} = -[0 \quad 0 \quad w\, l_{u,i}]^T$ is nodal weight (in fluid), and the added mass term ($\mathbf{F}_{add,i}$) in Equation (5.22) is a function of the accelerations and can be shifted to the left hand side of Equation (5.20). This term can be obtained as

$$\mathbf{F}_{add,i} = \begin{cases} [\mathbf{B}_1 + \mathbf{B}_2 \quad \mathbf{B}_2]\ [\ddot{\mathbf{r}}_2 \quad \ddot{\mathbf{r}}_3]^T & \text{for} \quad i = 2 \\ [\mathbf{B}_{i-1} \quad \mathbf{B}_{i-1} + \mathbf{B}_i \quad \mathbf{B}_i]\ [\ddot{\mathbf{r}}_{i-1} \quad \ddot{\mathbf{r}}_i \quad \ddot{\mathbf{r}}_{i+1}]^T & \text{for} \quad 2 < i < N \\ [\mathbf{B}_{N-1} \quad \mathbf{B}_{N-1} + \mathbf{B}_N]\ [\ddot{\mathbf{r}}_{N-1} \quad \ddot{\mathbf{r}}_N]^T & \text{for} \quad i = N \end{cases} \tag{5.23}$$

where $\mathbf{B}_i = \rho\, l_{u,i}\, A_e\, C_a\, \bar{\mathbf{B}}_i$. This form (Equation (5.23)) can be expanded for the whole point masses of the cable yielding the cable added mass matrix as

$$\mathbf{A}_{cable} = \begin{bmatrix} \mathbf{B}_1+\mathbf{B}_2 & \mathbf{B}_2 & 0 & 0 & 0 & \cdots & 0 \\ \mathbf{B}_2 & \mathbf{B}_2+\mathbf{B}_3 & \mathbf{B}_3 & 0 & 0 & \cdots & \vdots \\ 0 & \mathbf{B}_3 & \mathbf{B}_3+\mathbf{B}_4 & \mathbf{B}_4 & 0 & \cdots & \vdots \\ 0 & 0 & \mathbf{B}_4 & \mathbf{B}_4+\mathbf{B}_5 & \mathbf{B}_5 & \cdots & \vdots \\ \vdots & \vdots & \vdots & \vdots & \vdots & \vdots & \vdots \\ 0 & 0 & \cdots & 0 & \mathbf{B}_{N-2} & \mathbf{B}_{N-2}+\mathbf{B}_{N-1} & \mathbf{B}_{N-1} \\ 0 & 0 & \cdots & 0 & 0 & \mathbf{B}_{N-1} & \mathbf{B}_{N-1}+\mathbf{B}_N \end{bmatrix} \tag{5.24}$$

the equations of motion (Equation (5.20)) of the system of lumped masses of the discretized cable can be reformulated as

$$[\mathbf{A}_{cable} + \mathbf{M}_{cable}]\ [\ddot{\mathbf{r}}_2 \quad \ddot{\mathbf{r}}_3 \quad \ldots \quad \ddot{\mathbf{r}}_N]^T = [\mathbf{F}_{e*,2} \quad \mathbf{F}_{e*,3} \quad \ldots \quad \mathbf{F}_{e*,N}]^T \tag{5.25}$$

where the discretized cable mass matrix in vacuum $\mathbf{M}_{cable} = diag(\mathbf{M}_{e,2}\,, \mathbf{M}_{e,3}\,, \ldots\ldots\ \mathbf{M}_{e,N})$. Repeating the same procedure, the equations of motion of the whole mooring system comprised of all the mooring lines can be obtained.

5.6 Lumped Mass Model of the Bridle Configuration

The bridle mooring system description, properties, and quasi-static modeling were investigated earlier in Chapter 4. The lumped mass approach already developed for a single cable can be extended to model the dynamics of this configuration. The mooring line is modeled by 5 segments, as shown in Figure 5.3. Segments 1 and 2 represent the bridle, each of which is divided into N_{br} elements. Segment 3 represents the cable portion from the bridle connection to the suspension point of the clump mass and segment 4 is the remaining portion to the anchor point. The number of elements in segments 3 and 4 are N_u and N_l, respectively. The unstretched lengths of segments 1–4 are $L_{0\Delta}$, $L_{0\Delta}$, L_{0u} and L_{0l}, respectively, can be found in Table A.4 (n.b. $L_{0u} = s_1$ and $L_{0l} = L_{03} - s_1$). Segment 5 representing the clump weight and its suspension cable is comprised of 2 elements: the suspension cable is modeled as a single element with unstretched length L_{scu}, and the clump weight is also treated as a single element of unstretched length L_{0CL}.

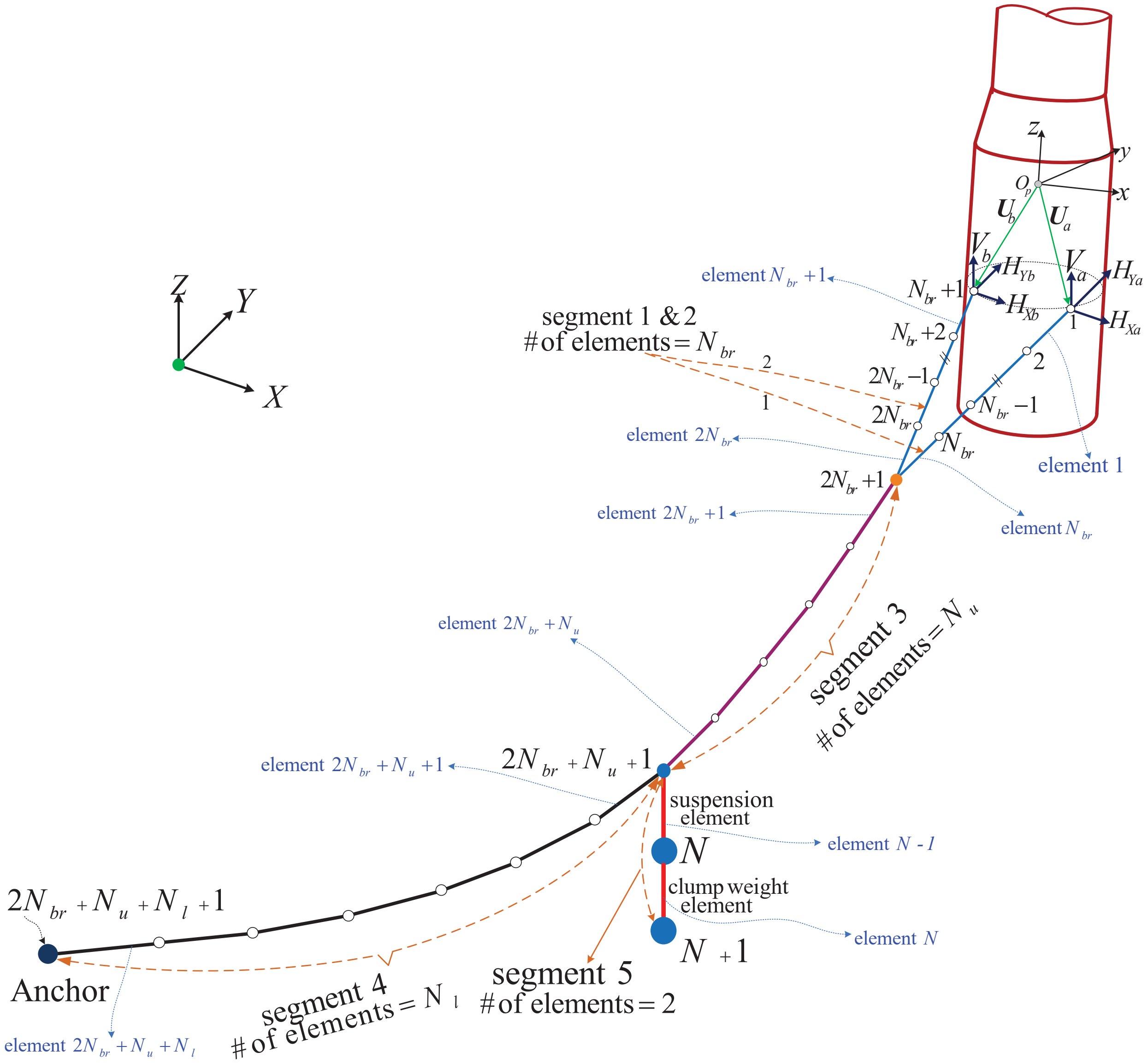

Figure 5.3: Lumped mass model of a bridle mooring system

The *element* indexing is ordered according to the order of segments, for example the index of the first element of segment 4 is $2N_{br} + N_u + 1$. The *node* indexing is illustrated in Figure 5.3. Node 1 represents the attachment point of segment 1 with the platform. The first node index of segment 2 is $N_{br} + 1$, and the nodes following (of segments 2, 3 and 4) are continuous and indexed sequentially to the anchor point (last node of segment 4). Segment 5 begins with the common node between segments 3 and 4, the following node continues the indexing of segment 4 such that the last two nodes represent the the clump weight element, as shown in Figure 5.3. The total number of elements and nodes are $N = 2N_{br} + N_u + N_l + 2$ and $N + 1$, respectively. It is then obvious that the equations of motion of the mooring line will be assembled for $N - 2$ nodes because the number of boundary nodes is 3.

The lumped internal and external forces acting on the line nodes are similar to Equation (5.22). However, calculating the forces acting on nodes $2N_{br} + 1$ and $2N_{br} + N_u + 1$, representing the bridle connection and common node among segments 3, 4 and 5, respectively, and as well as the last node are different.

$$\begin{aligned}
\mathbf{F}_{2N_{br}+1} =&(\mathbf{T}_{N_{br}} + \mathbf{T}_{2N_{br}} - \mathbf{T}_{2N_{br}+1}) + \tfrac{1}{2}(\mathbf{W}_{N_{br}} + \mathbf{W}_{2N_{br}} + \mathbf{W}_{2N_{br}+1}) \\
&+ \tfrac{1}{2}(\mathbf{H}_{e*,N_{br}} + \mathbf{H}_{e*,2N_{br}} + \mathbf{H}_{e*,2N_{br}+1}) + \tfrac{1}{2}(\mathbf{A}_{N_{br}} + \mathbf{A}_{2N_{br}} + \mathbf{A}_{2N_{br}+1}) \\
\mathbf{F}_{2N_{br}+N_u+1} =&(\mathbf{T}_{2N_{br}+N_u}) - (\mathbf{T}_{2N_{br}+N_u+1} + \mathbf{T}_{N-1}) + \tfrac{1}{2}(\mathbf{W}_{2N_{br}+N_u} + \mathbf{W}_{2N_{br}+N_u+1} + \mathbf{W}_{N-1}) \\
&+ \tfrac{1}{2}(\mathbf{H}_{e*,2N_{br}+N_u} + \mathbf{H}_{e*,2N_{br}+N_u+1} + \mathbf{H}_{e*,N-1}) \\
&+ \tfrac{1}{2}(\mathbf{A}_{2N_{br}+N_u} + \mathbf{A}_{2N_{br}+N_u+1} + \mathbf{A}_{N-1}) \\
\mathbf{F}_{N+1} =&\mathbf{T}_N + \tfrac{1}{2}\mathbf{W}_{CL} + \tfrac{1}{2}\mathbf{H}_{e*,N} + \tfrac{1}{2}\mathbf{A}_N
\end{aligned} \tag{5.26}$$

5.7 Static Solvers

Integrating the equations of motion of the lumped mass cable models requires proper initial conditions (ICs). An unrealistic choice of the ICs can lead to large startup transients in the simulation. It is usually considered best to use the cable equilibrium profile as the IC [120, 121].

Many techniques have been developed in the literature to solve this problem. Incremental methods [122] leads to a large system of nonlinear algebraic equations representing the equilibrium of the cable nodes, with a system size proportional to the cable discretization resolution. The dynamic relaxation approach [120, 122] uses the system dynamics to determine the static equilibrium allowing the system to settle to the equilibrium after the transient response decays. However, those techniques exhibit many deficiencies particularly in relation to their convergence capabilities. A review of these methods can be found in [120–122]. More recently, starting from the basic static principle of a two-force member, Masciola et al. [121] developed an efficient methodology to solve the problem. Their analysis reduces the size of system of equations to only 3, irrespective of the cable discretization resolution. However, this technique was developed for suspended cables. Adding the effect of the cable seabed reaction forces is challenging and adds more nonlinearity to the problem. A new approach is developed to solve the equilibrium of a cable while considering the cable-seabed reactions. This approach is also extended to similar problems of the bridle mooring system configuration.

5.7.1 Single cable

We will first consider the equilibrium of a suspended cable and then include the effect of the seabed. Consider the discretized cable depicted in Figure 5.4, the lumped mass weight in water of the interior nodes are $\breve{w} = w l_u$ while the exterior (boundary) node weight is $0.5\breve{w}$. The external load applied at the i-th node is ${}^{I}\mathbf{E}_i = [E_{X,i} \quad E_{Y,i} \quad E_{Z,i}]^T$. The stretched length of the i-th element is

$$L_i = l_{u,i}\left(1 + \frac{T_i}{EA}\right) = \sqrt{l_{X,i}^2 + l_{Y,i}^2 + l_{Z,i}^2} \tag{5.27}$$

where $T_i = \sqrt{H_{X,i}^2 + H_{Y,i}^2 + V_i^2}$, ${}^{I}\mathbf{r}_i - {}^{I}\mathbf{r}_{i+1} = [l_{X,i} \quad l_{Y,i} \quad l_{Z,i}]^T = L_i\,\hat{\mathbf{u}}_i$, $[H_{X,i} \quad H_{Y,i} \quad V_i]^T = T_i\,\hat{\mathbf{u}}_i$ and $\hat{\mathbf{u}}_i$ can be obtained from Equation (5.2) as

$$[s_{\theta_i}\, c_{\phi_i} \quad - s_{\phi_i} \quad c_{\theta_i}\, c_{\phi_i}]^T \tag{5.28}$$

From the cable geometry shown in Figure 5.4, the cable profile projected lengths, $\mathbf{r}_1 - \mathbf{r}_{N+1} = [l_X \quad l_Y \quad l_Z]^T$ can be obtained as

$$\begin{aligned}
l_X &= \sum_{i=1}^{N} l_{X,i} &&= \sum_{i=1}^{N} L_i \sin\theta_i \;\cos\phi_i &&= \sum_{i=1}^{N} l_{u,i} H_{X,i}\left[\frac{1}{\sqrt{H_{X,i}^2 + {}^{i}H_{Y,i}^2 + V_i{}^2}} + \frac{1}{EA}\right] \\
l_Y &= \sum_{i=1}^{N} l_{Y,i} &&= \sum_{i=1}^{N} -L_i \sin\phi_i &&= \sum_{i=1}^{N} l_{u,i} H_{Y,i}\left[\frac{1}{\sqrt{H_{X,i}^2 + {}^{i}H_{Y,i}^2 + V_i{}^2}} + \frac{1}{EA}\right] \\
l_Z &= \sum_{i=1}^{N} l_{Z,i} &&= \sum_{i=1}^{N} L_i \cos\theta_i \;\cos\phi_i &&= \sum_{i=1}^{N} l_{u,i} V_i\left[\frac{1}{\sqrt{H_{X,i}^2 + {}^{i}H_{Y,i}^2 + V_i{}^2}} + \frac{1}{EA}\right]
\end{aligned} \tag{5.29}$$

The i-th element tension components can be obtained from the equilibrium of the cable portion (bounded by nodes 1 and part of the respected element), as shown in Figure 5.4 (a).

$$H_{X,i} = H_X + \sum_{k=1}^{i} E_{X,k} \quad , \quad H_{Y,i} = H_Y + \sum_{k=1}^{i} E_{Y,k} \quad , \quad V_i = V - (i-0.5)\breve{w} + \sum_{k=1}^{i} E_{Z,k} \tag{5.30}$$

One can notice that the horizontal tension component of the elements ($H_{X,i}$ and $H_{Y,i}$) are constant along cable if $E_{X,i} = E_{Y,i} = 0$. It is assumed that $\mathbf{r}_1$ and $\mathbf{r}_{N+1}$ are known and then substituting Equation (5.30) into Equation (5.29) yields a system of 3 nonlinear algebraic equations with unknowns H_X, H_Y and V. This system can be solved using a Newton-Raphson method.

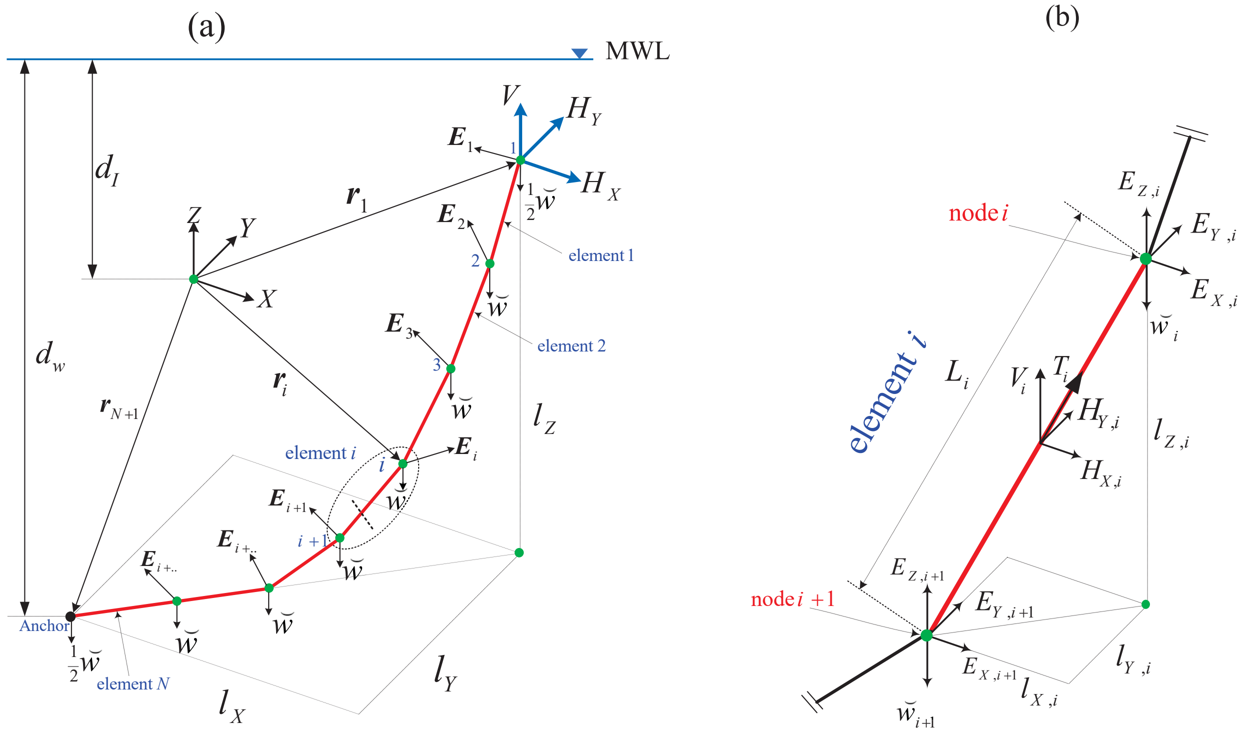

Figure 5.4: Lumped mass cable equilibrium

Once the system solved, substituting the solution back into Equation (5.30) yields the i-th tension components (T_i). Then, substituting the resulting tensions of each element into Equation (5.27) yields the stretched length (L_i). The Euler angles corresponding to the i-th element can be then obtained as

$$\begin{aligned}\theta_i &= \operatorname{atan2}(H_{X,i}, V_i) \\ \phi_i &= \begin{cases} \operatorname{atan2}(-H_{Y,i}, H_{X,i}/\sin(\theta_i)) & \text{for} \quad \cos(\theta_i) < \sin(\theta_i) \\ \operatorname{atan2}(-H_{Y,i}, V_i/\cos(\theta_i)) & \text{for} \quad \cos(\theta_i) \geq \sin(\theta_i) \end{cases}\end{aligned} \tag{5.31}$$

Now, the displacement of th i-th node can be determined as [121]

$$^{I}\mathbf{r}_{i+1} = {}^{I}\mathbf{r}_i - L_i\hat{\mathbf{u}}_i \quad , \quad i = 2, 3, \ldots, N+1 \tag{5.32}$$

The solution can be verified by calculating $\mathbf{r}_{N+1}$ and checking whether it matches the already known value (anchor point position).

The analysis developed above can be directly applied to solve for equilibrium positions of the cable nodes of a suspended cable by its own weight or if the external loads ($\mathbf{E}_i$) are well known. However, in many cases the external loads are unknown since they are function of the node position such as fluid– and soil–structure interaction forces. In this case, the solution for the cable equilibrium profile can be determined utilizing an iterative approach. For instance, if we consider the equilibrium of a cable subject to a steady current load, the equilibrium solution can be found iteratively as follows:

1. Solve for the equilibrium of nodes in the absence of the external loads (i.e. $\mathbf{E}_i = \mathbf{0}$).
2. Use the equilibrium positions of the cable nodes obtained from previous step to evaluate the drag forces and solve for the cable equilibrium, while including the external loads, to obtain another solution.
3. Repeat step 2 several times until the difference between the last successive solutions are within a certain satisfactory tolerance.

This iterative approach was also implemented in [121]. In fact, the iterative approach exhibits a quick convergence to an accurate solution for steady fluid drag problems. However, it was found to be numerically unstable for solving the equilibrium of a cable resting on the seabed.

A new solution of this problem is therefore developed based on the analysis formulated above (Equations (5.29) and (5.30)) to determine the equilibrium profile of the mooring line partially lying on the seabed as follows:

1. Substitute $E_{X,i} = 0$, $E_{Y,i} = 0$, and keep $E_{Z,i}$ as unknown into Equation (5.30) and substitute the resulting forms into Equation (5.29).
2. The seabed normal reaction force $E_{Z,i}$ can be formulated as

   $$E_{Z,i} = U_s(z_{sb,i})\, F_{Vsb,i} \tag{5.33}$$

   where U_s is a unit step function to constraint the seabed normal force to zero for nodes not in contact with the seabed, and $z_{sb,i} = (-r_{Z,i} + d_w - d_I)$, where $r_{Z,i} = r_{Z,i-1} - l_{Z,i-1}$ as shown in Figure 5.4, and $F_{Vsb,i}$ can be obtained from Equation (5.16)
3. The previous steps yield a system of $N + 3$ nonlinear algebraic equations which can be solved for H_X, H_Y, V and $E_{Z,i}$ using a Newton-Raphson method.

Solving the resulting system of algebraic equations above is quite complicated since the convergence to the solution is very sensitive to the choice of the initial guess which is attributed to the high seabed stiffness. This difficulty is circumvented by relaxing the soil shear strength at the seabed (S_{uo}) such that the system of equations is initially solved neglecting the seabed and the cable is suspended between the line ends. This solution is then used as an initial guess for the next iteration considering a very soft seabed (e.g. $S_{uo} = 10$). S_{uo} is then gradually increased for the next iterations and uses the last solution as an initial guess for the current iteration until reaching the actual S_{uo} value that yields the required solution. Figure 5.5 shows the cable equilibrium profile of the first and last iterations obtained using this approach. The minimum number of iterations required for a stable convergence to the solution using this approach is approximately $S_{uo}/20$.

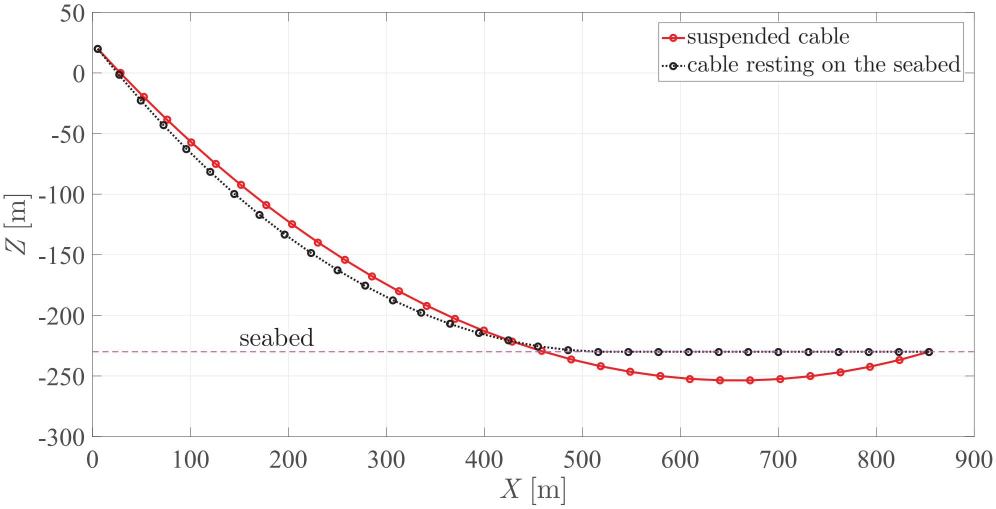

Figure 5.5: Equilibrium of a lumped mass cable, $N = 30$ elements, the fairlead and anchor point coordinates are (5.2,0,20) and (853.87,0,-230), respectively. $L_0 = 920.2$ m, $EA = 384243000$ N, and $w = 698.094$ N/m.

5.7.2 Bridle configuration

In general, the equilibrium positions of the bridle mooring line nodes (Figure 5.3) can be determined following a similar approach to that already developed for a single cable. However, the analysis becomes more complicated when dealing with multiple segments and clump weights. Another complexity also arises from different discretization resolutions of the segments

Prior to presenting the method of solution for the equilibrium configuration, the weight of cable nodes in fluid should be defined, which can be obtained based on the discretization scheme presented in Section 5.6 as

$$\breve{w}_i = \begin{cases} \frac{1}{2}\breve{w}_{br} & \text{for} \quad i = 1 \\ \breve{w}_{br} & \text{for} \quad 1 < i \leq N_{br} \\ \frac{1}{2}\breve{w}_{br} & \text{for} \quad i = N_{br} + 1 \\ \breve{w}_{br} & \text{for} \quad N_{br} + 1 < i \leq 2N_{br} \\ \breve{w}_{br} + \frac{1}{2}\breve{w}_u & \text{for} \quad i = 2N_{br} + 1 \\ \breve{w}_u & \text{for} \quad 2N_{br} + 1 < i \leq 2N_{br} + N_u \\ \frac{1}{2}(\breve{w}_u + \breve{w}_l) + W_{CL} & \text{for} \quad i = 2N_{br} + N_u + 1 \\ \breve{w}_l & \text{for} \quad 2N_{br} + N_u + 1 < i \leq 2N_{br} + N_u + N_l \end{cases} \tag{5.34}$$

where $\breve{w}_{br} = w\,L_{0\Delta}/N_{br}$, $\breve{w}_u = w\,L_{0u}/N_u$, $\breve{w}_l = w\,L_{0l}/N_l$. Solving for the equilibrium of this mooring line is then accomplished using the following steps

1. Substitute $l_X = l_{Xa}, l_Y = l_{Ya}, l_Z = l_{Za}$, $H_{X,i} = H_{Xa}$, $H_{Y,i} = H_{Ya}$, and $V_i = V_a - \sum_{k=1}^{i} \breve{w}_k$ into Equation (5.29) (summation limits are 1 and N_{br}) for the elements of segment 1.

2. Substitute $l_X = l_{Xb}, l_Y = l_{Yb}, l_Z = l_{Zb}$, $H_{X,i} = H_{Xb}$, $H_{Y,i} = H_{Yb}$, and $V_i = V_b - \sum_{k=N_{br}+1}^{i} \breve{w}_k$ into Equation (5.29) for the elements of segment 2, i.e. for $i = N_{br}+1, N_{br}+2, \ldots, 2N_{br}$.

3. For segment 3 and 4, substitute $l_X = l_{Xc}$, $H_{X,i} = H_{Xa} + H_{Xb}$, $H_{Y,i} = H_{Ya} + H_{Yb}$ into Equation (5.29) (summation limits are $2N_{br}+1$ and $2N_{br} + N_u + N_l$). These relations are obtained from the equilibrium condition of the connection node. Likewise, substitute $V_i = V_a + V_b - \sum_{k=1}^{i} \breve{w}_k + \sum_{k=1}^{i} E_{Z,k}$ into Equation (5.29)

4. The seabed normal reaction force $E_{Z,i}$ can be obtained as illustrated in step 2 (Equation (5.33)) in Section 5.7.1 for $i = 1, 2, \ldots, 2N_{br} + N_u + N_l$.

5. Substitute the right hand sides of the resulting equations generated from steps 1, 2, and 3 into the left hand sides of the following equations

$$
\begin{aligned}
l_{Xa} + l_{Xc} &= ({}^I\mathbf{r}_1 - {}^I\mathbf{r}_A)_X \quad , \quad l_{Xb} + l_{Xc} = \quad ({}^I\mathbf{r}_{N_{br}+1} - {}^I\mathbf{r}_A)_X \\
l_{Ya} + l_{Yc} &= ({}^I\mathbf{r}_1 - {}^I\mathbf{r}_A)_Y \quad , \quad l_{Yb} + l_{Yc} = \quad ({}^I\mathbf{r}_{N_{br}+1} - {}^I\mathbf{r}_A)_Y \\
l_{Za} + l_{Zc} &= ({}^I\mathbf{r}_1 - {}^I\mathbf{r}_A)_Z \quad , \quad l_{Zb} + l_{Zc} = \quad ({}^I\mathbf{r}_{N_{br}+1} - {}^I\mathbf{r}_A)_Z
\end{aligned}
\tag{5.35}
$$

   the right hand sides of Equation (5.35) are known from the boundary nodes (1, $N_{br}+1$ and $2N_{br} + N_u + N_l + 1$) positions.

6. The last two steps yield a system of $2N_{br} + N_u + N_l + 6$ nonlinear algebraic equations which can be solved for $H_{Xa}, H_{Xb}, H_{Ya}, H_{Yb}, V_a, V_b$, and $E_{Z,i}$ using a Newton-Raphson method.

Having solved the system of equations, we can substitute back into steps 1–3 to find V_i of each element of the mooring line segments and hence the tension and stretched length of each element. This allows evaluation of the Euler angles of each element using Equation (5.31) and eventually the nodes equilibrium positions utilizing Equation (5.32). Due to the discontinuity between the node N_{br} and $N_{br}+1$, Equation (5.31) should be applied for the continuous nodes i.e for $i = 1, 2, \ldots, N_{br}$ of segment 1, then apply it for the remaining nodes $i = N_{br} + 2, \ldots, 2N_{br} + N_u + N_l + 1$. Figure 5.6 illustrates the the equilibrium of the mooring line using the methodology discussed.

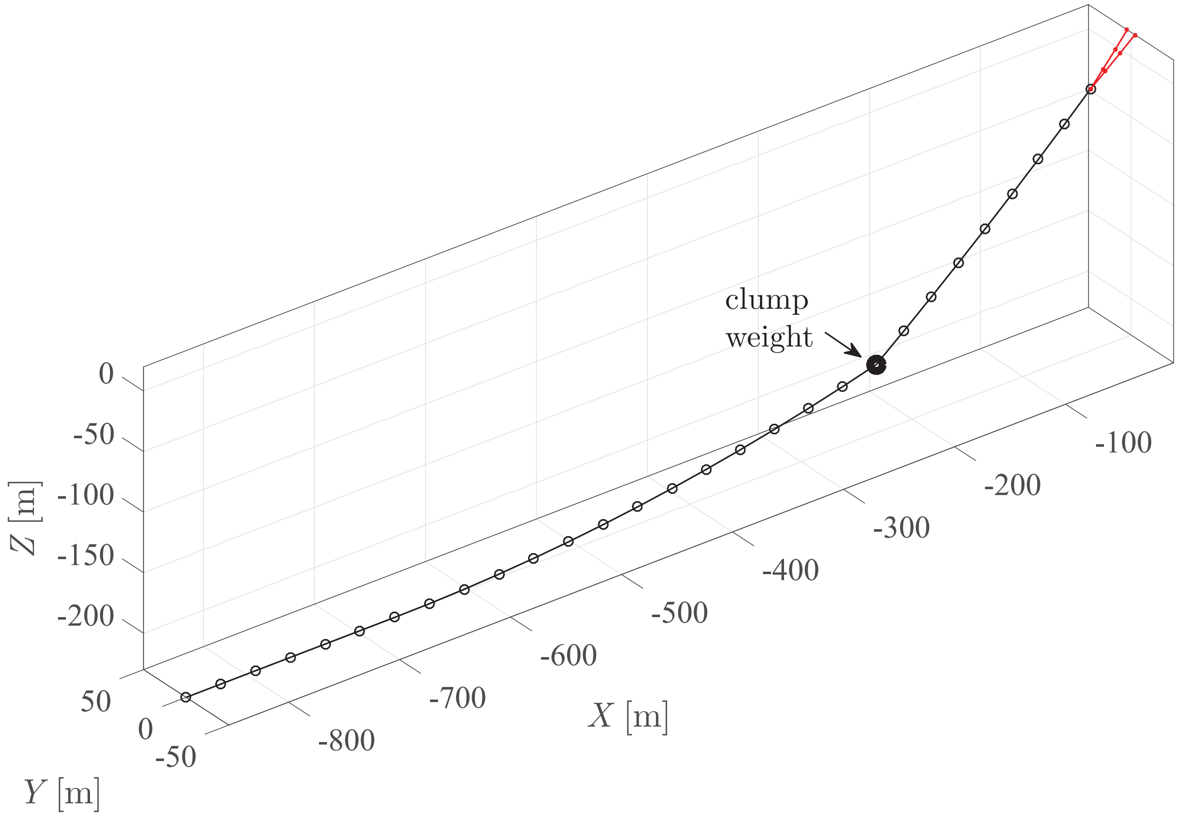

Figure 5.6: Equilibrium of a bridle mooring line, $N_{br} = 3$, $N_u = 8$, $N_l = 20$. The fairleads and anchor point coordinates are (-2.6000,4.5033, 20),(-2.6000,-4.5033, 20), and (-853.87,0, -230), respectively. $L_{0\Delta} = 50$ m, $L_{03} = 901.9772$ m, $EA = 384243000$ N, and $w = 353.2$ N/m

5.8 Mooring Loads for the Equations of Motion

The mooring force ($\mathbf{F}_{mor}$) and moment around the origin of the platform frame ($\mathbf{M}_{mor}$) are evaluated for the two the different mooring system configurations based on the lumped mass cable model. These loads are part of the right hand side of the equations of motion of the FOWT structure developed earlier in Chapter 2. For the single line mooring system configuration, these loads can be formulated as

$$
{}^{p}\mathbf{F}_{mor} = -\sum_{j=1}^{3} {}^{p}\mathbf{T}_{1}^{(j)} \quad , \quad {}^{p}\mathbf{M}_{mor} = -\sum_{j=1}^{3} {}^{p}\mathbf{r}_{POp}^{(j)} \times {}^{p}\mathbf{T}_{1}^{(j)} \tag{5.36}
$$

where the $\mathbf{T}_{1}^{(j)}$ denotes the tension force of the first element of the j-th mooring line (j=1,2, and 3), respectively. Similarly, these loads can be formulated for the bridle mooring system as

$$
\begin{aligned}
{}^{p}\mathbf{F}_{mor} &= -\sum_{j=1}^{3} \left({}^{p}\mathbf{T}_{1}^{(j)} + {}^{p}\mathbf{T}_{N_{br}+1}^{(j)}\right) \\
{}^{p}\mathbf{M}_{mor} &= -\sum_{j=1}^{3} \left({}^{p}\mathbf{U}_{1}^{(j)} \times {}^{p}\mathbf{T}_{1}^{(j)} + {}^{p}\mathbf{U}_{2}^{(j)} \times {}^{p}\mathbf{T}_{N_{br}+1}^{(j)}\right)
\end{aligned} \tag{5.37}
$$

One can compare Equation (5.36) with Equations (4.5) and (4.6) in which the mooring loads were computed using the quasi-static approach. As well, further comparison can be made between Equation (5.37) and Equations (4.19) and (4.20) for the multi-segmented configuration.

Chapter 6

VALIDATION AND CASE STUDIES

The previous chapters presented comprehensive high-fidelity multibody dynamic modeling methodologies for the FOWT system structural components. In addition, the external loads exerted on the system including hydrostatic, hydrodynamic, aerodynamic and mooring loads were also characterized. The present chapter combines the methodologies of the previous chapters to build a coupled simulation of the FOWT system under consideration. A series of simulations using different combinations of the component dynamic models, mooring configurations and cable models are presented for the following purposes:

1. Validating the developed FOWT dynamic models against the most popular FOWT simulation tools. The validation is performed by simulating the system response to defined environmental disturbances referred to as *load cases*.
2. Understanding the system dynamic behavior using the following case studies:
    (a) Investigating the influence of the tower flexibility on the system dynamics by comparing the dynamics responses of the FOWT obtained using the rigid and flexible dynamic models.
    (b) Discussing the influence of the mooring system configuration on dynamic response of the system by comparing responses of the single and bridle mooring system configurations.
    (c) Investigating the influence of the rotor gyroscopic effect on the system dynamics.
    (d) Exploring the influence of cable dynamics on the rigid and elastic motions of the structure as well as the mooring lines tensions by comparing the system responses obtained utilizing the quasi-static and lumped mass cable models.

6.1 Numerical Implementation

A large high-fidelity simulation code has been developed and implemented, structured as shown in Figure 6.1, to predict the dynamic performance of the FOWT system. The code is developed using MATLAB®, and allows easy selection of component models and environmental conditions.

Besides the rigid and flexible tower models, four cable models are developed: quasi-static single, quasi-static bridle, lumped mass single, and lumped mass bridle cable models. In terms of execution time, the fastest simulation is attained by a rigid body tower model coupled to a quasi–static cable model. By contrast, simulating the system response via flexible dynamic and lumped mass cable models is computationally the most expensive solution. The bridle configuration also requires higher computational effort than the single configuration. As well, computing the wave kinematics and wave loads exerted on the platform and cable (in the case of the lumped mass model) for regular waves requires considerably less computational effort compared to the irregular wave case. Consequently, the simulation setup should be chosen on the basis of the required simulation outcomes and execution time.

The equation of motions of the rigid and flexible multibody dynamic models are obtained via a MATLAB® symbolic manipulation code. This code is constructed based on the formulations discussed in Chapter 2. The implementation of the dynamic model follows the flowchart shown in Figure 6.1. The main code (in grey) allows the selection of the equations of motion of the rigid or flexible dynamic model. The hydrostatic, hydrodynamic, aerodynamic, quasi-static mooring model codes are called by the main code to determine their respective external forces and moments. The differential equations representing the equations of motion are subsequently integrated numerically using the *ode15s* solver which is the most accurate MATLAB® stiff ODE solver [123]. The resulting solution is also fed back to the external loads codes since these loads are functions of the system motion.

If cable dynamics is to be considered, the quasi-static cable model is disabled and the equations of motion of the lumped mass cable model are then incorporated into the system equations of motion. These of equations of motions of the structure and cables are coupled through the tension loads of the first elements of the cable segments attached to the platform,

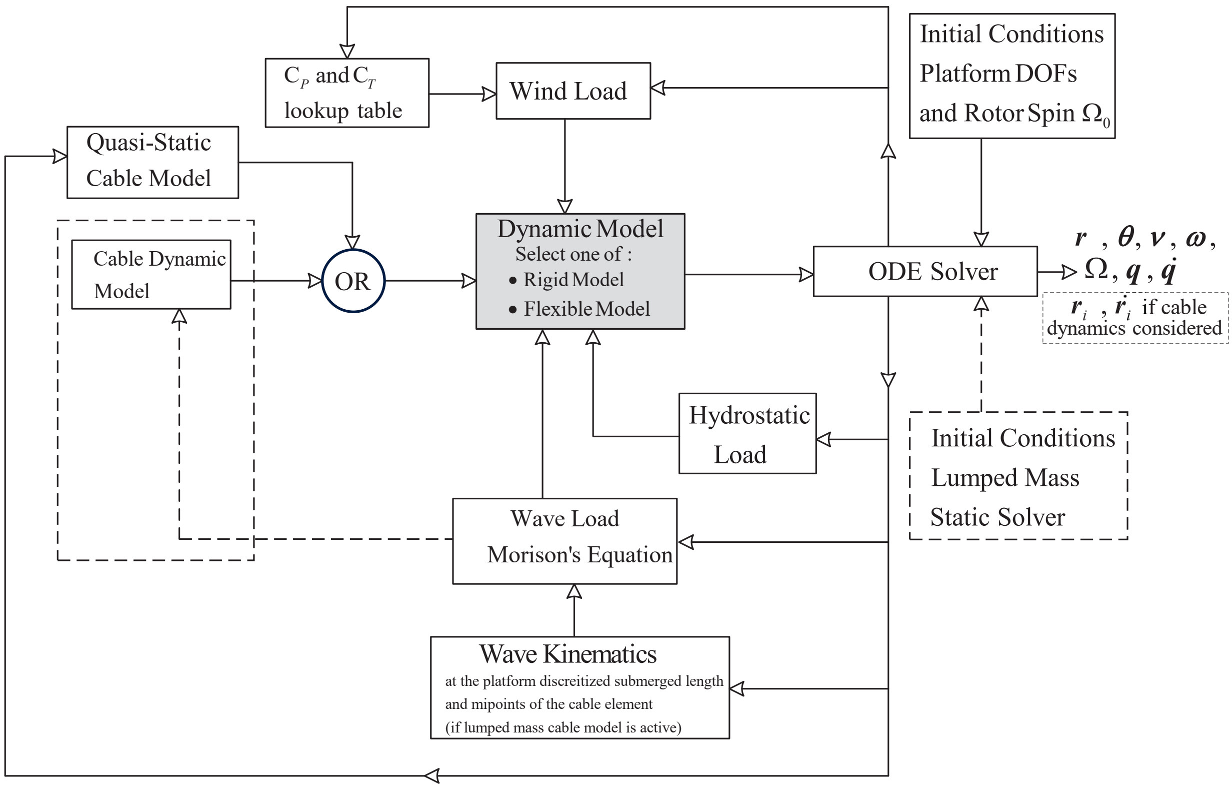

Figure 6.1: Structure of the simulation code of the FOWT dynamics

as discussed in Section 5.8. The wave load code then computes the hydrodynamic loads on the cable elements and on the platform. In the ODE solver, the initial conditions of the cable lumped masses are initialized using the lumped mass static solver (developed in Chapter 5).

6.1.1 Limitations

As demonstrated earlier in Chapter 2, the present simulation utilizes Morison's equation to characterize the hydrodynamic loads. This approach ignores the effects of radiation damping, wave diffraction and second order hydrodynamic loads which could excite the lower resonant frequencies of the system [16]. As well, it neglects the influence of the VIV which can be considerable when the substructure is subject to steady current or combined current and wave loads. All these aspect could reduce the accuracy of the predicted hydrodynamic loads exerted on the platform and mooring lines particularly in low and moderate fluid speeds which may affect the resulting system response.

The present simulation also ignores the blade flexibility which could influence the system dynamics, particularly the tower elastic motion response when the rotor experiences severe aerodynamic loads at which interaction between the blade and tower elastic motions can be evident.

6.2 Validation

The design of reliable FOWT systems demands trustworthy simulation tools capable of predicting the dynamic response of the structure [5, 69]. A well-known code-to-code comparison study was performed as a part of the Offshore Code Comparison Collaboration (OC3) project also under the Wind Task 23 of the International Energy Agency (IEA) [5]. Extensive comparisons of the simulation results obtained from different simulation tools were performed. These results were generated by many participants in the project from different institutions and countries utilizing different simulation tools. The dynamic response of these codes were examined under particular wind and wave load conditions, referred to as *load cases*, to allow for consistent comparisons among the codes results. The results of this large code-to-code comparison project were thoroughly investigated in [5, 124]. The present simulation results are therefore compared with those obtained from these codes for the four load cases in Table 6.1 to assess the validity of the current model. It is worth noting that the relevant simulation results of these simulation tools are only available for the listed load cases in Table 6.1. As well, some codes were not able to simulate all these load cases or to predict certain dynamic outputs such as the tower elastic motion because of their modeling limitations.

Table 6.1: Specifications of the load cases [5]

Load case	Wind condition	Wave condition	Analysis type
1.2	None	None (still water)	Eigen frequencies
1.4	None	None (still water)	Free decay test
4.2	None	Jonswap $H_s = 6$ m, $T_p = 10$ s	Power spectra
5.1	Steady wind speed $U = 8$ m/s	Regular wave, $\mathcal{H}_a = 6$ m, $T = 10$ s	Time series

It is also worth to noting that all the validation load cases are based on the single mooring configuration augmented with additional yaw mooring stiffness $K_{add} = 98.34 \times 10^6$ N.m/rad [6]. To consider this effect, the moment exerted by the mooring line tension about the origin of the body frame for the single configuration, previously presented in Equation (4.6), is modified as

$$ {}^{p}\mathbf{M}_{mor} = \sum_{i=1}^{3} {}^{p}\mathbf{r}_{POp}^{(i)} \times {}^{p}\mathbf{T}^{(i)} - K_{add} \left[0 \quad 0 \quad \psi\right]^{T} \tag{6.1} $$

6.2.1 Load case 1.2

Table 6.2 compares the system eigen frequencies obtained from present model with those reported from other simulation tools. In general, the results of all codes agree reasonably well. However, the eigen frequencies of the platform roll and pitch obtained from HAWC2 are higher than their counterparts from the other codes. The present code results agree well with most codes particularly FAST, Bladed, 3DFloat and SIMO. The 1st tower twist eigen frequency predicted by the present code could not be compared with any of the other codes because they were not reported in [5] although the twist DOF is considered in HAWC2 and Bladed codes. It is worth noting that FAST, Bladed and HAWC2 codes include additional eigenmodes associated with rotor blade flexibility, that are not presented here since the present code assumes the rotor to be a rigid body.

Table 6.2: System eigen-frequencies (Hz)

Eigen-mode	Present	FAST NREL	Bladed	HAWC2	3DFloat	Simo	SESAM /DeepC
Surge	0.00800	0.00805	0.0080	0.00768	0.00803	0.00802	0.00869
Sway	0.00800	0.00805	0.0120	0.00773	0.00803	0.00817	0.00800
Heave	0.03294	0.03243	0.0330	0.03237	0.03300	0.03246	0.03180
Roll	0.03329	0.03424	0.0317	0.04530	0.03210	0.03338	0.03050
Pitch	0.03332	0.03426	0.0317	0.04518	0.03210	0.03338	0.03050
Yaw	0.12111	0.12103	0.1220	0.10757	0.14000	0.12180	0.13300
1st (u_1)	0.48845	0.47320	0.4600	0.47961	0.47300	-	-
1st (u_2)	0.48141	0.45748	0.4500	0.48180	-	-	-
1st twist (φ)	1.84150	-	-	-	-	-	-

6.2.2 Load case 1.4 (free decay test)

This load case represents a free decay test whereby the platform is released from a specified non-equilibrium initial pose in still water and without wind. The decay tests separately excite the platform surge, heave, pitch and yaw displacements. These tests are quite important to examine the hydrodynamics, hydrostatic and mooring models functionality which are the main sources of stiffness and damping in the system. In the results presented in [5, 124], the structure is assumed to be a rigid multibody system i.e. the tower and blades flexibilities are ignored. In the present work, both the rigid and flexible models are used to perform this test. In the case of the flexible model, this is achieved by imposing an extremely large Young modulus (E) and modulus of rigidity (G) of the tower, hence the tower can behave nearly as a rigid body, with negligible flexible deflections. The simulation results from both dynamic models are found to be identical.

The decay test results are illustrated in Figure 6.2. Only the response of the perturbed platform DOF is presented here for brevity. Figure 6.2 (a) shows the surge decay responses due an initial perturbation of 21 m in surge. Our code is in excellent agreement with all the simulation tools particularly FAST and HAWC2. The present code also exhibits an excellent

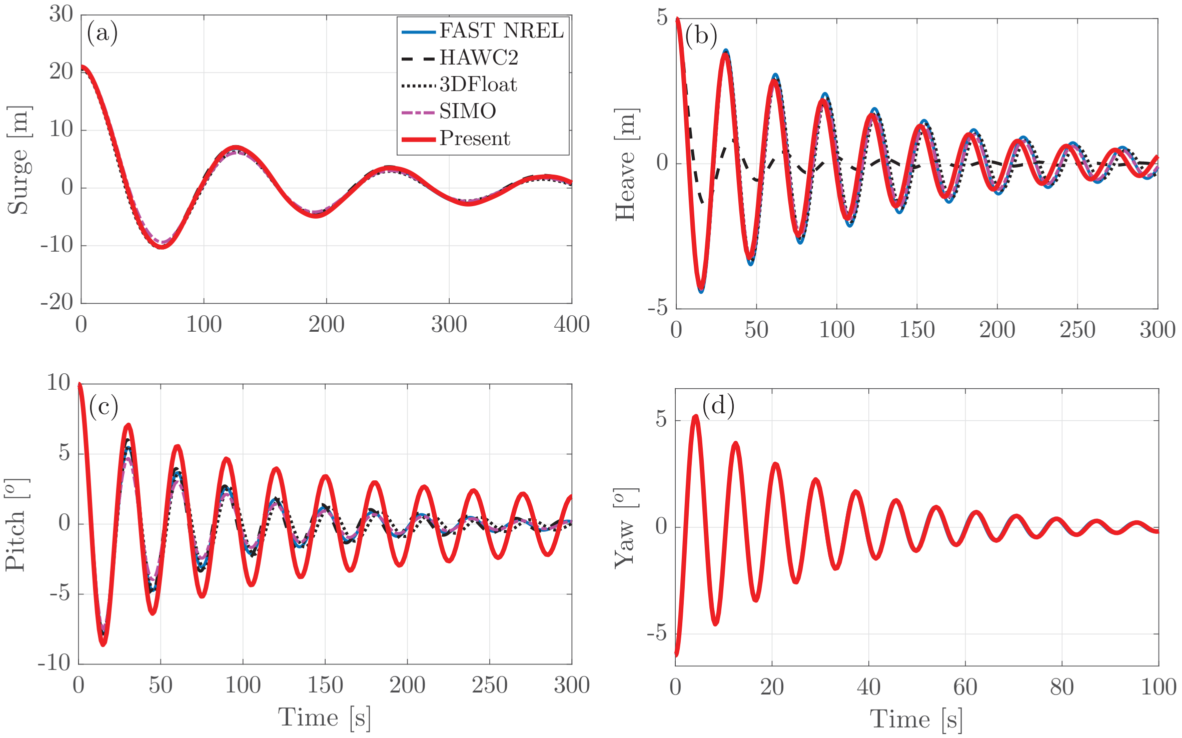

Figure 6.2: Free decay test of load case 1.4 due to: (a) initial perturbation of 21 m in surge; (b) initial perturbation of 5 m in heave; (c) initial perturbation of 10^o m in pitch; (d) initial perturbation of 6^o in yaw.

agreement with the reported results in the heave decay response (excited by a 5 m heave initial condition). The HAWC2 code predicts larger damping than the other codes, as seen in Figure 6.2 (b). As well, the present code shows good agreement with all the codes in the pitch decay (excited by a 10° pitch) response with identical peak locations but with less damping than the other codes, as seen in Figure 6.2 (c). This is attributed to the fact that the present code ignores the hydrodynamic radiation damping while this effect is considered in the other codes. The yaw decay response is almost identical for all codes, as illustrated in Figure 6.2 (d).

6.2.3 Load case 4.2

In this simulation scenario, the FOWT dynamic response is evaluated under excitations arising from an irregular wave, but without wind. This implies that the wind turbine rotor is parked (not spinning i.e. $\Omega = 0$). The wave kinematics are characterized by the Jonswap spectrum [96, 97] with $H_s = 6$ m, peak period $T_p = 10$ s, and a heading angle $\beta_w = 0$ (i.e.

the waves are propagating along the X-axis of the inertial frame). The power spectra of the platform displacements and tower tip fore-aft deflection (u_1 at $z = l$) are compared with the corresponding results of the simulation tools, as illustrated in Figure 6.3. In general, the present code results are in very good agreement with those obtained from the simulation tools. The results of all the codes conform well at the wave peak frequency (0.1 Hz).

The surge PSD exhibits two peaks corresponding to the surge and pitch natural frequencies at 0.008 Hz and 0.034 Hz, respectively, as seen in Figure 6.3 (a). The first peak is evident at the surge natural frequency for the present, SIMO and DeepC codes while the peak is offset slightly for the FAST code at 0.01 Hz. The heave PSDs of all codes agree well with minimal deviations in the vicinity of the heave natural frequency (0.032 Hz), as depicted in Figure 6.3 (b). All the codes are in excellent agreement in their pitch PSD predictions except Bladed, as illustrated in Figure 6.3 (c). The fore-aft (u_1) PSD results are presented in Figure 6.3 (d) for the present code, FAST, and Bladed codes since the remaining codes (DeepC and Simo) do not consider the tower elasticity. The results of the present and FAST codes are in excellent agreement while Bladed shows a reasonable agreement with the other

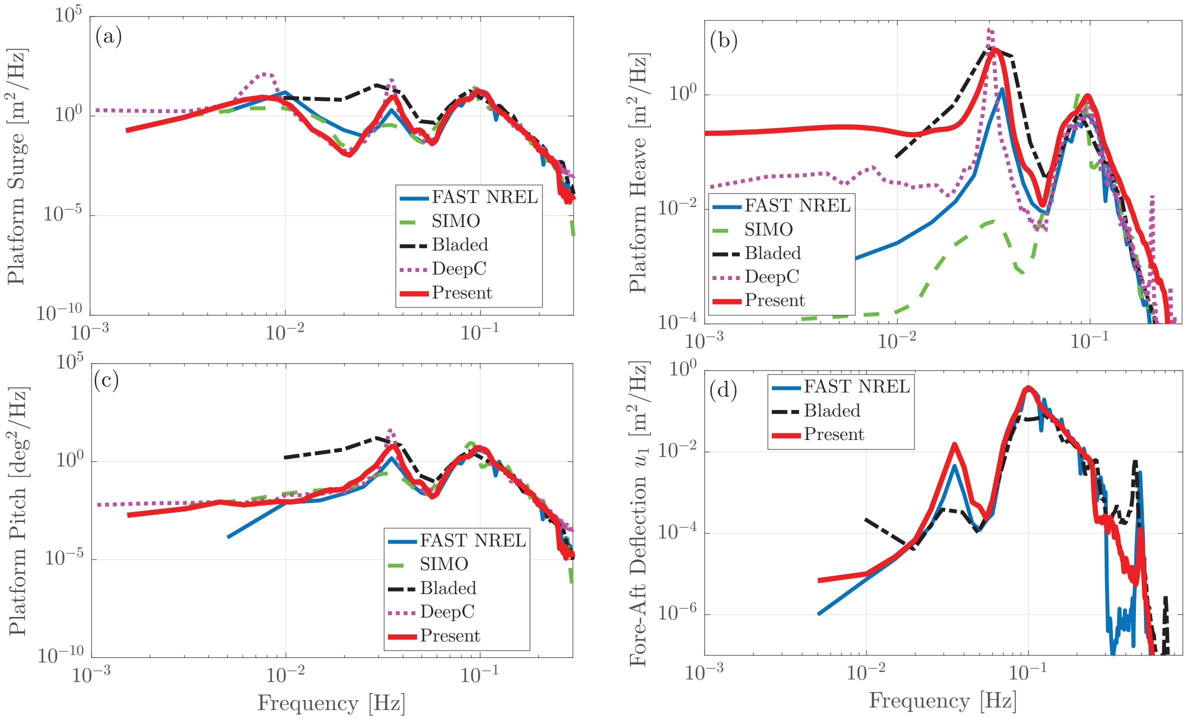

Figure 6.3: Power spectra of: (a) platform surge, (b) platform heave, (c) platform pitch, and (d) fore-aft deflection (u_1 at the tower tip) for load case 4.2.

codes. Dominant peaks are visible close to the pitch natural frequency and the first fore-aft tower bending natural frequency (0.48 Hz).

6.2.4 Load case 5.1

In this simulation scenario, the FOWT dynamic response is evaluated under excitations arising from a regular wave and steady uniform wind. The wave height is $\mathcal{H}_a = 6$ m and the period is $T = 10$ s, while the wind speed is $U = 8$ m/s. The characteristics of the steady-state harmonic time response of the system are relevant for this load case. The time response of the platform displacements, and fore-aft tower tip deflection responses are displayed in Figure 6.4, while the rotor speed response is presented in Figure 6.5. The surge response of the present code agrees well with other codes, particularly FAST, as shown in Figure 6.4 (a). The HAWC2 surge response is inconsistent with the other codes which likely implies an incorrect result, as discussed in [5]. Some discrepancies in the mean value and phase can be observed in the responses, while the amplitudes and periods of oscillations agree well. Figure 6.6 summarizes the peak-to-peak response amplitudes shown in Figures 6.4 and 6.5. Generally, all the codes relatively agree well in the amplitudes of oscillations. However, the Bladed code yields relatively larger amplitudes in surge and heave DOFs while it underestimates the amplitudes of fore-aft bending deflection.

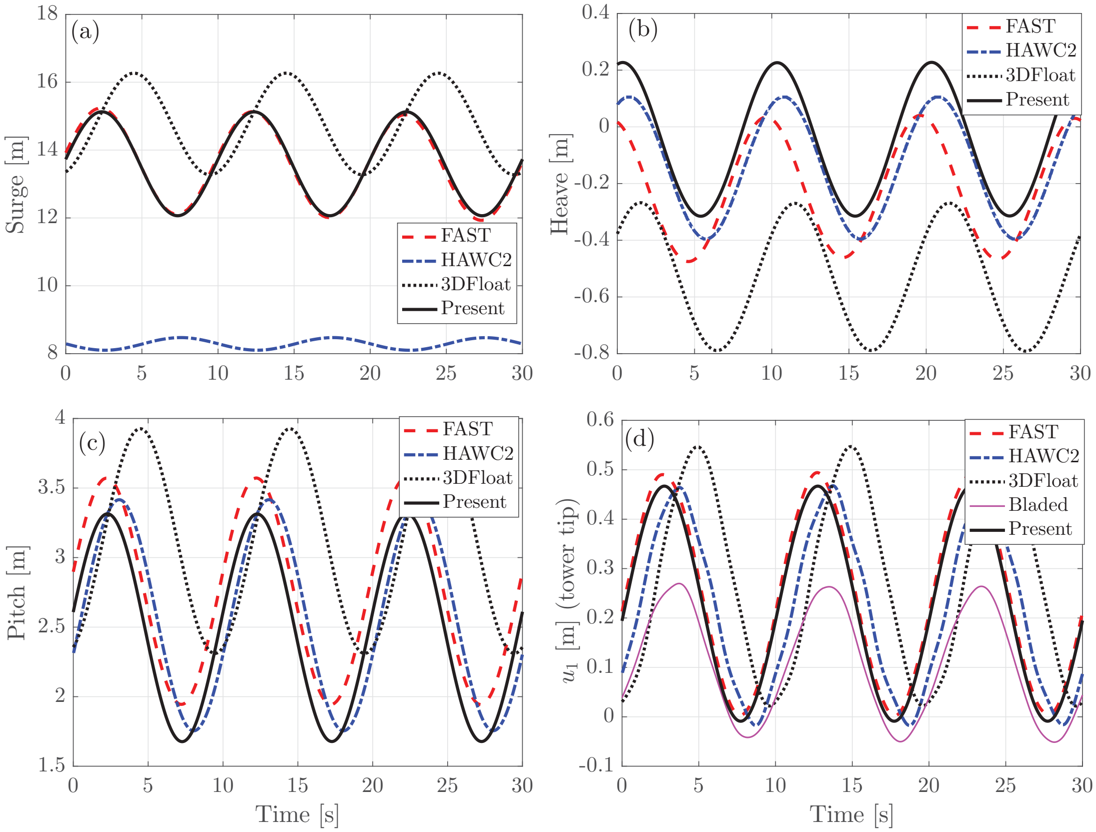

Figure 6.4: Steady-state response of: (a) platform surge, (b) platform heave, (c) platform pitch, and (d) fore-aft deflection (u_1 at the tower tip) for load case 5.1

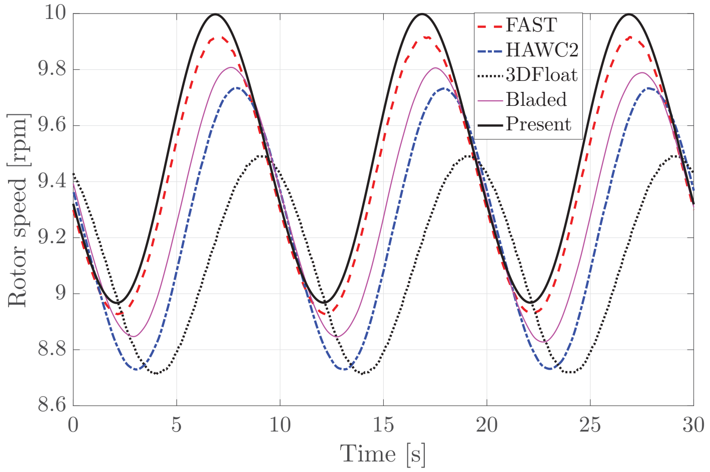

Figure 6.5: Steady-state response rotor spin speed for load case 5.1

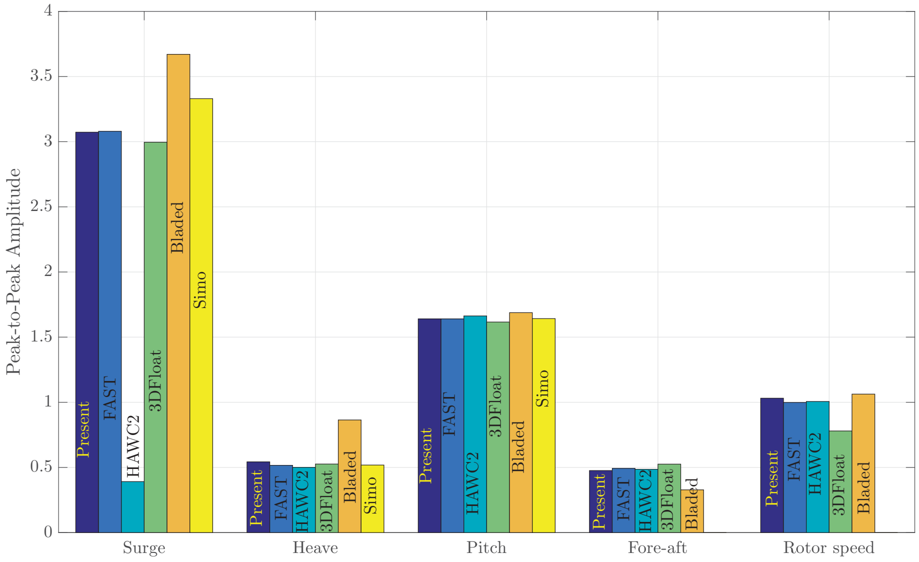

Figure 6.6: Peak-to-peak amplitudes for load case 5.1

6.3 Case Studies

We now proceed to use the simulation under different scenarios, such as varying model types and different system designs. The dynamics behavior of the system is closely related to the system stiffness, and material and inertial properties of the structure components (platform, tower, rotor blades, mooring system,.., etc). On the other hand, different modeling approaches used to characterize the system dynamics, environmental, and mooring loads may vary in their predictions of the system dynamic response. The exploration of the influence these factors on the system dynamics is quite important to allow efficient system analysis and design. Although there are many parameters and design aspects that can be studied, the discussion will be focused on the following main topics: tower flexibility; mooring configuration; rotor gyroscopic effect; and cable dynamics.

6.3.1 Tower flexibility (rigid vs. flexible)

The influence of the tower flexibility on the system dynamics is investigated by comparing the dynamic response of the rigid and flexible dynamic models developed in Chapter 2 under identical environmental loads, mooring system configuration and cable modeling approach. The quasi-static cable model of the single mooring system configuration (with K_{add}) is chosen to determine the mooring system loads. The simulations are performed assuming the system is subject to a steady wind speed ($U = 10$ m/s) and irregular water wave with heading angle $\beta_w = 30^o$. The wave kinematics are characterized by a Jonswap spectrum with $H_s = 11$ m, and $T_p = 14$ s.

The comparisons of the platform displacements time responses and rotor spin speed response obtained from the rigid and flexible models are displayed in Figures 6.7 and 6.8, respectively. The simulation results of the rigid model are in good agreement with the those obtained from the flexible model particularly in the surge, sway, heave, roll and pitch responses as well as the rotor spin rate response.

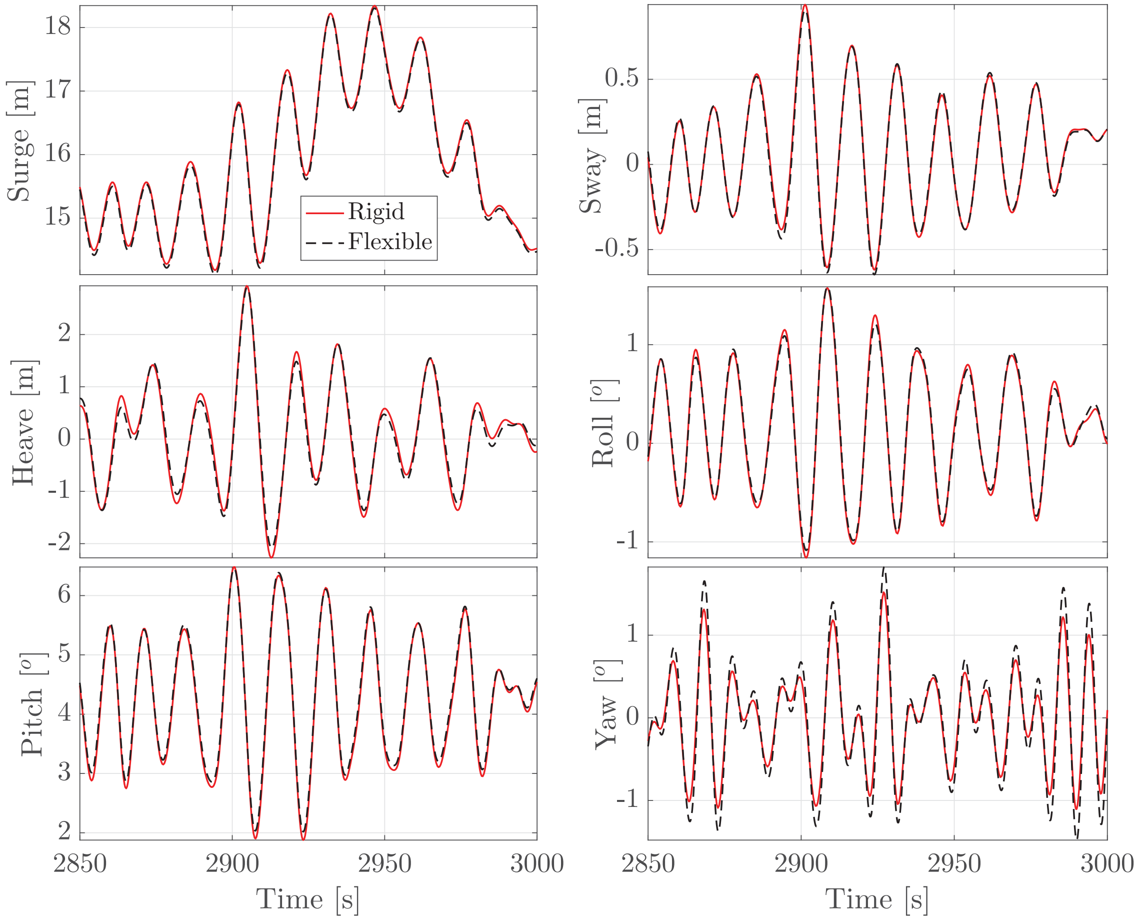

Figure 6.7: Platform displacements responses of the rigid and flexible models

In general, the results show that the tower flexibility does not significantly affect the platform displacements responses except the yaw. One important reason for this is that the mass of the Rotor Nacelle Assembly (RNA) is approximately 2.5% of the equivalent platform mass which is relatively very small. As well, large flexural and torsional stiffnesses of the tower yield small elastic deflections compared to the rigid body displacements.

The flexible model yields larger yaw response, as illustrated in Figure 6.7. This could be attributed to gyroscopic moments induced by the tower elastic rotations. This effect is more prominent in yaw since the the damping and mass moment of inertia of the platform in the yaw mode are the least among the platform DOFs. Moreover, due to platform slenderness, the added inertia of the platform in yaw is zero. This makes the platform yaw DOF is more responsive to small disturbances compared to the remaining platform DOFs.

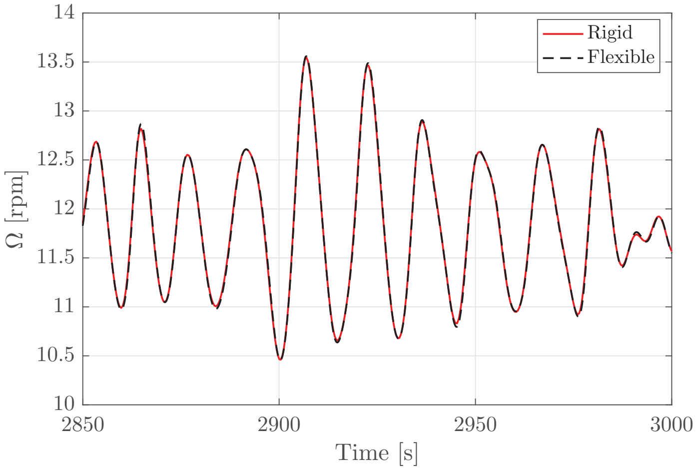

Figure 6.8: Rotor spin response as obtained from the rigid and flexible dynamic models

The tower tip bending deflection of the fore-aft (u_1) and side-side (u_2) and tower twist responses are illustrated in Figure 6.9. The fore-aft bending deflection is larger than that the side-side counterpart due to the RNA center of gravity offset from the tower tip center

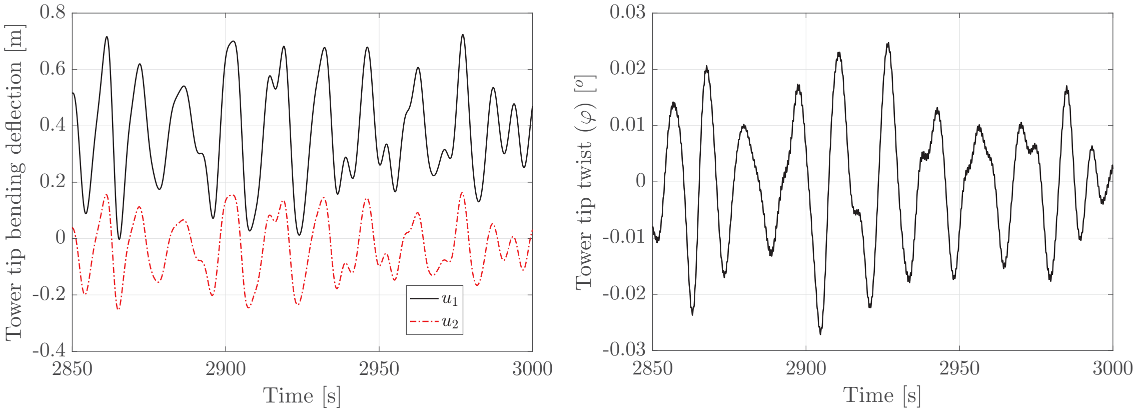

Figure 6.9: Tower tip elastic deflections

which yields a large bending moment leading to a higher fore-aft deflection. As well, the wave load is mainly acting along the $X-$axis exciting the fore-aft elastic motion more than the side-side motion. The tower twist response is extremely small, with amplitudes of oscillations less than 0.03°.

The platform displacements PSDs obtained from the rigid and flexible models are compared in Figure 6.10. The results of the two models agree well particularly at frequencies below 0.3 Hz while the flexible model shows a higher energy contents above that frequency. This is attributable to the flexible motions that are excited at their resonance frequencies which are much higher than those of the rigid body motion. All the PSD plots show a dominant peak at the wave spectral peak frequency (≈0.07 Hz). The PSD plots obtained using the flexible model exhibit peaks corresponding to the first mode of bending elastic motion at

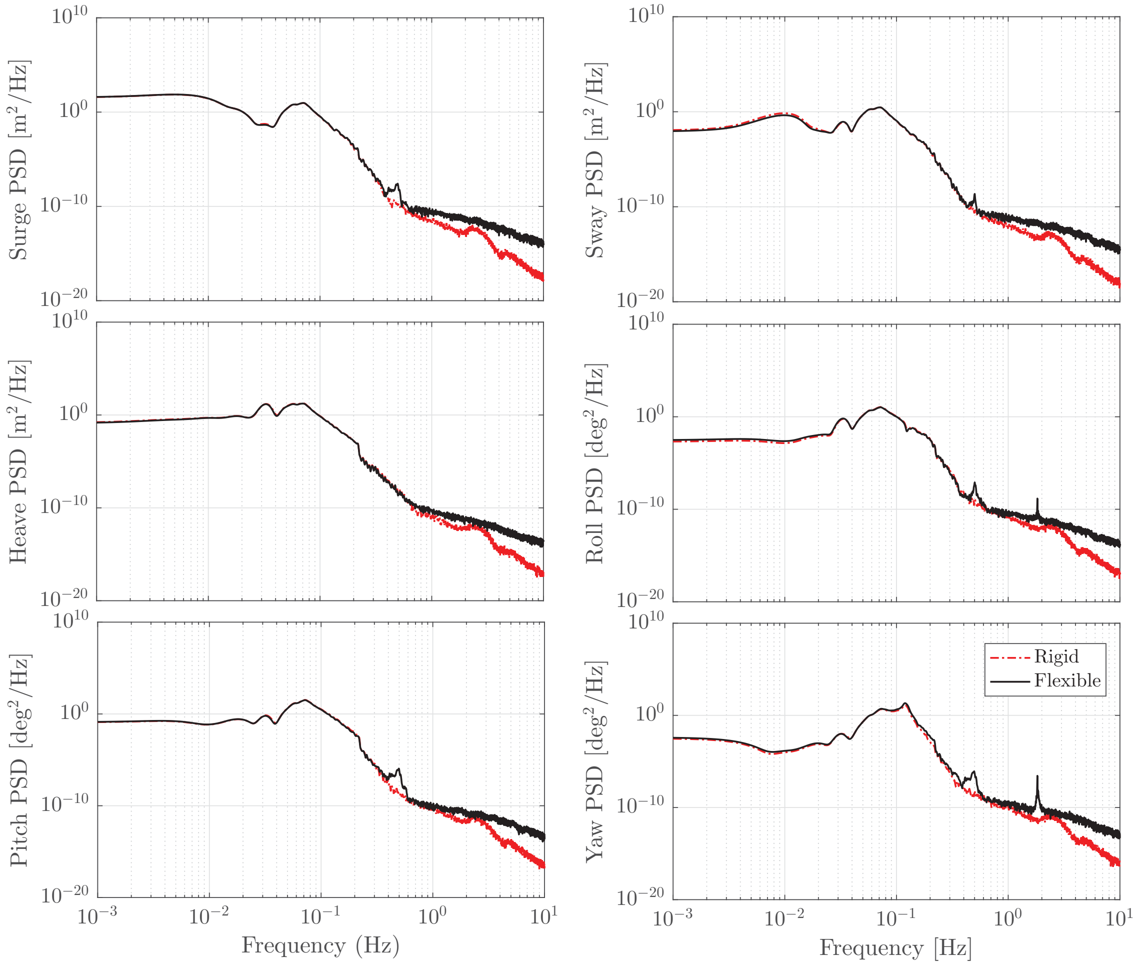

Figure 6.10: Platform DOFs PSDs

0.49 Hz. As well, another dominant peak at 1.84 Hz is also visible which corresponds to the 1st mode of the tower twist elastic motion. The peaks associated with resonant frequencies of the elastic motions are also evident in the PSD plots of the elastic motions, shown in Figure 6.11.

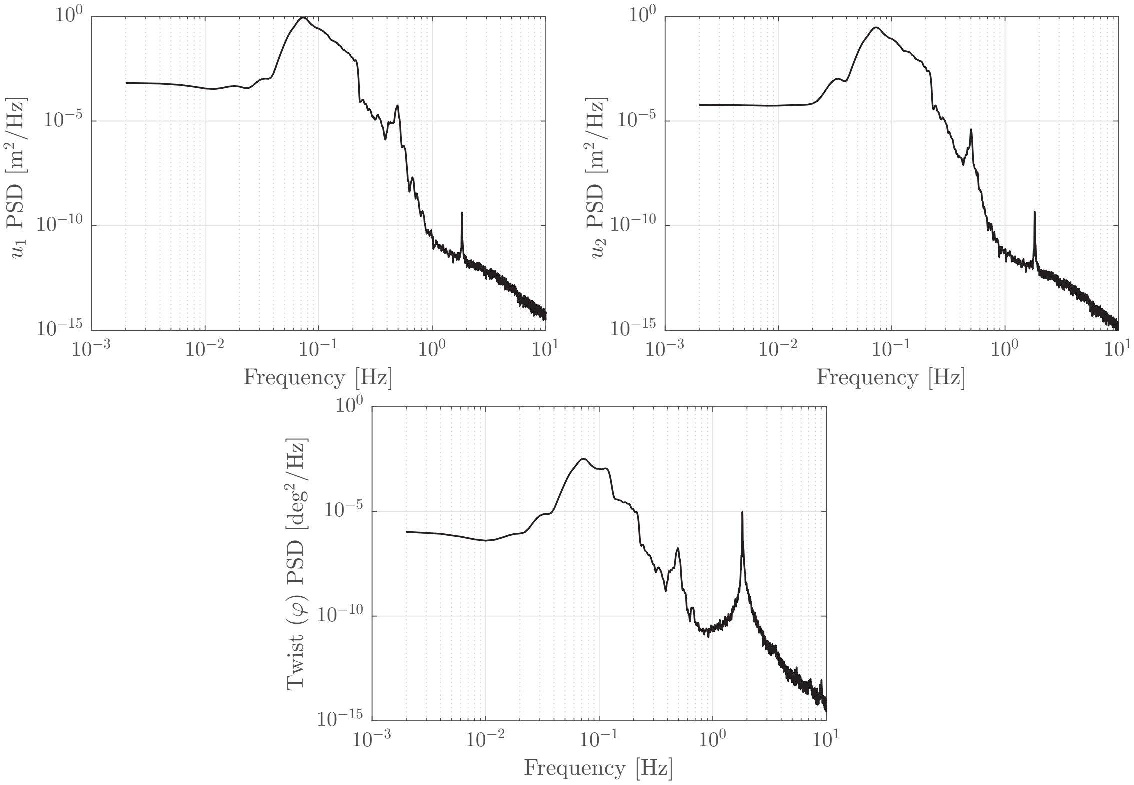

Figure 6.11: Tower tip elastic deflections PSDs

6.3.1.1 Tower twist

The high tower twist natural frequency (1.84 Hz) is far outside the water wave band frequency (0.04–0.22 Hz). Therefore, the tower twist is not significantly excited by the wave loads. As well, this mode is not directly excited by aerodynamic and hydrodynamic external moments since they are acting in directions normal to the tower twist axis. This results in minimal response as seen in Figure 6.9. Likely for these reasons, tower twist is not considered in most the simulation tools used for the FOWT dynamic simulation.

Moreover, we found that the dynamic simulation without tower twist is approximately 3 times faster than when it is considered, so that ignoring the twist DOF result in a much faster simulation. We also verified that neglecting the tower twist DOF does not affect the platform displacements nor the tower bending responses. Based on this, we chose to ignore the tower twist DOF for the remaining simulations of this chapter.

6.3.2 Mooring system configuration

Two mooring system configurations have been previously discussed, single and bridle. Moreover, the lines tensions of each of these configurations can be found using the quasi-static and lumped mass cable models developed earlier. Due to the differences between these configuration, the resulting restoring loads obtained from these configurations are different.

In reality, the Hywind prototype and the Hywind pilot project to be constructed [125] include a bridle mooring configuration. However, most dynamic analyses of the OC3-Hywind FOWT available in literature used a simplified single configuration augmented with an additional yaw stiffness to avoid the complexity of modeling the bridle configuration with suspended clump weights. This thesis has presented a new cable model that considers the bridle configuration, and the objective of this case study is to compare the dynamic behavior of the system when using the simplified single and the bridle configurations.

The system stiffness of a FOWT is due to a combination of the mooring system and the hydrostatics. Thus, the impact of the mooring configuration on the system stiffness should consider both effects. Table 6.3 illustrates the contribution of the hydrostatic and mooring stiffnesses to the system stiffness by comparing the diagonal stiffness coefficients from both sources. The hydrostatic stiffness coefficients are computed using the approach developed in Chapter 3. The mooring stiffness coefficients of the single configuration is determined using the expressions derived in Appendix D, while those of the bridle configuration are determined using the finite difference approach. The results in Table 6.3 show that the hydrostatic stiffness in the surge, sway, and yaw modes is nonexistent (which is a basic principle in hydrostatics), while the mooring stiffness exists in all DOFs. Moreover, the hydrostatic stiffnesses in heave, roll and pitch modes are much larger than their mooring counterparts. The comparison between the mooring stiffness of the single and bridle configurations reveals that the bridle configuration is stiffer in all modes except the heave mode which exhibits slightly less stiffness. However, because the hydrostatic stiffness is dominant in this DOF, this has little consequence.

The FOWT system natural frequencies are then computed for the two mooring configurations and listed in Table 6.4. The results show that the natural frequencies of the system with the bridle mooring is somewhat higher in surge and sway modes which is attributable to the larger mooring stiffness in these modes. The heave, roll, and pitch natural frequencies are insensitive to the choice of the mooring configuration because the hydrostatic heave, roll, and pitch stiffnesses are the main contributors to the system stiffness in these modes. Likewise, the tower bending natural frequencies are insensitive to the mooring stiffness since the structural stiffness is very large compared to those arising from the mooring stiffnesses. The results in Tables 6.3 and 6.4 will serve as the basis for understanding the system dynamics behavior due to these mooring configurations.

Table 6.3: Hydrostatic and mooring stiffnesses

Coefficient	**Hydrostatic**	**Mooring**	
		Single	**Bridle**
K_{11}, K_{22} (N/m)	0	4.12×10^4	5.13×10^4
K_{33} (N/m)	3.34×10^5	1.31×10^4	1.12×10^4
K_{44}, K_{55} (N.m/rad)	1.31×10^9	-7.07×10^6	6.38×10^6
K_{66} (N.m/rad)	0	$1.16 \times 10^7 + K_{add}$	1.22×10^8

Table 6.4: Influence of the mooring configuration on the system natural frequencies

Eigenmode (Hz)	**Single**	**Bridle**
Surge	0.00800	0.00893
Sway	0.00800	0.00893
Heave	0.03294	0.03291
Roll	0.03329	0.03348
Pitch	0.03332	0.03345
Yaw	0.12111	0.12776
1st (u_1)	0.48845	0.48846
1st (u_2)	0.48141	0.48142
1st tower twist	1.84150	1.84154

The FOWT system responses obtained using single (with K_{add}) and the bridle configurations are now compared for identical wave and wind loads. The system is subject to irregular waves load characterized by a Jonswap spectrum with $H_s = 11$ m, $T_p = 14$ s, and $\beta_w = 30^o$, and a steady wind with $U = 10$ m/s. Figure 6.12 compares the platform displacement responses obtained using the two mooring configurations. The results show that the roll and pitch responses are almost insensitive to the choice of mooring configuration. This is because the roll and pitch system stiffnesses are mainly due to hydrostatics so that varying the mooring stiffness in these modes will not considerably influence the system stiffness. The mean values of the surge and heave responses of the bridle configuration are lower than those of the single configuration. This is because the mean line tensions of the bridle configuration are larger than those of the single, hence larger mean tension yields lower mean surge/sway and heave. On the other hand, the fluctuations of the surge, sway and heave are in good agreement between the two configurations. The biggest difference between the two models is the discrepancy in the yaw response, where the response of the single configuration exhibits larger oscillations. This attributable to the larger mooring yaw stiffness of the bridle compared to the single configuration even with additional mooring yaw stiffness (11% larger than the single configuration as illustrated in Table 6.3). Thus, a better choice of K_{add} will result in a yaw response similar to that of the bridle configuration. The rotor spin, and the tower tip bending deflection responses in the fore-aft (u_1) and side-side (u_2) directions are not significantly affected by the choice of mooring configuration, and so are not shown here, for the sake of brevity.

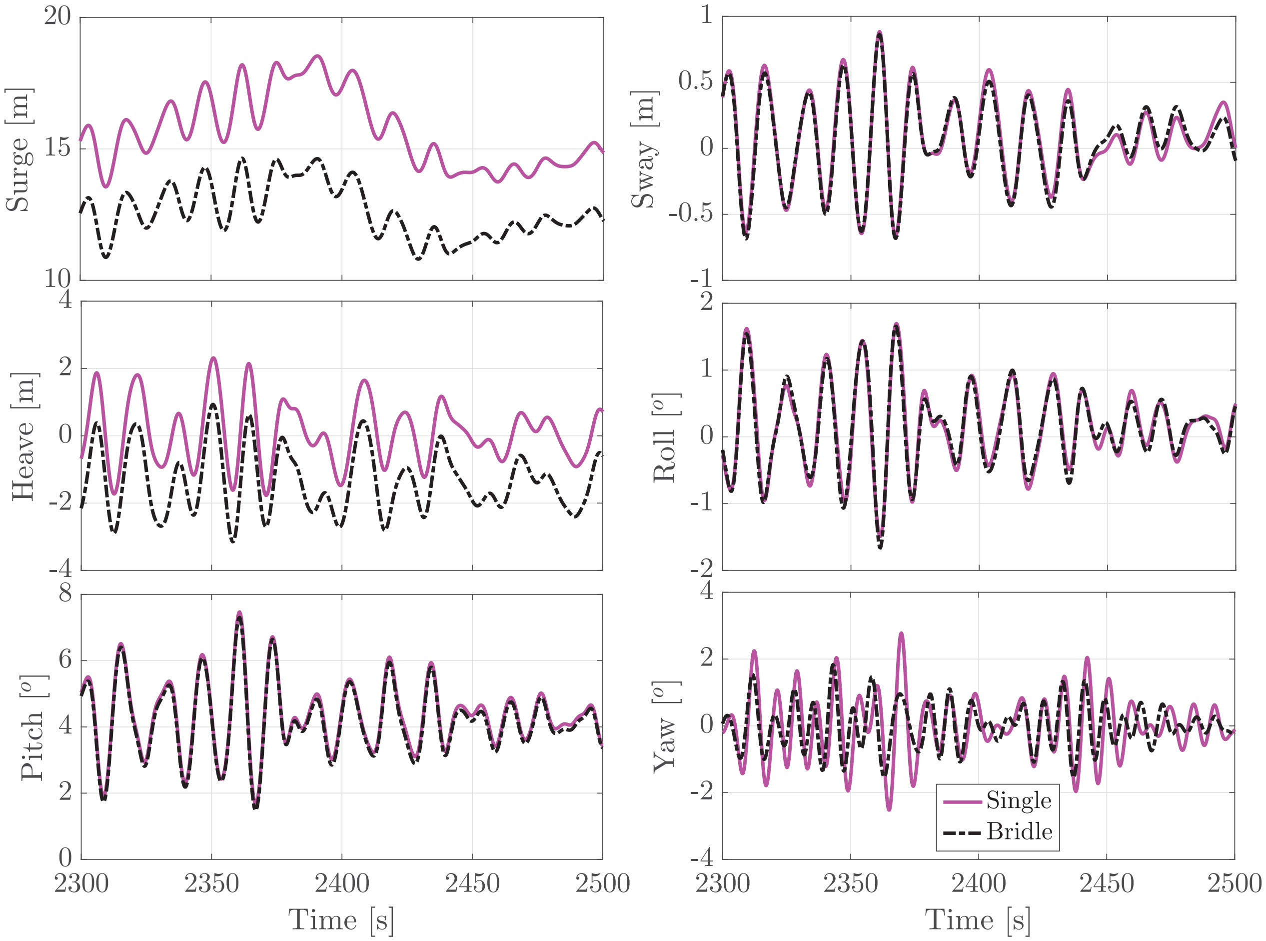

Figure 6.12: Comparison of platform displacements between the single-segmented (with additional yaw stiffness) and bridle mooring system with addition

6.3.3 Rotor gyroscopic effect

It is well known that the rotor spin induces gyroscopic moments proportional to the rotor spin speed and tower angular velocity. On the other hand, varying the rotor speed will alter the aerodynamic thrust and torque. To examine the impact of the rotor spin on the system dynamics separately from any concurrent effect of the aerodynamic loads, we set the aerodynamic loads to zero (i.e. there is no wind). This implies that the rotor is idling (without a generator load) at a constant speed. To reflect this, the equations of motion derived in Chapter 2 must be modified to analyze the system dynamics for constant rotor speed ($\dot{\Omega} = 0$), and that the generator torque control is no longer active. Accordingly, the equations of motion of the rigid model (Equation (2.19)) can be reformulated as

$$
\begin{gathered}
\left[\mathbf{M}_{sys} + \mathbf{A}\ \right] \begin{bmatrix} \dot{\boldsymbol{\nu}} \\ \dot{\boldsymbol{\omega}} \end{bmatrix} + \left[\tilde{\mathcal{S}}\, \mathbf{M}_{sys} + \mathbf{C}_A\right] \begin{bmatrix} \boldsymbol{\nu} \\ \boldsymbol{\omega} \end{bmatrix} = \\
\begin{bmatrix} \mathbf{R}^T \frac{\partial \mathcal{L}}{\partial \mathbf{r}} \\ \mathbf{J}^{-T} \frac{\partial \mathcal{L}}{\partial \boldsymbol{\theta}} \end{bmatrix} + \begin{bmatrix} {}^p\mathbf{F}_{hs} + {}^p\mathbf{F}_{aer} + {}^p\mathbf{F}_{mor} + {}^p\mathbf{F}_{hd*} \\ {}^p\mathbf{M}_{hs} + {}^p\mathbf{M}_{aer} + {}^p\mathbf{M}_{mor} + {}^p\mathbf{M}_{hd*} \end{bmatrix} + \begin{bmatrix} \mathbf{0}_{3\times 1} \\ {}^p\mathbf{M}_{gyro} \end{bmatrix}
\end{gathered}
\tag{6.2}
$$

where

$$
\tilde{\mathcal{S}} = \begin{bmatrix} \tilde{\boldsymbol{\omega}} & \mathbf{0}_{3\times 3} \\ \tilde{\boldsymbol{\nu}} & \tilde{\boldsymbol{\omega}} \end{bmatrix} \tag{6.3}
$$

The mass matrix ($\mathbf{M}_{sys}$) form is similar to that of Equation (2.13) but without the last row and column. The gyroscopic moment (${}^p\mathbf{M}_{gyro}$) in Equation (6.2) is expressed as

$$
{}^p\mathbf{M}_{gyro} = [0 \quad - I_{rx}\,\Omega\,\omega_z \quad I_{rx}\,\Omega\,\omega_y]^T \tag{6.4}
$$

Based on Equations (6.2) and (6.4), the rotor gyroscopic moments can be viewed as external moments that excite the pitch and yaw motions. The equations of motion of the flexible model can be similarly modified for constant rotor speed.

Two dynamic simulations are performed with the platform excited by an irregular wave characterized by a Jonswap spectrum with $H_s = 11$ m and $T_p = 14$ s and $\beta_w = 30^o$, while the wind loads are ignored ($\mathbf{F}_{aer} = \mathbf{M}_{aer} = \mathbf{0}$). Two cases are considered: one in which the wind turbine is parked ($\Omega = 0$), and the second simulation with the rotor idling at a constant spin rate of $\Omega = 4$ rpm. The system response obtained from these simulations are then compared to examine the influence of the rotor gyroscopic effect on the system dynamics.

The results show that the gyroscopic moment resulting from 4 rpm rotor spin yields a larger yaw response compared to that of the parked rotor, as shown in Figure 6.13. However, the remaining platform translational and rotational responses and tower elastic motions are not affected and thus are not presented here.

Although the gyroscopic moment has components in the y- and z-axes, as shown in Figure 6.14, only the platform yaw appears sensitive to this effect, while the pitch response is unaffected. This is because the pitch DOF is primary excited by a very large hydrodynamic moment compared to the pitch gyroscopic moment, as shown by comparing Figures 6.14 and 6.15. By contrast, the yaw DOF is not excited by hydrodynamic loads. Thus, the yaw gyroscopic moment is the main disturbing external moment. Moreover, the platform yaw mass moment of inertia is small compared to the corresponding roll and pitch, and the yaw motion can be more easily excited.

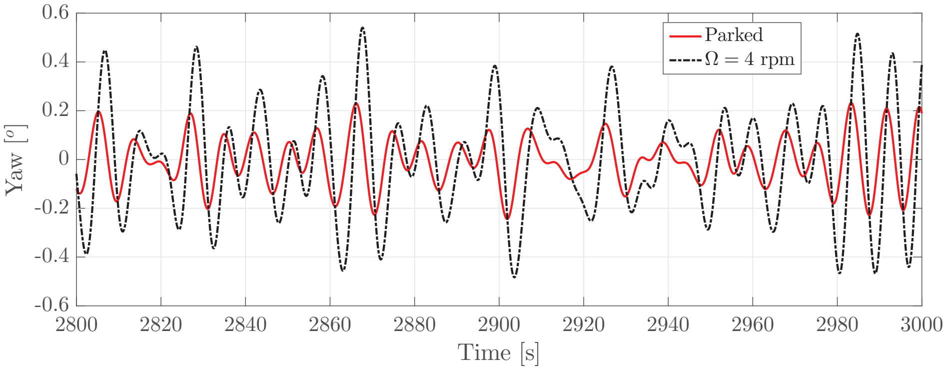

Figure 6.13: Yaw response for parked and spinning rotor

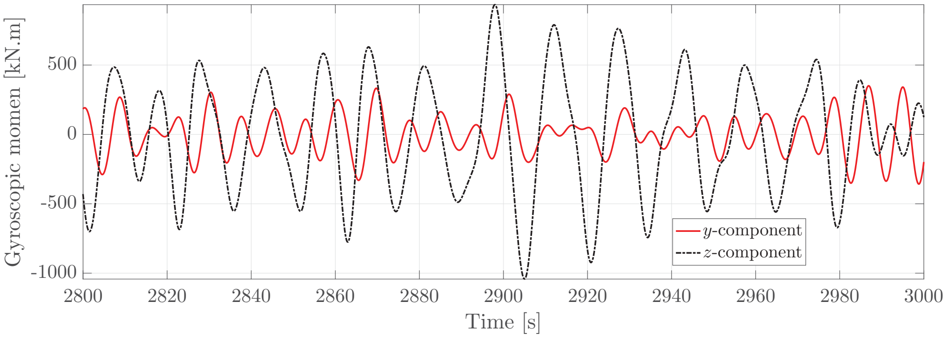

Figure 6.14: Gyroscopic moment components responses for $\Omega = 4$ rpm

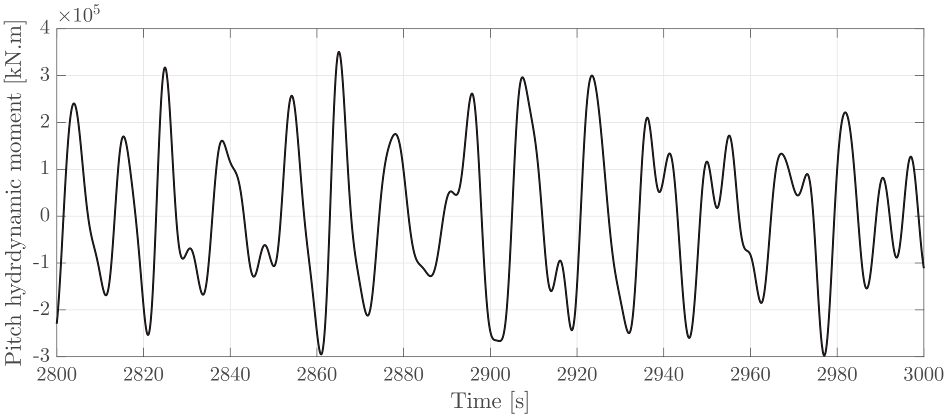

Figure 6.15: The y-component of the hydrodynamic moment time history for $\Omega = 4$ rpm

6.3.4 Cable dynamics

In the previous simulations, the cable loads were computed using quasi static cable models. By contrast, cable dynamic models consider the hydrodynamic loads exerted on the cable and the cable inertia. In general, incorporating the cable dynamics into the system dynamics leads to a better prediction of the systems dynamic response. However, the coupled dynamic model (structural + cable dynamics) involves a large number of DOFs which requires a much more computational effort.

To investigate the impact of cable dynamics on the dynamic behavior of the system, the lumped mass approach developed in Chapter 5 is now integrated into the system dynamics. Thus, the coupled equations of motion of the structure (developed in Chapter 2) together with equations of motion of the cable nodes (developed in Chapter 5) are solved simultaneously to obtain the system response. In addition, a separate simulation using the quasi static cable model with similar environmental conditions is used to calculate the cable tensions. The system responses obtained using the two cable models are then compared to assess any differences in their predictions of the system response and cable tensions.

The dynamic simulations are performed utilizing the flexible tower model and the bridle mooring configuration. The ocean environment is characterized by a Jonswap spectrum with $H_s = 11$ m, and $T_p = 14$ s, and $\beta_w = 30^o$. The wind turbine rotor is subject a steady wind of speed U=10 m/s. Each mooring line is discretized into a total of 26 elements, distributed as: $N_{br} = 2$, $N_u = 6$, and $N_l = 16$ elements. The drag coefficients of the mooring lines $C_{Dc} = 1.2$ based on [126] and the added mass coefficient $C_a = 1.0$ similar to the platform since they are both of slender cylindrical shape [96].

Figure 6.16 compares the platform translations obtained using the quasi-static and lumped mass models. The results show that the surge and and sway responses of the two cable models correlate well, while minor deviations in the mean of the oscillations still exist. The use of the lumped mass model yields around 10% reduction in the heave fluctuations amplitudes, which is likely attributable to the added damping introduced by cable hydrodynamic forces considered in the lumped cable model.

Figure 6.17 presents the Euler angle responses. The roll and pitch responses are nearly identical, indicating that these responses are insensitive to the choice of the cable model. The same observation can be made for the tower tip bending responses (u_1 and u_2), illustrated in Figure 6.18. This similarity between roll/pitch and u_1/u_2 behaviors is attributed to the fact that the pitch and roll motions are the main contributors to excitations of the tower bending deflections.

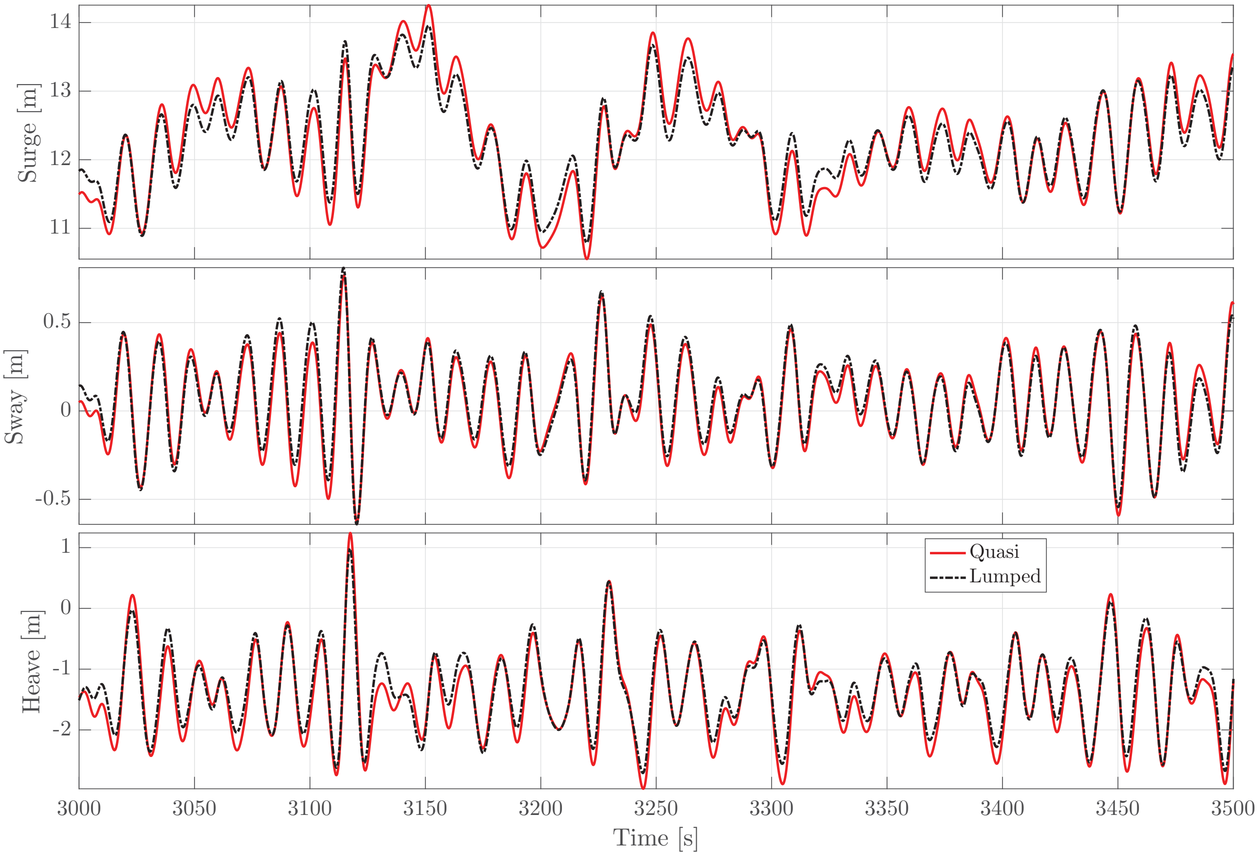

Figure 6.16: Platform translation responses as obtained using the quasi static and lumpud mass cable models

The rotor spin responses obtained using the two cable models are also in excellent agreement, as shown in Figure 6.19. The key difference between the cable models is in their predictions of the platform yaw response, with the quasi static cable model exhibiting about 40% higher peaks compared to the lumped mass model, as illustrated in Figure 6.17.

The insensitivity of the surge, sway, roll and pitch response to the cable dynamics is attributed to the small mooring hydrodynamic damping and inertia forces as compared to their counterparts on the platform. The effect of mooring hydrodynamic damping in the heave direction is more prominent yielding a relatively lower heave response. In addition, the large

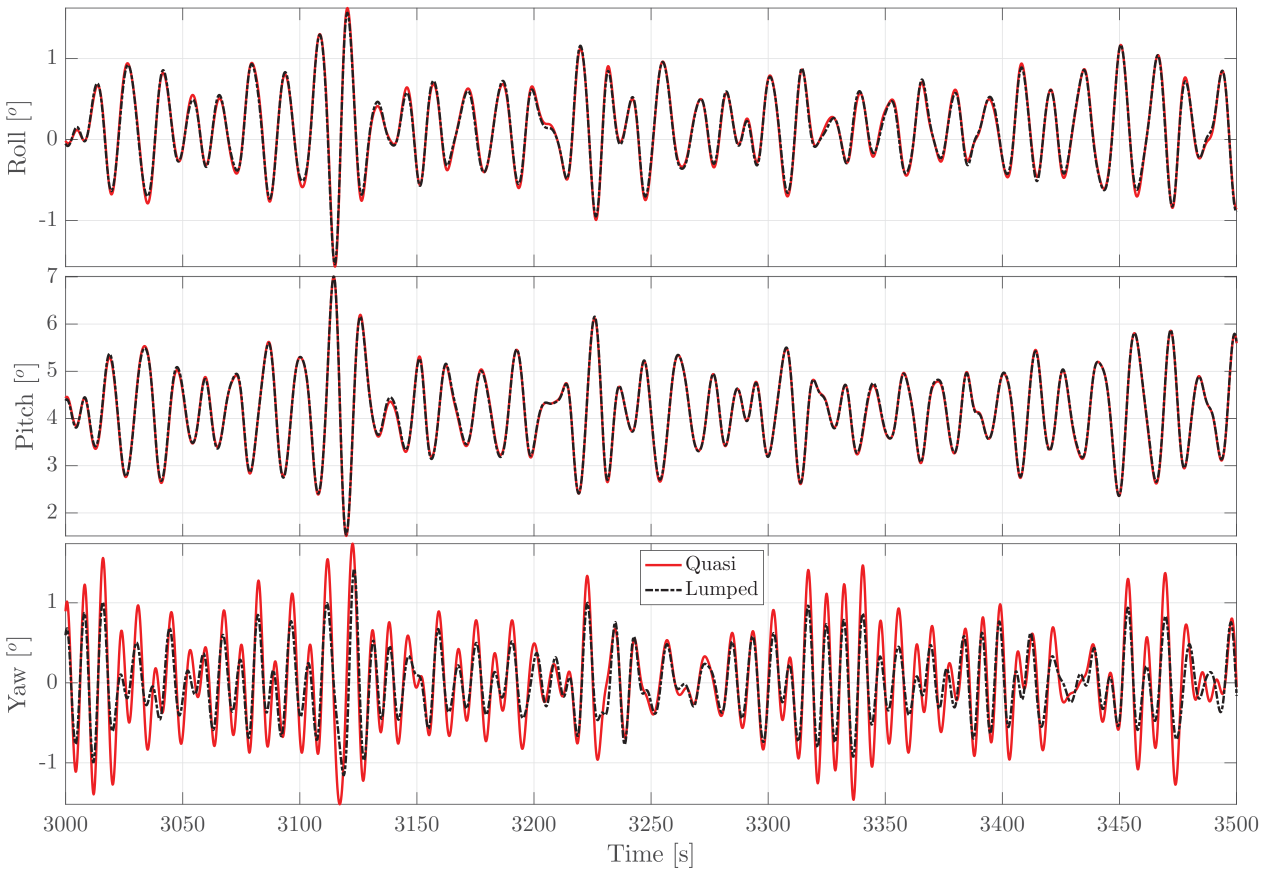

Figure 6.17: Platform rotation responses as obtained using the quasi static and lumpud mass cable models

discrepancy between the quasi static and lumped mass cable models in their predictions of the yaw response is attributed to the considerable mooring lines yaw inertia and hydrodynamics damping loads, particularly compared to the low platform yaw hydrodynamic damping.

Figures 6.20 and 6.21 present the power spectra of the platform displacements and tower tip bending deflections. In general, the lumped mass model exhibits lower energy contents particularly at higher frequencies beyond the first tower bending mode (0.49 Hz). There is also slightly less energy contents at some of the resonant peaks. All these differences can be attributed to the added damping of the mooring lines, present in the lumped mass model.

The time histories of the fairlead tensions are shown in Figure 6.22. The lumped mass model significantly predicts larger tension fluctuations than the quasi static model. This is attributable to the fluctuations of the hydrodynamic loads exerted on the mooring line. These observations are also reflected in the power spectra of the fairlead tensions in Figure 6.23

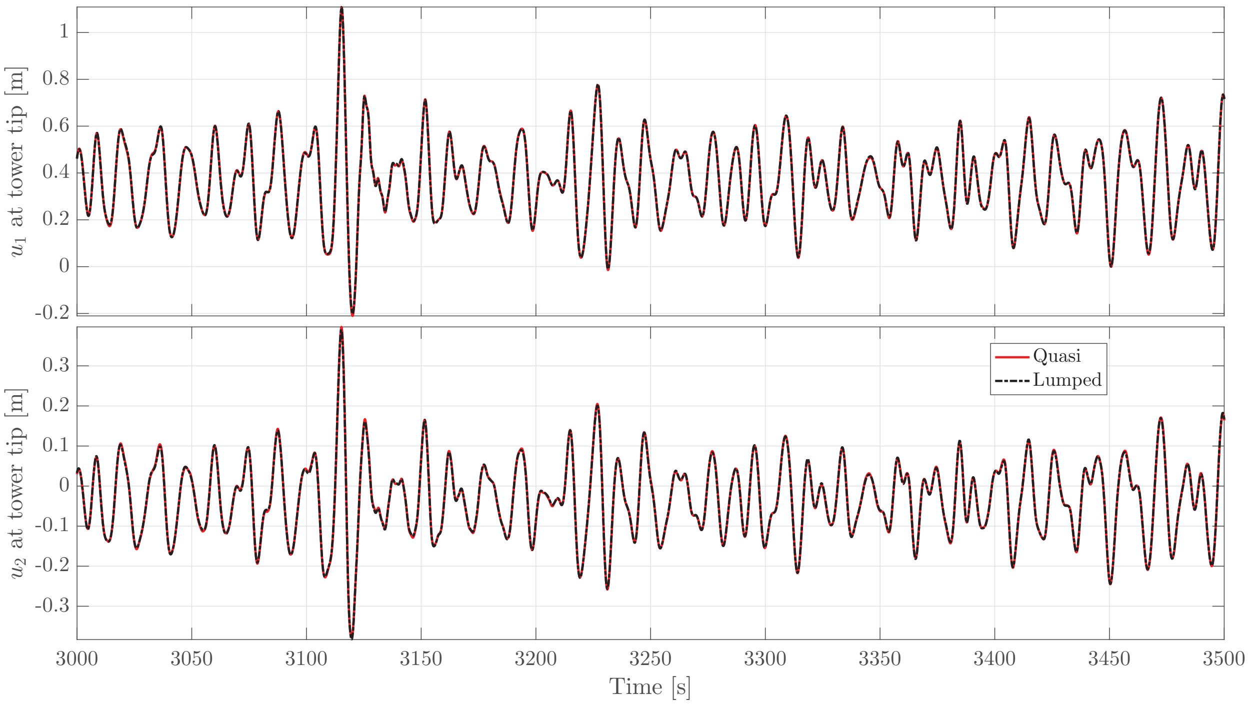

Figure 6.18: Tower tip bending deflections time histories as obtained using quasi static and lumped mass models

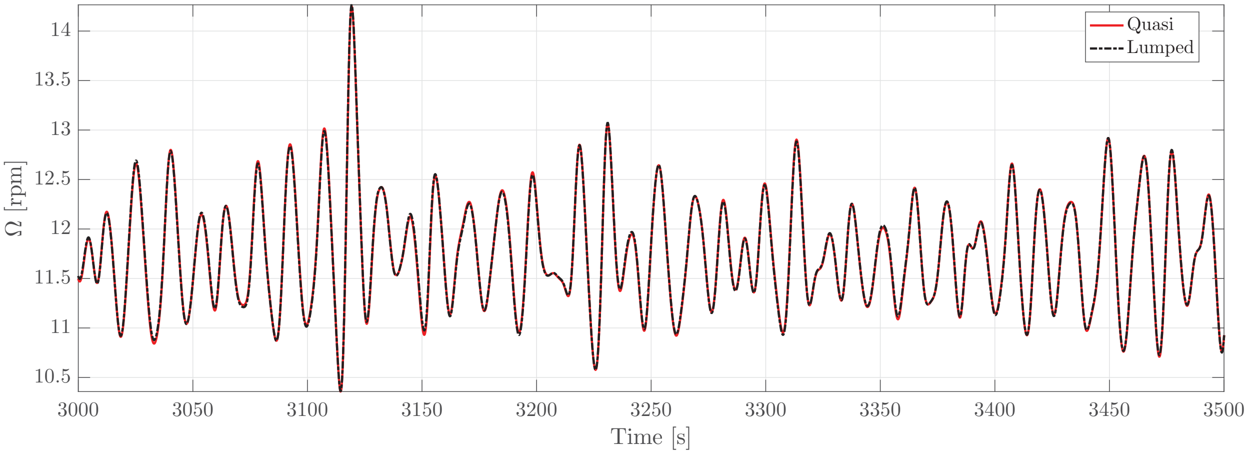

Figure 6.19: Rotor spin rate as obtained using quasi static and lumped mass models

where the lumped mass model exhibits considerably higher energy content across most the spectrum compared to the quasi static model. It is obvious that the lumped mass cable model predicts lower tension troughs and larger peaks as compared with those obtained by the quasi-static cable model (Figure 6.22). This enhances the observation reported in many recent studies [115, 127, 128] that the lumped mass cable model better predicts the snap loads of the mooring lines. A dominant peak in the vicinity of 0.35 Hz is also observed in the

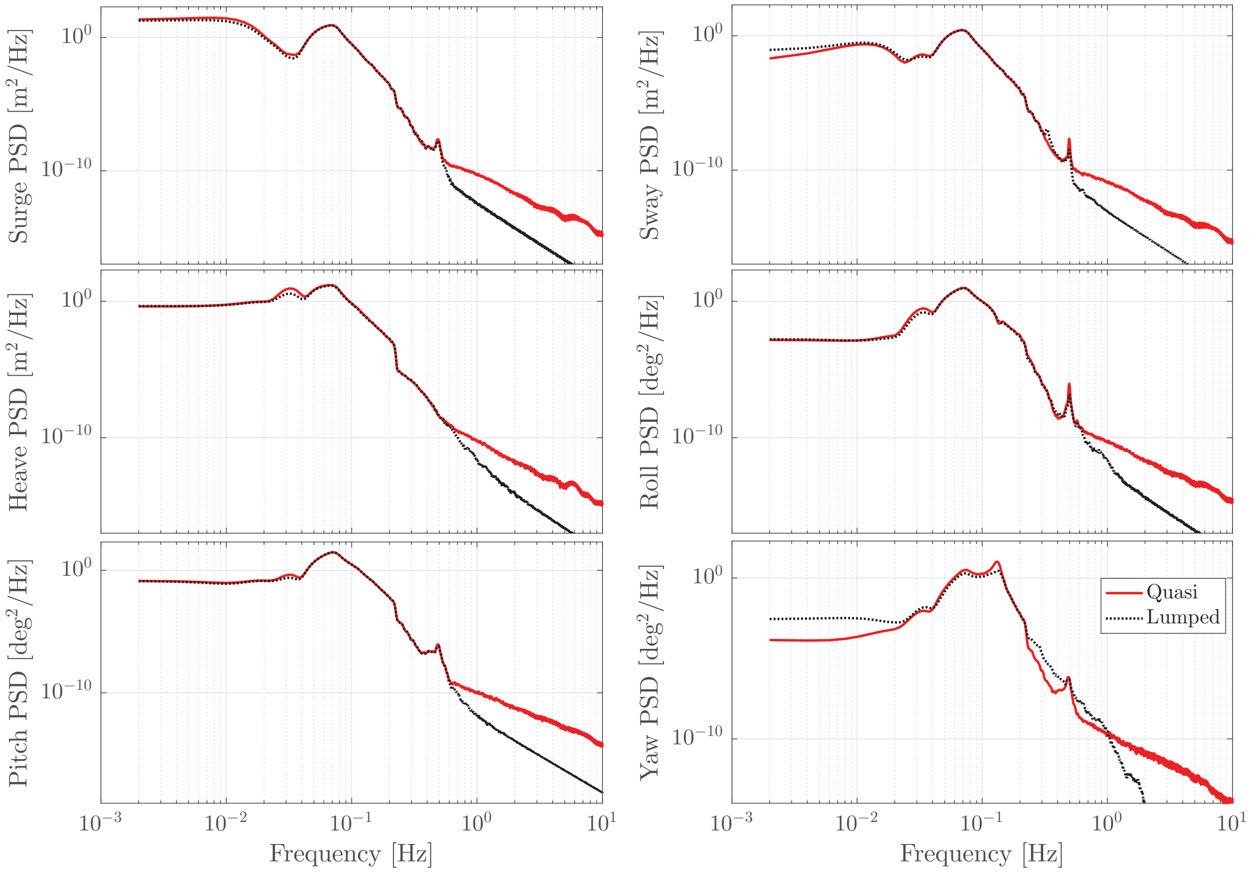

Figure 6.20: Power spectra of the platform translation and rotation responses as obtained using quasi static and lumped mass models

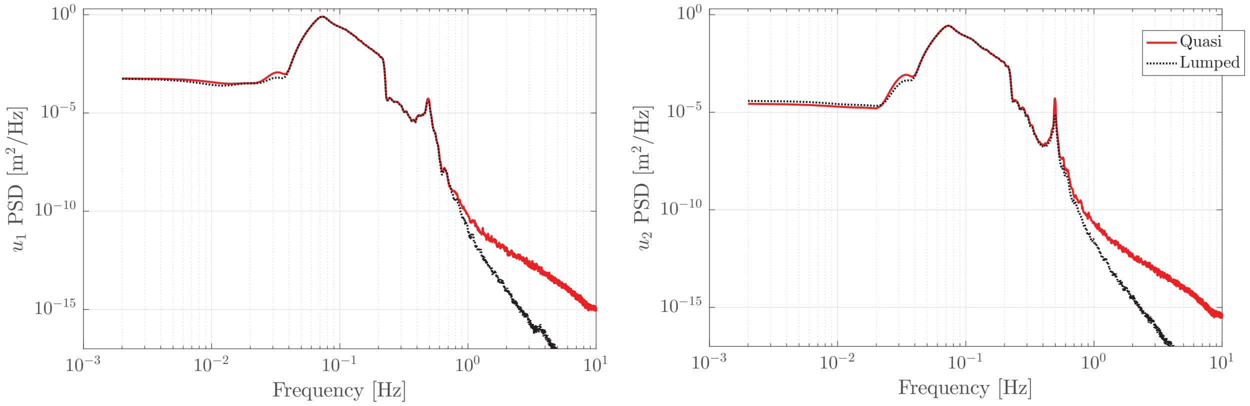

Figure 6.21: Power spectra of the tower tip bending responses as obtained using quasi static and lumped mass models

PSD plots of the cable tensions (Figure 6.23) which may correspond to a resonant frequency associated with the cable transverse motion.

Lastly, it is worth mentioning that the main conclusions drawn from the comparison of the quasi-static and lumped mass models with bridle mooring were also observed for the single mooring system configuration. Those results are not presented here for brevity.

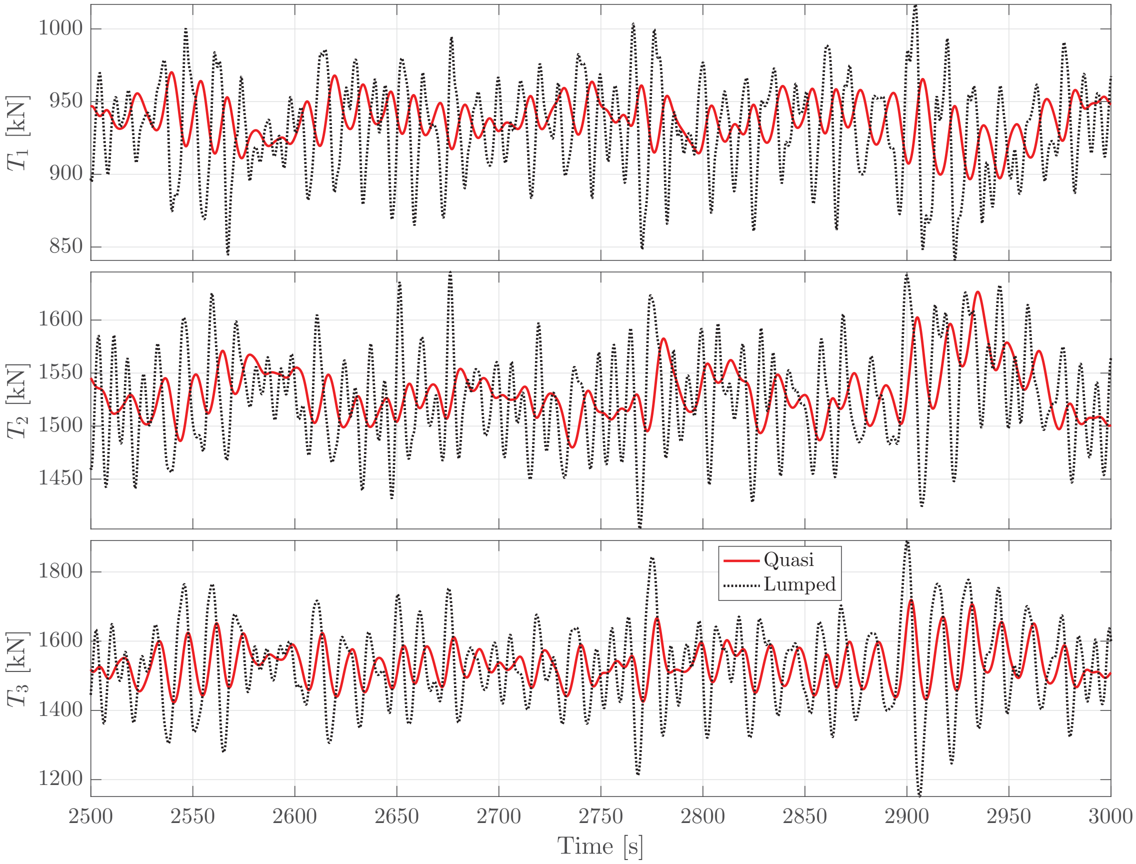

Figure 6.22: Cable tension as obtained using quasi static and lumped mass models

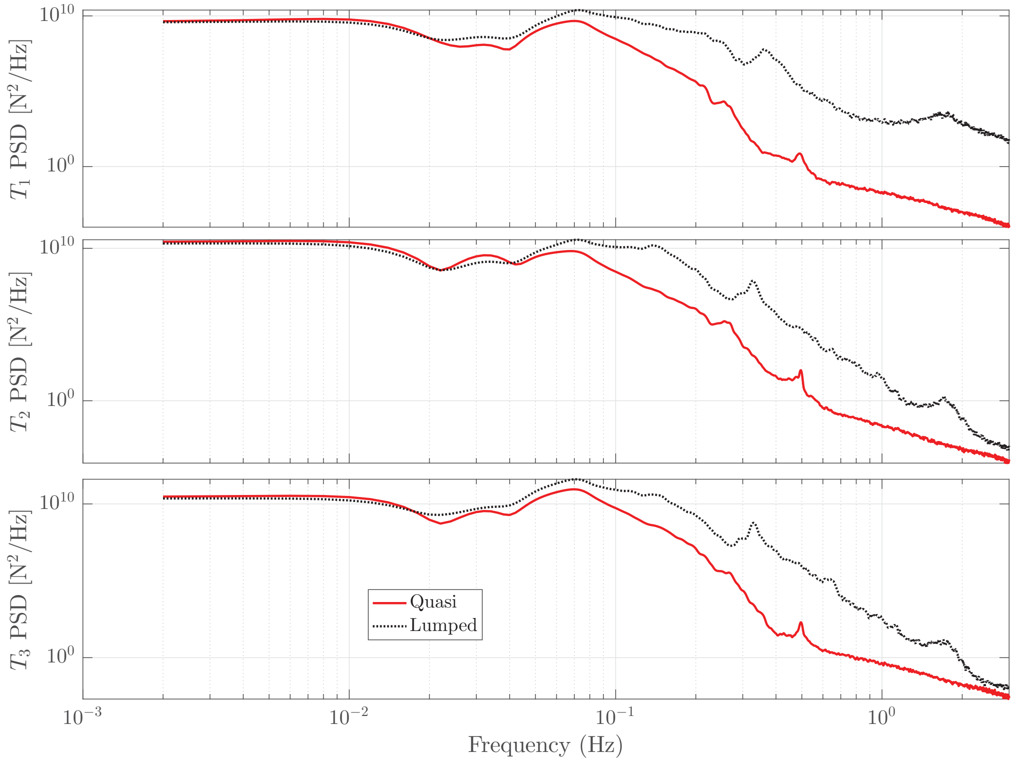

Figure 6.23: Power spectra of cable tensions as obtained using quasi static and lumped mass models

Chapter 7

CONCLUSIONS AND FUTURE WORK

This thesis focused on developing multibody dynamic models of a spar FOWT, with an emphasis on theoretical modeling of the hydrostatic and mooring system loads as primary sources of the system stiffness. These models were then used to build a validated large simulation tool to analyze the system dynamic response to environmental disturbances.

In Chapter 2, rigid and flexible multibody dynamic models of the FOWT system were developed. The modified form of Lagrange's equation was found to be an efficient way to derive the equations of motion of the platform in terms of its quasi coordinates. The orthogonal polynomial shape functions developed for the spacial discretization of the tower bending motion are very similar to the eigen functions of a cantilever beam but more computationally efficient in symbolic manipulation. The convergence of the AMM using these polynomials was tested by analyzing the dynamics of a spinning cantilever beam with a tip mass. The resulting beam bending response was found to be in excellent agreement with reported results obtained using FEM. Generating the equations of motion of the flexible FOWT model using symbolic programming was quick and produced error free results, particularly for complex equations of motion, as in our case. We found that modeling the internal damping of the tower improved the numerical stability and computational efficiency by reducing the transient period and accelerating the simulation. Incorporating the generator torque control allowed the model to capture the fluctuation of rotor spin speed which allowed simulations of different scenarios and load cases. The rotor spin response obtained using this model was in very good agreement with that reported from different simulation tools.

In general, the heave motion is mainly excited by the fluctuations of hydrostatic force induced by waves surface elevation variation crossing the platform, where submerged length is directly influenced by the wave height. A theoretical framework which included this effect was developed to calculate the exact buoyancy force and hydrostatic moments in Chapter 3. New exact water plane restoring moments expressions were derived and found to be directly related to the rotation matrix entries. As well, the 6×6 hydrostatic stiffness matrix was derived as function of the instantaneous position and orientation of the platform. The exact hydrostatic waterplane stiffnesses computed using the developed nonlinear approach, were found to be larger than those computed using the conventional linear approach particularly at large platform rotation. The exact hydrostatic analysis presented herein can offer an analytical solution to determine the 3D equilibrium of floating cylindrical platforms, thus replacing potentially slower numerical methods.

A novel 3D exact quasi-static cable model was developed to compute the mooring tensions of the bridle configuration, while considering the effect of suspended clump weights. The clump weight changes the cable profile and yields a higher tension and mooring line stiffness. A new analytical formulation was also presented to calculate the mooring system stiffness of suspended, partially resting on the seabed and taut cables. The influence of several mooring design parameters were investigated for a taut-leg mooring system. The parametric study revealed that increasing the anchor radius leads to an increase in the surge/sway mooring stiffness until certain threshold, and further increase results in a decrease in these stiffnesses. The mooring heave stiffness decreases with increasing the anchor radius while the yaw stiffness is affected in an adverse manner. The mooring system with fewer number of lines is stiffer if the lines are not taut. However, larger number of lines yields larger stiffness if the line are sag free. Including a bridle component yields larger yaw mooring stiffness, while the remaining stiffness coefficients are not affected.

A lumped mass cable model was formulated to capture the mooring lines dynamics. The model was extended to account for the cable-seabed contact and added mass. A new methodology was developed to compute the 3D equilibrium profile of the lumped mass cable model. This method is more comprehensive than existing approaches because it can consider cables in contact with the seabed with less computational effort.

A large simulation code was developed using MATLAB to implement the analytical models of the system dynamics and the applied loads. A validation process was then undertaken using four loads cases to determine the natural frequencies, platform free decay response, system frequency response due to stochastic wave loading, and system time response due to regular wave and steady wind loads. The current model results were in excellent agreement with those obtained from well known simulation tools such as FAST and HAWC2. Some deviations among the codes results were observed which were attributable to different techniques used, particularly for modeling the hydrodynamic and mooring loads. Following this, several case studies were designed to investigate the influences of the tower flexibility, mooring system configurations, rotor gyroscopic moment, and cable dynamics on the FOWT dynamic behavior. The main findings drawn from the results of these case studies are:

- The comparison between the simulation results of the rigid and flexible dynamic models showed that the tower flexibility yields 25% larger yaw response while the surge, sway, heave, roll and pitch motions of the platform are only slightly affected. As well, the flexible model responses exhibit more damping compared to those of the rigid body model due to the tower internal structural damping considered in the flexible model.

- The roll and pitch system stiffness are mainly due to the hydrostatic restoring loads. Thus varying the mooring system stiffness by using different mooring configurations does not affect the roll, pitch and tower elastic deformations responses. By contrast, the surge, sway and yaw responses are solely due to the mooring system stiffness characteristics and thus are much more affected by changes to the mooring configuration. For the same reason, the system natural frequencies in heave, roll/pitch and fore-aft/side-side tower bending are insensitive to the mooring stiffness while the remaining natural frequencies are affected by the mooring system stiffness.

- The influence of the tower twist on the platform displacements and tower bending deformations is negligible and results in a much slower simulation. It is therefore recommended to ignore this deformation.

- The rotor spin induces gyroscopic moments around the pitch and yaw axes. The gyroscopic effect in yaw is more prominent because of the small yaw mass moment inertia and the absence of yaw added inertia, rendering the yaw DOF more responsive to relatively small disturbances.

- Cable dynamics yields considerably lower yaw response due to the larger yaw cable inertia and hydrodynamic damping. As well, the hydrodynamic damping induced by cable dynamics yields lower heave response compared to that obtained using the quasi static model. The surge, sway, roll, pitch and tower bending deformations responses are not affected by the cable dynamics.
- The cable tension fluctuations predicted by the lumped mass cable model are larger than those of the quasi static cable model. This is attributable to the fluctuations of the hydrodynamic loads exerted on the cable due to the cable motion.

7.1 Suggested Future Research

Based on the work accomplished in this thesis, several directions to extend the current research work in future are proposed as follows:

- Modeling the rotor blades flexible motion and incorporating this into the system dynamics to capture the contribution of the rotor flexibility to the system dynamic behavior. This will improve the current model capabilities and better predict the system response and the rotor aeroelastic behavior.
- Development of a more elaborate hydrodynamic model that considers the wave diffraction effect, radiation damping, and the second order hydrodynamic load will improve the predictions of the hydrodynamic loads and hence the resulting system response.
- Including the effect of the vortex induced vibration on the platform and lumped mass cable model particularly when the system is subject to steady water current loads.
- The effect of wind turbulence and gusts may have significant influence on the system response. The wind field kinematics can be characterized in space and time using a wind turbulence model. Further validations of the current dynamic model for load cases associated with turbulent wind loading could be then performed.

- The drag and added mass coefficients of the platform and mooring lines were assumed to be constant. However, these coefficients are dependent on Reynolds and Keulegan-Carpenter numbers. Incorporating the relationships between these coefficients and dimensionless numbers into the hydrodynamic model will improve the predictions of inertial and drag terms in the Morison's equation.
- If experimental data becomes available from the Hywind pilot systems presently being deployed, it would be important to use this data to validate the present model.
- Develop a simple extension to improve the rigid body model to predict the tower tip elastic bending deformations in the fore-aft and side-side direction. The model can be altered by adding spring and damper at the tower tip and attached to the RNA in an appropriate manner to account for the tip deflections and equivalent internal tower damping. This would extend the rigid model to approximately predict the flexible tower motion with much less computational effort than the flexible model.
- Extending the present simulation code to analyze different types of platforms such as semi–submersible and hybrid platforms. This will allow to assess the dynamic behavior of FOWTs with different platform types.
- Examine the system dynamic behavior for different mooring arrangements such as taut–leg and tension leg mooring systems.

REFERENCES

[1] Robertson, A. N. and Jonkman, J., "Loads analysis of several offshore floating wind turbine concepts," *The 21st International Offshore and Polar Engineering Conference*, Maui, HI, June 2011.

[2] Statoil, "StatoilHydro to build first full scale offshore floating wind turbine," `http://www.statoil.com/en/NewsAndMedia/News/2008/Downloads/hywind_04.jpg`, 2008, Accessed on 10.11.2016.

[3] NREL's National Wind Technology Center, "NREL 5-MW reference turbine - CP, CQ, CT Coefficients," `https://wind.nrel.gov/forum/wind/viewtopic.php?f=2&t=582`, 2012, Accessed on 10.05.2015.

[4] Cai, G.-P., Hong, J.-Z., and Yang, S., "Dynamic analysis of a flexible hub-beam system with tip mass," *Mechanics Research Communications*, Vol. 32, No. 2, 2005, pp. 173–190.

[5] Jonkman, J. and Musial, W., "Offshore code comparison collaboration (OC3) for IEA task 23 offshore wind technology and deployment," Tech. Rep. NREL/TP-5000-48191, 2010.

[6] Jonkman, J., "Definition of the Floating System for Phase IV of OC3," Tech. Rep. NREL/TP-500-47535, National Renewable Energy Laboratory, Golden, CO, 2010.

[7] Karimirad, M. and Moan, T., "A simplified method for coupled analysis of floating offshore wind turbines," *Marine Structures*, Vol. 27, No. 1, 2012, pp. 45–63.

[8] International Energy Agency (IEA), "IEA wind 2011," Annual report, IEA, 2011.

[9] Breton, S.-P. and Moe, G., "Status, plans and technologies for offshore wind turbines in Europe and North America," *Renewable Energy*, Vol. 34, No. 3, 2009, pp. 646–654.

[10] Wang, C., Utsunomiya, T., Wee, S., and Choo, Y., "Research on floating wind turbines: A literature survey," *IES Journal Part A: Civil and Structural Engineering*, Vol. 3, No. 4, 2010, pp. 267–277.

[11] Musial, W., Jonkman, J., Sclavounos, P., and Wayman, L., "Engineering challenges for floating offshore wind turbines," *Copenhagen Offshore Wind 2005 Conference and Expedition Proceedings*, October 2005.

[12] Jonkman, J., "Dynamics of offshore floating wind turbines-model development and verification," *Wind Energy*, Vol. 12, No. 5, 2009, pp. 459–492.

[13] Journee, J. and Massie, W., *Offshore hydromechanics*, TU Delft, 2001.

[14] Isaacson, M. and Baldwin, J., "Moored structures in waves and currents," *Canadian Journal of Civil Engineering*, Vol. 23, No. 2, 1996, pp. 418–430.

[15] Skop, R., "Mooring systems: a state-of-the-art review," *Journal of Offshore Mechanics and Arctic Engineering*, Vol. 110, No. 4, 1988, pp. 365–372.

[16] Matha, D., Schlipf, M., Cordle, A., Pereira, R., and Jonkman, J., "Challenges in simulation of aerodynamics, hydrodynamics, and mooring-line dynamics of floating offshore wind turbines," *The 21st International Offshore and Polar Engineering Conference*, Maui, HI, 2011.

[17] Barltrop, N., *Floating structures: a guide for design and analysis*, Oilfield Publications Ltd., Herefordshire, UK, 1998.

[18] Faltinsen, O., *Sea loads on ships and offshore structures*, Cambridge University Press, Cambridge, UK, 1993.

[19] Johanning, L., Smith, G., and Wolfram, J., "Mooring design approach for wave energy converters," *Proceedings of the Institution of Mechanical Engineers Part M: Journal of Engineering for the Maritime Environment*, Vol. 220, No. 4, 2006, pp. 159–174.

[20] Fossen, T., *Handbook of marine craft hydrodynamics and motion control*, Wiley, New York, 2011.

[21] Ku, N., Cha, J.-H., Park, K.-P., and Lee, K.-Y., "Non-linear hydrostatic analysis of the floating crane considering the large angle of inclination," *Royal Institution of Naval Architects–International Conference on Marine Heavy Transport and Lift III*, London, UK, 2012.

[22] Zeng, X., Shen, X., and Wu, Y., "Nonlinear dynamic response of floating circular cylinder with taut tether," *Proceedings of 15th Offshore and Polar Engineering Conference*, Seoul, Korea, 2005, pp. 218–224.

[23] Soylemez, M., "Non-linear restoring forces of an offshore platform," *Ocean Engineering*, Vol. 25, No. 2-3, 1998, pp. 105–118.

[24] Dalane, O., Faye Knudsen, F., and Lset, S., "Nonlinear coupled hydrostatics of arctic conical platforms," *Journal of Offshore Mechanics and Arctic Engineering*, Vol. 134, No. 2, 2011.

[25] Yim, S., Nakhata, T., Bartel, W., and Huang, E., "Coupled nonlinear barge motions, Part I: deterministic models development, identification and calibration," *Journal of Offshore Mechanics and Arctic Engineering*, Vol. 127, No. 1, 2005, pp. 1–10.

[26] Witz, J., Ablett, C., and Harrison, J., "Roll response of semisubmersibles with non-linear restoring moment characteristics," *Applied Ocean Research*, Vol. 11, No. 3, 1989, pp. 153–166.

[27] Taylan, M., "The effect of nonlinear damping and restoring in ship rolling," *Ocean Engineering*, Vol. 27, No. 9, 2000, pp. 921–932.

[28] Neves, M. and Rodrguez, C., "On unstable ship motions resulting from strong non-linear coupling," *Ocean Engineering*, Vol. 33, No. 14-15, 2006, pp. 1853–1883.

[29] Liaw, C. and Bishop, S., "Nonlinear heave-roll coupling and ship rolling," *Nonlinear Dynamics*, Vol. 8, No. 2, 1995, pp. 197–211.

[30] Ibrahim, R. and Grace, I., "Modeling of ship roll dynamics and its coupling with heave and pitch," *Mathematical Problems in Engineering*, Vol. 2010, 2010.

[31] Zeng, X.-H., Shen, X.-P., and Wu, Y.-X., "Governing equations and numerical solutions of tension leg platform with finite amplitude motion," *Applied Mathematics and Mechanics (English Edition)*, Vol. 28, No. 1, 2007, pp. 37–49.

[32] Irvine, M., *Cable structures*, MIT University Press, Cambridge, MA, 1981.

[33] Jain, R., "A simple method of calculating the equivalent stiffnesses in mooring cables," *Applied Ocean Research*, Vol. 2, No. 3, 1980, pp. 139–142.

[34] Lee, J. and Cho, W., "Hydrodynamic analysis of wave interactions with a moored floating breakwater using the element-free Galerkin method," *Canadian Journal of Civil Engineering*, Vol. 30, No. 4, 2003, pp. 720–733.

[35] Sannasiraj, S., Sundar, V., and Sundaravadivelu, R., "Mooring forces and motion responses of pontoon-type floating breakwaters," *Ocean Engineering*, Vol. 25, No. 1, 1998, pp. 27–48.

[36] Loukogeorgaki, E. and Angelides, D., “Stiffness of mooring lines and performance of floating breakwater in three dimensions,” *Applied Ocean Research*, Vol. 27, No. 4-5, 2005, pp. 187–208.

[37] Senjanovi, I., Tomi, M., and Hadi, N., “Formulation of consistent nonlinear restoring stiffness for dynamic analysis of tension leg platform and its influence on response,” *Marine Structures*, Vol. 30, 2013, pp. 1–32.

[38] Jain, A., “Nonlinear coupled response of offshore tension leg platforms to regular wave forces,” *Ocean Engineering*, Vol. 24, No. 7, 1997, pp. 577–592.

[39] Chandrasekaran, S. and Jain, A., “Dynamic behaviour of square and triangular offshore tension leg platforms under regular wave loads,” *Ocean Engineering*, Vol. 29, No. 3, 2001, pp. 279–313.

[40] Senjanovi, I., Tomi, M., and Rudan, S., “Investigation of nonlinear restoring stiffness in dynamic analysis of tension leg platforms,” *Engineering Structures*, Vol. 56, 2013, pp. 117–125.

[41] Low, Y., “Frequency domain analysis of a tension leg platform with statistical linearization of the tendon restoring forces,” *Marine Structures*, Vol. 22, No. 3, 2009, pp. 480–503.

[42] Kane, T., Ryan, R., and Banerjee, A., “Dynamics of a cantilever beam attached to a moving base,” *Journal of Guidance, Control, and Dynamics*, Vol. 10, No. 2, 1987, pp. 139–151.

[43] Yoo, H. and Shin, S., “Vibration analysis of rotating cantilever beams,” *Journal of Sound and Vibration*, Vol. 212, No. 5, 1998, pp. 807–808.

[44] Gurgoze, M. and Zeren, S., “The influences of both offset and mass moment of inertia of a tip mass on the dynamics of a centrifugally stiffened visco-elastic beam,” *Meccanica*, Vol. 46, No. 6, 2011, pp. 1401–1412.

[45] Bhat, R., “Transverse vibrations of a rotating uniform cantilever beam with tip mass as predicted by using beam characteristic orthogonal polynomials in the Rayleigh-Ritz method,” *Journal of Sound and Vibration*, Vol. 105, No. 2, 1986, pp. 199–210.

[46] Yang, J., Jiang, L., and Chen, D., “Dynamic modelling and control of a rotating Euler-Bernoulli beam,” *Journal of Sound and Vibration*, Vol. 274, No. 3-5, 2004, pp. 863–875.

[47] Yang, H., Hong, J., and Yu, Z., “Dynamics modelling of a flexible hub-beam system with a tip mass,” *Journal of Sound and Vibration*, Vol. 266, No. 4, 2003, pp. 759–774.

[48] Bhadbhade, V., Jalili, N., and Nima Mahmoodi, S., "A novel piezoelectrically actuated flexural/torsional vibrating beam gyroscope," *Journal of Sound and Vibration*, Vol. 311, No. 3-5, 2008, pp. 1305–1324.

[49] Sakawa, Y. and Luo, Z., "Modeling and control of coupled bending and torsional vibrations of flexible beams," *IEEE Transactions on Automatic Control*, Vol. 34, No. 9, 1989, pp. 970–977.

[50] Cooley, C. and Parker, R., "Vibration of spinning cantilever beams with an attached rigid body undergoing bending-bending-torsional-axial motions," *Journal of Applied Mechanics, Transactions ASME*, Vol. 81, No. 5, 2014.

[51] Shi, P., McPhee, J., and Heppler, G., "A deformation field for Euler-Bernoulli beams with applications to flexible multibody dynamics," *Multibody System Dynamics*, Vol. 5, No. 1, 2001, pp. 79–104.

[52] Liu, J. and Hong, J., "Dynamics of three-dimensional beams undergoing large overall motion," *European Journal of Mechanics, A/Solids*, Vol. 23, No. 6, 2004, pp. 1051–1068.

[53] Sharf, I., "Geometric stiffening in multibody dynamics formulations," *Journal of Guidance, Control, and Dynamics*, Vol. 18, No. 4, 1995, pp. 882–890.

[54] Liu, J.-Y. and Lu, H., "Rigid-flexible coupling dynamics of three-dimensional hub-beams system," *Multibody System Dynamics*, Vol. 18, No. 4, 2007, pp. 487–510.

[55] Yoo, H., Ryan, R., and Scott, R., "Dynamics of flexible beams undergoing overall motions," *Journal of Sound and Vibration*, Vol. 181, No. 2, 1995, pp. 261–278.

[56] Boutaghou, Z., Erdman, A. G., and Stolarski, H. K., "Dynamics of flexible beams and plates in large overall motions," *Journal of Applied Mechanics, Transactions ASME*, Vol. 59, No. 4, 1992, pp. 991–999.

[57] Alkire, K., "An analysis of rotor blade twist variables associated with different Euler sequences and pretwist treatments," Tech. Rep. NASA TM-84394, NASA Ames Research Center, Moffett Field, CA, 1984.

[58] Larsen, J. and Nielsen, S., "Non-linear dynamics of wind turbine wings," *International Journal of Non-Linear Mechanics*, Vol. 41, No. 5, 2006, pp. 629–643.

[59] Kessentini, S., Choura, S., Najar, F., and Franchek, M., "Modeling and dynamics of a horizontal axis wind turbine," *JVC/Journal of Vibration and Control*, Vol. 16, No. 13, 2010, pp. 2001–2021.

[60] Lee, D., Hodges, D. H., and Patil, M. J., "Multi-flexible-body dynamic analysis of horizontal axis wind turbines," *Wind Energy*, Vol. 5, No. 4, 2002, pp. 281–300.

[61] Makarios, T. and Baniotopoulos, C., "Wind energy structures: modal analysis by the continuous model approach," *JVC/Journal of Vibration and Control*, Vol. 20, No. 3, 2014, pp. 395–405.

[62] Kang, N., Chul Park, S., Park, J., and Atluri, S., "Dynamics of flexible tower-blade and rigid nacelle system: dynamic instability due to their interactions in wind turbine," *JVC/Journal of Vibration and Control*, Vol. 22, No. 3, 2016, pp. 826–836.

[63] Matsukuma, H. and Utsunomiya, T., "Motion analysis of a floating offshore wind turbine considering rotor-rotation," *The IES Journal Part A: Civil & Structural Engineering*, Vol. 1, No. 4, 2008, pp. 268–279.

[64] Wang, L. and Sweetman, B., "Simulation of large-amplitude motion of floating wind turbines using conservation of momentum," *Ocean Engineering*, Vol. 42, 2012, pp. 155–164.

[65] Wang, L. and Sweetman, B., "Multibody dynamics of floating wind turbines with large-amplitude motion," *Applied Ocean Research*, Vol. 43, 2013, pp. 1–10.

[66] Sandner, F., Schlipf, D., Matha, D., Seifried, R., and Cheng, P. W., "Reduced nonlinear model of a spar-mounted floating wind turbine," *Proceedings of the German Wind Energy Conference DEWEK*, Bremen, Germany, 2012.

[67] Sandner, F., *Reduced model design of a floating wind turbine*, Master's thesis, University of Stuttgart, 2012.

[68] Ramachandran, G. K. V., Bredmose, H., Sørensen, J. N., and Jensen, J. J., "Fully coupled three-dimensional dynamic response of a tension-leg platform floating wind turbine in waves and wind," *Journal of Offshore Mechanics and Arctic Engineering*, Vol. 136, No. 2, 2014, pp. 020901.

[69] Cordle, A. and Jonkman, J., "State of the art in floating wind turbine design tools," *Proceedings of the 21st International Offshore and Polar Engineering Conference*, Maui, HI, 2011.

[70] Wayman, E. N., *Coupled dynamics and economic analysis of floating wind turbine systems*, Master's thesis, Massachusetts Institute of Technology, 2006.

[71] Matha, D., "Model development and loads analysis of an offshore wind turbine on a tension leg platform with a comparison to other floating turbine concepts," Tech. Rep. NREL/SR-500-45891, National Renewable Energy Laboratory (NREL), Golden, CO, 2010.

[72] Jonkman, J., "Modeling of the UAE wind turbine for refinement of FAST_AD," Tech. Rep. NREL/TP-500-34755, National Renewable Energy Laboratory, Golden, CO, 2001.

[73] Sclavounos, P., Lee, S., DiPietro, J., Potenza, G., Caramuscio, P., and De Michele, G., "Floating offshore wind turbines: tension leg platform and taught leg buoy concepts supporting 3-5 MW wind turbines," *European Wind Energy Conference EWEC*, Warsaw, Poland, April 2010.

[74] Skaare, B., Hanson, T. D., Nielsen, F. G., Yttervik, R., Hansen, A. M., Thomsen, K., and Larsen, T. J., "Integrated dynamic analysis of floating offshore wind turbines," *European Wind Energy Conference*, Milan, Italy, 2007.

[75] Karimirad, M. and Moan, T., "Stochastic dynamic response analysis of a tension leg spar-type offshore wind turbine," *Wind Energy*, Vol. 16, No. 6, 2013, pp. 953–973.

[76] Karimirad, M. and Moan, T., "Extreme dynamic structural response analysis of catenary moored spar wind turbine in harsh environmental conditions," *Journal of Offshore Mechanics and Arctic Engineering*, Vol. 133, No. 4, 2011.

[77] Triantafyllou, M. S., *Cable mechanics with marine applications*, Lecture notes, Department of Ocean Engineering, Massachusetts Institute of Technology, 1990.

[78] van den Boom, H., "Dynamic behaviour of mooring lines," *Proceedings of Behaviour of Offshore Structures*, 1985, pp. 359–368.

[79] Kreuzer, E. and Wilke, U., "Dynamics of mooring systems in ocean engineering," *Archive of Applied Mechanics*, Vol. 73, No. 3-4, 2003, pp. 270–281.

[80] Buckham, B. J., *Dynamics modelling of low-tension tethers for submerged remotely operated vehicles*, Ph.D. thesis, University of Victoria, 2003.

[81] Masciola, M., Jonkman, J., and Robertson, A., "Extending the capabilities of the mooring analysis program: a survey of dynamic mooring line theories for integration into FAST," *ASME 2014 33rd International Conference on Ocean, Offshore and Arctic Engineering*, Anchorage, Alaska, 2014, pp. V09AT09A032–V09AT09A032.

[82] Jefferys, E. and Patel, M., "On the dynamics of taut mooring systems," *Engineering Structures*, Vol. 4, No. 1, 1982, pp. 37–43.

[83] Buckham, B., Driscoll, F., and Nahon, M., "Development of a finite element cable model for use in low-tension dynamics simulation," *Journal of Applied Mechanics, Transactions ASME*, Vol. 71, No. 4, 2004, pp. 476–485.

[84] Chakrabarti, S., *Handbook of Offshore Engineering (2-volume set)*, Elsevier Science, Illinois, USA, 2005.

[85] Haritos, N., "Introduction to the analysis and design of offshore structures- an overview," *Electronic Journal of Structural Engineering*, Vol. 7, 2007, pp. 55–65.

[86] Manwell, J. F., McGowan, J. G., and Rogers, A. L., *Wind energy explained: theory, design and application*, Wiley, New York, 2010.

[87] Jonkman, J., Butterfield, S., Musial, W., and Scott, G., "Definition of a 5-MW reference wind turbine for offshore system development," Tech. Rep. NREL/TP-500-38060, National Renewable Energy Laboratory, Golden, CO, 2009.

[88] Baruh, H., *Analytical dynamics*, WCB/McGraw-Hill, Boston, 1999.

[89] Meirovitch, L. and Tuzcu, I., "Integrated approach to the dynamics and control of maneuvering flexible aircraft," Tech. Rep. NASA/CR-2003-211748, NASA Langley Research Center, Hampton, VA, 2003.

[90] Meirovitch, L. and Stemple, T., "Hybrid equations of motion for flexible multibody systems using quasicoordinates," *Journal of Guidance, Control, and Dynamics*, Vol. 18, No. 4, 1995, pp. 678–688.

[91] Meirovitch, L., "Hybrid state equations of motion for flexible bodies in terms of quasi-coordinates," *Journal of Guidance, Control, and Dynamics*, Vol. 14, No. 5, 1991, pp. 1008–1013.

[92] Rao, S. S., *Vibration of continuous systems*, Wiley, New York, 2007.

[93] Meirovitch, L., *Fundamentals of vibrations*, McGraw-Hill, Boston, 2001.

[94] Junkins, J. L., *Introduction to dynamics and control of flexible structures*, AIAA, Washington, DC, 1993.

[95] Wilson, J. F., *Dynamics of offshore structures*, Wiley, New York, 2003.

[96] DNV-RP-C205, "Environmental conditions and environmental loads," recommended practice, Det Norske Veritas, April 2007.

[97] Jonkman, J., "Dynamics modeling and loads analysis of an offshore floating wind turbine," Tech. Rep. NREL/TP-500-41958, National Renewable Energy Laboratory, Golden, CO, 2007.

[98] Belenky, V., "On self-repeating effect in reconstruction of irregular waves," *Contemporary ideas on ship stability and capsizing in waves*, Springer, 2011, pp. 589–597.

[99] Sarpkaya, T. and Isaacson, M., *Mechanics of wave forces on offshore structures*, Van Nostrand Reinhold, New York, 1981.

[100] Blevins, R. D., *Formulas for natural frequency and mode shape*, Van Nostrand Reinhold Co., New York, 1979.

[101] Gavassoni, E., Gonalves, P., and Roehl, D., "Nonlinear vibration modes and instability of a conceptual model of a spar platform," *Nonlinear Dynamics*, Vol. 76, No. 1, 2014, pp. 809–826.

[102] Kim, M.-H., *Spar platforms: technology and analysis methods*, American Society of Civil Engineers, 2012.

[103] Blevins, R., *Flow-induced vibration*, Van Nostrand Reinhold, New York, 1990.

[104] Halkyard, J., Sirnivas, S., Holmes, S., Constantinides, Y., Oakley, O. H., and Thiagarajan, K., "Benchmarking of truss spar vortex induced motions derived from CFD with experiments," *ASME 2005 24th International Conference on Offshore Mechanics and Arctic Engineering*, Halkidiki, Greece, 2005, pp. 895–902.

[105] Irani, M. and Finn, L., "Model testing for vortex induced motions of spar platforms," *ASME 2004 23rd International Conference on Offshore Mechanics and Arctic Engineering*, Vancouver, Canada, 2004, pp. 605–610.

[106] van Dijk, R. R., Voogt, A., Fourchy, P., and Mirza, S., "The effect of mooring system and sheared currents on vortex induced motions of truss spars," *ASME 2003 22nd International Conference on Offshore Mechanics and Arctic Engineering*, Cancun, Mexico, 2003, pp. 285–292.

[107] Luo, N., Vidal, Y., and Acho, L., *Wind turbine control and monitoring*, Springer, 2014.

[108] Johnson, K., Pao, L., Balas, M., and Fingersh, L., "Control of variable-speed wind turbines: standard and adaptive techniques for maximizing energy capture," *IEEE Control Systems Magazine*, Vol. 26, No. 3, 2006, pp. 70–81.

[109] Johnson, K. E., "Adaptive torque control of variable speed wind turbines," Tech. Rep. NREL/TP-500-36265, National Renewable Energy Laboratory, Golden, CO, 2004.

[110] Biran, A., *Ship hydrostatics and stability*, Butterworth-Heinemann, Oxford, UK, 2003.

[111] Luo, X.-H., Xiao, R.-C., and Xiang, H.-F., "Cable element based on exact analytical expressions," *Journal of Tongji University*, Vol. 33, No. 4, 2005, pp. 445–450.

[112] Yang, Y. and Tsay, J.-Y., "Geometric nonlinear analysis of cable structures with a two-node cable element by generalized displacement control method," *International Journal of Structural Stability and Dynamics*, Vol. 7, No. 4, 2007, pp. 571–588.

[113] Lee, K. H., *Responses of floating wind turbines to wind and wave excitation*, Master's thesis, Massachusetts Institute of Technology, 2005.

[114] Nahon, M., Gilardi, G., and Lambert, C., "Dynamics/control of a radio telescope receiver supported by a tethered aerostat," *Journal of Guidance, Control, and Dynamics*, Vol. 25, No. 6, 2002, pp. 1107–1115.

[115] Masciola, M. D., *Dynamic analysis of a coupled and an uncoupled tension leg platform*, Ph.D. thesis, McGill University, 2011.

[116] Randolph, M. and Quiggin, P., "Non-linear hysteretic seabed model for catenary pipeline contact," *Proceedings of the ASME 2009 28th International Conference on Ocean, Offshore and Arctic Engineering*, Honolulu, HI, 2009, pp. 145–154.

[117] Aubeny, C. P. and Biscontin, G., "Seafloor-riser interaction model," *International Journal of Geomechanics*, Vol. 9, No. 3, 2009, pp. 133–141.

[118] Orcina Ltd., "OrcaFlex manual," Version 9.7a, 2013.

[119] Taylor, R. and Valent, P., "Design guide for drag embedment anchors," Tech. Rep. N-1688, Naval Civil Engineering Laboratory, Port Hueneme, CA, 1984.

[120] Wu, S., "Adaptive dynamic relaxation technique for static analysis of catenary mooring," *Marine Structures*, Vol. 8, No. 5, 1995, pp. 585–599.

[121] Masciola, M. D., Nahon, M., and Driscoll, F. R., "Static analysis of the lumped mass cable model using a shooting algorithm," *Journal of Waterway, Port, Coastal, and Ocean Engineering*, Vol. 138, No. 2, 2011, pp. 164–171.

[122] Webster, R., "On the static analysis of structures with strong geometric nonlinearity," *Computers and Structures*, Vol. 11, No. 1-2, 1980, pp. 137–145.

[123] MathWorks, “Choose an ODE solver,” `https://www.mathworks.com/help/matlab/math/choose-an-ode-solver.html`, 2017, Accessed on 24.03.2017.

[124] Vorpahl, F., Strobel, M., Jonkman, J., Larsen, T. J., Passon, P., and Nichols, J., “Verification of aero-elastic offshore wind turbine design codes under IEA Wind Task XXIII,” *Wind Energy*, Vol. 17, No. 4, 2014, pp. 519–547.

[125] Statoil, “Statoil to build the worlds first floating wind farm: Hywind Scotland,” `http://www.statoil.com/en/NewsAndMedia/News/2015/Pages/03Nov_HywindScotland_news_page.aspx`, 2015, Accessed on 24.11.2016.

[126] DNV-RP-H103, “Modelling and analysis of marine operations,” recommended practice, Det Norske Veritas, 2011.

[127] Hall, M. and Goupee, A., “Validation of a lumped-mass mooring line model with DeepCwind semisubmersible model test data,” *Ocean Engineering*, Vol. 104, 2015, pp. 590–603.

[128] Masciola, M., Robertson, A., Jonkman, J., Coulling, A., and Goupee, A., “Assessment of the importance of mooring dynamics on the global response of the DeepCwind floating semisubmersible offshore wind turbine,” *The Twenty-third International Offshore and Polar Engineering Conference*, International Society of Offshore and Polar Engineers, 2013.

[129] Schwertassek, R., Wallrapp, O., and Shabana, A., “Flexible multibody simulation and choice of shape functions,” *Nonlinear Dynamics*, Vol. 20, No. 4, 1999, pp. 361–380.

[130] Meirovitch, L. and Kwak, M. K., “Convergence of the classical Rayleigh-Ritz method and the finite element method,” *AIAA journal*, Vol. 28, No. 8, 1990, pp. 1509–1516.

Appendix A

SYSTEM PROPERTIES

A.1 Mass and Inertial Properties of the Platform

Table A.1: Platform dimensions, mass, and inertial properties [6]

Parameter	Value	Unit
m_p	7,466,330	[kg]
I_{px}	4,229,230,000	[kg.m^2]
I_{py}	4,229,230,000	[kg.m^2]
I_{pz}	164,230,000	[kg.m^2]
a	99.9155	[m]
a_{pf}	30.0845	[m]
a_1	108	[m]
a_2	8	[m]
a_3	14	[m]
d_1	9.4	[m]
d_2	6.5	[m]
L_c	120	[m]

A.2 Rigid Body Model Properties

Table A.2: Rigid body model dimensions, mass, and inertial properties [6]

Parameter	**Value**	**Unit**
m_t	249646	[kg]
I_{tx}	120213488	[kg.m^2]
I_{ty}	120213488	[kg.m^2]
I_{tz}	1817977	[kg.m^2]
m_{nc}	240,000	[kg]
I_{ncx}	4,901,094	[kg.m^2]
I_{ncy}	22,785	[kg.m^2]
I_{ncz}	2,607,890	[kg.m^2]
m_r	110,000	[kg]
I_{rx}	38,759,228	[kg.m^2]
I_{ry}	19379614	[kg.m^2]
I_{rz}	19379614	[kg.m^2]
d_r	5.462	[m]
d_{nc}	1.90	[m]
D_t	133.3463	[m]
D_r	179.5670	[m]

A.3 Flexible Tower Properties

The tower is modeled as a cylindrical hollow tapered beam of height $l = 77.6$ m, as shown in Figure A.1. Based on that data in [6, 87], the tower base external diameter is $D_o(0) = 6.5$ m and the tip diameter $D_o(l) = 3.87$ m. The tower structure thickness is linearly varying with tower height (z). The base thickness, $t_{tw}(0) = 0.027$ m, and at the tip $t_{tw}(l) = 0.019$ m. Therefore, the tower thickness and external and internal diameter can be expressed as functions of z

$$\begin{aligned} t_{tw}(z) &= 0.027 - (0.008/77.6)\,z \\ D_o(z) &= 6.5 - (2.63/77.6)\,z \\ D_i(z) &= D_o - 2\,t_{tw}(z) \end{aligned} \tag{A.1}$$

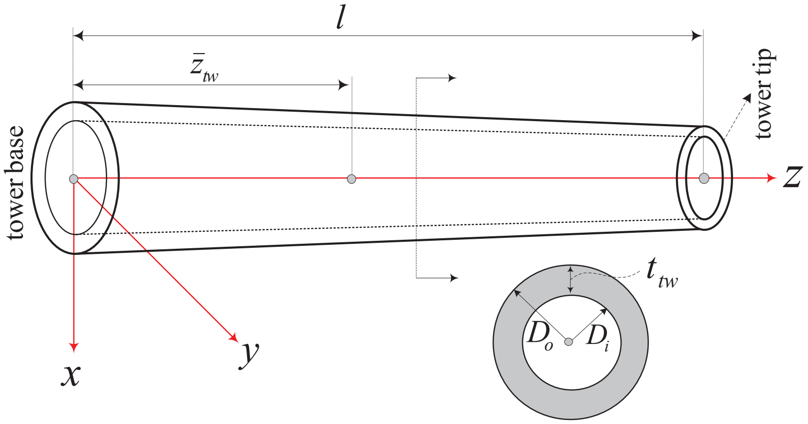

Figure A.1: Tower structure

The effective tower structure density is $\rho_t = 8500$ kg/m^3. The mass per unit length of the tower is

$$\bar{m}_t(z) = \rho_t A_t = \rho_t(\pi/4)(D_o^2 - D_i^2) = \rho_t \pi t_{tw}(D_o - t_{tw}) \tag{A.2}$$

$\bar{m}_t(z)$ is quadratic in z which can be obtained by substituting Equation (A.1) into Equation (A.2). The tower cross section second moment of area and polar moment of inertia area as functions of z are

$$\begin{aligned} I_{t,xx} = I_{t,yy} = &\quad (\pi/64)(D_o^4 - D_i^4) \\ J_t = I_{t,xx} + I_{t,yy} = &\quad (\pi/32)(D_o^4 - D_i^4) \end{aligned} \tag{A.3}$$

Similarly, substituting Equation (A.1) into Equation (A.3) to find the final form as function of z. The tower Young's modulus is E=210 GPa and the shear modulus is G=80.8 GPa. The tower mass can be calculated as

$$m_t = \int_0^l \bar{m}_t dz = 249646 \text{ kg} \tag{A.4}$$

and the center of gravity of the undeformed tower is

$$\bar{z}_{tw} = \frac{1}{m_t} \int_0^l z\, \bar{m}_t dz = 33.3463 \text{ m} \tag{A.5}$$

The mass moment of inertia of the tower structure around the tower base center about the x and y axes can be calculated as

$$I_{txb} = I_{tyb} = \int_0^l \left(\rho_t I_{t,xx} + \bar{m}_t z^2\right) dz \tag{A.6}$$

The mass moment of inertia of the tower structure around its center of gravity $(0, 0, \bar{z}_{tw})$ can be calculated using the parallel axis theorem as

$$I_{tx} = I_{ty} = I_{txb} - m_t\, \bar{z}_{tw}^2 = 120213488 \text{ kg.m}^2 \tag{A.7}$$

The mass moment of inertia of the tower structure around z axis can be calculated as

$$I_{tz} = \int_0^l \rho_t\ J_t\ dz = 1817977 \text{ kg.m}^2 \tag{A.8}$$

A.4 Mooring System Properties

A.4.1 Single configuration

The single mooring system properties listed in Table A.3 ass

Table A.3: Platform dimensions, mass, and inertial properties [6]

Parameter	**Symbol**	**Value**	**Unit**
Water Depth	d_w	320	[m]
fairlead Depth Below MWL	D	70	[m]
Anchors radius	d_w	853.87	[m]
fairlead radius	R_f	5.2	[m]
Unstretched line length	L_0	902.2	[m]
Cable diameter	d_c	0.09	[m]
Mass per unit length	$\bar{m}_c$	77.7066	[kg/m]
Equivalent weight in water	w	698.094	[N/m]
Extensional stiffness	EA	384,243,000	[N]

A.4.2 Bridle configuration

The properties of the bridle configuration are similar except for $\bar{m}_c$ and w which are illustrated for the bridle configuration in Table A.4. The clump weight length and diameter are 2 and 1.67 m, respectively.

Table A.4: Bridle mooring system properties [7]

Component	**Unstretched length [m]**	**Weight/length in water [N/m]**	**Mass/length [kg/m]**
Bridle line (segments 1 and 2)	$L_{0\Delta}$=50	353.2	42.525
Main line (segment 3)	L_{03}=850.2 ($s1 = 250.2$)	353.2	42.525
Clump weight	2	147.15×10^3	17252.7

Appendix B

ASSUMED MODE METHOD: SHAPE FUNCTIONS AND CONVERGENCE

B.1 Orthogonal Polynomial Shape Functions of a Cantilever Beam

$$\Phi_1 = \frac{1}{3}\hat{z}^4 - \frac{4}{3}\hat{z}^3 + 2\,\hat{z}^2$$

$$\Phi_2 = \frac{182}{19}\hat{z}^5 - \frac{661}{19}\hat{z}^4 + \frac{824}{19}\hat{z}^3 - \frac{326}{19}\;\hat{z}^2$$

$$\Phi_3 = \frac{57376}{595}\hat{z}^6 - \frac{218966}{595}\hat{z}^5 + \frac{61163}{119}\hat{z}^4 - \frac{36224}{119}\hat{z}^3 + \frac{7498}{119}\hat{z}^2$$

$$\Phi_4 = \frac{2124096}{3467}\hat{z}^7 - \frac{44146336}{17335}\hat{z}^6 + \frac{70839756}{17335}\hat{z}^5 - \frac{10829283}{3467}\hat{z}^4 + \frac{3879604}{3467}\hat{z}^3 - \frac{509634}{3467}\;\hat{z}^2$$

$$\begin{aligned}\Phi_5 =& \frac{93617550}{28631}\hat{z}^8 - \frac{426344880}{28631}\hat{z}^7 + \frac{3896636744}{143155}\hat{z}^6 - \frac{3625862604}{143155}\hat{z}^5 + \frac{358055847}{28631}\hat{z}^4\\ & - \frac{87557156}{28631}\hat{z}^3 + \frac{8102442}{28631}\;\hat{z}^2\end{aligned}$$

$$\begin{aligned}\Phi_6 =& \frac{132109516}{8285}\hat{z}^9 - \frac{658061874}{8285}\hat{z}^8 + \frac{1354376928}{8285}\hat{z}^7 - \frac{296469656}{1657}\hat{z}^6 + \frac{923419434}{8285}\hat{z}^5\\ & - \frac{323567649}{8285}\hat{z}^4 + \frac{58114976}{8285}\hat{z}^3 - \frac{4034766}{8285}\;\hat{z}^2\end{aligned}$$

$$\begin{aligned}
\Phi_7 =& \frac{270583104}{3673}\hat{z}^{10} - \frac{1468232524}{3673}\hat{z}^{9} + \frac{3365779806}{3673}\hat{z}^{8} - \frac{4232857152}{3673}\hat{z}^{7} + \frac{53909627240}{62441}\hat{z}^{6} \\
& - \frac{24410987874}{62441}\hat{z}^{5} + \frac{6446071527}{62441}\hat{z}^{4} - \frac{892809928}{62441}\hat{z}^{3} + \frac{48516498}{62441}\hat{z}^{2} \\
\Phi_8 =& \frac{772787453568}{2352305}\hat{z}^{11} - \frac{4546300328768}{2352305}\hat{z}^{10} + \frac{2299894902888}{470461}\hat{z}^{9} - \frac{3266942071374}{470461}\hat{z}^{8} \\
& + \frac{2854994608848}{470461}\hat{z}^{7} - \frac{7900287408104}{2352305}\hat{z}^{6} + \frac{2742861301264}{2352305}\hat{z}^{5} - \frac{113790293047}{470461}\hat{z}^{4} \\
& + \frac{12582969436}{470461}\hat{z}^{3} - \frac{551849882}{470461}\hat{z}^{2} \\
\Phi_9 =& \frac{1399974687111}{979273}\hat{z}^{12} - \frac{44435634369828}{4896365}\hat{z}^{11} + \frac{123016536600518}{4896365}\hat{z}^{10} - \frac{38955270772748}{979273}\hat{z}^{9} \\
& + \frac{38871180318699}{979273}\hat{z}^{8} - \frac{25386245096088}{979273}\hat{z}^{7} + \frac{54529489623084}{4896365}\hat{z}^{6} - \frac{15068499195064}{4896365}\hat{z}^{5} \\
& + \frac{506189488807}{979273}\hat{z}^{4} - \frac{45868003196}{979273}\hat{z}^{3} + \frac{1661824946}{979273}\hat{z}^{2} \\
\Phi_{10} =& \frac{131486440250}{21513}\hat{z}^{13} - \frac{896628649475}{21513}\hat{z}^{12} + \frac{4496527093448}{35855}\hat{z}^{11} - \frac{7852396284898}{35855}\hat{z}^{10} \\
& + \frac{1761079340218}{7171}\hat{z}^{9} - \frac{1324679063589}{7171}\hat{z}^{8} + \frac{677758634528}{7171}\hat{z}^{7} - \frac{1170155714244}{35855}\hat{z}^{6} \\
& + \frac{5027239676826}{681245}\hat{z}^{5} - \frac{419860718569}{408747}\hat{z}^{4} + \frac{31815241672}{408747}\hat{z}^{3} - \frac{323318738}{136249}\hat{z}^{2}
\end{aligned}$$

B.2 AMM Convergence

The AMM convergence is mainly dependent on the choice of mode shapes [94, 129, 130]. According to the problem type, different families of mode shapes may may change the convergence performance. Thus, it is important to examine the convergence of the selected mode shape used to discretize the elastic motion of FOWT system prior to performing the dynamic simulation. The applicability of the developed orthogonal polynomial comparison functions is examined here by analyzing the dynamics of a spinning cantilever beam with a tip point mass, as shown in Figure B.1. This is a well-known problem typically used in flexible dynamics research for analysis and validation [51]. As well, it resembles the FOWT flexible structure under consideration. The beam spins with angular velocity $\Omega_b(t)$ around the z-axis, expressed as [51, 55]

$$\Omega_b = \begin{cases} \Omega_s \left[\tau - (1/2\pi)\sin(2\pi\tau)\right] & \text{for} \quad 0 \leq \tau \leq 1 \\ \Omega_s & \text{for} \quad \tau \geq 1 \end{cases} \tag{B.1}$$

where the xyz frame is attached to the beam, $\tau = t/T_s$, $T_s = 15$ s, and $\Omega_s = 6$ rad/s. The coupled bending (u_2) and longitudinal motions (u_1) (resulting from the shortening due to bending and expansion due to stretch (s)) of the cantilever beam are considered. The stretch (s) is discretized in space using two eigen mode shapes corresponding to the longitudinal vibration of a fixed free bar which are similar to the form in Equation (2.32), while the bending u_2 is discretized in space using three orthogonal polynomial comparison functions developed herein.

The bending deflection response of the tip mass, u_2, is compared with the results of Cai et al. [4] where they analyzed the problem using a FEM, as shown in Figure B.2. The result of the present approach utilizing the AMM with the polynomial mode shapes developed herein shows excellent agreement with the results of [4]. This gives a strong indication that these polynomials can be efficiently used to discretize the bending elastic motions of the FOWT flexible model in space.

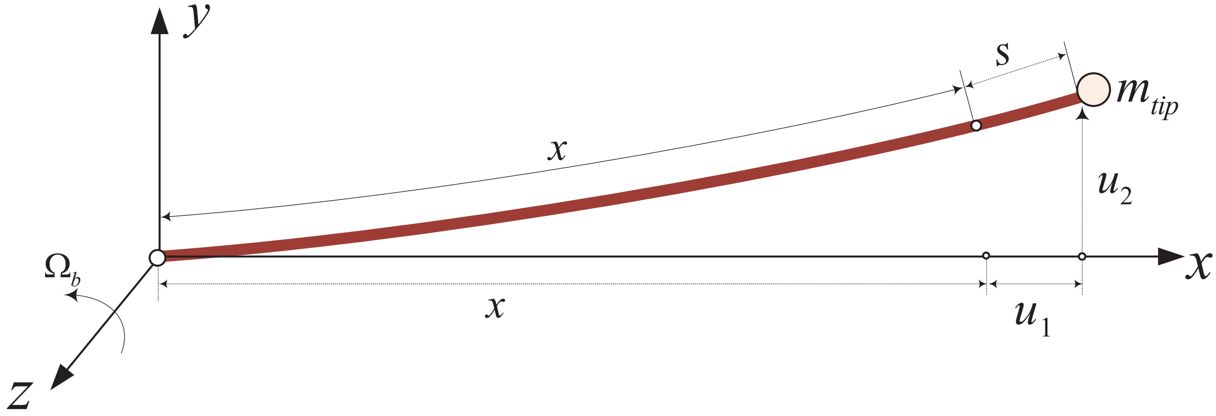

Figure B.1: Spinning cantilever beam with a tip mass (beam deflections are in the xy plane). Length l=8 m, density =2.7667×10^3 kg/m^3, Young's modulus $E = 6.8952\times10^{10}$ Pa, cross sectional area $A = 7.2968 \times 10^{-5}$ m^2, moment of inertia of the cross section $I_{yy} = I_{zz}= 8.2189 \times 10^{-9}$ m^4, and $m_{tip} = 0.085$ kg [4]

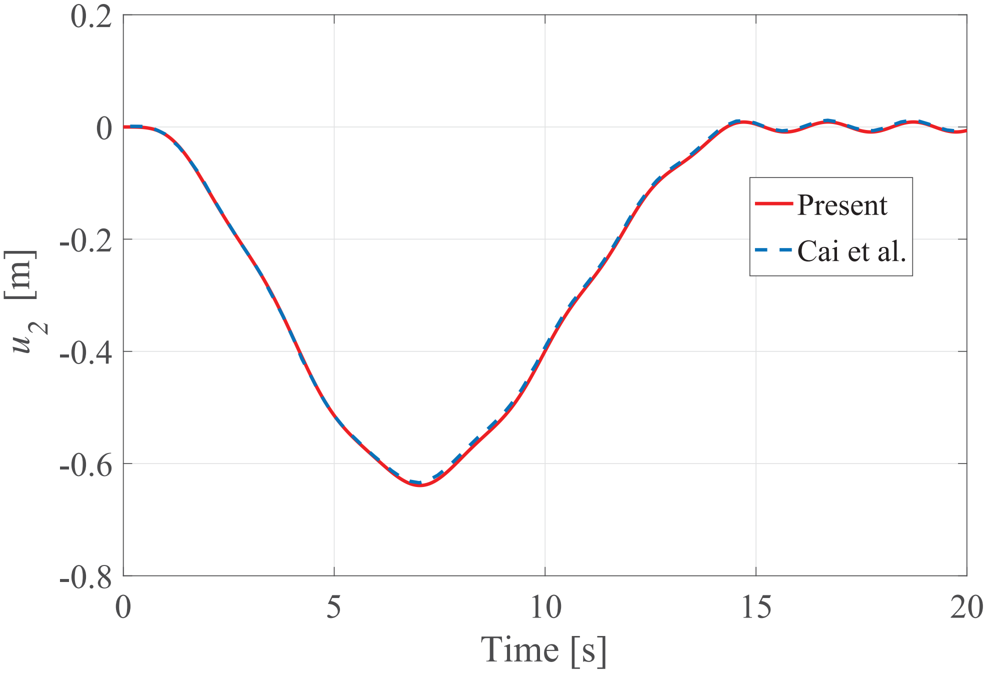

Figure B.2: Bending response of a rotating cantilever beam with a point tip mass

Appendix C

HYDROSTATIC CALCULATIONS

C.1 Hydrostatic Stiffness Matrix

The submerged length and its partial derivatives with respect to the heave displacement and Euler angles are

$$\begin{gathered} L_{cf} = \left(L_c - r_Z + z_f + x_f\, s_\theta - z_f\, c_\phi\, c_\theta - y_f\, s_\phi\, c_\theta\right)/\left(c_\phi\, c_\theta\right) \\ \frac{\partial L_{cf}}{\partial r_Z} = -\frac{1}{c_\phi\, c_\theta} \quad , \quad \frac{\partial L_{cf}}{\partial \phi} = \frac{\left(L_c - r_Z + z_f\right) s_\phi}{c_\phi^2\, c_\theta} + \frac{t_\theta\, s_\phi}{c_\phi^2} x_f - \frac{y_f}{c_\phi^2} \\ \frac{\partial L_{cf}}{\partial \theta} = \frac{\left(L_c - r_Z + z_f\right) s_\theta}{c_\theta^2\, c_\phi} + \frac{x_f}{c_\theta^2\, c_\phi} \quad , \quad \frac{\partial L_{cf}}{\partial \psi} = 0 \end{gathered} \tag{C.1}$$

The partial derivatives of X_F and Y_F with respect to the heave and Euler angles are

$$\begin{aligned} \frac{\partial X_F}{\partial \phi} &= \left(s_\phi\, s_\psi + c_\phi s_\theta\, c_\psi\right)\left(0.5\, \frac{\partial L_{cf}}{\partial \phi} + y_f\right) + \left(z_f + 0.5 L_{cf}\right)\left(c_\phi\, s_\psi - s_\phi\, s_\theta\, c_\psi\right) \\ \frac{\partial X_F}{\partial \theta} &= 0.5 \frac{\partial L_{cf}}{\partial \theta}\left(s_\phi\, s_\psi + c_\phi\, s_\theta\, c_\psi\right) + c_\phi\, c_\theta\, c_\psi\left(z_f + 0.5 L_{cf}\right) + y_f\, s_\phi\, c_\theta\, c_\psi - x_f\, s_\theta\, c_\psi \\ \frac{\partial X_F}{\partial \theta} &= 0.5 \frac{\partial L_{cf}}{\partial \theta}\left(s_\phi\, s_\psi + c_\phi\, s_\theta\, c_\psi\right) + c_\phi\, c_\theta\, c_\psi\left(z_f + 0.5 L_{cf}\right) + y_f\, s_\phi\, c_\theta\, c_\psi - x_f\, s_\theta\, c_\psi \\ \frac{\partial X_F}{\partial \psi} &= -y_f\left(c_\phi\, c_\psi + s_\phi\, s_\theta\, s_\psi\right) - x_f\, c_\theta\, s_\psi + \left(z_f + 0.5 L_{cf}\right)\left(s_\phi\, c_\psi - c_\phi\, s_\theta\, s_\psi\right) \\ \frac{\partial Y_F}{\partial r_Z} &= -0.5\left(s_\phi\, c_\psi - c_\phi\, s_\theta\, s_\psi\right)\frac{\partial L_{cf}}{\partial r_Z} \\ \frac{\partial Y_F}{\partial \phi} &= 0.5 \frac{\partial L_{cf}}{\partial \phi}\left(c_\phi s_\theta\, s_\psi - s_\phi\, c_\psi\right) + y_f\left(c_\phi\, s_\theta\, s_\psi - s_\phi\, c_\psi\right) - \left(c_\phi\, c_\psi + s_\phi\, s_\theta\, s_\psi\right)\left(z_f + 0.5 L_{cf}\right) \\ \frac{\partial Y_F}{\partial \theta} &= 0.5 \frac{\partial L_{cf}}{\partial \theta}\left(s_\phi\, c_\psi - c_\phi\, s_\theta\, s_\psi\right) + y_f\, s_\phi\, c_\theta\, s_\psi - x_f\, s_\theta\, s_\psi + c_\phi\, c_\theta\, s_\psi\left(z_f + 0.5 L_{cf}\right) \\ \frac{\partial Y_F}{\partial \psi} &= \left(s_\phi\, s_\psi + c_\phi\, s_\theta\, c_\psi\right)\left(z_f + 0.5 L_{cf}\right) + \left(s_\phi\, s_\theta\, c_\psi - c_\phi s_\psi\right) y_f + c_\theta\, c_\psi x_f \end{aligned} \tag{C.2}$$

The buoyancy stiffness matrix coefficients (third row) are

$$K_B^{33} = \frac{\rho g\, A_c}{c_\phi c_\theta}, \quad K_B^{34} = -\rho g\, A_c \,\frac{\partial L_{cf}}{\partial \phi}, \quad K_B^{35} = -\rho g\, A_c \,\frac{\partial L_{cf}}{\partial \theta}\,, \quad K_B^{36} = 0 \tag{C.3}$$

The buoyancy stiffness matrix coefficients (4th row) are

$$\begin{aligned}
K_B^{43} &= -F_B \frac{\partial Y_F}{\partial r_Z} - Y_F \frac{\partial F_B}{\partial r_Z} = -F_B \frac{\partial Y_F}{\partial r_Z} + Y_F K_B^{33} \\
K_B^{44} &= -\left[M_{wp}^y + \tfrac{\partial M_{wp}^z}{\partial \phi}\right](s_\phi\, s_\psi + c_\phi\, s_\theta\, c_\psi) + Y_F K_B^{34} - F_B \tfrac{\partial Y_F}{\partial \phi} \\
&\quad - \left[\tfrac{\partial M_{wp}^y}{\partial \phi} - M_{wp}^z\right](s_\phi\, s_\theta\, c_\psi - c_\phi\, s_\psi) - \tfrac{\partial M_{wp}^x}{\partial \phi} c_\theta\, c_\psi \\
K_B^{45} &= -\tfrac{\partial M_{wp}^z}{\partial \theta}\,(s_\phi\, s_\psi + c_\phi\, s_\theta\, c_\psi) + Y_F K_B^{35} - \tfrac{\partial M_{wp}^y}{\partial \theta}\,(s_\phi\, s_\theta\, c_\psi - c_\phi\, s_\psi) - F_B \tfrac{\partial Y_F}{\partial \theta} + M_{wp}^x\, s_\theta\, c_\psi \\
&\quad - \tfrac{\partial M_{wp}^x}{\partial \theta} c_\theta\, c_\psi - M_{wp}^z\, c_\phi\, c_\theta\, c_\psi - M_{wp}^y\, s_\phi\, c_\theta\, c_\psi \\
K_B^{46} &= -M_{wp}^z\,(s_\phi\, c_\psi - c_\phi\, s_\theta\, s_\psi) + M_{wp}^y\,(c_\phi\, c_\psi + s_\phi\, s_\theta\, s_\psi) - F_B \frac{\partial Y_F}{\partial \psi} + M_{wp}^x\, c_\theta\, s_\psi
\end{aligned} \tag{C.4}$$

The buoyancy stiffness matrix coefficients (5th row) are

$$\begin{aligned}
K_B^{53} &= F_B \frac{\partial X_F}{\partial r_Z} - X_F K_B^{33} \\
K_B^{54} &= F_B \frac{\partial X_F}{\partial \phi} - X_F K_B^{34} - \left[M_{wp}^y + \frac{\partial M_{wp}^z}{\partial \phi}\right](c_\phi\, s_\theta\, s_\psi - s_\phi\, c_\psi) \\
&\quad - \left[\frac{\partial M_{wp}^y}{\partial \phi} - M_{wp}^z\right](c_\phi\, c_\psi + s_\phi\, s_\theta\, s_\psi) - \frac{\partial M_{wp}^x}{\partial \phi}\; c_\theta s_\psi \\
K_B^{55} &= F_B \frac{\partial X_F}{\partial \theta} - X_F K_B^{35} - \frac{\partial M_{wp}^y}{\partial \theta}\,(c_\phi\, c_\psi + s_\phi\, s_\theta\, s_\psi) - \frac{\partial M_{wp}^z}{\partial \theta}\,(c_\phi\, s_\theta\, s_\psi - s_\phi c_\psi) + M_{wp}^x\, s_\theta\, s_\psi \\
&\quad - \frac{\partial M_{wp}^x}{\partial \theta}\; c_\theta\, s_\psi - M_{wp}^z\, c_\phi\, c_\theta\, s_\psi - M_{wp}^y\, s_\phi\, c_\theta\, s_\psi \\
K_B^{56} &= F_B \frac{\partial X_F}{\partial \psi} - M_{wp}^y\,(s_\phi\, s_\theta\, c_\psi - c_\phi\, s_\psi) - M_{wp}^z\,(s_\phi\, s_\psi + c_\phi\, s_\theta\, c_\psi) - M_{wp}^x\, c_\theta\, c_\psi
\end{aligned} \tag{C.5}$$

The weight restoring stiffness matrix $\mathbf{K}_G$ enteries are

$$
\begin{aligned}
K_G^{44} &= -W_c\,\left[y_g\,(s_\phi\,c_\psi - c_\phi\,s_\theta\,s_\psi) + \,z_g\,(c_\phi\,c_\psi + s_\phi\,s_\theta\,s_\psi)\right] \\
K_G^{45} &= W_c\,s_\psi\,(\,z_g c_\phi\,c_\theta - x_g s_\theta + y_g\,s_\phi\,c_\theta) \\
K_G^{46} &= W_c\,\left[z_g\,(s_\phi\,s_\psi + c_\phi\,s_\theta\,c_\psi) - y_g\,(c_\phi\,s_\psi - s_\phi\,s_\theta\,c_\psi) + \,x_g\,c_\theta\,c_\psi\right] \\
K_G^{54} &= -W_c\,\left[y_g\,(s_\phi\,s_\psi + c_\phi\,s_\theta\,c_\psi) + \,z_g\,(c_\phi\,s_\psi - s_\phi\,s_\theta\,c_\psi)\right] \\
K_G^{55} &= -W_c\,c_\psi\,(\,z_g\,c_\phi\,c_\theta - x_g\,s_\theta + y_g\,s_\phi\,c_\theta) \\
K_G^{56} &= W_c\,\left[y_g\,(c_\phi\,c_\psi + s_\phi\,s_\theta\,s_\psi) - \,z_g\,(s_\phi\,c_\psi - c_\phi\,s_\theta\,s_\psi) + \,x_g\,c_\theta\,s_\psi\right]
\end{aligned}
\tag{C.6}
$$

C.2 Method of Calculating V_d, a_{CV} and I_{add}

The variation of the diameter of the submerged volume as shown in Figure 2.8 can be expressed as

$$
d(z) = \begin{cases}
d_1 & \text{for} \quad z \le a_1 \\
d_1 + \frac{d_2 - d_1}{a_2}\,(z - a_1) & \text{for} \quad a_1 < z \le a_1 + a_2 \\
d_2 & \text{for} \quad a_1 + a_2 < z \le a_1 + a_2 + a_3 \\
d_2 + \frac{d_{tip} - d_2}{l}\,(z - a_1 - a_2 - \; a_3) & \text{for} \quad z > a_1 + a_2 + a_3
\end{cases}
\tag{C.7}
$$

where d_{tip} is the tower tip diameter. The last inequality considers the case when the tower sinks in water. The submerged length L_{cf} can be calculated from Equation (3.42). The submerged volume V_d can be expressed as

$$
V_d = \int_0^{L_{cf}} A_c\,dz \tag{C.8}
$$

where the platform cross section area is $A_c = (\pi/4)d^2(z)$. The center of the submerged volume position relative to the platform base is

$$a_{CV} = \frac{1}{V_d} \int_0^{L_{cf}} z\, A_c\, dz \tag{C.9}$$

The moment of inertia of the platform cross section area is $I_c(z) = (\pi/64)d^4(z)$. Thus, the mass moment of inertia of the displaced volume around the platform base center about axes parallel to x and y can be calculated as

$$I_{bb} = \rho \int_0^{L_{cf}} \left(I_c + z^2 A_c\right) dz \tag{C.10}$$

The added inertia I_{aa} around the origin of the platform frame (xyz) can be obtained using the parallel axis theorem

$$I_{add} = I_{bb} - \rho V_d\, a_{pf}\, (a_{pf} - a_{CV}) \tag{C.11}$$

The integrands in the integrals of Equations (C.8) to (C.10) are piecewise functions based on Equation (C.7).

Appendix D

MOORING STIFFNESS MATRIX

The mooring stiffness matrix ($\mathbf{K}_m$) coefficients (1st row)

$$\begin{aligned}
K_{11} &= -\frac{\partial T_X}{\partial r_X} = \cos\beta \frac{\partial H}{\partial l}\frac{\partial l}{\partial r_X} - H\sin\beta\frac{\partial \beta}{\partial r_X} = K^p_{11}\cos^2\beta + \frac{H}{l}\sin^2\beta \\
K_{12} &= -\frac{\partial T_X}{\partial r_Y} = \sin\beta\cos\beta\left(K^p_{11} - \frac{H}{l}\right) \\
K_{13} &= -\frac{\partial T_X}{\partial r_Z} = \cos\beta\frac{\partial H}{\partial r_Z} = \cos\beta\, K^p_{12} \\
K_{14} &= -\frac{\partial T_X}{\partial \phi} = \cos\beta\frac{\partial H}{\partial \phi} - H\sin\beta\frac{\partial \beta}{\partial \phi} = \cos\beta\left(K^p_{11}\frac{\partial l}{\partial \phi} + K^p_{12}\frac{\partial h}{\partial \phi}\right) - H\sin\beta\frac{\partial\beta}{\partial\phi} \\
K_{15} &= -\frac{\partial T_X}{\partial \theta} = \cos\beta\left(K^p_{11}\frac{\partial l}{\partial \theta} + K^p_{12}\frac{\partial h}{\partial \theta}\right) - H\sin\beta\frac{\partial\beta}{\partial\theta} \\
K_{16} &= -\frac{\partial T_X}{\partial \psi} = \cos\beta\left(K^p_{11}\frac{\partial l}{\partial \psi} + K^p_{12}\frac{\partial h}{\partial \psi}\right) - H\sin\beta\frac{\partial\beta}{\partial\psi}
\end{aligned} \tag{D.1}$$

The coefficients of the 2nd row

$$\begin{aligned}
K_{21} &= -\frac{\partial T_Y}{\partial r_X} = K_{12} \\
K_{22} &= -\frac{\partial T_Y}{\partial r_Y} = \sin^2\beta\ K^p_{11} + \cos^2\beta\frac{H}{l} \\
K_{23} &= -\frac{\partial T_Y}{\partial r_Z} = \frac{\partial(H\sin\beta\,)}{\partial r_Z} = \sin\beta\, K^p_{12} \\
K_{24} &= -\frac{\partial T_Y}{\partial \phi} = \sin\beta\left(K^p_{11}\frac{\partial l}{\partial \phi} + K^p_{12}\frac{\partial h}{\partial \phi}\right) + H\cos\beta\frac{\partial\beta}{\partial\phi} \\
K_{25} &= -\frac{\partial T_Y}{\partial \theta} = \sin\beta\left(K^p_{11}\frac{\partial l}{\partial \theta} + K^p_{12}\frac{\partial h}{\partial \theta}\right) + H\cos\beta\frac{\partial\beta}{\partial\theta} \\
K_{26} &= -\frac{\partial T_Y}{\partial \psi} = \sin\beta\left(K^p_{11}\frac{\partial l}{\partial \psi} + K^p_{12}\frac{\partial h}{\partial \psi}\right) + H\cos\beta\frac{\partial\beta}{\partial\psi}
\end{aligned} \tag{D.2}$$

The coefficients of the 3rd row

$$\begin{aligned}
K_{31} =& -\frac{\partial T_Z}{\partial r_X} = K_{13} \\
K_{32} =& -\frac{\partial T_Z}{\partial r_Y} = K_{23} \\
K_{33} =& K_{22}^p \\
K_{34} =& -\frac{\partial T_Z}{\partial \phi} = \left(K_{21}^p \frac{\partial l}{\partial \phi} + K_{22}^p \frac{\partial h}{\partial \phi} \right) \\
K_{35} =& -\frac{\partial T_Z}{\partial \theta} = \left(K_{21}^p \frac{\partial l}{\partial \theta} + K_{22}^p \frac{\partial h}{\partial \theta} \right) \\
K_{36} =& -\frac{\partial T_Z}{\partial \psi} = \left(K_{21}^p \frac{\partial l}{\partial \psi} + K_{22}^p \frac{\partial h}{\partial \psi} \right)
\end{aligned} \tag{D.3}$$

The coefficients of the 4th row

$$\begin{aligned}
K_{41} =& -\frac{\partial M_X}{\partial r_X} = \left(Y_p - r_Y\right) \frac{\partial T_Z}{\partial r_X} - \left(Z_p - r_Z\right) \frac{\partial T_Y}{\partial r_X} = \left(Y_p - r_Y\right) K_{31} - \left(Z_p - r_Z\right) K_{21} \\
K_{42} =& -\frac{\partial M_X}{\partial r_Y} = \left(Y_p - r_Y\right) K_{32} - \left(Z_p - r_Z\right) K_{22} \\
K_{43} =& -\frac{\partial M_X}{\partial r_Z} = \left(Y_p - r_Y\right) K_{33} - \left(Z_p - r_Z\right) K_{23} \\
K_{44} =& -\frac{\partial M_X}{\partial \phi} = \left(Y_p - r_Y\right) K_{34} - \left(Z_p - r_Z\right) K_{24} + V \frac{\partial Y_p}{\partial \phi} - H \sin\beta \frac{\partial Z_p}{\partial \phi} \\
K_{45} =& -\frac{\partial M_X}{\partial \theta} = \left(Y_p - r_Y\right) K_{35} - \left(Z_p - r_Z\right) K_{25} + V \frac{\partial Y_p}{\partial \theta} - H \sin\beta \frac{\partial Z_p}{\partial \theta} \\
K_{46} =& -\frac{\partial M_X}{\partial \psi} = \left(Y_p - r_Y\right) K_{36} - \left(Z_p - r_Z\right) K_{26} + V \frac{\partial Y_p}{\partial \psi} - H \sin\beta \frac{\partial Z_p}{\partial \psi}
\end{aligned} \tag{D.4}$$

The coefficients of the 5th row

$$
\begin{aligned}
K_{51} &= -\frac{\partial M_Y}{\partial r_X} = (Z_p - r_Z)\,K_{11} - (X_p - r_X)\,K_{31} \\
K_{52} &= -\frac{\partial M_Y}{\partial r_Y} = (Z_p - r_Z)\,K_{12} - (X_p - r_X)\,K_{32} \\
K_{53} &= -\frac{\partial M_Y}{\partial r_Z} = (Z_p - r_Z)\,K_{13} - (X_p - r_X)\,K_{33} \\
K_{54} &= -\frac{\partial M_Y}{\partial \phi} = (Z_p - r_Z)\,K_{14} - (X_p - r_X)\,K_{34} + H\cos\beta\frac{\partial Z_p}{\partial \phi} - V\frac{\partial X_p}{\partial \phi} \\
K_{55} &= -\frac{\partial M_Y}{\partial \theta} = (Z_p - r_Z)\,K_{15} - (X_p - r_X)\,K_{35} + H\cos\beta\frac{\partial Z_p}{\partial \theta} - V\frac{\partial X_p}{\partial \theta} \\
K_{56} &= -\frac{\partial M_Y}{\partial \psi} = (Z_p - r_Z)\,K_{16} - (X_p - r_X)\,K_{36} + H\cos\beta\frac{\partial Z_p}{\partial \psi} - V\frac{\partial X_p}{\partial \psi}
\end{aligned}
\tag{D.5}
$$

The coefficients of the 6th row

$$
\begin{aligned}
K_{61} &= -\frac{\partial M_Z}{\partial r_X} = (X_p - r_X)\,K_{21} - (Y_p - r_Y)\,K_{11} = K_{16} \\
K_{62} &= -\frac{\partial M_Z}{\partial r_Y} = (X_p - r_X)\,K_{22} - (Y_p - r_Y)\,K_{12} = K_{26} \\
K_{63} &= -\frac{\partial M_Z}{\partial r_Z} = (X_p - r_X)\,K_{23} - (Y_p - r_Y)\,K_{13} = K_{36} \\
K_{64} &= -\frac{\partial M_Z}{\partial \phi} = (X_p - r_X)\,K_{24} - (Y_p - r_Y)\,K_{14} + H\sin\beta\frac{\partial X_p}{\partial \phi} - H\cos\beta\frac{\partial Y_p}{\partial \phi} \\
K_{65} &= -\frac{\partial M_Z}{\partial \theta} = (X_p - r_X)\,K_{25} - (Y_p - r_Y)\,K_{15} + H\sin\beta\frac{\partial X_p}{\partial \theta} - H\cos\beta\frac{\partial Y_p}{\partial \theta} \\
K_{66} &= -\frac{\partial M_Z}{\partial \psi} = (X_p - r_X)\,K_{26} - (Y_p - r_Y)\,K_{16} + H\sin\beta\frac{\partial X_p}{\partial \psi} - H\cos\beta\frac{\partial Y_p}{\partial \psi}
\end{aligned}
\tag{D.6}
$$

The mooring line attachment point P displacement ($\mathbf{r}_m$) partial derivatives with respect to rotational displacements (Equation (4.34)), can be expressed as

$$
\begin{gathered}
\begin{bmatrix} \frac{\partial X_p}{\partial \phi} \\ \frac{\partial Y_p}{\partial \phi} \\ \frac{\partial Z_p}{\partial \phi} \end{bmatrix} = \begin{bmatrix} -c_\psi \, s_\theta & c_\psi \, c_\theta \, s_\phi & c_\psi \, c_\theta \, c_\phi \\ -s_\psi \, s_\theta & s_\psi \, c_\theta \, s_\phi & s_\psi \, c_\theta \, c_\phi \\ -c_\theta & -s_\theta \, s_\phi & -s_\theta \, c_\phi \end{bmatrix} \begin{bmatrix} x_{po} \\ y_{po} \\ z_{po} \end{bmatrix} \\
\begin{bmatrix} \frac{\partial X_p}{\partial \theta} \\ \frac{\partial Y_p}{\partial \theta} \\ \frac{\partial Z_p}{\partial \theta} \end{bmatrix} = \begin{bmatrix} 0 & c_\psi \, s_\theta \, c_\phi + s_\psi \, s_\phi & -c_\psi \, s_\theta \, s_\phi + s_\psi \, c_\phi \\ 0 & s_\psi \, s_\theta \, c_\phi - c_\psi \, s_\phi & -s_\psi \, s_\theta \, s_\phi - c_\psi \, c_\phi \\ 0 & c_\theta \, c_\phi & -c_\theta \, s_\phi \end{bmatrix} \begin{bmatrix} x_{po} \\ y_{po} \\ z_{po} \end{bmatrix} \\
\begin{bmatrix} \frac{\partial X_p}{\partial \psi} \\ \frac{\partial Y_p}{\partial \psi} \\ \frac{\partial Z_p}{\partial \psi} \end{bmatrix} = \begin{bmatrix} -s_\psi \, c_\theta & -s_\psi \, s_\theta \, s_\phi - c_\psi \, c_\phi & -s_\psi \, s_\theta \, c_\phi + c_\psi \, s_\phi \\ c_\psi \, c_\theta & c_\psi \, s_\theta \, s_\phi - s_\psi \, c_\phi & c_\psi \, s_\theta \, c_\phi + s_\psi \, s_\phi \\ 0 & 0 & 0 \end{bmatrix} \begin{bmatrix} x_{po} \\ y_{po} \\ z_{po} \end{bmatrix}
\end{gathered}
\tag{D.7}
$$